T·H·E
OHIO
STATE
UNIVERSITY

APPENDIX
JOINT SERVICES ELECTRONICS PROGRAM
Eleventh Annual Report

The Ohio State University

ElectroScience Laboratory

Department of Electrical Engineering
Columbus, Ohio 43212

Annual Report Appendix 720440-1
Contract No. N00014-88-K-0004
November 1988

DTIC
ELECTE
14 FEB 1989
S E D

Department of the Navy
Office of Naval Research
800 North Quincy Street
Arlington, Virginia 22217

89 2 13 285

NOTICES

When Government drawings, specifications, or other data are
used for any purpose other than in connection with a definitely
related Government procurement operation, the United States
Government thereby incurs no responsibility nor any obligation
whatsoever, and the fact that the Government may have formulated,
furnished, or in any way supplied the said drawings, specifications,
or other data, is not to be regarded by implication or otherwise as
in any manner licensing the holder or any other person or corporation,
or conveying any rights or permission to manufacture, use, or sell
any patented invention that may in any way be related thereto.

50272-101

REPORT DOCUMENTATION PAGE	1. REPORT NO.	2.	3. Recipient's Accession No.

4. Title and Subtitle	5. Report Date
APPENDIX - JOINT SERVICES ELECTRONICS PROGRAM - Eleventh Annual Report	November 1988
	6.

7. Author(s)	8. Performing Organization Rept. No.
Leon Peters, Jr.	720440-1 Appendix

9. Performing Organization Name and Address	10. Project/Task/Work Unit No.
The Ohio State University ElectroScience Laboratory 1320 Kinnear Road Columbus, Ohio 43212	
	11. Contract(C) or Grant(G) No
	(C)N00014-88-K-0004
	(G)

12. Sponsoring Organization Name and Address	13. Type of Report & Period Covered
Department of the Navy Office of Naval Research 800 North Quincy Street Arlington, VA 22217	Annual Report Appendix 10/1/87 thru 9/30/88
	14.

15. Supplementary Notes

16. Abstract (Limit: 200 words)

17. Document Analysis   a. Descriptors

b. Identifiers/Open-Ended Terms

c. COSATI Field/Group

(See ANSI–Z39.18)　　　　　　See Instructions on Reverse　　　　　　OPTIONAL FORM 272 (4–77)
(Formerly NTIS–35)
Department of Commerce

Contents

Accession For

NTIS GRA&I ☒
DTIC TAB ☐
Unannounced ☐
Justification___

By___
Distribution/
Availability Codes

Dist	Avail and/or Special
A-1	

INTRODUCTION

This Appendix contains the reprints published under JSEP in the time October 1987 to September 1988.

In addition to the reprints contained herein, there are 19 papers already accepted for publication during the next contract period, 12 papers submitted and 9 papers in preparation.

JSEP REFEREED JOURNAL PAPERS
PUBLISHED SEPTEMBER 1987 TO SEPTEMBER 1988

1. M.W. Ganz, R.T. Compton, Jr., "The Effects of Gaussian Interference on Communication Systems with Adaptive Arrays," *IEEE Transactions on Aerospace and Electronic Systems*, Vol. AES-23, No. 5, pp. 654- 663, September 1987.

2. A.S. Al-Ruwais, R.T. Compton, Jr., "Adaptive Array Behavior with Periodic Phase Modulated Interference," *IEEE Transactions on Aerospace and Electronic Systems*, Vol. AES-23, No. 5, pp. 602-611, September 1987.

3. M.W. Ganz, R.T. Compton, "Protection of a Narrow-Band BPSK Communication System with an Adaptive Array," *IEEE Transactions on Communications*, Vol., COM-35, No. 10, pp. 1005-1011, October 1987.

4. R.G. Rojas, "Comparison Between Two Asymptotic Methods," *IEEE Transactions on Antennas and Propagation*, Vol. AP-35, No. 12, December 1987.

5. R. Paknys and N. Wang, "Excitation of Creeping Waves on a Circular Cylinder with a Thick Dielectric Coating," *IEEE Transactions on Antennas and Propagation*, Vol. AP-35, No. 12, pp. 1487-1489, December 1987.

6. R.G. Rojas, "Weiner-Hopf Analysis of the EM Diffraction by an Impedance Discontinuity in a Planar Surface and by an Impedance Half-Plane," *IEEE Transactions on Antennas and Propagation*, Vol. AP-36, No. 1, pp. 71-83, January 1988.

7. A. Altintas, P.H. Pathak, M.C. Liang, "A Selective Modal Scheme for the Analysis of EM Coupling Into or Radiation from Large Open-Ended Waveguides," *IEEE Transactions on Antennas and Propagation*, Vol. AP-36, No. 1, pp. 84-96, January 1988.

8. R.T. Compton, Jr., "The Bandwidth Performance of a Two-element Adaptive Array with Tapped Delay-Line Processing," *IEEE Transactions on Antennas and Propagation*, Vol. AP-36, No. 1, pp. 5- 14, January 1988.

9. R.T. Compton, "The Relationship Between Tapped Delay-Line and FTT Processing in Adaptive Arrays," *IEEE Transactions on Antennas and Propagation*, Vol. AP-36, No. 1, pp. 15-26, January 1988.

10. R.G. Rojas, "Scattering by an Inhomogeneous Dielectric/Ferrite Cylinder of Arbitrary Cross-Section Shape – Oblique Incidence Case," *IEEE Transactions on Antennas and Propagation*, Vol. AP-36, No. 2, pp. 238-245, February 1988.

11. E.H. Newman, "An Overview of the Hybrid MM/Green's Function Method in Electromagnetics," *Proceedings of the IEEE*, Vol. 76, No. 3, pp. 270-282, March 1988.

12. E.H. Newman, J.L. Blanchard, "TM Scattering by an Impedance Sheet Extension of a Parabolic Cylinder," *IEEE Transactions on Antennas and Propagation*, Vol. AP-36, No. 4, pp. 527-534, April 1988.

13. R.G. Rojas, "Electromagnetic Diffraction of an Obliquely Incident Plane Wave Field by a Wedge with Impedance Faces," *IEEE Transactions on Antennas and Propagation*, Vol. AP-36, No. 7, pp. 956-970, July 1988.

14. R.G. Rojas, "Generalized Impedance Boundary Conditions for EM Scattering Problems," *Electronics Letters*, Vol. 24, No. 17, pp. 1093-1094, August 18, 1988.

15. E.H. Newman, "Simple Examples of the Method of Moments in Electromagnetics," *IEEE Transactions on Antennas and Propagation*, Vol. AP-31, No. 3, pp. 193-200, August 1988.

JSEP RELATED BOOK SECTIONS
PUBLISHED SEPTEMBER 1987 TO SEPTEMBER 1988

1. P.H. Pathak, "Techniques for High-Frequency Problems," in Antenna Handbook (Theory, Applications and Design), ed. Y.T. Lo and S.W. Lee, (0-442-25843-7), Van Nostrand Reinhold Publishers, New York, 1988.

2. R.G. Kouyoumjian, section on RCS in Antenna Theory, J.D. Kraus, McGraw-Hill Publishers, New York, 1988.

3. E.H. Newman, section on Moment Methods in Antenna Theory by J.D. Kraus, McGraw Hill Publishers, New York, 1988.

JSEP RELATED REFEREED JOURNAL PAPERS
ACCEPTED FOR PUBLICATION
SEPTEMBER 1987 TO SEPTEMBER 1988

1. C.W. Chuang and P.H. Pathak, "Ray Analysis of Modal Reflection for Three-Dimensional Open-Ended Waveguides," *IEEE Transactions on Antennas and Propagation.*

2. A. Nagamune and P.H. Pathak, "An Efficient Plane Wave Spectral Analysis to Predict the Focal Region Fields of Parabolic Reflector Antennas for Small and Wide Angle Scanning," *IEEE Transactions on Antennas and Propagation.*

3. S. Barkeshli, P.H. Pathak and M. Marin, "An Asymptotic Closed From Microstrip Surface Green's Function for the Efficient Moment Method Analysis of Mutual Coupling in Microstrip Antenna Arrays," *IEEE Transactions on Antennas and Propagation.*

4. L. Ersoy and P.H. Pathak, "An Asymptotic High Frequency Analysis of the Radiation by a Source on a Perfectly Conducting Convex Cylinder with an Impedance Surface Patch," *IEEE Transactions on Antennas and Propagation.*

5. R. Rojas and P.H. Pathak, "Diffraction of EM Waves Normally Incident on the Edge of a Thin Dielectric/Ferrite Half-Plane and Related Configurations," *IEEE Transactions on Antennas and Propagation.*

6. A.K. Dominek and L. Peters, Jr., "RCS Measurements of Small Circular Holes," *IEEE Transactions on Antennas and Propagation.*

7. O.M. Buyukdura, S.D. Goad and R.G. Kouyoumjian, "A Spherical Wave Representation of the Dyadic Green's Function for a Wedge," *IEEE Transactions on Antennas and Propagation.*

8. R. Tiberio, R. Manara, G. Pelosi and R.G. Kouyoumjian, "High Frequency EM Scattering of Plane Waves from Double Wedges," *IEEE Transactions on Antennas and Propagation.*

9. R. Tiberio, G. Pelosi, R. Manara and P.H. Pathak, "High Frequency Scattering from a Wedge with Impedance Faces Illuminated by a Line Source," *IEEE Transactions on Antennas and Propagation.*

10. P.H. Pathak and M.C. Liang, "On a Uniform Asymptotic Solution Valid Across Smooth Caustics of Rays Reflected by Smoothly Indented Boundaries," *IEEE Transactions on Antennas and Propagation.*

11. C.W. Chuang and M.C. Liang, "A Uniform High Frequency Asymptotic Analysis of the Diffraction by an Edge in a Curved Screen for Near Grazing Incidence," *J. Radio Science.*

12. J.H. Richmond, "Scattering by a Conducting Elliptic Cylinder with Dielectric Coating," *J. Radio Science.*

13. E.H. Newman, R.J. Marhefka, "Overview of Moment Method and Uniform Theory of Diffraction Method at the Ohio State University," *Proceedings of the IEEE.*

14. G. Turhan and D.L. Moffatt, "K-Pulse Estimation and Target Identification of Low-Q Radar Targets," *Wave Motion.*

15. C.W. Chuang, "Generalized Admittance for a slotted Parallel Plate Waveguide," *IEEE Transactions on Antennas and Propagation.*

16. R. Tiberio, G. Pelosi, G. Manara and P.H. Pathak, "A UTD Diffraction Coefficient for a Wedge with Impedance Faces Illuminated by a Line Source," *J. Radio Science.*

17. C.W. Chuang, P.H. Pathak, "Efficient Hybrid Combination of Asymptotic High Frequency and Modal Techniques for Analyzing the EM Scattering by Open Ended Semi-Infinite Circular and Rectangular Waveguides with Simple Interior Terminations," *IEEE Transactions on Antennas and Propagation.*

18. S. Barkeshli and P.H. Pathak, "A Useful Uniform Asymptotic Approximation for for the Planar Microstrip Green's Function," *IEEE Transactions on Antennas and Propagation.*

19. M. Marin, S. Barkeshli and P.H. Pathak, "Efficient Analysis of Planar Microstrip Geometries Using a Closed Form Asymptotic Representation of the Grounded Dielectric Slab Green's Function," *IEEE Transactions of Microwave Theory and Techniques.*

JSEP RELATED PAPERS
SUBMITTED FOR PUBLICATION
SEPTEMBER 1987 TO SEPTEMBER 1988

1. E.H. Newman and J. Blanchard, "Numerical Generation of Parabolic Cylinder Functions," *IEEE Transactions on Antennas and Propagation.*

2. E.H. Newman, "Generation of Wideband Data from the Method of Moments by Interpolating the Impedance Matrix," *IEEE Transactions on Antennas and Propagation.*

3. P.H. Pathak and A. Altintas, "An Efficient High Frequency Analysis of Modal Reflection and Transmission Coefficients for a Class of Waveguide Discontinuities," *J. Radio Science.*

4. K.D. Trott, P.H. Pathak and F. Molinet, "A Uniform GTD Type Analysis of EM Plane Wave Scattering by a Fully Illuminated Perfectly Conducting Cone," *IEEE Transactions on Antennas and Propagation.*

5. S. Barkeshli and P.H. Pathak, "Radially Propagating and Steepest Descent Path Representation of the Planar Microstrip Dyadic Green's Function," *IEEE Transactions on Antennas and Propagation.*

6. M. Marin, S. Barkeshli and P.H. Pathak, "On the Location of Surface and Leaky Wave Poles for the Grounded Dielectric Slab," *IEEE Transactions on Antennas and Propagation.*

7. M. Marin, S. Barkeshli and P.H. Pathak, "Efficient Analysis of Planar Microstrip Geometries Using a Closed-Form Asymptotic Representation of the Green's Function," *IEEE Transactions on Antennas and Propagation.*

8. P.H. Pathak and R.J. Burkholder, "Modal, Ray and Beam Techniques for Analyzing the EM Scattering by Open-Ended Waveguide Cavities," *IEEE Transactions on Antennas and Propagation.*

9. J.H. Richmond, "Axial Slot Antenna on Dielectric-Coated Elliptic Cylinder," *IEEE Transactions on Antennas and Propagation.*

10. R. Rojas and Z. Al-Hekail, "Generalized Impedance/Resistive Boundary Conditions for EM Scattering Problems," *Radio Science*, August 1988.

11. H.T. Kim and N. Wang, "UTD Solution for the Electromagnetic Scattering by a Circular Cylinder with Thin Lossy Coatings," *IEEE Transactions on Antennas and Propagation*.

12. S. Barkeshli and P.H. Pathak, "An Efficient Exact Integral Representation for the Planar Microstrip Green's Function," *J. Radio Science*.

JSEP RELATED PAPERS
IN PREPARATION FOR PUBLICATION
SEPTEMBER 1987 TO SEPTEMBER 1988

1. E.H. Newman, "Plane Wave Scattering by a Material Coated Parabolic Cylinder."

2. E.H. Newman (edited by), *IEEE Press Collection of Reprints* "Application of the Moment of Methods in EM Radiation and Scattering."

3. J.H. Richmond, "On Variational Properties of the Moment Method."

4. M.C. Liang, P.H. Pathak and C.W. Chuang, "An Analysis of the Scattering by an Open-Ended Dielectric Filled Cavity in a Ground Plane," *IEEE Transactions on Antennas and Propagation.*

5. K.C. Hill and P.H. Pathak, "A UTD Analysis of the Diffraction of Surface Rays by an Edge in an Edge in an Otherwise Smooth Convex Surface for Non-Grazing Angles of Incidence," *J. Radio Science.*

6. H. Ly, H. Shamansky and R.G. Kouyoumjian, "Closed Form Solutions for the Elements of the Voltage Matrix in the Moment Method Solution of Linear Antennas," *IEEE Transactions on Antennas and Propagation.*

7. R.G. Rojas, Ling Miao Chou and P.H. Pathak, "Generalized Impedance Boundary Conditions for the Diffraction by a Dielectric Half Plane on a Conducting Ground Plane," *J. Radio Science.*

8. R.G. Rojas and P.H. Pathak, "Diffraction by the Edge of a Thin Dielectric/Ferrite Half Plane and Related Configurations for the Case of Skew Incidence at the Edge," *IEEE Transactions on Antennas and Propagation.*

9. R.J. Burkholder, C.W. Chuang and P.H. Pathak, "An Analysis of the EM Scattering by an S-Shaped Open Ended Waveguide with an Interior Termination," *IEEE Transactions on Antennas and Propagation.*

JSEP RELATED CONFERENCES/ORAL PRESENTATIONS
SEPTEMBER 1987 TO SEPTEMBER 1988

1. S. Barkeshli and P.H. Pathak, "An Efficient Moment Method Analysis of Finite Phased Arrays of Microstrip Dipoles Using an Asymptotic Closed Form Approximation for the Planar Microstrip Green's Function," 1988 IEEE AP-S International Symposium and URSI Symposium in Syracuse, New York, during June 6-10, 1988.

2. P.H. Pathak and M.C. Liang, "On a Uniform Asymptotic Solution Valid Across Smooth Caustics of Rays Reflected by Smoothly Indented Boundaries," 1988 IEEE AP-S International Symposium and URSI Symposium in Syracuse, New York during June 6-10, 1988.

3. M.C. Liang, P.H. Pathak and C.W. Chuang, "A Generalized UTD Analysis of the Diffraction by a Wedge with Convex Faces to Include Surface Ray Effects and Grazing Angles of Incidence/Diffraction," 1988 IEEE AP-S International Symposium and URSI Symposium in Syracuse, New York during June 6-10, 1988.

4. R.G. Rojas, L.M. Chou and P.H. Pathak, "Diffraction by a Magnetic Dielectric Half-Plane Using Generalized Impedance/Resistive Boundary Conditions," 1988 IEEE AP-S International Symposium and URSI Symposium in Syracuse, New York during June 6-10, 1988.

5. N. Wang, "A Simple Pulse-Galerkin Formulation for the Scattering by a Coated Cylinder," 1988 IEEE AP-S International Symposium and URSI Symposium in Syracuse, New York during June 6-10, 1988.

6. S. Kato and N. Wang, "Scattering of a Plane Wave from a Coated Circular Cylinder at Oblique Incidence – GTD Solution," 1988 IEEE AP-S International Symposium and URSI Symposium in Syracuse, New York during June 6-10, 1988.

7. E.H. Newman, "Generation of Wideband Data from the Method of Moments by Interpolating the Impedance Matrix," 1988 IEEE AP-S International Symposium and URSI Symposium in Syracuse, New York during June 6-10, 1988.

JSEP RELATED M.Sc. THESES AND PH.D. DISSERTATIONS

Dissertations:

1. S. Barkeshli, "Efficient Approaches for Evaluating the Planar Microstrip Green's Function and Its Applications to the Analysis of Microstrip Antennas," Summer 1988.

2. M.C. Liang, "A Generalized Uniform GTD Ray solution for the Diffraction by a Perfectly-Conducting Wedge with Convex Faces," Summer 1988.

Theses:

1. S. Kato, "A GTD Solution to Scattering of Plane Waves at Oblique Incidence by a Dielectric Coated Circular Cylinder," Spring 1988.

2. M. Kragalott, "Method of Moments Solution to TM Scattering by a General Cylinder," Summer 1988.

11

REPRINTS
JSEP REFEREED JOURNAL PAPERS
PUBLISHED SEPTEMBER 1987 TO SEPTEMBER 1988

12

The Effects of Gaussian Interference on Communication Systems with Adaptive Arrays

M.W. Ganz

R.T. Compton, Jr.

The Effects of Gaussian Interference on Communication Systems with Adaptive Arrays

M.W. GANZ
M.I.T. Lincoln Laboratory

R.T. COMPTON, JR.
The Ohio State University

The performance of a bandlimited binary phase-shift-keyed (BPSK) communication system is examined when the received BPSK signal is corrupted by both thermal noise and a directional Gaussian noise interfering signal. The system uses an LMS adaptive array to suppress this interference. The effects of signal power levels, arrival angles, bandwidths, and the array bandwidth are examined. The performance of a system that uses tapped delay lines for the array weights is also examined. It is shown that the performance of a system with tapped delay lines is not affected by the interference bandwidth for a single interferer.

I. INTRODUCTION

Adaptive arrays can be used to protect communication systems from interference. This protection is achieved when the array steers pattern nulls on the interfering signals and pattern beams on desired signals.

Methods for employing the LMS adaptive array [1] in several types of digital communication systems have been developed. Th' ~ ., 's include conventional binary phase-shift-key.ng (BPSK) [2], quadrature phase-shift-keying (QPSK) [3], and binary frequency-shift-keying (FSK) [4, 5]. Recently the authors have examined the performance of each of these communication systems with adaptive arrays when the desired signal is corrupted by CW interference. In [6] the performance of the LMS array with BPSK signaling and CW interference has been examined using the bit error probability at the receiver output as the performance measure. The results presented in [7] show that the performance of BPSK, QPSK, FSK, and binary differential PSK systems with CW interference are similar. These systems generally perform best when the array input bandwidth is as small as possible and when the interference arrives from an angle outside the main beam of the quiescent array pattern. In [7] and [8] the effects of the array bandwidth on system performance are more closely examined.

In this paper we calculate the performance of a BPSK communication system with an LMS adaptive array when the desired signal is corrupted by both thermal noise and a directional Gaussian interference signal. In general, the performance of an adaptive array is poorer with broadband interference than with CW interference [9]. Also, the degradation with broadband interference is largest when the interference power is large and when the interference arrives near endfire. Here, we examine the effects of the interference bandwidth, the array bandwidth, the signal power levels, and the signal arrival angles. We show that, for a fixed input interference power, the system performance becomes worse as the interference bandwidth increases, up to the point where the interference bandwidth exceeds the desired signal bandwidth.

In [1] and [9–11] the use of tapped delay lines (TDLs) behind the elements in an LMS array was suggested. The TDL LMS array can reject broadband interference since the weights can be set to optimize performance over a band of frequencies. In this paper, we also examine the performance of the communication system with a TDL LMS array. We show that, with a single broadband interference source, this array achieves the same performance as the standard LMS array with a zero-bandwidth interferer.

In Section II we describe the BPSK communication system, the LMS array, and the TDL LMS array. In Section III we present the results from the performance calculations. Finally, in Section IV we present the conclusions.

II. PROBLEM FORMULATION

Consider the BPSK communication system shown in Fig. 1. In this system the baseband NRZ-L [12] signal is filtered so that the signal at the filter output satisfies the

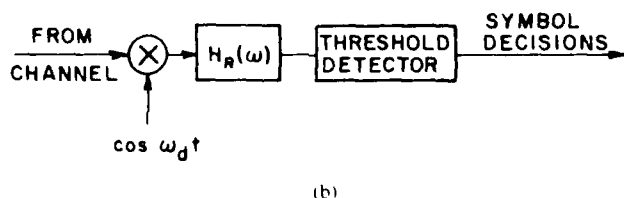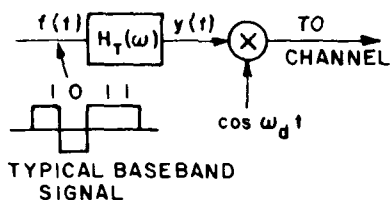TYPICAL BASEBAND
SIGNAL

(a)

(b)

Fig. 1   BPSK communication system. (a) Transmitter (b) Receiver.

Nyquist pulse shaping criterion [13]. In order to achieve the same bit error probability as unfiltered BPSK in white Gaussian noise with no intersymbol interference (ISI) the baseband bandwidth of the system must be at least $1/2T$ Hz (the Nyquist bandwidth), where T is the bit duration [14]. For simplicity, we assume here that the transmitted signal occupies the Nyquist equivalent channel with this minimum bandwidth. Therefore, the (double sideband) radio frequency signal that is transmitted across the channel has a rectangular spectrum of width $1/T$ Hz.

The baseband transmit and detector filters required to produce a rectangular signal spectrum are not physically realizable. However, good approximations to many of the members of the raised cosine family of filters are realizable and can be used to obtain signals that satisfy the Nyquist pulse shaping criterion. Some of the practical aspects of the design of narrowband BPSK systems are discussed by Bayless et al. [15] and Feher [16].

At the receiving end, the detector filter output is sampled at the end of each bit interval and a bit decision is made based upon the sign of the sample. Since we have assumed that the baseband signal occupies the rectangular Nyquist equivalent channel, the detector filter is an ideal low-pass filter (LPF) with a cutoff frequency of $1/2T$ Hz. The baseband signal at this filter output consists of a series of sinc (i.e., $\sin(x)/x$) pulses centered about the sampling instants. The sinc pulse corresponding to the kth bit has zero crossings at the sampling instants for every other bit. Therefore there is no ISI for this signaling method.

When the desired signal is corrupted by zero-mean Gaussian noise and zero-mean Gaussian interference, the bit error probability $P(e)$ at the detector output is given by

$$P(e) = \text{erfc}\left(\sqrt{\frac{2p_d}{p_n + p_i}}\right) \tag{1}$$

where p_d, p_i, and p_n are the desired, interfering, and noise powers at the output of the detector LPF and $\text{erfc}(x)$ is the complementary error function defined by

$$\text{erfc}(x) = \frac{1}{\sqrt{2\pi}} \int_x^\infty \exp(-x^2/2)dz. \tag{2}$$

We now determine the performance of the communication system described above when we add an LMS adaptive array to the system at the detector input. A three-element LMS adaptive array is shown in Fig. 2.
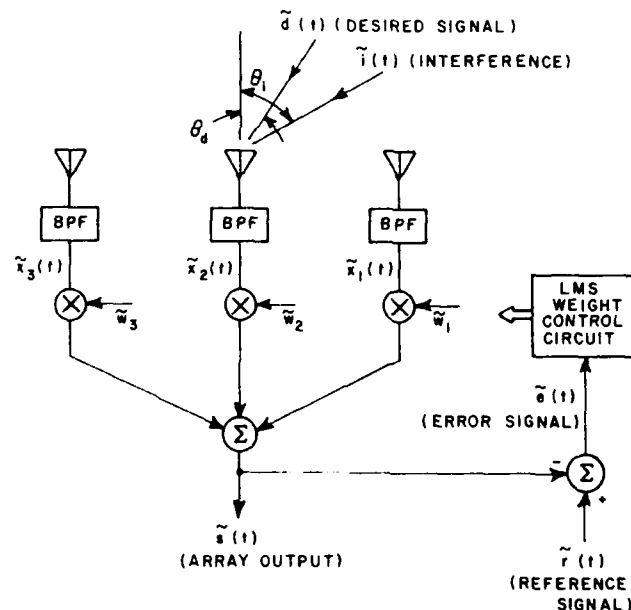
Fig. 2.   LMS adaptive array.

The signals that arrive at the element inputs are filtered by ideal bandpass filters (BPFs) which limit the thermal noise at the array input and reject out-of-band interference. We denote by X the vector composed of the analytic signals at the BPF outputs; that is, $X = [\tilde{x}_1(t) \ \tilde{x}_2(t) \ \tilde{x}_3(t)]^T$, where superscript T denotes the transpose. We similarly define the weight for the array by W, where $W = [\tilde{w}_1 \ \tilde{w}_2 \ \tilde{w}_3]^T$. The array output signal $\tilde{s}(t)$ is the weighted sum of the array input signals,

$$\tilde{s}(t) = W^T X. \tag{3}$$

We assume that the desired, interfering, and thermal noise signals at the array input are uncorrelated zero-mean signals. We divide the input signal vector into its desired signal, interference, and noise components,

$$X = X_d + X_i + X_n \tag{4}$$

where $X_d = [\tilde{d}(t) \ \tilde{d}(t - T_d) \ \tilde{d}(t - 2T_d)]$, $X_i = [\tilde{i}(t) \ \tilde{i}(t - T_i) \ \tilde{i}(t - 2T_i)]$, and $X_n = [\tilde{n}_1(t) \ \tilde{n}_2(t) \ \tilde{n}_3(t)]$. In these expressions $\tilde{d}(t)$ and $\tilde{i}(t)$ are the analytic desired and interfering signals at the output of the BPF at the first

element and $\bar{n}_1(t)$, $\bar{n}_2(t)$, and $\bar{n}_3(t)$ are the noise signals at the BPF outputs. T_d and T_i are the interelement time delays for the desired and interfering signals, respectively.

We assume that the thermal noise signals at the input to each BPF is white with a two-sided PSD of $\eta/2$ everywhere. The noise signals at the filter outputs are mutually uncorrelated Gaussian random processes each with power σ^2. We define the autocorrelation function for the thermal noise process at the output of the jth BPF as

$$R_{\bar{n}}(\tau) = E[\bar{n}_j^*(t)\bar{n}_j(t+\tau)]$$

$$= \sigma^2 \operatorname{sinc}(\pi B \tau) \exp(j\omega_d\tau) \quad (5)$$

where $E[\cdot]$ denotes the expected value, the asterisk denotes the complex conjugate, B is the BPF bandwidth in Hz, and

$$\sigma^2 = \eta B. \quad (6)$$

The output of the LMS array is subtracted from a locally generated reference signal, $\bar{r}(t)$, to produce an error signal, $\bar{e}(t)$. The steady-state LMS weights minimize the mean-square value of this error signal. The steady state LMS weight vector is given by [1],

$$W = \Phi^{-1}S \quad (7)$$

where Φ is the covariance matrix,

$$\Phi = E[X^*X^T]. \quad (8)$$

S, the reference correlation vector, is given by

$$S = E[X^*\bar{r}(t)]. \quad (9)$$

Since the desired, interference, and noise signals are independent zero-mean signals we can separate the covariance matrix into three components,

$$\Phi = \Phi_d + \Phi_i + \Phi_n \quad (10)$$

where $\Phi_d = E[X_d^*X_d^T]$, $\Phi_i = E[X_i^*X_i^T]$, and $\Phi_n = E[X_n^*X_n^T]$. These matrices are given by

$$\Phi_d = \begin{pmatrix} R_{\bar{d}}(0) & R_{\bar{d}}(-T_d) & R_{\bar{d}}(-2T_d) \\ R_{\bar{d}}(T_d) & R_{\bar{d}}(0) & R_{\bar{d}}(-T_d) \\ R_{\bar{d}}(2T_d) & R_{\bar{d}}(T_d) & R_{\bar{d}}(0) \end{pmatrix} \quad (11)$$

$$\Phi_i = \begin{pmatrix} R_i(0) & R_i(-T_i) & R_i(-2T_i) \\ R_i(T_i) & R_i(0) & R_i(-T_i) \\ R_i(2T_i) & R_i(T_i) & R_i(0) \end{pmatrix} \quad (12)$$

$$\Phi_n = \begin{pmatrix} R_{\bar{n}}(0) & 0 & 0 \\ 0 & R_{\bar{n}}(0) & 0 \\ 0 & 0 & R_{\bar{n}}(0) \end{pmatrix} \quad (13)$$

where $R_{\bar{d}}(\tau)$, and $R_i(\tau)$ are the autocorrelation functions for the desired and interfering signals, respectively.

Fig. 3 shows the power spectral density (PSD) of $\bar{d}(t)$. This spectrum is centered about the frequency ω_d and the signal bandwidth is $1/T$ Hz. The PSD is equal to E_b W/Hz everywhere in this region, where E_b is the received energy per bit at each element input. We define
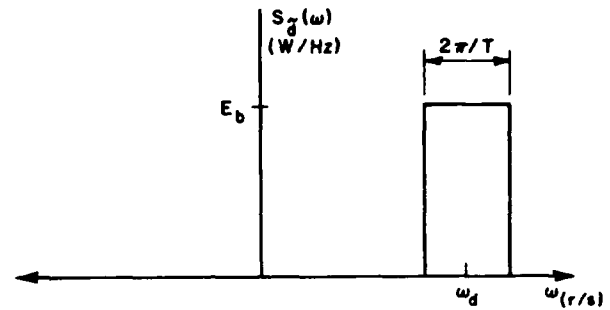

Fig. 3. PSD of transmitted signal.

the relative bandwidth B_d of the desired signal as the ratio of the signal bandwidth to the center frequency, that is,

$$B_d = \frac{(2\pi/T)}{\omega_d}. \quad (14)$$

The autocorrelation function for the desired signal is the inverse Fourier transform of the PSD shown in Fig. 3. This autocorrelation function is given by

$$R_{\bar{d}}(\tau) = E[\bar{d}^*(t)\bar{d}(t+\tau)]$$

$$= \frac{E_b}{T} \operatorname{sinc}\left(\frac{\pi\tau}{T}\right) \exp(j\omega_d\tau). \quad (15)$$

The interference is assumed to be a zero-mean Gaussian random process with a PSD that is constant in a bandwidth $\Delta\omega_i$ centered about the desired signal center frequency.[1] We define E_i to be the interference energy received by each element during each bit interval. We define the relative bandwidth of the interference as

$$B_i = \Delta\omega_i/\omega_d. \quad (16)$$

If the interference bandwidth is wider than the bandwidth of the element BPFs, we replace the numerator in (16) with the BPF bandwidth so that B_i represents the relative bandwidth of the interference at the BPF outputs. The autocorrelation function for the interference is given by

$$R_i(\tau) = E[\bar{i}^*(t)\bar{i}(t+\tau)]$$

$$= \sigma_i^2 \operatorname{sinc}\left(\frac{B_i\omega_i\tau}{2}\right) \exp(j\omega_i\tau) \quad (17)$$

where σ_i^2 is the power in the interfering signal at the output of each element BPF.

We assume one-half wavelength spacing between elements at the desired signal center frequency. We further assume that the desired signal is incident from an angle of θ_d (measured from the broadside direction) and a single interfering signal is incident from angle θ_i. For the desired and interfering signals the interelement propagation delays are given by

$$T_d = (L/c) \sin \theta_d \quad (18)$$

[1]It is shown in [7] that the signal power levels at the array output do not change appreciably even if the interference and desired signal center frequencies differ by a few percent.

and

$$T_i = (L/c) \sin \theta_i \tag{19}$$

respectively, where L is the element spacing and c is the propagation velocity.

The interelement propagation delays produce corresponding interelement phase shifts. For one-half wavelength element spacing these phase shifts are given by

$$\phi_d = \pi \sin \theta_d \tag{20}$$

and

$$\phi_i = \pi \sin \theta_i \tag{21}$$

respectively.

Using (11), and (14)–(21) we can show that the desired signal, interference, and noise covariance matrices are given by

the array output using (9). It is straightforward to show that the power in the desired, interfering, and noise signals are given by

$$P_d = \frac{1}{2} W^+ \Phi_d W \tag{26}$$

$$P_i = \frac{1}{2} W^+ \Phi_i W \tag{27}$$

$$P_n = \frac{1}{2} W^+ \Phi_n W \tag{28}$$

where $^+$ denotes the conjugate transpose.

From these power levels we can determine p_d, p_i, and p_n, the power levels at the output of the detector filter. The desired signal power at this filter output is given by

$$p_d = P_d/4. \tag{29}$$

$$\Phi_d = \frac{E_b}{T} \begin{pmatrix} 1 & \mathrm{sinc}\left(\dfrac{B_d\phi_d}{2}\right) e^{-j\phi_d} & \mathrm{sinc}(B_d\phi_d) e^{-j2\phi_d} \\ \mathrm{sinc}\left(\dfrac{B_d\phi_d}{2}\right) e^{j\phi_d} & 1 & \mathrm{sinc}\left(\dfrac{B_d\phi_d}{2}\right) e^{-j\phi_d} \\ \mathrm{sinc}(B_d\phi_d) e^{j2\phi_d} & \mathrm{sinc}\left(\dfrac{B_d\phi_d}{2}\right) e^{j\phi_d} & 1 \end{pmatrix} \tag{22}$$

$$\Phi_i = \frac{E_i}{T} \begin{pmatrix} 1 & \mathrm{sinc}\left(\dfrac{B_i\phi_i}{2}\right) e^{-j\phi_i} & \mathrm{sinc}(B_i\phi_i) e^{-j2\phi_i} \\ \mathrm{sinc}\left(\dfrac{B_i\phi_i}{2}\right) e^{j\phi_i} & 1 & \mathrm{sinc}\left(\dfrac{B_i\phi_i}{2}\right) e^{-j\phi_i} \\ \mathrm{sinc}(B_i\phi_i) e^{j2\phi_i} & \mathrm{sinc}\left(\dfrac{B_i\phi_i}{2}\right) e^{j\phi_i} & 1 \end{pmatrix} \tag{23}$$

$$\Phi_n = \sigma^2 I \tag{24}$$

where I is the 3×3 identity matrix. The three matrices given in (21)–(24) are added to determine the covariance matrix Φ.

We assume the reference signal is perfectly correlated with the desired signal at the input to the first element input and uncorrelated with the interference and noise. Methods for generating a reference signal for the array with phase-shift-keyed modulation are described in [2] and [3]. The reference correlation vector, from (9), is given by

$$S = \mu \begin{pmatrix} 1 \\ R_d(T_d) \\ R_d(2T_d) \end{pmatrix} \tag{25}$$

where μ is a constant which is determined from the amplitudes of the reference signal and the desired signal.

Now that we have determined Φ and S we can determine the array weights using (7) and the signals at

The factor of 1/4 in this equation is caused by the power loss of 1/2 that occurs during both the multiplication (i.e., the heterodyning to baseband) and filtering processes in the detector.

The noise power at the detector output is given by

$$p_n = \frac{1}{4} P_n \left(\frac{1}{TB}\right). \tag{30}$$

The ratio $1/TB$ in this equation is the ratio of the detector filter bandwidth ($1/2T$ Hz) to the baseband noise bandwidth ($B/2$ Hz). This ratio is the fraction of the thermal noise signal that is not rejected by the detector filter.

If the baseband interference bandwidth is less than or equal to the detector LPF bandwidth (i.e., if $B_i \leq B_d$), then $p_i = P_i/4$. However, if the interference bandwidth is greater than the detector filter bandwidth then we must

calculate the portion of the interference power at the array output that lies in the frequency band to which the detector is sensitive. We note that the interference PSD at the array output is not necessarily white in this passband since the array acts as a transversal filter to the interfering signal [7]. We can calculate the interference power at the array output in the frequency band of interest using (27) and (12). However, for the interference autocorrelation function $R_i(\tau)$ in (12) we use the autocorrelation function of the portion of the interference that lies in the band of frequencies to which the detector is sensitive. This autocorrelation function is given by

$$R_i(\tau) = \sigma_i^2 \left(\frac{B_d}{B_i}\right) \text{sinc}\left(\frac{\pi\tau}{T}\right) . \tag{31}$$

With this substitution in (12) when $B_i > B_d$, p_i is equal to $P_i/4$, where P_i is given by (27). Once we have found p_d, p_i, and p_n we can use (1) to calculate $P(e)$.

Before we present the results of performance calculations for the system described above we describe a modified LMS array that offers improved performance in some signal environments. As we shall show in Section III, the conventional LMS array (i.e., the array described above) often has difficulty nulling interference with nonzero bandwidth. Improved performance against broadband interference can be achieved if TDL filters are used as the weighting elements for the array. Fig. 4 is a block diagram of a three-element TDL LMS array. For this array each element weight is implemented by a TDL with a single quarter-wavelength delay element and two complex weights. Compton [11] examined the optimum delay line length and number of taps for suppression of a single broadband interferer. This study indicated that the length of the delay lines is not critical as long as it is less than $\lambda/4B$, where λ is the signal wavelength and B is the bandwidth. Also, extremely short delay lines should be avoided since they require a larger dynamic range for the weights. Compton also shows that, with a single interferer with $B_i \le 0.5$, an array with 2-tap TDL weights has essentially the same output signal-to-interference-plus-noise ratio (SINR) that a conventional LMS array has with narrowband ($B_i \approx 0$) interference.
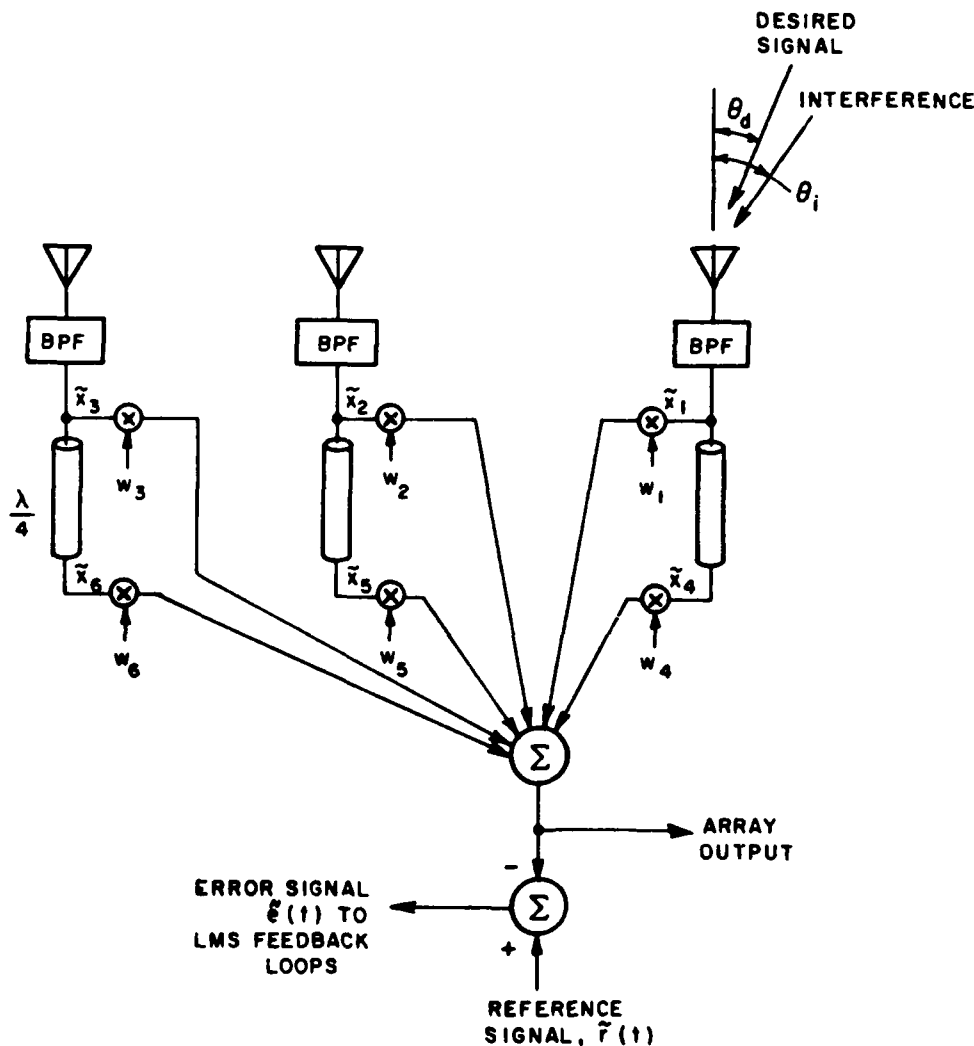

Fig. 4. Tapped delay line LMS array.

For the array shown in Fig. 4 we define the signals at the tap outputs by $\tilde{x}_1$ through $\tilde{x}_6$. These signals are given by

$$\tilde{x}_1(t) = \tilde{d}(t) + \tilde{i}(t) + \tilde{n}_1(t) \tag{32}$$

$$\tilde{x}_2(t) = \tilde{d}(t - T_d) + \tilde{i}(t - T_i) + \tilde{n}_2(t) \tag{33}$$

$$\tilde{x}_3(t) = \tilde{d}(t - 2T_d) + \tilde{i}(t - 2T_i) + \tilde{n}_3(t) \tag{34}$$

$$\tilde{x}_4(t) = \tilde{x}_1(t - \delta) \tag{35}$$

$$\tilde{x}_5(t) = \tilde{x}_2(t - \delta) \tag{36}$$

$$\tilde{x}_6(t) = \tilde{x}_3(t - \delta) \tag{37}$$

where δ is the delay produced by each delay line.

The 6×6 covariance matrices for the desired, interfering, and noise signals are given by

III. RESULTS

In this section we present the results from performance calculations for communication systems that use conventional LMS array and the TDL LMS array with directional Gaussian interference. Fig. 5 shows the performance of the system using a conventional LMS array for $\theta_d = 0°$, $\theta_i = 80°$, $B_d = 0.1$, $B = 1/T$, and $E_h/\eta = 8$ dB.[2] For a given value of E_i/η the total interference power at the array input is the same for each B_i value. From Fig. 5 we see that $P(e)$ increases slightly with E_i/η; however, the system performance is approximately equal for each of the interference bandwidths considered. For the cases shown in this figure the interference is located outside the main beam of the quiescent antenna pattern. In these cases the array

$$\Phi_d = \begin{pmatrix} R_d(0) & R_d(-T_d) & R_d(-2T_d) & R_d(-\delta) & R_d(-T_d-\delta) & R_d(-2T_d-\delta) \\ R_d(T_d) & R_d(0) & R_d(-T_d) & R_d(T_d-\delta) & R_d(-\delta) & R_d(-T_d-\delta) \\ R_d(2T_d) & R_d(T_d) & R_d(0) & R_d(2T_d-\delta) & R_d(T_d-\delta) & R_d(-\delta) \\ R_d(\delta) & R_d(-T_d+\delta) & R_d(-2T_d+\delta) & R_d(0) & R_d(-T_d) & R_d(-2T_d) \\ R_d(T_d+\delta) & R_d(\delta) & R_d(-T_d+\delta) & R_d(T_d) & R_d(0) & R_d(-T_d) \\ R_d(2T_d+\delta) & R_d(T_d+\delta) & R_d(\delta) & R_d(2T_d) & R_d(T_d) & R_d(0) \end{pmatrix} \tag{38}$$

$$\Phi_i = \begin{pmatrix} R_i(0) & R_i(-T_i) & R_i(-2T_i) & R_i(-\delta) & R_i(-T_i-\delta) & R_i(-2T_i-\delta) \\ R_i(T_i) & R_i(0) & R_i(-T_i) & R_i(T_i-\delta) & R_i(-\delta) & R_i(-T_i-\delta) \\ R_i(2T_i) & R_i(T_i) & R_i(0) & R_i(2T_i-\delta) & R_i(T_i-\delta) & R_i(-\delta) \\ R_i(\delta) & R_i(-T_i+\delta) & R_i(-2T_i+\delta) & R_i(0) & R_i(-T_i) & R_i(-2T_i) \\ R_i(T_i+\delta) & R_i(\delta) & R_i(-T_i+\delta) & R_i(T_i) & R_i(0) & R_i(-T_i) \\ R_i(2T_i+\delta) & R_i(T_i+\delta) & R_i(\delta) & R_i(2T_i) & R_i(T_i) & R_i(0) \end{pmatrix} \tag{39}$$

$$\Phi_n = \begin{pmatrix} R_n(0) & 0 & 0 & R_n(-\delta) & 0 & 0 \\ 0 & R_n(0) & 0 & 0 & R_n(-\delta) & 0 \\ 0 & 0 & R_n(0) & 0 & 0 & R_n(-\delta) \\ R_n(\delta) & 0 & 0 & R_n(0) & 0 & 0 \\ 0 & R_n(\delta) & 0 & 0 & R_n(0) & 0 \\ 0 & 0 & R_n(\delta) & 0 & 0 & R_n(0) \end{pmatrix} \tag{40}$$

We now can calculate the covariance matrix for the composite input signal using (10).

The reference correlation vector is given by

$$S = \mu \begin{pmatrix} R_d(0) \\ R_d(T_d) \\ R_d(2T_d) \\ R_d(\delta) \\ R_d(T_d+\delta) \\ R_d(2T_d+\delta) \end{pmatrix} \tag{41}$$

Now that we have determined Φ and S we can determine the array weights for the TDL LMS array using (7) and the signals at the array output using (3). We then can calculate the bit error probability for the detector exactly as we did for the system using the conventional LMS array.

effectively suppresses the interference for each of the B_i values shown.

Fig. 6 shows the system performance when θ_i is reduced to $40°$. All other parameters are the same as those of Fig. 5. From Fig. 6 we see that the system performance becomes worse as the interference bandwidth increases. This sensitivity to interference bandwidth becomes most pronounced when the input INR is greater than about 10 dB. Fig. 7 shows the performance when θ_i is reduced further to $10°$. We see here that $P(e)$ increases by more than 5 orders of magnitude at large values of

[2]Note that E_h, η is the per-element signal-to-noise ratio (SNR). The three-element array with no interference provides a 4.77 dB SNR improvement. Hence the $P(e)$ value at the left-hand side of the curves represents the BPSK detector when the array output SNR is 12.77 dB.
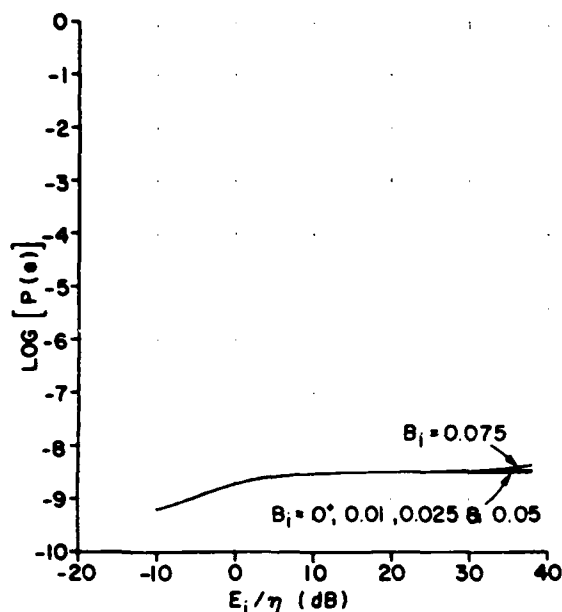
Fig. 5. Performance of three-element LMS array for several interference bandwidths. ($\theta_d = 0°$, $\theta_i = 80°$, $B_d = 0.1$, $B = 1/T$, $E_b/\eta = 8$ dB.)

Fig. 7. Performance of three-element LMS array for several interference bandwidths ($\theta_d = 0°$, $\theta_i = 10°$, $B_d = 0.1$, $B = 1/T$, $E_b/\eta = 8$ dB.)
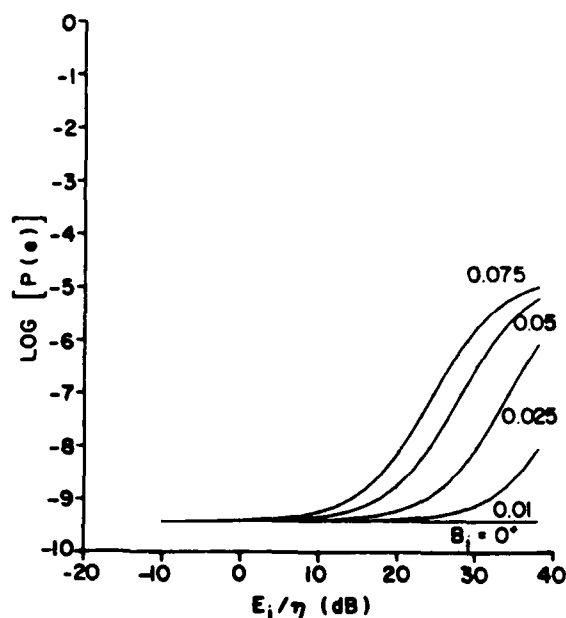

Fig. 6. Performance of a three-element LMS array for several interference bandwiths. ($\theta_d = 0°$, $\theta_i = 40°$, $B_d = 0.1$, $B = 1/T$, $E_b/\eta = 8$ dB.)

E_i/η for each of the interference bandwidths considered.[2] The increase in $P(e)$ for INR values below about 10 dB is caused by the insertion loss for the desired signal that occurs when the array forms the null on the interference. An array with more elements would have better resolution and would be better able to steer pattern nulls and maxima close together.

[3]The smallest bandwidth considered is labeled 0^+ to indicate a very small but finite interference bandwidth. If the interference bandwidth were truly 0, the interference would be a CW signal and not an ergodic Gaussian random process as we have assumed.
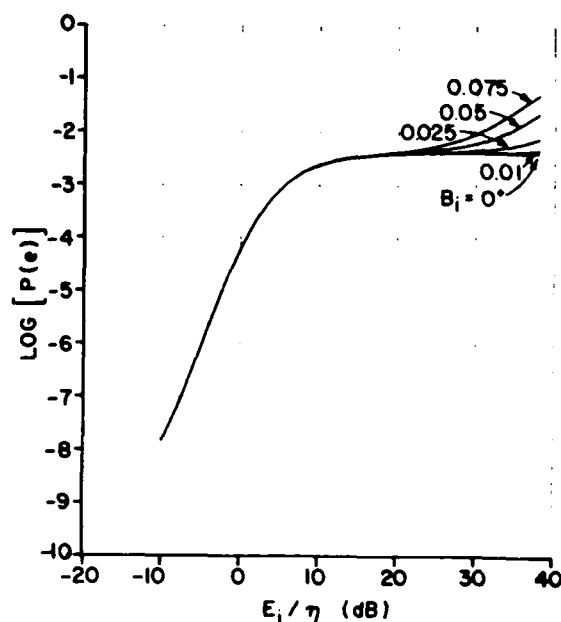
Two somewhat conflicting processes occur as we move the interference arrival angle from 80° to 10°. First, the system performance generally decreases as we move the desired and interfering signals closer together. This decrease is caused by the increase in insertion loss for the desired signal as we move the pattern null closer to the desired signal direction. The second process that occurs as we move the interference closer to the broadside direction is the improved ability of the array to steer a broadband null on the interference. This ability is a result of the reduced interelement propagation time for the interference for small θ_i values. In the limiting case, when $\theta_i = 0°$ (and $T_i = 0$), the array can steer an infinite bandwidth null on the interference.

From Figs. 6 and 7 we see that the system performance becomes worse as the interference bandwidth increases. However, in each of the cases shown in these figures, the interference lies totally within the bandpass of both the input BPFs and the detector LPF. In order to better understand the effects of the array input bandwidth and the interference bandwidth on the system performance, we examine this performance for 4 cases:

Case A: $B_d = 0.1$, $0^+ \leq B_i \leq 0.075$, $B = 1/T$.
Case B: $B_d = 0.01$, $0^+ \leq B_i \leq 0.075$, $B = 1/T$.
Case C: $B_d = 0.1$, $0^+ \leq B_i \leq 0.075$, $B = 20/T$.
Case D: $B_d = 0.01$, $0^+ \leq B_i \leq 0.075$, $B = 20/T$.

In each case $\theta_d = 40°$, $\theta_i = 60°$, and $E_d/\eta = 8$ dB. In case A the array bandwidth is equal to the desired signal bandwidth and the interference bandwidth is always less than the array bandwidth. For Case B the desired signal bandwidth is reduced by a factor of 10. The array input bandwidth is also reduced by this factor since $B = 1/T$ in both cases A and B. In case B some of the interference signal is blocked by the input BPFs when

B_i is greater than 0.01. $B = 20/T$ for cases C and D. The other variables are the same as in cases A and B, respectively.

Fig. 8 shows the system performance for case A. From this figure we see that the system becomes sensitive to the bandwidth of the signal for values of E_i/η greater than approximately 10 dB.

we had for case A for these B_i values.[3] For the other cases shown in this figure the input BPFs reject some of the interference and the performance improves as the interference bandwidth increases. Therefore, for the minimum bandwidth system (i.e., when $B = 1/T$) a fixed-power interference signal is most disrupting when its bandwidth is equal to the desired signal bandwidth.

Fig. 10 shows the results for Case C. As in Case A, the interference is passed by both the input BPFs and the

Fig. 8   Performance of three-element LMS array for several interference bandwidths, case A
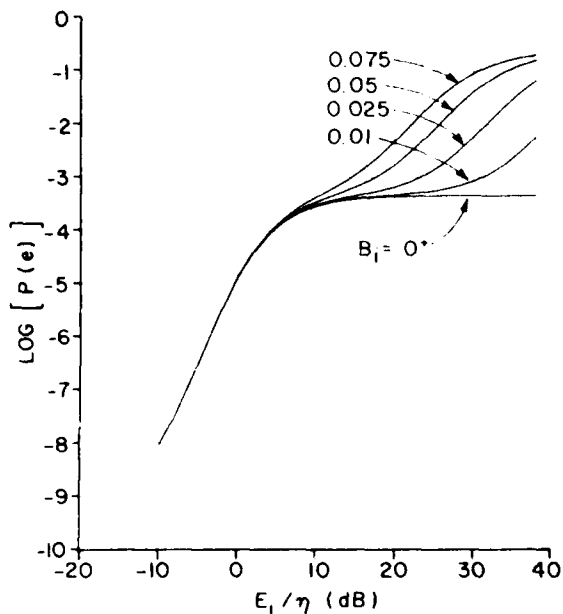

Fig. 10   Performance of three-element LMS array for several interference bandwidths, case C

Fig. 9 shows the results for case B. The two curves in this figure that show the performance when $B_i = 0$ and $B_i = 0.01$ are the same as the corresponding curves in Fig. 8. For these cases the interference is passed entirely by the input BPFs and we see the same performance that
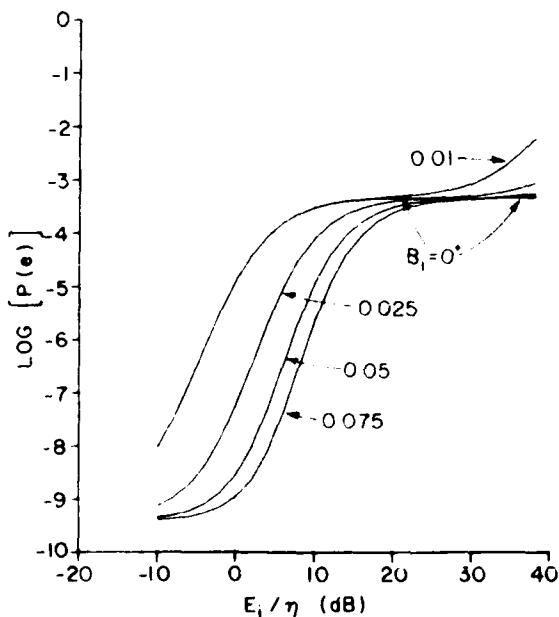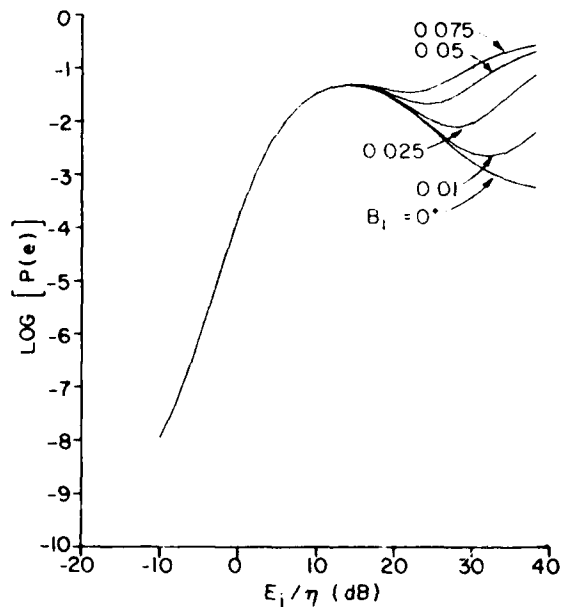

Fig. 9   Performance of three-element LMS array for several interference bandwidths, case B

detector filter. The only difference between Cases A and C is the increase in the array bandwidth by a factor of 20 for Case C. We see that this increase has two effects. First, a large hump appears in the $P(e)$ versus E_i/η curves. This hump is caused by the larger thermal noise power at the BPF outputs for the larger value of filter bandwidth. As the input interference power increases, the array does not begin to form a null on the interference until the interference and noise power levels at the BPF outputs are approximately equal. In case C, the residual interference power at the array output when E_i/η is between approximately 5 and 25 dB causes the hump in the curves. The second effect that we note is the movement of the point where the curves begin to diverge. In case C, where the noise power at the BPF outputs is 13 dP higher than it is in case A, the E_i/η value where the curves begin to diverge is approximately 13 dB higher than it is in case A.

Fig. 11 shows the results for case D. For this case the interference is always passed by the input BPFs, but it is partially rejected by the detector LPF when $B_i > 0.01$. When B_i increases above 0.01 two conflicting processes occur. First, the total interference power at the array

[4] We note that the array performance is essentially independent of B_d for $B_d < 0.1$ [9]
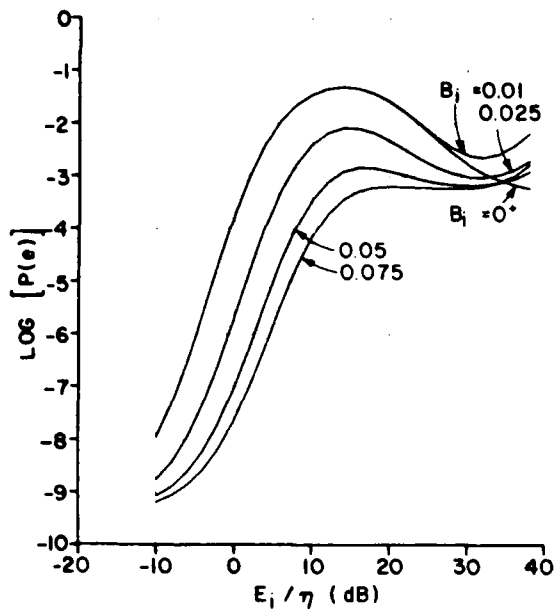
Fig. 11 Peformance of three-element LMS array for several
interference bandwidths, case D.

Fig. 12 Performance of three-element tapped delay line LMS array
for case A.

output increases since the array has more difficulty
nulling a broadband interfering signal. Second, the
detector LPF rejects some of the interference. The first of
these effects causes an increase in $P(e)$ while the second
effect causes a decrease in $P(e)$. From Fig. 11 we see
that the second effect is dominant for the case D signal
scenario. $P(e)$ is highest when the interfering bandwidth
is equal to the desired signal bandwidth.

We next examine the performance of the three-
element TDL LMS array with Gaussian interference. As
an example we consider the same signal scenario used in
case A above. Fig. 12 shows the performance of the TDL
LMS array for this scenario. From this figure we see that
this array achieves the same performance for each of the
B_i values that the conventional LMS array had for
$B_i = 0$. These results support the conclusion made by
Compton in [11] that, with a single interference signal
(with B_i less than approximately 0.5), the TDL array
performance is equal to that of the conventional array
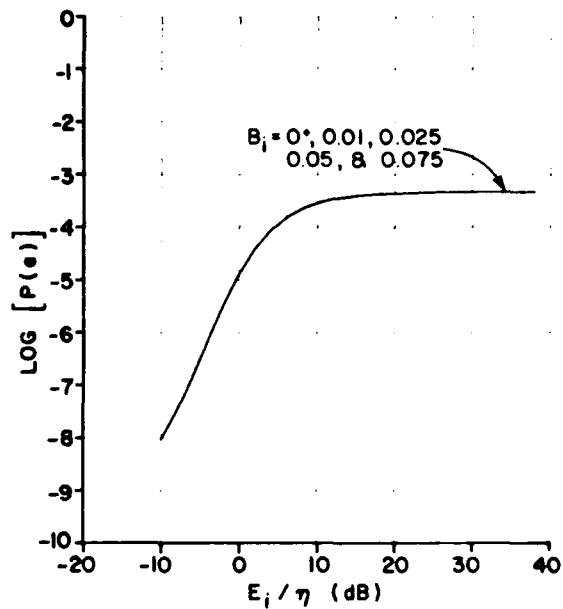with CW interference.

IV. CONCLUSION

In this paper we have calculated the performance of a
BPSK communication system that uses an LMS adaptive
array to protect the system from Gaussian noise
interference. We showed that the system performs best
when the interference is located outside the main beam of
the quiescent array pattern. The system is most vulnerable
to broadband interference when the interference arrives
from a direction near endfire since this is the direction
where the interelement propagation delay for the
interference is largest. We found that the system
generally performed best when the array bandwidth was
as small as possible. The interference was found to be
most effective when its bandwidth was equal to the
desired signal bandwidth. This was found to be true
regardless of the array bandwidth. Finally, we found that
the performance of a system using the TDL LMS array is
not dependent upon the interference bandwidth for a
single interfering signal.

REFERENCES

[1] Widrow, B., Mantey, P.E., Griffiths, L.J., and Goode, B.B. (1967)
Antenna systems.
Proceedings of the IEEE, 55, 12 (Dec. 1967), 2143.

[2] Compton, R.T., Jr. (1978)
Adaptive array in a spread spectrum communication system.
Proceedings of the IEEE, 66, 3 (Mar. 1978), 289.

[3] Winters, J.H. (1982)
Spread spectrum in a four-phase communication system employing adaptive arrays.
IEEE Transactions on Communications, COM-30 (May 1982), 929.

[4] Hudson, E.C. (1980)
Use of an adaptive array in a frequency-shift keyed communication system
Report 712684-1, The Ohio State University ElectroScience Laboratory, Columbus, Aug. 1980.

[5] Ganz, M.W. (1982)
On the performance of an adaptive array in a frequency-shift keyed communication system.
M.Sc. Thesis, Department of Electrical Engineering, The Ohio State University, Columbus, 1982.

[6] Ganz, M.W., and Compton, R.T., Jr. (1986)
Protection of a BPSK communication system with an adaptive array
Presented at MONTECH '86 Conference on Antennas and Propagation, Montréal, Canada, Aug. 1986.

[7] Ganz, M.W. (1986)
Performance of digital communication systems with adaptive arrays
Ph.D. Dissertation, The Ohio State University, Columbus, 1986

[8] Ganz, M.W., and Compton, R.T., Jr. (1986)
Protection of a narrowband communication system with an adaptive array.
To appear in IEEE Transactions on Communications, COM-35, October 1987.

[9] Compton, R.T., Jr. (1987)
Adaptive Antennas—Concepts and Performance.
Englewood Cliffs, N.J.: Prentice-Hall, 1987.

[10] Rogers, W.E., and Compton, R.T., Jr. (1979)
Adaptive array bandwidth with tapped delay-line processing
IEEE Transactions on Aerospace and Electronic Systems, AES-15, 1 (Jan. 1979), p. 21.

[11] Compton, R.T., Jr. (1985)
The bandwidth performance of a two-element adaptive array with tapped delay-line processing.
Report 717253-3, The Ohio State University ElectroScience Laboratory, Columbus, prepared under Contract N00019-85-C-0119 for Naval Air Systems Command, April 1986

[12] Lindsey, W.C., and Simon, M.K. (1973)
Telecommunication System Engineering.
Englewood-Cliffs, N.J.: Prentice-Hall, 1973.

[13] Ziemer, R.E., and Peterson, R.L. (1985)
Digital Communications and Spread Spectrum Systems
New York: MacMillan, 1985.

[14] Luckey, R.W., Salz, J., and Weldon, E.J. (1968)
Principles of Data Communications.
New York: McGraw-Hill, 1968.

[15] Bayless, J.W., Collins, A.C., and Pederson, R.D. (1979)
The specification of bandlimited digital radio systems.
IEEE Transactions on Communications, COM-27 (Dec. 1979), 1763–1770.

[16] Feher, K. (1981)
Digital Communications—Microwave Applications.
Englewood Cliffs, N.J.: Prentice-Hall, 1981, ch. 3.

Matthew W. Ganz (S'82—M'87) was born in Toledo, Ohio, on March 18, 1959. He received the B.S., M.S., and Ph.D. degrees in electrical engineering from The Ohio State University in 1981, 1982, and 1986, respectively.

In 1980–1982 and 1985–1986 he was a Fellow Research Associate, a Graduate Research Associate, and a Postdoctoral Research Associate at The Ohio State University ElectroScience Laboratory, where he studied communications and radar applications of adaptive antenna systems. From 1982–1984 he was an Associate Engineer in the Space Department of The Johns Hopkins University Applied Physics Laboratory. There he worked primarily on satellite communication and tracking systems. He is currently a Member of the Technical Staff in the Radar Systems Group at M.I.T. Lincoln Laboratory where he is working on radar applications of adaptive arrays.

Dr. Ganz is a member of Tau Beta Pi, Eta Kappa Nu, and Sigma Xi.

R.T. Compton, Jr., (F'84) was born in St. Louis, Mo., on July 26, 1935. He received the S.B. degrees from Massachusetts Institute of Technology, Cambridge, in 1958, and the M.Sc. and Ph.D. degrees from The Ohio State University, Columbus, in 1961 and 1964, all in electrical engineering.

Dr. Compton is a Professor of Electrical Engineering at The Ohio State University. From 1965 to 1967, he was an Assistant Professor of Engineering at Case Institute of Technology, Cleveland, Ohio, and from 1967 to 1968, he was an NSF Postdoctoral Fellow at the Technische Hochschule, Munich, Germany. He spent the 1983–1984 academic year at the Naval Research Laboratory, Washington, D.C.

Dr. Compton is a member of Sigma Xi and Pi Mu Epsilon. In 1983 he received the M. Barry Carlton Award for best paper from the IEEE Aerospace and Electronic Systems Society.

Adaptive Array Behavior with Periodic Phase Modulated Interference

ABDULAZIZ S. AL-RUWAIS
King Saud University
Saudi Arabia

R.T. COMPTON, JR.
ElectroScience Laboratory

We consider a least mean square (LMS) adaptive array [1] receiving a phase modulated interference signal. The phase modulation is assumed to be periodic and to have finite bandwidth. Under these assumptions, we determine the time-varying array weights, the modulation on the array output desired signal, and the time-varying output interference-to-noise ratio (INR) and SINR (signal-to-interference-plus-noise ratio).

We present numerical results describing the behavior of a 2-element adaptive array that receives an interference signal with sinusoidal phase modulation. We show how each signal parameter (arrival angle, power, modulation index, and modulation frequency) affects the performance of the array.

I. INTRODUCTION

The performance of a least mean square (LMS) adaptive array [1] can be affected by modulation on an interference signal. For example, pulsed interference can make the weights in an adaptive array vary between two sets of values, one when the interference is on and the other when it is off [2]. Interference modulation has two deleterious effects on an adaptive array. First, it can cause the array to modulate the desired signal. Second, it can make the array output SINR (signal-to-interference-plus-noise ratio) vary with time. In a digital communication system, such SINR variation usually results in an increased bit error probability. The effects of interference modulation on an array are usually most significant when the modulation rate is close to the natural response speed of the array and when the interference arrival angle is close to that of the desired signal [2–4].

In previous studies, the authors have examined the effects of pulsed interference [2], interference with sinusoidal envelope modulation [3], and interference with arbitrary periodic envelope modulation [4] on adaptive arrays. Each of these studies involved envelope modulation but not phase modulation.

The purpose of the present paper is to extend the earlier work to the case of phase modulated interference. In Section II of this paper, we formulate the problem of an adaptive array receiving an interference signal with periodic phase modulation. We solve for the resulting time-varying weights in the array, and from the weights we determine the output desired signal modulation and SINR variation. In Section III, we present numerical results for a 2-element array that receives interference with sinusoidal phase modulation. We show how the interference modulation parameters affect the desired signal modulation, the SINR variation and the bit error probability when the desired signal is a DPSK (differential phase-shift keyed) communication signal. Section IV contains our conclusions.

II. FORMULATION OF THE PROBLEM

Assume an adaptive array consists of J isotropic elements with half wavelength spacing, as shown in Fig. 1. Let $\tilde{x}_j(t)$ denote the analytic signal received on element j. The signal $\tilde{x}_j(t)$ is multiplied by a complex weight w_j and then summed to produce the array output $\tilde{s}(t)$. The array weights are controlled by LMS (least mean square) feedback loops [1], which obtain each weight w_j by integrating the product of $\tilde{x}_j(t)$ with the error signal $\tilde{e}(t)$. The error signal is the difference between a reference signal $\tilde{r}(t)$ and the array output $\tilde{s}(t)$ [1]. The array weights satisfy the differential equation

$$\frac{dW}{dt} + k\Phi W = kS \qquad (1)$$

where $W = [w_1, w_2, ..., w_J]^T$ is the weight vector, t is time, Φ is the covariance matrix,

$$\Phi = E[X^*X^T] \qquad (2)$$

S is the reference correlation vector,

$$S = E[X^*\bar{r}(t)] \qquad (3)$$

and k is the LMS loop gain. In these equations, X is the signal vector,

$$X = [\bar{x}_1(t), \bar{x}_2(t), ..., \bar{x}_J(t)]^T \qquad (4)$$

T denotes transpose, * complex conjugate, and $E[\cdot]$ expectation.

We assume a desired signal and an interference signal are incident on the array, and also that independent thermal noise is present in each element signal. The signal vector then contains three terms,

$$X = X_d + X_i + X_n \qquad (5)$$

where X_d, X_i, and X_n are the desired, interference, and noise vectors, respectively.

Let the desired signal be a CW (single frequency) signal incident from angle θ_d relative to broadside (θ is defined in Fig. 1). The desired signal vector is then
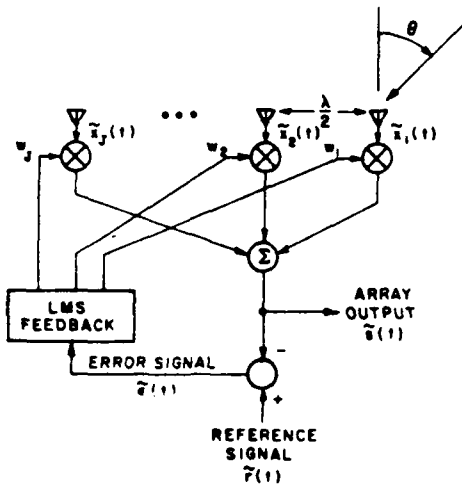
$$X_d = A_d e^{j(\omega_0 t + \psi_d)} U_d \qquad (6)$$

Fig 1. LMS adaptive array.

where A_d is the amplitude, ω_0 is the carrier frequency, ψ_d is the carrier phase angle, and U_d is a vector containing the interelement phase shifts,

$$U_d = [1, e^{-j\phi_d}, ..., e^{-jK\phi_d}]^T \qquad (7)$$

where

$$\phi_d = \pi \sin \theta_d \qquad (8)$$

and where, to simplify later notation, we let

$$K = J - 1. \qquad (9)$$

We assume ψ_d is a random variable uniformly distributed on $(0, 2\pi)$.

Next, assume a phase modulated interference signal arrives from angle θ_i. The interference signal vector is

$$x_i = A_i e^{j(\omega_0 t + \psi_i)} U_i(t) \qquad (10)$$

with

$$U_i(t) = \begin{bmatrix} e^{j\gamma_i(t)} \\ e^{j[\gamma_i(t-T_i)-\phi_i]} \\ e^{j[\gamma_i(t-2T_i)-2\phi_i]} \\ \vdots \\ e^{j[\gamma_i(t-KT_i)-K\phi_i]} \end{bmatrix} \qquad (11)$$

where $\gamma_i(t)$ is the phase modulation as received on element 1, A_i is the interference amplitude, and ψ_i is the carrier phase angle. The variables T_i and ϕ_i are the interelement time delay and carrier phase shift,

$$T_i = \frac{\pi}{\omega_0} \sin \theta_i \qquad (12)$$

and

$$\phi_i = \omega_0 T_i = \pi \sin \theta_i. \qquad (13)$$

We assume ψ_i is a random variable, uniformly distributed on $(0, 2\pi)$ and statistically independent of ψ_d.

Finally, we assume each element signal contains a zero-mean, independent Gaussian thermal voltage $\bar{n}_i(t)$ of power σ^2. The noise vector is

$$X_n = [\bar{n}_1(t), \bar{n}_2(t), ..., \bar{n}_J(t)]^T \qquad (14)$$

where

$$E[\bar{n}_j^*(t)\bar{n}_k(t)] = \sigma^2 \delta_{jk}, \qquad 1 \le j, k \le J \qquad (15)$$

with δ_{jk} the Kronecker delta. The $\bar{n}_i(t)$ are assumed statistically independent of both ψ_d and ψ_i.

Under these assumptions, the covariance matrix in (2) is the sum of a desired, an interference, and a noise term.

$$\Phi = \Phi_d + \Phi_i + \Phi_n. \qquad (16)$$

The desired signal term is

$$\Phi_d = E[X_d^* X_d^T] = A_d^2 U_d^* U_d^T. \qquad (17)$$

The interference term is

$$\Phi_i = E[X_i^* X_i^T]$$

$$= A_i^2 \begin{bmatrix} 1 & e^{j[\chi_{01}(t)-\phi_i]} & \cdots & e^{j[\chi_{0K}(t)-K\phi_i]} \\ e^{j[\chi_{10}(t)+\phi_i]} & 1 & \cdots & e^{j[\chi_{1K}(t)-(K-1)\phi_i]} \\ \vdots & \vdots & \ddots & \vdots \\ e^{j[\chi_{K0}(t)+K\phi_i]} & e^{j[\chi_{K1}(t)+(K-1)\phi_i]} & \cdots & 1 \end{bmatrix} \qquad (18)$$

where

$$\chi_{pq}(t) = \gamma_i(t - qT_i) - \gamma_i(t - pT_i) \qquad (19)$$

and where p and q are integers in the range $0 \le p, q \le K$. The noise term is

$$\Phi_n = \sigma^2 I \qquad (20)$$

with I the identity matrix.

To compute the reference correlation vector S in (3), we must specify the reference signal $\tilde{r}(t)$. In practical applications, the reference signal is derived from the array output [5–7]. To make the array perform properly, it must be a signal correlated with the desired signal and uncorrelated with the interference. Here we assume the reference signal to be a replica of the desired signal,

$$\tilde{r}(t) = A_r e^{j(\omega_0 t + \psi_d)} \qquad (21)$$

where A_r is its amplitude. Equation (3) then yields

$$S = A_r A_d U_d^* . \qquad (22)$$

When (16) and (22) are substituted into (1), one finds that the weights satisfy a system of differential equations with a constant vector S on the right but with time-varying coefficients due to Φ_i. This equation may be solved for the weights as follows.

First, we write the interference covariance matrix in a more compact form. We define the J vectors,

$$V_0 = [1, 0, 0, \dots, 0, 0]^T$$

$$V_1 = [0, e^{-j\phi_i}, 0, \dots, 0, 0]^T$$

$$V_2 = [0, 0, e^{-j2\phi_i}, \dots, 0, 0]^T$$

$$\vdots$$

$$V_K = [0, 0, 0, \dots, 0, e^{-jK\phi_i}]^T . \qquad (23)$$

Note that these J vectors form an orthonormal set,

$$V_j^T V_k^* = \delta_{jk}, \qquad 0 \le j, k \le K . \qquad (24)$$

In terms of these vectors, Φ_i in (18) may be written

$$\Phi_i = A_i^2 \sum_{p=0}^{K} \sum_{q=0}^{K} e^{jX_{pq}(t)} V_p^* V_q^T \qquad (25)$$

so (1) becomes

$$\frac{dW}{dt} + k[A_d^2 U_d^* U_d^T + A_i^2 \sum_{p=0}^{K} \sum_{q=0}^{K} e^{jX_{pq}(t)} V_p^* V_q^T$$

$$+ \sigma^2 I] W = k A_r A_d U_d^* . \qquad (26)$$

Next, we normalize (26). Dividing by $k\sigma^2$ gives

$$\frac{dW(t')}{dt'} + [\Phi_2 + \xi_i \sum_{p=0}^{K} \sum_{q=0}^{K} e^{jX_{pq}(t')} V_p^* V_q^T] W(t')$$

$$= \frac{A_r}{\sigma} \sqrt{\xi_d} U_d^* \qquad (27)$$

where

$$\Phi_2 = I + \xi_d U_d^* U_d^T$$

$$\xi_d = \frac{A_d^2}{\sigma^2}$$

$$= \text{input signal-to-noise ratio (SNR) per element}$$

$$\xi_i = \frac{A_i^2}{\sigma^2}$$

$$= \text{input interference-to-noise ratio (INR) per element} \qquad (28)$$

and where

$$t' = k\sigma^2 t = \text{normalized time.} \qquad (29)$$

Also, note that the constant $\frac{A_r}{\sigma}$ on the right in (27) will just appear as a scale factor in the solution for $W(t')$. It has no effect on the array output SINR to be discussed below. Hence we arbitrarily set $\frac{A_r}{\sigma} = 1$ to eliminate it. Eq. (27) is then

$$\frac{dW(t')}{dt'} + [\Phi_2 + \xi_i \sum_{p=0}^{K} \sum_{q=0}^{K} e^{jX_{pq}(t')} V_p^* V_q^T] W(t')$$

$$= \sqrt{\xi_d} U_d^* . \qquad (30)$$

Next, so that we may solve (30), we make the assumption that the phase modulation $\gamma_i(t)$ is a periodic function of time. If $\gamma_i(t)$ is periodic, the functions $\exp(jX_{pq}(t'))$ are also periodic, so each of them may be expanded in a Fourier series. To simplify later notation, we also include the constant ξ_i in this expansion. Thus, we write

$$\xi_i e^{jX_{pq}(t)} = \sum_{l=-\infty}^{\infty} f_{lpq} e^{jl\omega_m' t'} \qquad (31)$$

where f_{lpq} is the lth Fourier coefficient of $\xi_i \exp(jX_{pq}(t'))$ and ω_m' is the normalized fundamental frequency of $\gamma_i(t')$, i.e.,

$$\omega_m' = \frac{\omega_m}{k\sigma^2} \qquad (32)$$

where ω_m is the fundamental frequency of $\gamma_i(t)$. Note that if $p = q$, then $X_{pq}(t') = 0$, so the series in (31) contains only a zero frequency term, i.e.,

$$f_{lpp} = \xi_i \delta_{l0}. \qquad (33)$$

Also, it is easily shown that

$$f_{lqp} = f_{(-l)pq}^* \qquad (34)$$

and

$$f_{l(p+1)(q+1)} = f_{lpq} e^{-jl\omega_m' T_i'} \qquad (35)$$

where $T_i' = k\sigma^2 T_i$, with T_i given in (12).

In addition to assuming $\gamma_i(t)$ periodic, we also assume that the bandwidth of the interference is finite, i.e., that (31) contains only a finite number of nonzero terms. Specifically, suppose the coefficients in (31) are zero for $|l| > L$, where L is some integer. Then

$$\xi_i e^{jX_{pq}(t')} = \sum_{l=-L}^{L} f_{lpq} e^{jl\omega_m' t'} . \qquad (36)$$

Since (30) is a linear differential equation with

periodic coefficients, the solution for $W(t')$ is a periodic function of time after any initial transients have died out [8]. In this paper, we do not consider the initial transients, but only the periodic steady-state solution. Once initial transients are over, $W(t')$ can be written as a Fourier series,

$$W(t') = \sum_{n=-\infty}^{\infty} C_n e^{jn\omega'_m t'} \qquad (37)$$

where C_n is a vector Fourier coefficient. Substituting this series into (30) and enforcing the resulting equation for each frequency component separately gives

$$(\Phi_2 + jn\omega'_m I)C_n + \sum_{l=-L}^{L} \sum_{p=0}^{K} \sum_{q=0}^{K} f_{lpq} V_p^* V_q^T C_{n-l}$$
$$= \sqrt{\xi_d} U_0^{\ddagger} \delta_{n0}, \qquad -\infty < n < \infty. \quad (38)$$

Equation (38) is an infinite system of vector equations, one for each n. To solve for the C_n, we assume there is some integer N such that the Fourier coefficients C_n are negligible for $|n| > N$, i.e., we assume $W(t')$ can be adequately approximated by a finite sum,

$$W(t') = \sum_{n=-N}^{N} C_n e^{jn\omega'_m t'}. \qquad (39)$$

Such an approximation will hold because the feedback loops controlling the array weights in $W(t')$ are lowpass filter loops that cannot respond above a certain speed.

If we set $C_n = 0$ for $|n| > N$, then (38) yields a finite system of equations for the remaining C_n. Each vector C_n has J scalar components, so the result is a system of $(2N + 1)J$ linear equations in the unknown scalar components. One could solve for $W(t')$ by solving this system of equations numerically. However, solving (38) is greatly simplified if we first express each C_n in terms of its components along the vectors V_k in (23). (Since each C_n has J components, the J orthonormal vectors V_k can be used as basis vectors.) We write

$$C_n = \sum_{k=0}^{K} \alpha_{nk} V_k^* \qquad (40)$$

where the α_{nk} are scalar coefficients. The coefficient α_{nk} is the component of C_n along the unit vector V_k^*. Substituting (40) into (38), multiplying the result on the left by V_a^T (for $a = 0, 1, \ldots, K$) and using (24) yields

$$jn\omega'_m \alpha_{na} + \sum_{k=0}^{K} Q_{ak} \alpha_{nk} + \sum_{l=-L}^{L} \sum_{q=0}^{K} f_{laq} \alpha_{(n-l)q}$$
$$= \sqrt{\xi_d} (V_a^T U_0^{\ddagger}) \delta_{n0}, \qquad 0 \le a \le K \quad (41)$$

where

$$Q_{ak} = V_a^T \Phi_2 V_k^*. \qquad (42)$$

Because we assume $C_n = 0$ for $|n| > N$, the coefficients α_{nq} in (41) are nonzero only for $|n| \le N$. The variable Q_{ak} is readily found from (23) and (28),

$$Q_{ak} = \delta_{ak} + \xi_d e^{j(a-k)(\Phi_d - \Phi_I)}. \qquad (43)$$

Also, from (7) and (23), one finds

$$V_a^T U_0^{\ddagger} = e^{ja(\Phi_d - \Phi_I)}, \qquad 0 \le a \le K. \qquad (44)$$

Equation (41), when written out, yields a finite system of equations of the form,

$$MA = B \qquad (45)$$

where A is a vector containing the unknown coefficients α_{nk},

$$A = [\alpha_{N0}, \alpha_{N1}, \ldots, \alpha_{NK}, \alpha_{(N-1)1}, \ldots,$$
$$\alpha_{(N-1)K}, \ldots, \alpha_{(-N)1}, \ldots, \alpha_{(-N)K}]^T \quad (46)$$

B is a vector obtained from the right side of (41), and M is the matrix of coefficients obtained from the left side of (41). The results presented below have been obtained by solving (45) numerically.

For this method to yield accurate results, N must be chosen large enough that at least $2LJ$ of the α_{nk} are essentially zero on each end of the vector A in (46). If this vector has $2LJ$ zeros on each end, the solution obtained from (41) will yield the same result as the solution of the infinite system in (38). In practice, a suitable value of N may be determined by increasing N until the additional α_{nk} obtained remain negligible and until the α_{nk} in the middle of vector A are unaffected by further increases in N. Experience shows how large N must be in specific cases. Once the α_{nk} have been found, the C_n may be found from (40) and $W(t')$ from (39).

Time-varying weights have two effects on array performance. They cause the array to modulate the desired signal, and they cause the array output $SINR$ to vary with time. These effects are calculated as follows.

Given a time-varying weight vector $W(t')$, the desired signal component of the array output is

$$\bar{s}_d(t') = A_d W^T(t') U_d e^{j(\omega_0' t' + \psi_d)} \qquad (47)$$

where $\omega_0' = \omega_0/k\sigma^2$. The modulation on $\bar{s}_d(t)$ is contained in the term $A_d W^T(t') U_d$, which may be written

$$A_d W^T(t') U_d = a_d(t') e^{j\eta_d(t')}. \qquad (48)$$

Then $a_d(t') = A_d |W^T(t') U_d|$ is the envelope modulation and $\eta_d(t') = \langle W^T(t') U_d$ is the phase modulation. We define $a_{dn}(t')$ to be the envelope normalized to its value in the absence of interference,

$$a_{dn}(t') = \frac{a_d(t')}{A_d |W_0^T U_d|} \qquad (49)$$

where W_0 is the steady-state weight vector that would occur without interference,

$$W_0 = (\Phi_d + \Phi_n)^{-1} S \qquad (50)$$

(Φ_d, Φ_n, and S are given in (17), (20), and (22).) We present our results below in terms of $a_{dn}(t')$, rather than $a_d(t')$, because it is easy to see the effect of the interference by comparing $a_{dn}(t')$ with unity.

The output signal powers may also be computed from $W(t')$. The output desired signal power is

$$P_d(t') = \tfrac{1}{2} E[|\bar{s}_d(t')|^2] = \tfrac{1}{2} A_d^2 |W^T(t') U_d|^2. \qquad (51)$$

The output interference power is

$$P_i(t') = \tfrac{1}{2} A_i^2 |W^T(t') U_i(t')|^2 \qquad (52)$$

where $U_i(t')$ is the vector of phasors in (11) but written in terms of normalized time $t' = k\sigma^2 t$. The output thermal noise power is

$$P_n(t') = \frac{\sigma^2}{2} W^T(t') W^*(t'). \qquad (53)$$

From these quantities, the output interference-to-noise ratio

$$\text{output INR} = \frac{P_i(t')}{P_n(t')} \qquad (54)$$

and the output SINR

$$\text{SINR} = \frac{P_d(t')}{P_i(t') + P_n(t')} \qquad (55)$$

may be computed as functions of t'.

In the next section, we apply these equations to a 2-element array receiving interference with sinusoidal phase modulation.

III. A 2-ELEMENT ARRAY

Consider an array with two elements, so $J = 2$ and $K = 1$. Let the interference have sinusoidal phase modulation,

$$\gamma_i(t') = \beta \sin(\omega_m' t') \qquad (56)$$

where β is the maximum phase deviation (or modulation index) and ω_m' is the normalized modulation frequency. From (19) and standard trigonometric identities, one finds that

$$e^{j\chi_{01}(t')} = e^{j\beta \sin\left[\omega_m\left(t - \frac{T'}{2}\right) - \frac{\pi}{2}\right]} \qquad (57)$$

where

$$\beta' = 2\beta \sin\left(\frac{\omega_m' T_i'}{2}\right) \qquad (58)$$

(and $T_i' = k\sigma^2 T_i$). Using the Fourier series expansion [9]

$$e^{jz \sin \rho} = \sum_{l=-\infty}^{\infty} J_l(z) e^{jl\rho} \qquad (59)$$

where $J_l(z)$ is the Bessel function of the first kind of order l, we find

$$\xi_i e^{j\chi_{01}(t')} = \sum_{l=-\infty}^{\infty} f_{l01} e^{jl\omega_m' t'} \qquad (60)$$

where

$$f_{l01} = \xi_i J_l(\beta') e^{-jl\left(\frac{\omega_m' T_i'}{2} + \frac{\pi}{2}\right)}. \qquad (61)$$

Because

$$J_{-l}(\beta') = (-1)^l J_l(\beta') \qquad (62)$$

we also have from (34),

$$f_{l10} = f_{(-l)01}^* = (-1)^l f_{l01}. \qquad (63)$$

To truncate the series in (60), we use the fact that

$$J_l(z) \cong 0 \text{ for } |l| > z + 1. \qquad (64)$$

Thus, we approximate

$$\xi_i e^{j\chi_{01}(t')} = \sum_{l=-L}^{L} f_{l01} e^{jl\omega_m' t'} \qquad (65)$$

with

$$L = \{\beta' + 1\} = \{2\beta \sin \frac{\omega_m' T_i'}{2} + 1\} \qquad (66)$$

where $\{r\}$ denotes the smallest integer greater than or equal to r.

With these assumptions, we have solved (41) numerically for the α_{nk} and then computed the C_n and $W(t')$ from (40) and (39). From $W(t')$, we have calculated the envelope and phase modulation on the output desired signal from (48) and (49) and the output INR and SINR from (54) and (55).

We present our results as follows. In subsection A below, we show typical curves of desired signal modulation and output INR and SINR as functions of time. In subsections B–E, we describe the effect of each interference signal parameter on the desired signal modulation. In subsection F, we assume the array is used in a DPSK communication system [10] and show how the bit error probability is affected by the phase modulated interference.

A. Typical Waveforms

Fig. 2 shows curves of the normalized envelope modulation $a_{dn}(t')$ for the specific case where $\theta_d = 30^\circ$,

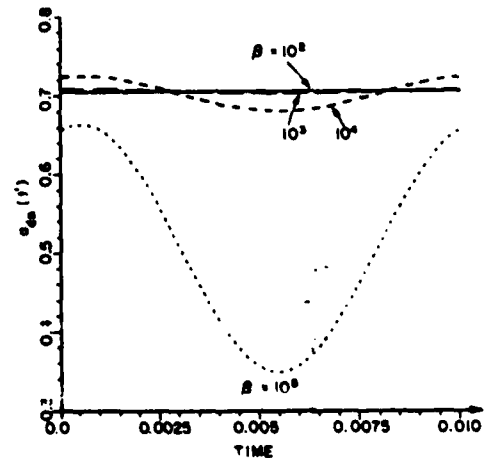

Fig. 2. $a_{dn}(t')$ versus time. $\theta_d = 30^\circ$, $\theta_i = 45^\circ$, $\xi_d = 10$ dB. $\xi_i = 30$ dB, $f_m' = 10^2$, $f_0' = 10^8$.

$\theta_i = 45°$, $\xi_d = 10$ dB, $\xi_i = 30$ dB, $f'_m = \dfrac{\omega'_m}{2\pi} = 10^2$, $f'_0 = \dfrac{\omega'_0}{2\pi} = 10^8$ and for $\beta = 10^2$, 10^3, 10^4, and 10^5.

These parameter values have been chosen to illustrate that the envelope modulation on the desired signal can be substantial, especially for larger values of β. (The reason that $a_{dn}(t') < 1$ even for small β, when there is little envelope modulation, is that a 2-element array has insufficient resolution to separate interference at $\theta_i = 45°$ from the desired signal at $\theta_d = 30°$. The desired signal is on the edge of the interference null and suffers the attenuation seen in $a_{dn}(t')$.)

It turns out that for this 2-element array, phase modulated interference does not cause phase modulation on the desired signal. This result was discovered by calculating $\eta_d(t')$ for numerous values of θ_d, ξ_d, θ_i, ξ_i, β, and f'_m. One finds that $\eta_d(t')$ does not change with time regardless of the signal parameters. The reason for this behavior is as follows. Both the amplitudes of the two weights are equal at each instant of time. The phase angle of each weight contains a term constant with time, which depends on the interference arrival angle (and is different on each element), and a term that varies sinusoidally with time. The sinusoidally varying term has the same amplitude but is 180° out of phase on the two elements. When a desired signal is passed through these weights, the phase modulation produced on the desired signal by one weight is 180° out of phase with that produced by the other weight. The resulting array output signal contains only envelope modulation, no phase modulation.

Figs. 3 and 4 show typical curves of the output INR and SINR as functions of time, over one period and for the same signal parameters as in Fig. 2. The figures show that as β is increased, the average output INR increases, the SINR decreases, and the INR and SINR variations with time are more pronounced. The reason for this behavior is that at low β, the array feedb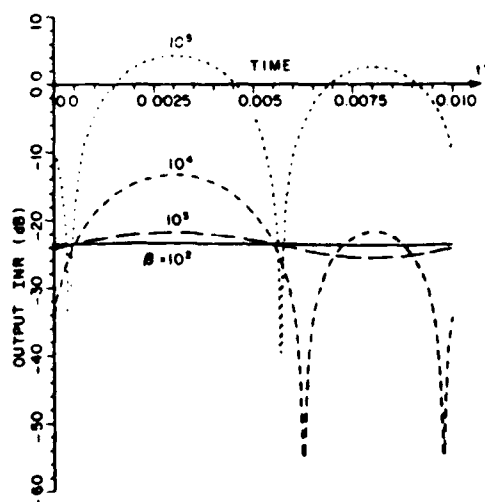ack is able to track the incoming phase modulation. But as β increases, the rate of change of the interference phase becomes too large for the array weights to follow.

The curves above were intended merely to illustrate typical results. In general, one finds that the array behavior changes substantially as the signal parameters θ_d, ξ_d, θ_i, ξ_i, f'_m, and β are varied. In subsections B-E, we show the effect of each of these parameters on the desired signal modulation. Then, in subsection F, we show how bit error probability is affected by the phase modulated interference when the array is used with a DPSK communication signal.

To characterize the desired signal modulation, it is helpful to define the following quantities. First, let a_{max} and a_{min} be the maximum and minimum values of $a_{dn}(t')$ during the modulation period. Then, let

$$m = \frac{a_{max} - a_{min}}{a_{max}}. \qquad (67)$$

a_{max} is the *peak* value of the envelope during the period, and m is the envelope *variation* normalized to its peak. It may be thought of as "fractional modulation", analogous to percentage modulation in AM. In subsections B-E, we describe the effect of each signal parameter on a_{max} and m.

B. The Effect of Angle of Arrival

Desired signal modulation is small when θ_i is far from θ_d. When θ_i approaches θ_d, the envelope variation m increases and the peak a_{max} drops.

Figs. 5 and 6 show typical curves of m and a_{max} as functions of θ_i for $\theta_d = 0°$, $\xi_d = 10$ dB, $\xi_i = 40$ dB, $f'_m = 10^3$, and $f'_0 = 10^8$. Four curves are shown, for $\beta = 2 \times 10^3$, 4×10^3, 8×10^3, and 10^4. It is seen how m increases and a_{max} drops when θ_i approaches θ_d. (When θ_i is very close to θ_d, m drops to zero. This peculiar behavior occurs because when $\theta_i = \theta_d$, the desired signal is nulled. In this case it turns out that a_{max} and a_{min} become equal, so m drops to zero. However, the
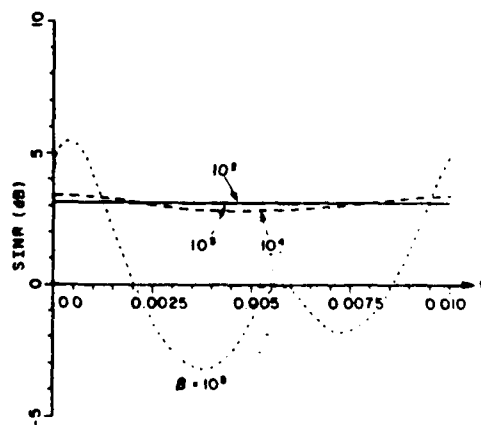

Fig. 3. Output INR versus time. $\theta_d = 30°$, $\theta_i = 45°$, $\xi_d = 10$ dB. $\xi_i = 30$ dB. $f'_m = 10^2$, $f'_0 = 10^8$.

Fig. 4. SINR versus time. $\theta_d = 30°$, $\theta_i = 45°$, $\xi_d = 10$ dB. $\xi_i = 30$ dB, $f'_m = 10^3$, $f'_0 = 10^8$.

Fig. 5. m versus θ_i. $\theta_d = 0°$, $\xi_d = 10$ dB, $\xi_i = 40$ dB, $f'_m = 10^3$, $f'_0 = 10^8$.
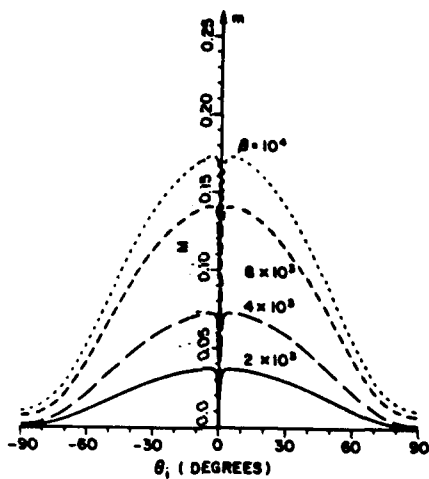

Fig. 6. a_{max} versus θ_i. $\theta_d = 0°$, $\xi_d = 10$ dB, $\xi_i = 40$ dB, $f'_m = 10^3$, $f'_0 = 10^8$.

behavior of m for $\theta_i = \theta_d$ is of little importance, since the desired signal is nulled anyway.)

C. The Effect of Modulation Index and Frequency

The envelope peak a_{max} is largest at low f'_m and drops as f'_m increases. The variation m peaks at intermediate f'_m.

Figs. 7 and 8 show typical results, for the case $\theta_d = 30°$, $\theta_i = 45°$, $\xi_d = 10$ dB, $\xi_i = 30$ dB, $f'_0 = 10^8$ and for β between 2×10^3 and 10^4. At high f'_m, both a_{max} and m drop off because the array has a limited speed of response that prevents the weights from responding to the modulation when f'_m is too high. At low f'_m, m is also small because, with a low modulating frequency, the *interelement* phase shift for the interference does not vary with time. To see this, note that only the interelement phase shift affects the array weights. (A constant carrier phase angle, such as ψ_i in (10), does not appear in the interelement phase shift and hence has no effect on the array weights.) In order for the interelement phase shift to vary with time, the
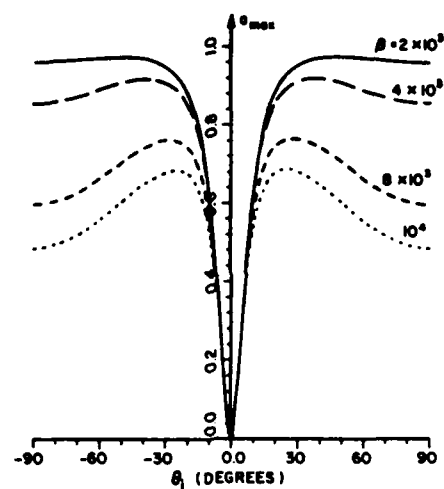
interference phase must vary rapidly enough to change significantly during the time it takes for the interference to propagate across the array. When this happens, the result is a time-varying interelement phase shift. (A time-varying interelement phase shift is electrically equivalent to a time-varying arrival angle.) The feedback then produces time-varying weights in response.

D. The Effect of Interference-to-Noise Ratio

The input INR has only a small effect on the behavior of a_{max}, but greatly affects the envelope variation m.

Figs. 9 and 10 show a_{max} and m versus f'_m for $\theta_d = 30°$, $\theta_i = 45°$, $\xi_d = 10$ dB, $\beta = 10^4$, $f'_0 = 10^8$ and for values of ξ_i, the input INR, between 20 and 45 dB. As Fig. 9 shows, a_{max} is relatively unaffected by the input INR. However, as seen in Fig. 10, the peak value of m increases quickly with input INR. The reason is that the larger the INR, the higher the speed of response of the loops.
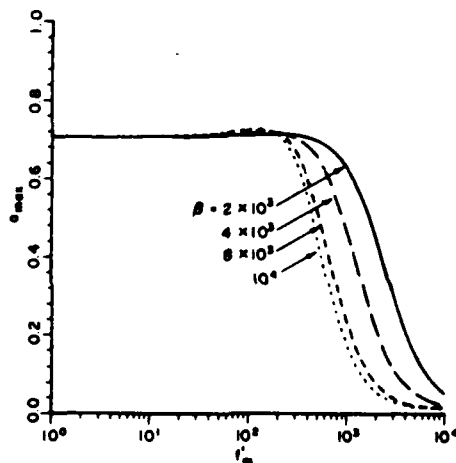

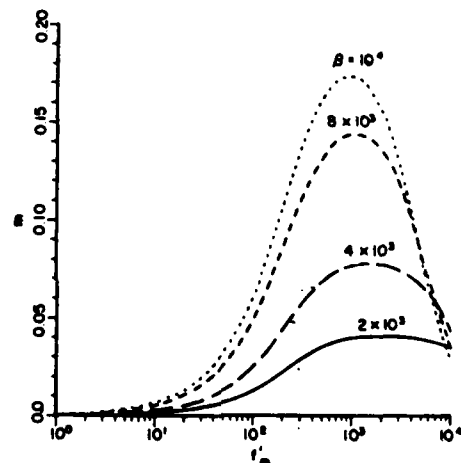Fig. 7. a_{max} versus f'_m. $\theta_d = 30°$, $\theta_i = 45°$, $\xi_d = $ dB, $\xi_i = 30$ dB, $f'_0 = 10^8$

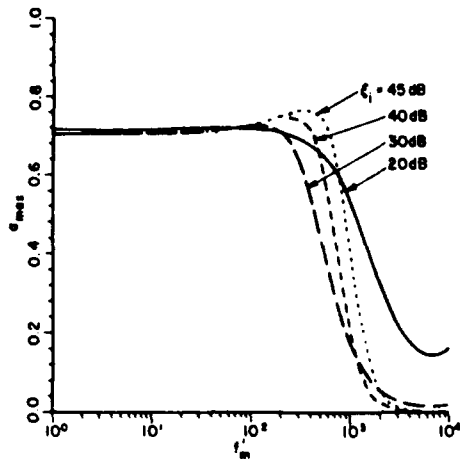Fig. 8. m versus f'_m. $\theta_d = 30°$, $\theta_i = 45°$, $\xi_d = 10$ dB, $\xi_i = 30$ dB, $f'_0 = 10^8$

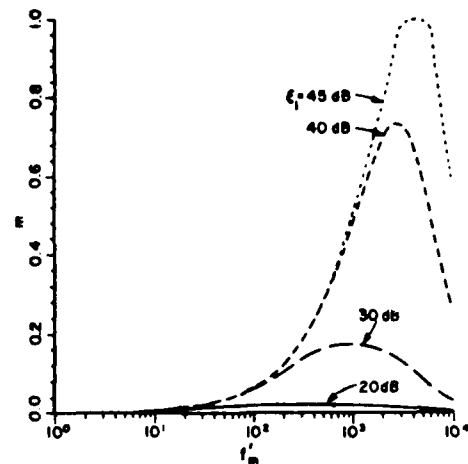Fig. 9. a_{max} versus f'_m. $\theta_d = 30°$, $\theta_i = 45°$, $\xi_d = 10$ dB, $\beta = 10^4$, $f'_0 = 10^8$.

Fig. 10. m versus f'_m. $\theta_d = 30°$, $\theta_i = 45°$, $\xi_d = 10$ dB, $\beta = 10^4$, $f'_0 = 10^8$.

E. The Effect of Desired Signal-to-Noise Ratio

Desired signal modulation is greatest for low SNR and drops as the input SNR increases.

Figs. 11 and 12 show typical results. Fig. 11 shows m and Fig. 12 shows a_{max}, both versus f'_m for $\theta_d = 30°$, $\theta_i = 45°$, $\xi_i = 30$ dB, $f'_0 = 10^8$, $\beta = 10^4$, and for four SNRs (ξ_ds) between 10 and 40 dB. As may be seen, the peak a_{max} approaches unity and the variation m drops as the SNR increases.

F. Bit Error Probability

To evaluate the effect of the time-varying SINR, we assume the desired signal is a DPSK communication signal [10]. We assume that the bit rate of the desired signal is much higher than the modulation frequencies in $a_d(t')$ and that the reference signal $\bar{r}(t)$ is a replica of the desired signal. As discussed in [2, 3], under these assumptions we may obtain an effective bit error probability $\bar{P}_e$ by averaging the instantaneous bit error probability $P_e(t')$ over one period of the interference modulation, where

$$P_e(t') = \tfrac{1}{2}e^{-\text{SINR}(t')}. \tag{68}$$

Fig. 13 shows typical curves of $\bar{P}_e$ as a function of f'_m for $\theta_d = 30°$, $\theta_i = 45°$, $\xi_d = 10$ dB, $\xi_i = 30$ dB, $f'_0 = 10^8$ and for β between 2×10^3 and 10^4. Fig. 14 shows $\bar{P}_e$ versus f'_m for $\beta = 10^4$ and for several values of input INR. At low f'_m, when the modulating frequency is small, $\bar{P}_e$ does not depend on β. The same value of $\bar{P}_e$ would be obtained if a CW interference signal arrived with the same INR. In the frequency range $10^2 \le f'_m \le 10^4$, $\bar{P}_e$ is affected by β because this is the range where the desired signal modulation and the SINR are affected by β, as seen above. At high f'_m, the array weights no longer track the modulation, and $\bar{P}_e$ approaches a constant value.

IV. CONCLUSIONS

We have calculated the periodic steady-state weights of a 2-element adaptive array receiving interference with sinusoidal phase modulation. This interference causes the
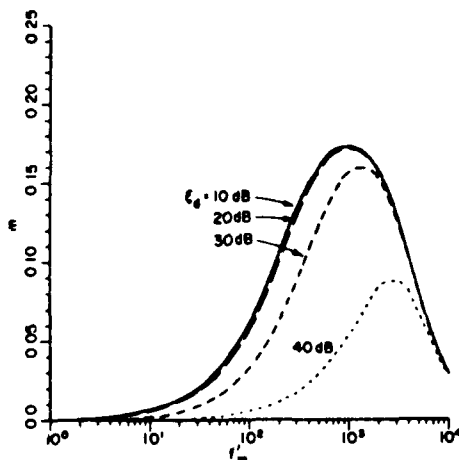

Fig. 11. m versus f'_m. $\theta_d = 30°$, $\theta_i = 45°$, $\xi_d = 30$ dB, $\beta = 10^4$, $f'_0 = 10^8$.
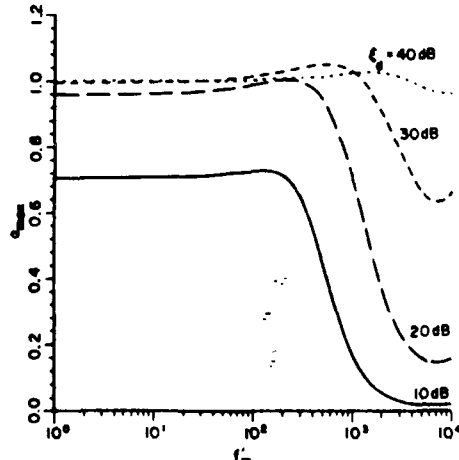
Fig. 12. a_{max} versus f'_m. $\theta_d = 30°$, $\theta_i = 45°$, $\xi_d = 30$ dB, $\beta = 10^4$, $f'_0 = 10^8$.
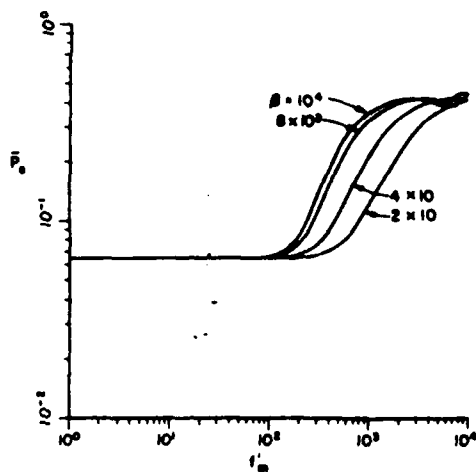
Fig. 13. Bit error probability versus f'_m. $\theta_d = 30°$, $\theta_i = 45°$, $\xi_d = 10$ dB, $\xi_i = 30$ dB. $f'_0 = 10^8$.
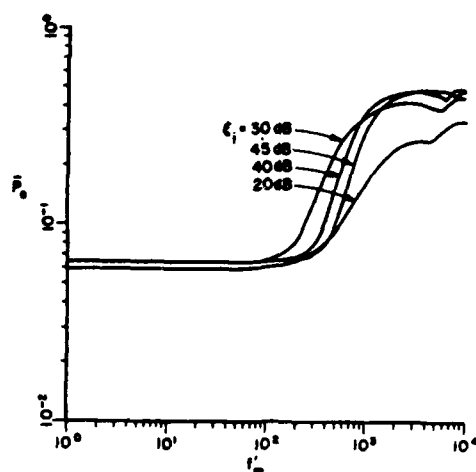
Fig. 14. Bit error probability versus f'_m. $\theta_d = 30°$, $\theta_i = 45°$, $\xi_d = 10$ dB, $\beta = 10^4$, $f'_0 = 10^8$.

array weights to vary periodically with time in such a way that the desired signal is envelope modulated but not phase modulated. We have examined the effects of the signal parameters (arrival angles, powers, modulation index, and modulation frequency) on the array performance. We find that the desired signal envelope modulation is largest when the interference arrives close to the desired signal, when the interference modulation index is large, when the interference power is high, and when the desired signal power is low.

REFERENCES

[1] Widrow, B., Mantey, P.E., Griffiths, L.J., and Goode, B.B. (1967)
Adaptive antenna systems.
Proceedings of the IEEE, 55 (Dec. 1967), 2143.

[2] Compton, Jr., R.T. (1982)
The effect of a pulsed interference signal on an adaptive array
IEEE Transactions on Aerospace and Electronic Systems, AES-18 (May 1982), 297.

[3] Al-Ruwais, A.S., and Compton, Jr., R.T. (1983)
Adaptive array behavior with sinusoidal envelope modulated interference
IEEE Transactions on Aerospace and Electronic Systems, AES-19 (Sept 1983), 677.

[4] Al-Ruwais, A.S., and Compton, Jr., R.T. (1985)
Adaptive array behavior with periodic envelope modulated interference.
IEEE Transactions on Aerospace and Electronic Systems, AES-21 (Nov. 1985), 757.

[5] Compton, Jr., R.T., Huff, R.J., Swarner, W.G., and Ksienski, A.A. (1978)
Adaptive arrays for communication systems: An overview of research at The Ohio State University.

IEEE Transactions on Antennas and Propagation, AP-24 (Sept. 1978), 599.

[6] Compton, Jr., R.T. (1978)
An adaptive array in a spread spectrum communication system.
Proceedings of the IEEE, 66 (March 1978), 289

[7] Winters, J.H. (1982)
Spread spectrum in a four-phase communication system employing adaptive antennas.
IEEE Transactions on Communications, COM-30 (May 1982), 929.

[8] D'Angelo, H. (1970)
Linear Time-Varying Systems Analysis and Synthesis.
Boston, Mass.: Allyn and Bacon, 1970.

[9] Morse, P.M., and Feshback, H. (1953)
Methods of Theoretical Physics
New York: McGraw-Hill, 1953, p 620

[10] Ziemer, R.E., and Tranter, W.H. (1976)
Principles of Communications
Boston, Mass.: Houghton-Mifflin, 1976

[11] Lindsey, W.C., and Simon, M.K. (1973)
Telecommunication Systems Engineering
Englewood Cliffs, N.J.: Prentice-Hall, 1973.

Abdulaziz S. Al-Ruwais was born in Alkharj, Saudi Arabia, on March 10, 1953. He received the B.Sc. degree from King Saud University, Riyadh, Saudi Arabia, in 1975, the M.Sc. degree from the University of Colorado, Boulder, in 1978, and the Ph.D. from The Ohio State University, Columbus, in 1982, all in electrical engineering.

From 1980 to 1982, he was a Graduate Research Associate with the Electroscience Laboratory, The Ohio State University. He is currently an Assistant Professor of Electrical Engineering at King Saud University, Riyadh, Saudi Arabia. His research and teaching are in the areas of communications, adaptive arrays, radio propagation, and radar.

R.T. Compton, Jr., (F'84) was born in St. Louis, Mo., on July 26, 1935. He received the S.B. degrees from Massachusetts Institute of Technology, Cambridge, in 1958, and the M.Sc. and Ph.D. degrees from The Ohio State University, Columbus, in 1961 and 1964, all in electrical engineering.

Dr. Compton is a Professor of Electrical Engineering at The Ohio State University. From 1965 to 1967, he was an Assistant Professor of Engineering at Case Institute of Technology, Cleveland, Ohio, and from 1967 to 1968, he was an NSF Postdoctoral Fellow at the Technische Hochschule, Munich, Germany. He spent the 1983–1984 academic year at the Naval Research Laboratory, Washington, D.C.

Dr. Compton is a member of Sigma Xi and Pi Mu Epsilon. In 1983 he received the M. Barry Carlton Award for best paper from the IEEE Aerospace and Electronic Systems Society.

Protection of a Narrow-Band BPSK Communication System with an Adaptive Array

MATTHEW W. GANZ, MEMBER, IEEE, AND R. T. COMPTON, JR., FELLOW, IEEE

Abstract—This paper describes the performance of an adaptive array when used with narrow-band BPSK communication signals. A previous paper [11] described the performance of an adaptive array with a standard BPSK signal when the array bandwidth is several times the signal bandwidth. These earlier results are extended to the case where the array bandwidth is as small as possible, equal to the desired signal symbol rate. To realize such a bandwidth reduction, it is necessary to reshape the BPSK signaling waveform before transmission to prevent intersymbol interference. This is done by passing the BPSK signal through a pulse-shaping filter at the transmitter. The performance of the optimal detector for the narrow-band BPSK signal is determined when this detector operates behind an adaptive array that is subjected to CW interference. The bit error probability is obtained as a function of the desired signal and interference powers and arrival angles as well as the array bandwidth.

I. INTRODUCTION

ADAPTIVE array antennas can be used to protect communication systems from interference. The array suppresses interference by steering antenna pattern nulls in the direction of the interfering signal(s). The LMS array, due to Widrow *et al.* [1], is most often suggested for communications applications.

The LMS array steers a pattern beam in the direction of a signal correlated with a locally generated reference signal and steers nulls in the directions of signals uncorrelated with this reference signal. Methods of generating a suitable reference signal for the LMS array have been developed for several types of desired signal modulation, such as binary phase-shift keying (BPSK) [2], quadrature phase-shift keying (QPSK) [3], conventional amplitude modulation (AM) [4], and frequency-shift keying (FSK) [5], [6].

Early adaptive array studies used the signal-to-interference-plus-noise ratio (SINR) at the array output as the measure of system performance [7]-[9]. However, the bit error probability at the receiver output $P(e)$ cannot be determined from SINR alone [10]. Recently, the authors have examined the performance of communications systems with adaptive arrays using $P(e)$ as the figure of merit [11]-[13]. These studies considered the performance of adaptive arrays with continuous wave (CW) interference when the array bandwidth is several times the symbol rate of the desired signal. These studies showed that the array performance improves as the array input bandwidth is reduced. However, the signal and detector

models used in these studies were only appropriate when the array bandwidth is several times the desired signal symbol rate.

In this paper, we examine the performance of an adaptive array with BPSK signals when the array bandwidth is as small as the desired signal symbol rate. In order to operate a system in this manner, it is necessary to filter the standard BPSK signal prior to transmission so that the signal bandwidth (in Hz) equals the transmitted symbol rate. This narrow-band BPSK signal allows the array bandwidth to be set equal to the signal bandwidth without introducing intersymbol interference (ISI). The narrow-band BPSK signal has the property that it allows the same $P(e)$ as conventional BPSK with white Gaussian noise. We calculate the performance of the adaptive array with such a signal when both white Gaussian noise and CW interference are present. We calculate $P(e)$ for the combined array and BPSK detector as a function of the desired signal and interference powers, the signal arrival angles, and the array input bandwidth.

Section II describes the narrow-band BPSK modulation technique and calculates $P(e)$ when the BPSK signal is corrupted by CW interference. Section III presents a description of the LMS array and its operation. Section IV describes the performance of the combined LMS array and the BPSK detector. Finally, Section V contains the conclusions.

II. THE NARROW-BAND BPSK COMMUNICATION SYSTEM

In this section, we describe a narrow-band BPSK communication system. We calculate $P(e)$ for this system when the received signal is corrupted by additive white Gaussian noise and CW interference. Fig. 1 shows a block diagram of the communication system. The baseband nonreturn to zero (NRZ) signal is filtered prior to carrier modulation and transmission to limit the bandwidth of the BPSK signal. We choose a pulse-shaping transmit filter with transfer function $H_T(\omega)$ given by

$$H_T(\omega) = \begin{cases} \dfrac{1}{\text{sinc}\left(\dfrac{\omega T}{2}\right)}, & |\omega| < \dfrac{\pi}{T} \\[4mm] 0, & |\omega| \geq \dfrac{\pi}{T} \end{cases} \tag{1}$$

where sinc (x) denotes sin $(x)/x$ and T is the bit duration.

The power spectral density (PSD) of the NRZ baseband signal at the filter input is proportional to sinc^2 $(\omega T/2)$ [14]. Therefore, the PSD of the signal at the filter output is a constant for $|\omega| < \pi/T$ and zero outside this region. Since the signal at the filter output satisfies the Nyquist pulse shaping criterion, the system is free from ISI [15]. The filtered baseband signal modulates a carrier signal cos $(\omega_d t)$. The channel attenuates the signal and adds white Gaussian noise and (possibly) CW interference.
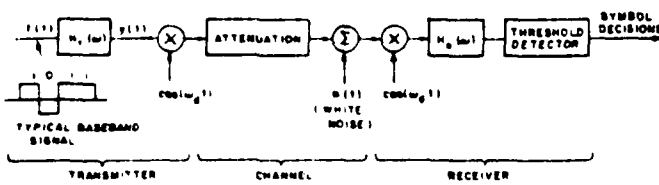
Fig. 1 The narrow-band BPSK communication system.

The signal at the receiver is given by

$$Z(t) = d(t) + i(t) + n(t) \qquad (2)$$

where

$$d(t) = \sum_k A_d b_k \text{ sinc} \left(\frac{\pi(t - kT)}{T} \right) \cos (\omega_d t + \psi_d) \qquad (3)$$

where A_d is the desired signal amplitude, b_k is equal to $+1$ or -1 depending on the kth transmitted bit, and ψ_d is a random variable uniformly distributed on $[0, 2\pi]$. The received interference signal $i(t)$ is given by

$$i(t) = A_i \cos (\omega_i t + \psi_i) \qquad (4)$$

where A_i is the interference amplitude, ω_i is the interference frequency. and ψ_i is a random variable uniformly distributed on $[0, 2\pi]$ that is independent of ψ_d. $n(t)$ is a white Gaussian noise signal with two-sided PSD $\eta/2$.

As previously noted, the rectangular shape of the desired signal spectrum satisfies the Nyquist pulse shaping criterion. We therefore can minimize $P(e)$ with white Gaussian noise and no other interference by filtering the baseband transmitted and received signals with appropriate filters [15]. In the present case, the appropriate filter at both the transmitter and the receiver is the ideal low-pass filter (LPF) with a cutoff frequency of $1/2T$ Hz. A separate transmit ideal LPF is not required since the PSD at the output of the transmit pulse-shaping filter is already rectangular.

At the receiver, the signal is multiplied by $\cos (\omega_d t + \psi_d)$. This multiplication coherently heterodynes the desired signal down to baseband. The baseband signal is passed through the ideal low-pass filter LPF with bandwidth $1/2T$ Hz which limits the thermal noise without distorting the desired signal. Although both the transmit and receive filters assumed in the model described above are not realizable, they lead to a straightforward mathematical formulation of the problem. Physically realizable filters which achieve nearly optimal performance with nearly minimal bandwidth have been built [14], [16].

In the absence of thermal noise or interference, a single rectangular baseband pulse of width T centered about time $t = 0$, when applied to the transmit filter input, produces a corresponding pulse at the receiver output which is of the form

$$Z_d = \frac{A_d}{2} \text{ sinc} \left(\frac{\pi t}{T} \right). \qquad (5)$$

The receiver samples the receive filter output at $t = kT$ and decides whether the kth bit was a "0" or a "1" based upon the sign of this sample. Since sinc $(\pi t/T) = 0$ for $t = kT$ (and $k \neq 0$) we see that the 0th bit produces no ISI for any preceding or following bits.

We now determine the signals that appear at the receive filter output when interference and noise are added in the channel. Since the detector processing is linear, the desired signal is still given by (5). The interference signal at the receive filter output is given by

$$Z_i = \frac{A_i}{2} \cos (\Gamma) \qquad (6)$$

where $\Gamma = [(\omega_d - \omega_i)t + \psi_d - \psi_i]$. Since ψ_d and ψ_i are each uniformly distributed on $[0, 2\pi]$, Γ is also uniformly distributed on this same interval [17]. Each thermal noise sample at the output of the receive filter is an independent zero-mean Gaussian random variable with variance $\eta/4T$. We denote the noise sample at the kth bit by $Z_n(k)$.

We assume that "0" and "1" bits are equally likely. The probability of error, given the random variable Γ, is given by

$$P(e|\Gamma) = \frac{1}{2} P(e|"0", \Gamma) + \frac{1}{2} P(e|"1", \Gamma). \qquad (7)$$

Therefore, the probability of error is given by

$$P(e|\Gamma) = \frac{1}{2} P \left[Z_n(k) < -\frac{A_d}{2} + \frac{A_i}{2} \cos (\Gamma) \right]$$

$$+ \frac{1}{2} P \left[Z_n(k) > \frac{A_d}{2} + \frac{A_i}{2} \cos (\Gamma) \right]. \qquad (8)$$

Since $Z_n(k)$ is a zero-mean Gaussian random variable, the probabilities in (8) are easily evaluated. The resulting expression for the probability of error, given Γ, is

$$P(e|\Gamma) = \frac{1}{2} \text{ erfc} \left(A_d \sqrt{\frac{T}{\eta}} + A_i \sqrt{\frac{T}{\eta}} \cos (\Gamma) \right)$$

$$+ \frac{1}{2} \text{ erfc} \left(A_d \sqrt{\frac{T}{\eta}} - A_i \sqrt{\frac{T}{\eta}} \cos (\Gamma) \right) \qquad (9)$$

where erfc (x) is the complementary error function defined by

$$\text{erfc } (x) = \frac{1}{\sqrt{2\pi}} \int_x^\infty e^{-z^2/2} dz. \qquad (10)$$

We average this expression for $P(e|\Gamma)$ over the uniformly distributed random variable Γ to determine $P(e)$:

$$P(e) = \frac{1}{2\pi} \int_0^{2\pi} \text{ erfc} \left(A_d \sqrt{\frac{T}{\eta}} + A_i \sqrt{\frac{T}{\eta}} \cos (\Gamma) \right) d\Gamma. \qquad (11)$$

Note that when we integrate (9) to obtain (11), the contributions of the error functions are equal (and are therefore combined) since we are integrating over a whole cycle of Γ.

We define E_d as the received energy per bit of the desired signal and E_i as the received energy in the interference per bit interval. Since $E_d = A_d^2 T/2$ and $E_i = A_i^2 T/2$ we can rewrite (11) as

$$P(e) = \frac{1}{2\pi} \int_0^{2\pi} \text{ erfc} \left(\sqrt{\frac{2E_d}{\eta}} + \sqrt{\frac{2E_i}{\eta}} \cos (\Gamma) \right) d\Gamma. \qquad (12)$$

We note that if $E_i = 0$, then (12) becomes $P(e) = $ erfc $(\sqrt{2E_d/\eta})$, the well-known result for standard BPSK signaling in white noise. Therefore, in the absence of CW interference, the narrow-band BPSK system achieves the same performance as standard BPSK.

Fig. 2 shows how $P(e)$ varies as a function of E_i/η, the interference-to-noise ratio (INR), for several values of E_d/η, and the signal-to-noise ratio (SNR). From this figure, we see that the system performance degrades monotonically as the INR increases. When the interference power at the receiver input exceeds the desired signal power the bit error probability rapidly approaches $1/2$. In the next section, we examine how the addition of the adaptive array affects the performance of this system.
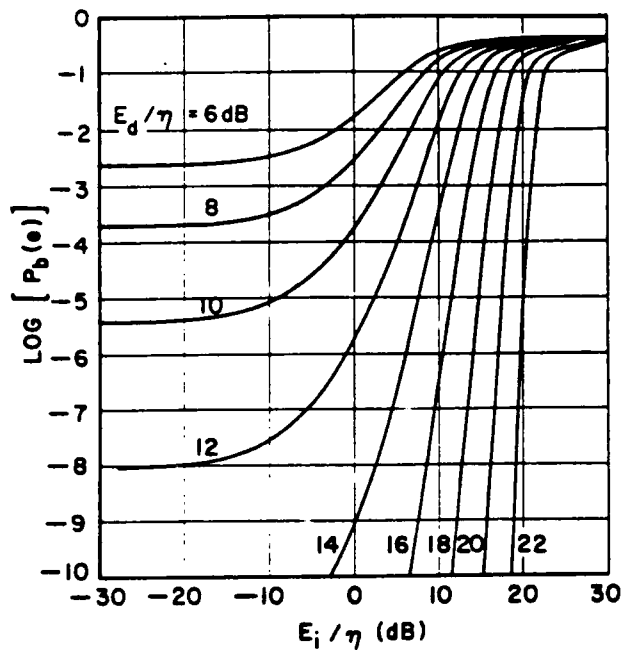
Fig. 2. Performance of narrow-band BPSK detector with CW interference $(\omega_i = \omega_d)$.

Fig. 3. The LMS array.

III. THE LMS ARRAY

In this section. we calculate the performance of the narrow-band BPSK communication system when we add an LMS adaptive array at the receiving end of the channel. We use analytic signal notation for each of the signals in the array [18]. Fig. 3 shows a three-element LMS array. The signals that arrive at the array elements are filtered by ideal bandpass filters (BPF's) which limit the thermal noise at the array input and reject out-of-band interference. The bandwidth of these filters must be a least $1/T$ so that the desired signal is passed without distortion. We shall find that the system performance is closely related to this bandwidth and. in the next section, we calculate this performance for several array input bandwidths.

The signals at the outputs of the BPF's. which we denote by $\tilde{x}_1(t)$, $\tilde{x}_2(t)$, and $\tilde{x}_3(t)$, are each multiplied by a complex weight
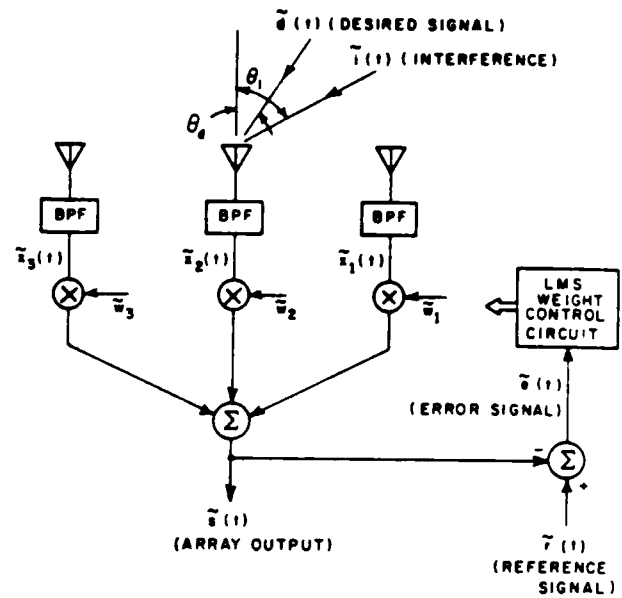
and the weighted signals are summed to produce the array output signal $\tilde{s}(t)$. This output signal is given by

$$\tilde{s}(t) = W^T X \tag{13}$$

where W is the weight vector, $W = [w_1, w_2, w_3]^T$, X is the input signal vector, $X = [\tilde{x}_1(t), \tilde{x}_2(t), \tilde{x}_3(t)]^T$, and T denotes the transpose.

The array output is subtracted from a locally generated reference signal $\tilde{r}(t)$ to produce the error signal $\tilde{e}(t)$. The steady-state LMS weights minimize the mean-square value of this error signal. In steady state, the LMS weight vector is given by [18]

$$W = \Phi^{-1} S, \tag{14}$$

where Φ is the covariance matrix,

$$\Phi = E[X^* X^T] \tag{15}$$

where $E[\cdot]$ denotes the expected value, $*$ denotes the complex

conjugate. and S denotes the reference correlation vector given by

$$S = E[X^* \tilde{r}(t)]. \tag{16}$$

We assume that the three antenna elements are linearly arranged and one half wavelength apart. We assume that the desired signal arrives from an angle θ_d and that a single CW interfering signal arrives from an angle θ_i. Both θ_d and θ_i are measured from the broadside direction.

At the output of each BPF, the thermal noise is a zero-mean Gaussian random process with variance

$$\sigma^2 = \eta B \tag{17}$$

where B is the BPF bandwidth in Hz. The noise signals at the BPF outputs are assumed to be mutually statistically independent.

It is straightforward to show that. for the signal models described above, the covariance matrix is given by

$$\Phi = \begin{pmatrix} R_d(0) + R_i(0) + \sigma^2 & R_d(-T_d) + R_i(-T_i) & R_d(-2T_d) + R_i(-2T_i) \\ R_d(T_d) + R_i(T_i) & R_d(0) + R_i(0) + \sigma^2 & R_d(-T_d) + R_i(-T_i) \\ R_d(2T_d) + R_i(2T_i) & R_d(T_d) + R_i(T_i) & R_d(0) + R_i(0) + \sigma^2 \end{pmatrix} \tag{18}$$

where $R_d(\tau)$ and $R_i(\tau)$ are the autocorrelation functions for the desired and interfering signals. respectively, and T_d and T_i are the interelement propagation delays for these signals. The desired signal and interference autocorrelation functions are given by

$$R_d(\tau) = A_d^2 \, \text{sinc}\left(\frac{\pi\tau}{T}\right) \exp(j\omega_d\tau) \tag{19}$$

$$R_i(\tau) = A_i^2 e^{j\omega_i\tau}. \tag{20}$$

We assume that the reference signal is perfectly correlated with the desired signal as seen at the input to element 1. Therefore, from (16), the reference correlation vector is given by

$$S = \mu \begin{pmatrix} R_d(0) \\ R_d(T_d) \\ R_d(2T_d) \end{pmatrix} \tag{21}$$

where μ is a constant that is determined from the amplitudes of the desired and reference signals.

Now that we have determined Φ and S, we determine the array weights using (14) and the array output signals at the array output using (13). The array output signal consists of the desired signal, a thermal noise signal, and the residual interference that the array was unable to null. These signals are applied to the narrow-band BPSK receiver described in Section II and $P(e)$ is calculated using (12).

We assume that the interelement time delay for the desired signal is much shorter than the bit interval (i.e., that $T_d \ll T$). With this assumption, we neglect any distortion in the desired signal modulation that occurs due to the summing of the time delayed versions of the desired signal in the array processing.

IV. RESULTS

In this section, we present the results of performance calculations for the narrow-band BPSK communication system with the LMS adaptive array. We consider the effects of the desired signal power level, the CW interfering signal power level, the signal arrival angles, and the array bandwidth.

In each of the cases that we examine in this paper, we assume that the desired signal relative bandwidth B_d is equal to 0.1 (where $B_d = 2\pi B/\omega_d$). It is shown in [18] that the signal power levels at the array output are essentially independent of B_c for most signal scenarios for values of B_d less than approximately 1/2.

First, for later comparison, we show the system performance when the array bandwidth is large. The results for this case are identical to those presented in [11] for the LMS array with conventional BPSK signaling and CW interference. Fig. 4 shows the performance of the system when the interfering signal arrives from an angle 80° from broadside. The array bandwidth for the cases shown in this figure is 20 times the data bandwidth or 20/T. When we compare Figs. 4 and 2, we see that the array does improve the system performance.[1]

Fig. 5 shows the performance when the interference arrival angle is reduced to 10° with the array bandwidth still equal to 20/T. For this case, the interference lies in the main beam of the quiescent array pattern (i.e., the array pattern with no interference).

The most prominent features of the curves shown in Figs. 4 and 5 are humps in the $P(e)$ versus INR curves. At low INR values, the thermal noise is stronger than the interference at the array inputs. As the INR increases, the interference power at the array output and $P(e)$ both increase. As the INR increases to approximately 10 dB, the array begins to null the interference. It is at this point that the interference and noise powers at the array input are equal. As the INR increases further, the null becomes deeper and the interference power at the array output begins to diminish. At very high INR values, the null is very deep and the interference power at the array output is negligible.

Since the resolution properties of the three-element array are limited, it is more difficult for the array to null the interference while maintaining a good response in the desired signal direction when θ_d and θ_i are close. Therefore, we see better performance in Fig. 4 than in Fig. 5.

Fig. 6 shows the performance of the system when the array input bandwidth is reduced to 1/T. All other parameters are unchanged from the cases shown in Fig. 5. From this figure, we see that there are no humps in the $P(e)$ versus INR curves for this narrow array bandwidth. Therefore, we might at first be tempted to conclude that the system performance is best

[1] We should note that, even with no interference, the SNR at the output of the three-element array is 4.77 dB greater than the SNR at each element input due to the array gain. This 4.77 dB SNR improvement would also be seen if a three-element fixed (i.e., nonadaptive) array were used and the desired signal were located at a pattern maximum.

Fig. 4. Performance of narrow-band BPSK communication system with three-element adaptive array and CW interference ($B = 20/T$, $|\omega_d - \omega_i| < 20\pi/T$, $\theta_i = 80°$).

Fig. 5. Performance of narrow-band BPSK communication system with three-element adaptive array and CW interference ($B = 20/T$, $|\omega_d - \omega_i| < 20\pi/T$, $\theta_i = 10°$).

when the array bandwidth is as small as possible (i.e., $B = 1/T$). However, when we carefully compare Figs. 5 and 6, we see that $P(e)$ is higher for the narrow-band system than it is for the wideband system at the left-hand side of the curves. Thus, we make the unexpected observation that, for low INR values,
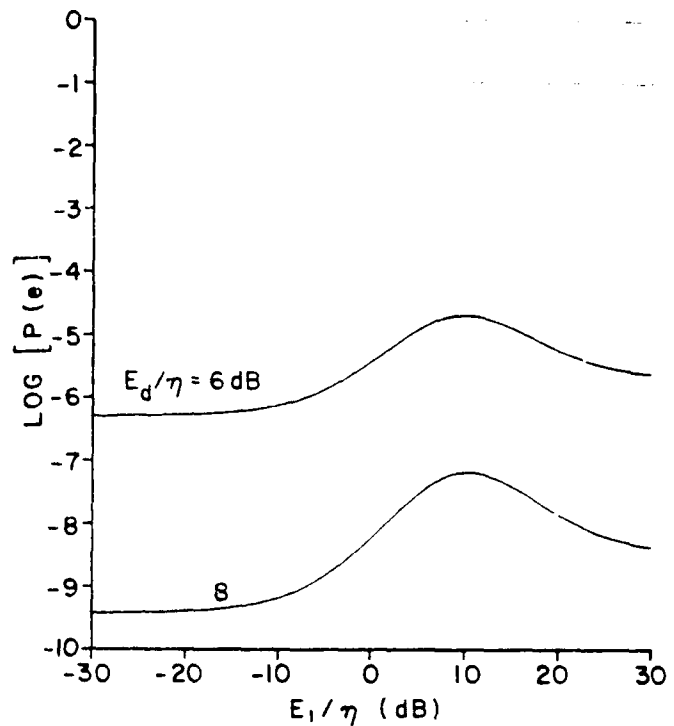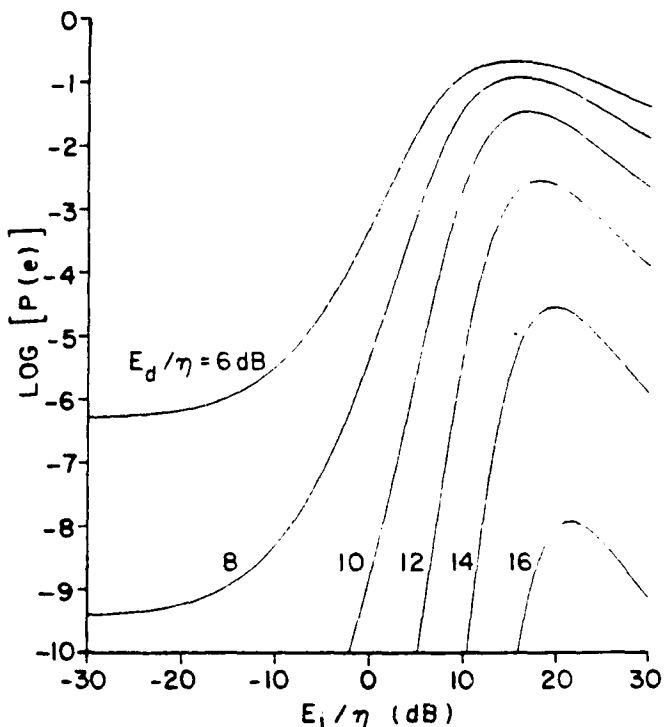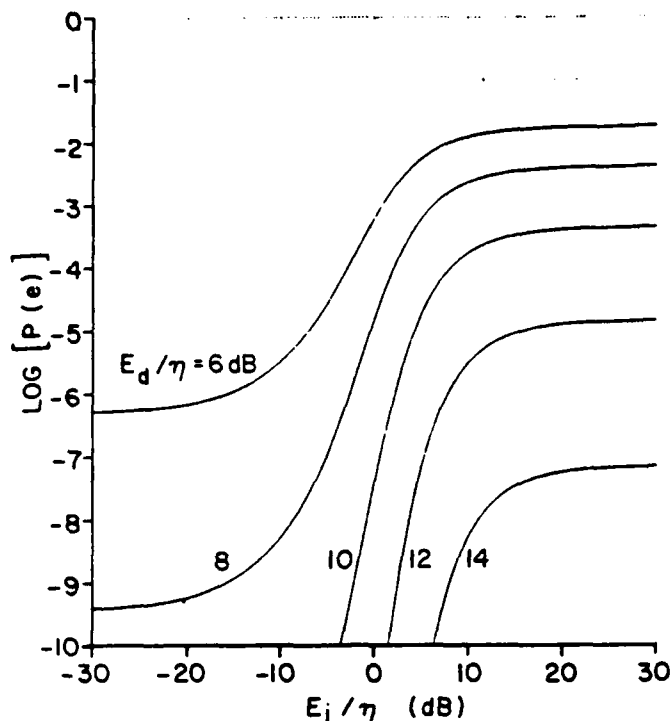
Fig. 6. Performance of narrow-band BPSK communication system with three-element adaptive array and CW interference ($B = 1/T$, $|\omega_d - \omega_i| < \pi/T$, $\theta_i = 10°$).

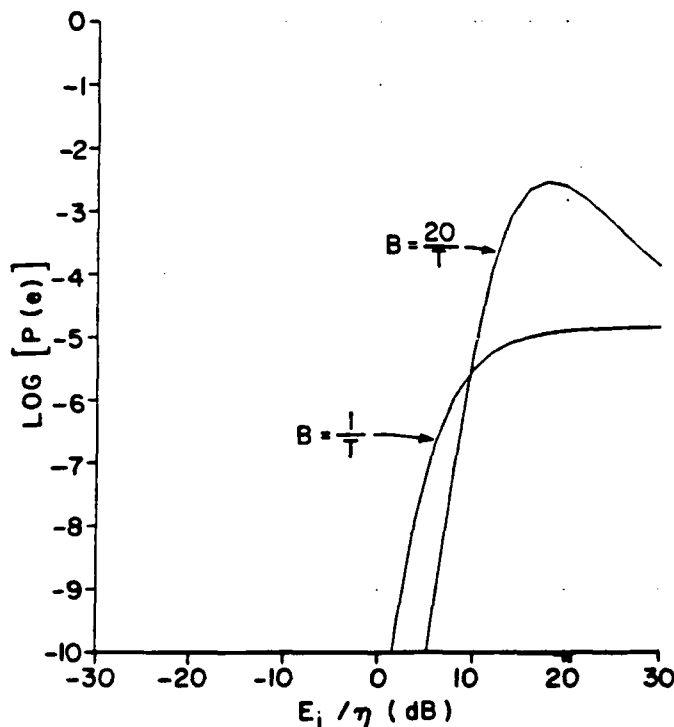Fig. 8. Adapted antenna pattern for $B = 20/T$, $E_i/\eta = 5$ dB.

Fig. 7. Performance of three-element array for two array bandwidths ($|\omega_d - \omega_i| < \pi/T$, $\theta_i = 10°$, $E_d/\eta = 12$ dB).

the system performance improves when the noise power at the array input increases.

For easy comparison, curves showing the performance of both the wide-band ($B = 20/T$) and narrow-band ($B = 1/T$) systems are plotted in Fig. 7 for an SNR value of 12 dB. For INR values above approximately 10 dB, the narrow-band
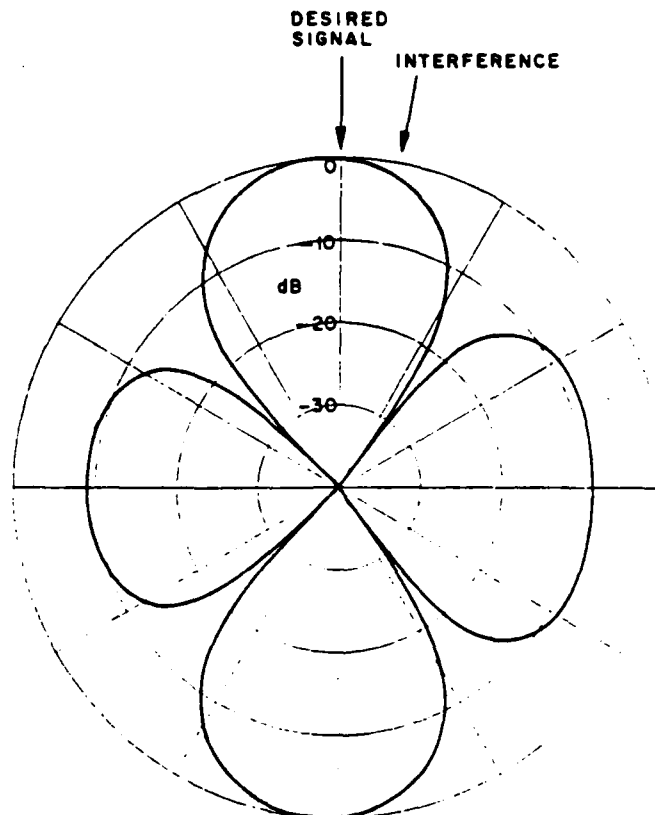
system performs better than the wide-band system. However, for INR values below 10 dB, the wide-band system performs better.

There is a simple explanation for this behavior. As the INR increases, the array begins to null the interference when the interference and noise powers at the array input are approximately equal. Therefore, the null begins to form at a lower INR value when $B = 1/T$ than it does when $B = 20/T$. Consider the cases shown in Fig. 7 for an INR value of 5 dB. Figs. 8 and 9 show the adapted array patterns for the wideband and narrow-band arrays, respectively. From these figures, we see that the wide-band array has not formed a null in the interference direction and the desired signal is very close to a pattern maximum. However, the narrow-band system has formed a pattern null on the interference. Furthermore, since the desired and interfering signals are spatially close, the array no longer keeps the desired signal near a pattern maximum. Therefore, the SNR at the array output is lower for the narrow-band array than it is for the wide-band array for the case shown. The increase in $P(e)$ due to the narrow-band array pattern null is greater than that which occurs for the wide-band system due to the residual interference at the array output.

Fig. 10 shows the system performance for three different array bandwidths, $B = 1/T$, $B = 2/T$, and $B = 4/T$. The curves shown in this figure indicate that there is no value of input bandwidth that offers a minimal $P(e)$ for all INR values. The curve for $B = 2/T$ lies significantly below that for $B = 1/T$ for INR values below approximately 12 dB. For larger INR values, $P(e)$ for $B = 2/T$ is only slightly greater than that for $B = 1/T$. For $B = 4/T$, we see even better performance below 12 dB, but a hump is beginning to form in the curve above 12 dB. $P(e)$ versus INR curves were plotted for several other values of SNR and θ_i and similar results were obtained. In each case, the humps in the INR curves appear for B values greater than approximately $4/T$.

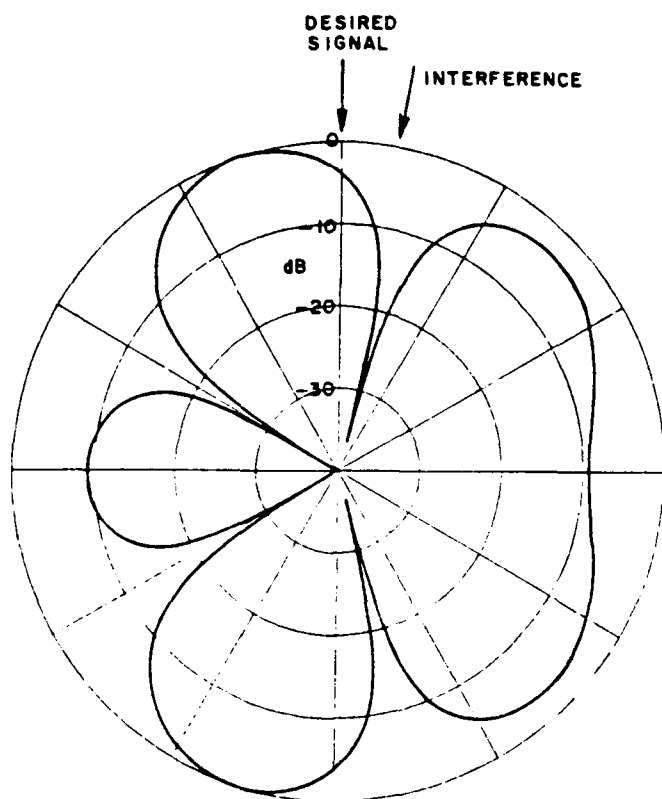If the array bandwidth is greater than $1/T$, then the input

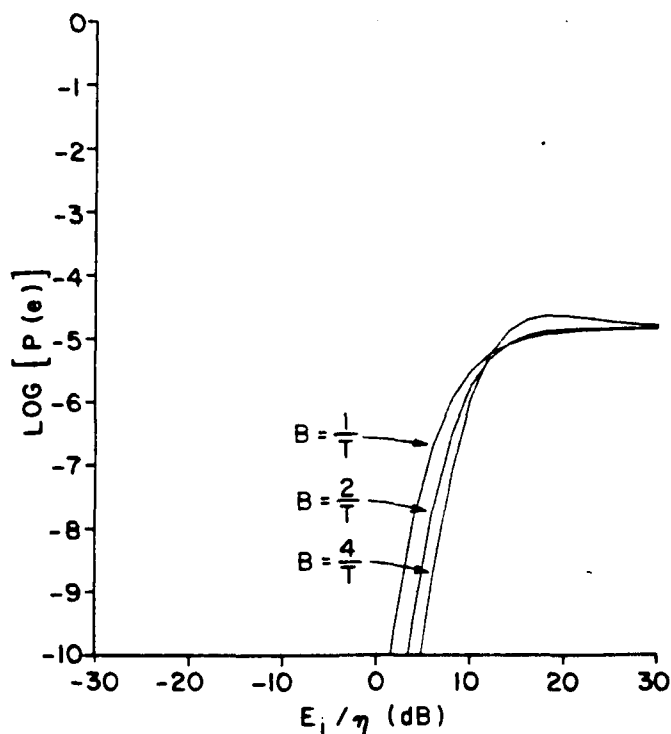Fig 9. Adapted antenna pattern for $B = 1/T$, $E_i/\eta = 5$ dB.

Fig. 11. Performance of narrowband BPSK communication system with three-element adaptive array and CW interference ($B = 20/T$, $\pi/T < |\omega_d - \omega_i| < 20\pi/T$, $\theta_i = 10°$).

direction may be reduced by the null. We can calculate the system performance for this case using the methods of Section III to compute the signals at the array output and then using (12) with E_i set to zero to compute $P(e)$. Fig. 11 shows the performance of the three-element array with $B = 20/T$ Hz, $\theta_i = 10°$, and $\pi T < |\omega_d - \omega_i| < 20\pi/T$. For these values of ω_i, the interference is passed by the input BPF's, but rejected by the detector LPF. In this case, the array still nulls the interference. From Fig. 11, we see that $P(e)$ increases with INR due to the reduction in desired signal response caused by the null on the interference. Therefore, for maximum resistance to out-of-band interference, the array input bandwidth should be made as small as possible.

V. CONCLUSIONS

In this paper, we have examined the performance of a bandlimited BPSK system with an adaptive array. We found that the performance with CW interference is best for array bandwidths less than approximately $4/T$ since the humps in the $P(e)$ versus INR curves appear for larger bandwidths. With CW interference, whose frequency is within the passband of the detector, the performance for bandwidths between $2/T$ and $4/T$ is never much worse than that for $B = 1/T$ (and sometimes it is better). Therefore, we conclude that, for this type of interference, there is little reason to expend great cost or effort to reduce the bandwidth below $4/T$. However, if the array bandwidth is greater than $1/T$, the system will be susceptible to out-of-band interference. We found that out-of-band interference causes a performance degradation due to the pattern null when the interfering and desired signals are spatially close. Finally, we found that the best performance is achieved when the interfering signal arrives from an angle outside the main beam of the interference-free antenna pattern.

Fig. 10. Performance of three-element array for three array bandwidths ($|\omega_d - \omega_i| < \pi/T$, $\theta_i = 10°$, $E_d/\eta = 12$ dB).

BPF's will pass interfering signals that lie at frequencies to which the detector is not sensitive. Although such an interfering signal will not adversely affect the detector, the array will still respond to the interference. If the interference is spatially close to the desired signal, the response in the desired signal
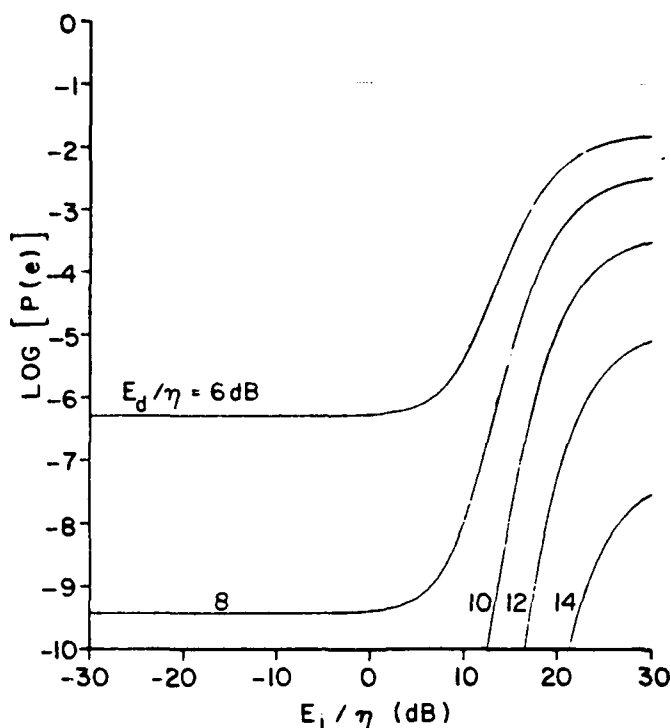
REFERENCES

[1] B. Widrow, P. E. Mantey, L. J. Griffiths, and B. B. Goode, "Adaptive antenna systems," Proc. IEEE, vol. 55, p. 2143, Dec. 1967.

[2] R. T. Compton. Jr., "An adaptive array in a spread spectrum communication system." *Proc. IEEE*, vol. 66. p. 289. Mar. 1978.

[3] J. H. Winters. "Spread spectrum in a four-phase communication system employing adaptive arrays." *IEEE Trans. Commun.*, vol. COM-30. p. 929. May 1982.

[4] R. T. Compton. Jr., R. J. Huff. W. G. Swarner. and A. A. Ksienski. "Adaptive arrays for communication systems: An overview of research at The Ohio State University." *IEEE Trans. Antennas Propagat.*, vol. AP-24. p. 599. Sept. 1976.

[5] E. C. Hudson. "Use of an adaptive array in a frequency-shift keyed communication system." The Ohio State Univ. ElectroSci. Lab.. Columbus. Rep. 712684-1. Aug. 1980.

[6] M. W. Ganz. "On the performance of an adaptive array in a frequency-shift keyed communication system." M.Sc. thesis. Dep. Elec. Eng., The Ohio State Univ.. Columbus. 1982.

[7] I. J. Gupta. "Effect of jammer power on the performance of adaptive arrays." *IEEE Trans. Antennas Propagat.*, vol. AP-32. pp. 933-938. Sept. 1984.

[8] R. J. Compton. Jr., "On eigenvalues. SINR. and element patterns in adaptive arrays." *IEEE Trans. Antennas Propagat.*, vol. AP-32. pp. 643-647. June 1984.

[9] I. J. Gupta and A. A. Ksienski. "Dependence of adaptive array performance on conventional array design." *IEEE Trans. Antennas Propagat.*, vol. AP-32. pp. 549-533. July 1982.

[10] M. W. Ganz. "Performance of digital communication systems with adaptive arrays." Ph.D. dissertation. The Ohio State Univ.. Columbus. 1986.

[11] M. W. Ganz and R. T. Compton. Jr., "Protection of a BPSK communication system with an adaptive array." in *Proc. IEEE MONTECH '86 Conf. Antennas Propagat.*, Montreal. P.Q.. Canada. Sept. 1986.

[12] M. W. Ganz. "Protection of a BPSK communication system with an LMS adaptive array." The Ohio State Univ. ElectroSci. Lab.. Columbus. Rep. 717253-1. Oct. 1985.

[13] ——. "Protection of a QPSK communication system with an LMS adaptive array." The Ohio State Univ. ElectroSci. Lab.. Columbus. Rep. 717253-2. Jan. 1986.

[14] K. Feher. *Digital Communications—Microwave Applications*. Englewood Cliffs. NJ: Prentice-Hall. 1981. ch. 3.

[15] R. E. Ziemer and R. L. Peterson. *Digital Communications and Spread Spectrum Systems*. New York: Macmillan. 1985. pp. 135-141.

[16] J. W. Bayless. A. C. Collins. and R. D. Pederson. "The specification of bandlimited digital radio systems." *IEEE Trans. Commun.*, vol. COM-27. pp. 1763-1770. Dec. 1979.

[17] F. J. Scire. "A probability density function for the modulo Y values of the sum of two statistically independent processes." *Proc. IEEE*, vol. 56. pp. 204-205. Feb. 1968.

[18] R. T. Compton. Jr., *Adaptive Antennas—Concepts and Performance*. Englewood Cliffs. NJ: Prentice-Hall. to be published in 1987.

★

Matthew W. Ganz (S'82-M'87) was born in Toledo. OH. on March 8. 1959. He received the B.S.. M.S.. and Ph.D. degrees in electrical engineering from The Ohio State University. Columbus. in 1981. 1982. and 1986. respectively.

From 1980 to 1982 and 1985 to 1986. he was a Fellow Research Associate. a Graduate Research Associate. and a Postdoctoral Research Associate at The Ohio State University ElectroScience Laboratory where he studied communications and radar applications of adaptive antenna systems. From 1982 to 1984. he was an Associate Engineer in the Space Department of The Johns Hopkins University Applied Physics Laboratory. There he worked primarily on satellite communication and tracking systems. He is currently a member of the Technical Staff in the Radar Systems Group at M.I.T. Lincoln Laboratory. Lexington. MA. where he is working on radar applications of adaptive arrays.

Dr. Ganz is a member of Tau Beta Pi. Eta Kappa Nu. and Sigma Xi.

★

R. T. Compton. Jr. (S'58-M'59-M'81-SM'82-F'84) was born in St. Louis. MO. on July 26. 1935. He received the S.B. degree from Massachusetts Institute of Technology. Cambridge. in 1958 and the M.Sc. and Ph.D. degrees from The Ohio State University. Columbus. in 1961 and 1964. respectively. all in electrical engineering.

He is a Professor of Electrical Engineering at The Ohio State University. From 1965 to 1967. he was an Assistant Professor of Engineering at Case Institute of Technology. Cleveland. OH. and from 1967 to 1968 he was an NSF Postdoctoral Fellow at the Technische Hochschule. Munich. Germany. He spent the 1983-1984 academic year at the Naval Research Laboratory. Washington. DC.

Dr. Compton is a member of Sigma Xi and Pi Mu Epsilon. He received the M. Barry Carlton Award for best paper from the IEEE Aerospace and Electronic Systems Society in 1983.

Comparison Between Two Asymptotic Methods

Roberto G. Rojas

Comparison Between Two Asymptotic Methods

ROBERTO G. ROJAS

Abstract—Two complete asymptotic expansions of an integral with many simple pole singularities and a first-order, isolated, saddle point evaluated by two different methods are compared. It is shown that both expansions are exactly the same (term by term) inside and outside the transition regions.

I. INTRODUCTION

It is common to express the solution of electromagnetic diffraction problems in terms of an integral, which, in general, cannot be evaluated in closed form. However, it is possible to obtain its complete asymptotic expansion for large values of a parameter. There

are several methods to obtain the asymptotic expansion, the most general being the method followed by Bleistein [1]. For the type of integral being considered here, the most commonly used technique is the method of steepest descents [2]. In order to apply this method, it is necessary to deform the original contour of integration to the steepest descent path (SDP), taking into account any singularities that may be crossed during the deformation. The integral along the steepest descent path can then be expressed as follows:

$$I(\Omega) = \int_{SDP} g(z) e^{\Omega f(z)} \, dz \qquad (1)$$

where $g(z)$ and $f(z)$ are analytic functions of the complex variable z along the integration path SDP. The parameter Ω is real and positive and the end points of SDP are at infinity. It is assumed that the integrand in (1) has an isolated, first-order saddle point at z_s, i.e., $f'(z) = 0$ and $f''(z) \neq 0$ at $z = z_s$. Furthermore, even though the function $g(z)$ is analytic along the SDP, it has M simple poles $\{z_i\}_{i=1}^{M}$ near the saddle point z_s.

Since $f(z)$ has an isolated first-order saddle point at z_s, the following transformation is appropriate

$$f(z) = f(z_s) - s^2. \qquad (2)$$

Substituting (2) into (1) yields

$$I(\Omega) = e^{\Omega f(z_s)} \int_{-\infty}^{\infty} G(s) e^{-\Omega s^2} \, ds \qquad (3)$$

where

$$G(s) = g(z) \frac{dz}{ds}; \frac{dz}{ds} = \frac{-2s}{f'(z)}; \frac{dz}{ds}\bigg|_{s=0} = \left[\frac{-2}{f''(z_s)}\right]^{1/2}. \qquad (4)$$

There are two procedures found in the literature to evaluate (3) for large values of Ω. The first one, which appears to have been originally introduced by Van der Waerden [3], is discussed in detail by Felsen and Marcuvitz [4]. In this method, $G(s)$ is expressed as the sum of two functions such that

$$G(s) = C(s) + P(s) \qquad (5)$$

where $C(s)$ contains all the pole singularities of $G(s)$ and $P(s)$ is regular in the neighborhood of $s = 0$. Thus, the original integral in (3) is reduced to the sum of two integrals; namely, the integral of $C(s)$ which can be expressed in terms of a Fresnel-type integral, and the integral of $P(s)$ which can be expanded (asymptotically) in a series of inverse powers of Ω. Felsen and Marcuvitz obtain the complete uniform asymptotic expansion of an integral similar to (3), given in [4, eq. (4.4.16)], except that they consider the case where $G(s)$ has one simple pole near $s = 0$. It is noted that the solution presented in [4, eq. (4.4.16)] is valid for the general case where the pole may cross the steepest descent path anywhere in the complex z-plane. The generalization of Felsen's results to the present case is straightforward as shown in Section II.

The second procedure is the Pauli-Clemmow method [5] in which the function $G(s)$ is expressed as the product of two functions, namely

$$G(s) = T(s) B(s) \qquad (6)$$

where $T(s)$ is regular near $s = 0$ and $B(s)$ contains all the singularities of $G(s)$. Since $T(s)$ is regular in the neighborhood of $s = 0$, it is expanded in a Taylor series around $s = 0$ and after multiplying the Taylor series by $B(s)$, it is formally integrated term by term. Thus, each term of the asymptotic series contains a Fresnel integral plus inverse powers of Ω. Recently, Gennarelli and Palumbo [6] obtained the complete asymptotic expansion of (3) following the Pauli-Clemmow method. However, unlike previous results obtained

by this method, the authors in [6] isolated the Fresnel integral, which is present in every term of the Pauli-Clemmow series, in the leading $\Omega^{-1/2}$ order term.

It is shown in Section III that the complete uniform asymptotic expansions obtained by the two methods described above are identical (term by term) inside and outside the transition regions corresponding to each pole of $G(s)$. It was observed by Hutchins and Kouyoumjian [7] and independently by Boersma and Rahmat-Samii [8] that the two asymptotic series of $I(\Omega)$ are equivalent for the special case where $G(s)$ has one pole near $s = 0$.

Yip and Chiavetta [9] show that the function on the right hand side of (6) can always be expressed as the sum of two functions, namely

$$T(s) B(s) = L(s) + M(s) \qquad (7)$$

where $L(s)$ is a function containing all the singularities of $T(s) B(s)$ and $M(s)$ is regular near $s = 0$. It is then shown in [9] that $L(s) = C(s)$ and $M(s) = P(s)$ which is to be expected since $C(s) + P(s)$ and $T(s) B(s)$ represent the same function $G(s)$. Thus, substituting (7) into (3), Yip and Chiavetta reduce the original integral in (3) to the sum of two integrals (as in the first method described above) where one integral can be expressed in terms of a Fresnel integral and the second in inverse powers of Ω. However, this is not what is done in the Pauli-Clemmow method. As mentioned before, the function $T(s) B(s)$ is expanded in a series where each term contains all the singularities of $G(s)$ and consequently each term of the asymptotic series of $I(\Omega)$ will contain a Fresnel integral. In order to compare the Pauli-Clemmow and Van der Waerden methods, it is necessary to study the complete asymptotic series of $I(\Omega)$. In the process of integrating $T(s) B(s)$ and $C(s) + P(s)$, orders of integration and summation are freely interchanged without rigorous justification. Thus, it is not possible to conclude a priori that the asymptotic series of $I(\Omega)$ obtained by the two methods are the same.

Volakis and Herman [10] extended Felsen's result [4] to the case of multiple pole singularities and obtained only the leading term of $I(\Omega)$. It appears by the comments made in the Introduction of [10] that Volakis and Herman did not realize that the solution in [6] is applicable for the general case where the poles of $g(z)$ can cross the steepest descent path anywhere in the complex z-plane.

II. FIRST METHOD (Van der Waerden)

Since $G(s)$ is an analytic function with M simple poles $\{s_i\}_{i=1}^{M}$, it can be written as follows:

$$G(s) = \sum_{i=1}^{M} \frac{r_i}{s - s_i} + P(s) = \sum_{i=1}^{M} \frac{r_i}{s - s_i} + \sum_{n=0}^{\infty} \frac{P^{(n)}(0)}{n!} s^n \qquad (8)$$

where $P(s)$ is a regular function near $s = 0$ and r_i is the residue of $G(s)$ at the pole s_i, namely

$$r_i = \lim_{s \to s_i} G(s)(s - s_i). \qquad (9)$$

Because $P(s)$ is a regular function, it can be expanded in a Taylor series around $s = 0$ as shown in (8). It is noted that $P^{(n)}(0)$ is the nth derivative of $P(s)$ evaluated at $s = 0$.

Substituting (8) into (3), one obtains

$$I(\Omega) \sim e^{\Omega f(z_s)} \left\{ \sum_{i=1}^{M} \pm 2jr_i \sqrt{\pi} e^{-\Omega s_i^2} Q(\mp js_i \sqrt{\Omega}) \right. $$
$$\left. + \frac{1}{\sqrt{\Omega}} \sum_{n=0}^{\infty} \frac{P^{(2n)}(0) \Gamma\left(n + \frac{1}{2}\right)}{(2n)! \Omega^n} \right\}; \quad \text{Im } (s_i) \gtrless 0 \qquad (10)$$

where $\Gamma(n + 1/2)$ is the Gamma function, $j = \sqrt{-1}$ and

$$Q(y) = \int_y^\infty e^{-t^2} \, dt; \quad Q(y) + Q(-y) = \sqrt{\pi}. \tag{11}$$

It is noted that when s_i is complex, the condition $Q(\mp js_i\sqrt{\Omega})$ for $\mathrm{Im}(s_i) \geqq 0$, implies that $\mathrm{Re}\ (\mp js_i\sqrt{\Omega}) > 0$ in (10).

In order to compare (10) to the expression obtained by the Pauli–Clemmow method, it is convenient to express $Q(y)$ in terms of the transition function $F(x)$ which is given by [11]

$$F(x) = 2j\sqrt{x}e^{jx} \int_{\sqrt{x}}^\infty e^{-jt^2} \, dt; \quad -\frac{3\pi}{2} < \arg\ (x) < \pi/2 \tag{12}$$

where x can be complex. Due to the presence of the square root function $\sqrt{x}$ in (12), and in order for $F(x)$ to be a single-valued function, it is necessary to introduce a branch cut in the x-plane [12], [13]. Furthermore, to assure the convergence of $F(x)$ as $|x| \to \infty$, the branch cut is chosen as depicted in Fig. 1. It follows from (11) and (12) that

$$Q(y) = \frac{F(-jy^2)e^{-y^2}}{2y} + \sqrt{\pi}\,U(-\mathrm{Re}\ (y)) \tag{13}$$

where U is the unit step function. Substituting (13) into (10), keeping in mind that $\mathrm{Re}\ (\mp js_i\sqrt{\Omega}) > 0$ in (10), yields

$$I(\Omega) \sim \frac{e^{\Omega f(z_s)}}{\sqrt{\Omega}} \left\{ \sqrt{\pi} \sum_{i=1}^M \frac{r_i}{s_i} (1 - F(j\Omega s_i^2)) + G(0)\sqrt{\pi} \right.$$
$$\left. + \sum_{n=1}^\infty \frac{A_n \Gamma(n + 1/2)}{\Omega^n} \right\} \tag{14}$$

where

$$A_n = \frac{G^{(2n)}(0)}{(2n)!} + \sum_{i=1}^M \frac{r_i}{s_i^{2n+1}}. \tag{15}$$

III. SECOND METHOD (Pauli-Clemmow)

Let $T(s)$ be a regular function given by

$$T(s) = G(s) \prod_{i=1}^M (s - s_i) = \sum_{n=0}^\infty \frac{T^{(n)}(0)}{n!} s^n \tag{16}$$

where $G(s)$ was defined in (4) and $\{s_i\}_{i=1}^M$ are the poles of $G(s)$. Solving for $G(s)$ in (16) yields

$$G(s) = \frac{T(s)}{\displaystyle\prod_{i=1}^M (s - s_i)} = T(s) \sum_{i=1}^M \frac{C_i}{(s - s_i)} = T(s)B(s) \tag{17}$$

where

$$C_i = \frac{1}{\displaystyle\prod_{\substack{k=1 \\ k \neq i}}^M (s_i - s_k)}. \tag{18}$$

It is noted that for $M = 1$, $C_1 = 1$. By means of (16), the asymptotic series of $I(\Omega)$, given in [6], can be rewritten as follows:

$$I(\Omega) \sim \sqrt{\frac{\pi}{\Omega}} e^{\Omega f(z_s)} \left\{ \sum_{i=1}^M \frac{r_i}{s_i} (1 - F(j\Omega s_i^2)) - T(0) \sum_{i=1}^M \frac{C_i}{s_i} \right\}$$
$$+ \sqrt{\Omega} e^{\Omega f(z_s)} \sum_{n=2}^\infty \frac{\Gamma(n - 1/2)}{\Omega^n}$$
$$\cdot \left\{ \sum_{i=1}^M \frac{C_i T(s_i)}{s_i^{2n-1}} - \sum_{k=0}^{2n+M-3} \frac{T^{(k)}(0)}{k!} \sum_{i=1}^M C_i s_i^{k-2n+1} \right\}. \tag{19}$$
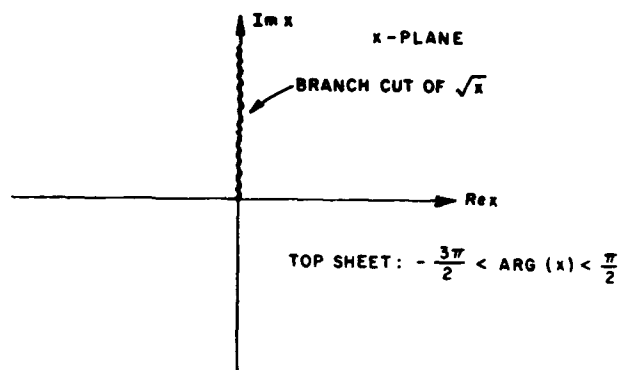
Fig. 1. Branch cut definition of the $\sqrt{x}$ function in (12).

Evaluating (17) at $s = 0$ and substituting that expression into (19) yields

$$I(\Omega, \phi) \sim \sqrt{\frac{\pi}{\Omega}} e^{\Omega f(z_s)} \left\{ \sum_{i=1}^M \frac{r_i}{s_i} (1 - F(j\Omega s_i^2)) + G(0) \right\}$$
$$+ \frac{e^{\Omega f(z_s)}}{\sqrt{\Omega}} \sum_{n=1}^\infty \frac{\Gamma(n + 1/2)}{\Omega^n}$$
$$\cdot \left\{ \sum_{i=1}^M \frac{r_i}{s_i^{2n+1}} - \sum_{k=0}^{2n+M-1} \frac{T^{(k)}(0)}{k!} \sum_{i=1}^M \frac{C_i s_i^k}{s_i^{2n+1}} \right\}. \tag{20}$$

It follows from (17) that

$$\sum_{k=0}^{2n+M-1} \frac{T^{(k)}(0)}{k!} \sum_{i=1}^M \frac{C_i s_i^k}{s_i^{2n+1}}$$

$$= \begin{cases} -\dfrac{G^{(2n)}(0)}{(2n)!}, & \text{for } M = 1 \\[2ex] -\dfrac{G^{(2n)}(0)}{(2n)!} + \displaystyle\sum_{k=0}^{M-2} \frac{T^{(k+2n+1)}(0)}{(k+2n+1)!} \sum_{i=1}^M C_i s_i^k, & \text{for } M \geqslant 2. \end{cases}$$

$$\tag{21}$$

However, it can be shown that

$$\sum_{i=1}^M C_i s_i^l = 0, \quad \text{for } l = 0, 1, \cdots, M - 2. \tag{22}$$

Therefore, (20) can be written in the following manner:

$$I(\Omega) \sim \sqrt{\frac{\pi}{\Omega}} e^{\Omega f(z_s)} \left\{ \sum_{i=1}^M \frac{r_i}{s_i} (1 - F(j\Omega s_i^2)) + G(0) \right\}$$
$$+ \frac{e^{\Omega f(z_s)}}{\sqrt{\Omega}} \sum_{n=1}^\infty \frac{\Gamma(n + 1/2)}{\Omega^n} \left\{ \sum_{i=1}^M \frac{r_i}{s_i^{2n+1}} + \frac{G^{(2n)}(0)}{(2n)!} \right\}. \tag{23}$$

The asymptotic expansions of $I(\Omega)$ given in (14) and (23) are exactly the same.

As a final check, the asymptotic series in (23) can be simplified even further when the function $G(s)$ does not have any poles near s

$= 0$. Thus, when the poles of $G(s)$ are far from $s = 0$, the magnitude $j\Omega s_i^2$ is large and the asymptotic expansion of $F(j\Omega s_i^2)$ is given by

$$F(j\Omega s_i^2) \sim 1 + \frac{1}{\sqrt{\pi}} \sum_{l=1}^{\infty} \frac{\Gamma(l+1/2)}{(\Omega s_i^2)^l} \; ; \quad -\frac{3\pi}{2} < \arg (j\Omega s_i^2) < \frac{\pi}{2} \; . \quad (24)$$

Substituting (24) into (23) yields

$$I(\Omega) \sim \frac{e^{\Omega f(z_s)}}{\sqrt{\Omega}} \sum_{n=0}^{\infty} \frac{G^{(2n)}(0)\Gamma(n+1/2)}{(2n)!\Omega^n} \quad (25)$$

which is the correct expression for the case when $g(z)$ does not have any poles near z_s.

IV. Conclusion

Two complete uniform asymptotic expansions (for large Ω) of the integral shown in (1), obtained by two different methods, were compared. It was shown that both expansions are exactly the same (term by term). It was also observed that the uniform asymptotic solutions given in [6] (multiple pole singularities) and in [4, eq. (4.4.16)] (one pole singularity) are applicable for the general case where the pole(s) of $g(z)$ cross the SDP path anywhere in the z-plane. Obviously, the generalization of Felsen's result [4] to multiple pole singularities is still valid for the general case described above. Furthermore, for the special case when all the poles of $g(z)$ are far from the saddle point, the transition function $F(x)$ was replaced by its own asymptotic series for large $|x|$. As expected, the asymptotic series in (25) is the same as the one obtained by Felsen [4] when $g(z)$ is regular near the saddle point.

References

[1] N. Bleistein, "Uniform asymptotic expansions of integrals with many nearby stationary points and algebraic singularities," *J. Math. Mech.*, vol. 17, pp. 533–559, 1967.

[2] A. Erdelyi, *Asymptotic Expansions*. New York: Dover, 1956, ch. 2.

[3] B. L. Van der Waerden, "On the method of saddle points," *Appl. Sci. Res.*, B2, pp. 33–45, 1951.

[4] L. B. Felsen and N. Marcuvitz, *Radiation and Scattering of Waves*. Englewood Cliffs, NJ: Prentice-Hall, 1973, ch. 4.

[5] P. C. Clemmow, "Some extensions to the method of integration by steepest descents," *Quart. J. Mech. Appl. Math.*, vol. 3, pp. 241–256, 1950.

[6] C. Gennarelli and L. Palumbo, "A uniform asymptotic expansion of a typical diffraction integral with many coalescing simple pole singularities and a first-order saddle point," *IEEE Trans. Antennas Propagat.*, vol. AP-32, pp. 1122–1124, Oct. 1984.

[7] D. L. Hutchins and R. G. Kouyoumjian, "Asymptotic series describing the diffraction of a plane wave by a wedge," Ohio State Univ. ElectroSci. Lab., Techn. Rep. 2183-3, Dec. 1969.

[8] J. Boersma and Y. Rahmat-Samii, "Comparison of two leading uniform theories of edge diffraction with the exact uniform asymptotic solution," *Radio Sci.*, vol. 15, pp. 1179–1194, Nov.-Dec. 1980.

[9] E. L. Yip and R. J. Chiavetta, "Comparison of uniform asymptotic expansions of diffraction integrals," *IEEE Trans. Antennas Propagat.*, to appear.

[10] J. L. Volakis and M. I. Herman, "A uniform asymptotic evaluation of integrals," *Proc. IEEE*, vol. 74, pp. 1043–1044, July 1986.

[11] R. G. Kouyoumjian and P. H. Pathak, "A uniform geometrical theory of diffraction for an edge in a perfectly conducting surface," *Proc. IEEE*, vol. 62, pp. 1448–1461, 1974.

[12] R. Tiberio and G. Pelosi, "High-frequency scattering from the edges of impedance discontinuities on a flat plane," *IEEE Trans. Antennas Propagat.*, vol. 31, pp. 590–596, July 1983.

[13] R. G. Rojas, "A uniform GTD analysis of the EM diffraction by a thin dielectric/ferrite half-plane and related configurations," Ph.D. dissertation, Ohio State Univ., 1985.

INTRODUCTION

This work examines the transverse electric (TE) surface ray field excited by a magnetic line source in the presence of a perfectly conducting circular cylinder with a dielectric coating. The line source and the field point are both positioned at the dielectric-air interface.

The surface field is first calculated from a rigorous eigenfunction series. Next, through the Watson transform, the alternate creeping wave representation is examined. The dielectric coating does not have to be thin, and an example is given whereby the creeping wave field on a thick coating must be represented as two creeping wave modes.

This work differs from previous papers in that no one has examined the case where both the source and field points reside on the cylinder. Kodis [1], Kodis and Wu [2], and Rao and Hamid [3], have examined bistatic scattering and have given a geometrical optics interpretation. Wang [4] has recently obtained numerical results for the case of plane wave scattering and an interpretation of scattering resonances in terms of a reflected field plus creeping waves.

Fig. 1 shows the pertinent geometry. The conducting cylinder has a radius $\rho = a$ and the dielectric coating has a radius $\rho = b$. The magnetic line source is ℓ directed, has a strength of M_0 V, and is positioned at $(\rho', \phi') = (b, 0)$. The field point is at $(\rho, \phi) = (b, \phi)$. Since the coating is nonmagnetic, $\mu_1 = \mu_0$ and the dielectric constant is ϵ_1.

A. Eigenfunction Solution

The magnetic field has only a ℓ component and can be computed from the eigenfunction series of the inhomogeneous Helmholtz equation. The solution must also satisfy the boundary conditions $E_\phi = 0$ at $\rho = a$, E_ϕ and H_ℓ continuous at $\rho = b$, and the radiation condition as $\rho \to \infty$. An $e^{-i\omega t}$ time dependence is assumed. Using G to denote the Green's functions, the magnetic field is then $\bar{H} = \ell i \omega \epsilon_0 M_0 G$, where

$$
G(\phi)|_{\rho=b} = \frac{-1}{2\pi k_0 b} \sum_{m=0}^{\infty} \frac{e_m H_m^{(1)}(k_0 b) \cos(m\phi)}{H_m^{(1)'}(k_0 b) + i C_m H_m^{(1)}(k_0 b)} \tag{1}
$$

and

$$
C_m = i \frac{k_1}{k_0} \frac{\epsilon_0}{\epsilon_1} \frac{J_m'(k_1 b) N_m'(k_1 a) - J_m'(k_1 a) N_m'(k_1 b)}{J_m(k_1 b) N_m'(k_1 a) - J_m'(k_1 a) N_m(k_1 b)}.
$$

$H_m^{(1)}$ is a Hankel function of the first kind of order m. J_m and N_m are Bessel functions of the first and second kind. The wavenumbers are $k_{1,0} = \omega \sqrt{\mu_0 \epsilon_{1,0}}$ and $e_0 = 2$, $e_m = 1$ for $m \neq 0$.

The main difficulty in evaluating this series is that it converges very slowly, so its remainder must be summed in closed form. This is accomplished by using Debye's asymptotic formulas for cylinder functions of large order:

$$
\frac{H_m^{(1)'}(x)}{H_m^{(1)}(x)} \sim \frac{-1}{\sqrt{(m/x)^2 - 1}} \approx \frac{-x}{m} \left[1 - \frac{1}{2} \left(\frac{x}{m} \right)^2 + \cdots \right]
$$

and for C_m

$$
C_m \sim i \left[\frac{k_1}{k_0} \frac{\epsilon_0}{\epsilon_1} \right] \sinh \alpha_b \tanh [m(\gamma_b - \gamma_a)]
$$

where

$$
\sinh \alpha_b = \sqrt{(m/k_1 b)^2 - 1}
$$

Excitation of Creeping Waves on a Circular Cylinder with a Thick Dielectric Coating

ROBERT PAKNYS AND NAN WANG, MEMBER, IEEE

Abstract— A magnetic line source on a dielectric coated conducting cylinder excites a creeping wave field. The coating is not necessarily thin, so more than one mode can exist. It is found that as the coating thickness is increased, the surface field on the dielectric-air interface exhibits a distinctive beat pattern resulting from the interaction between two creeping-wave modes.

R. Paknys is with Clarkson University, Potsdam, NY 13676.
N. Wang is with the ElectroScience Laboratory, The Ohio State University, Columbus, OH 43212.

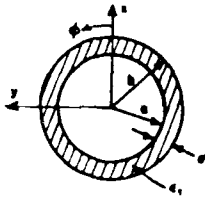Fig. 1. Coordinates for the dielectric coated cylinder.

Fig. 2. Ray encirclements associated with the summation index n.

and

$$\gamma_{a,b} = \tanh(\alpha_{a,b}) - \alpha_{a,b}.$$

If $m \gg k_1 a$, and $m \gg k_1 b$, it can be shown that $\gamma_b - \gamma_a \approx \ln(b/a)$ and consequently

$$\tanh[m(\gamma_b - \gamma_a)] \approx \frac{(b/a)^m - (b/a)^{-m}}{(b/a)^m + (b/a)^{-m}}.$$

If $(b/a)^{2m} \gg 1$, then

$$C_m - i\frac{k_1}{k_0}\frac{\epsilon_0}{\epsilon_1}\sqrt{(m/k_{1b})^2 - 1} \approx i\frac{\epsilon_0}{\epsilon_1}\frac{m}{k_0 b}\left[1 - \frac{1}{2}\left(\frac{k_1 b}{m}\right)^2 + \cdots\right].$$

The above approximations for H'_m/H_m and C_m then give

$$\frac{H_m^{(1)}(k_0 b)}{H_m^{(1)\prime}(k_0 b) + iC_m H_m^{(1)}(k_0 b)} \sim \frac{-\epsilon}{1 + \epsilon}\frac{k_0 b}{m}$$

where $\epsilon = \epsilon_1/\epsilon_0$. By using the formula [5]

$$\sum_{m=1}^{\infty} \frac{\cos m\phi}{m} = -\ln(2\sin(\phi/2))$$

one can compute the infinite sum in (1). For the cases presented, the first $m = 6 k_0 b$ terms were summed numerically.[1]

B. Residue Series

Through Watson transformation [6], the following equivalent representation of the Green's function is established

$$G(\phi) = \sum_{n=-\infty}^{\infty} G_\infty(\phi + 2n\pi) \tag{2}$$

where

$$G_\infty(\phi) = \sum_{p=1}^{\infty} L_p e^{i\nu_p|\phi|} \tag{3}$$

$$L_p = \frac{-i}{k_0 b} \frac{H_{\nu_p}^{(1)}(k_0 b)}{\frac{\partial}{\partial\nu}[H_\nu^{(1)\prime}(k_0 b) + iC_\nu H_\nu^{(1)}(k_0 b)]|\nu = \nu_p} \tag{4}$$

and ν_p are the complex roots [7] of

$$H_{\nu_p}^{(1)\prime}(k_0 b) + iC_{\nu_p} H_{\nu_p}^{(1)}(k_0 b) = 0 \tag{5}$$

in the upper ν plane. $G(\phi)$ is 2π periodic in ϕ whereas $G_\infty(\phi)$ satisfies the radiation condition in the infinite angular domain $-\infty < \phi < \infty$. A given mode p of the residue series in (3) is interpreted as a creeping wave propagating along a curved surface as shown in Fig. 2. The total field in (2) is obtained by summing up, over n, the multiply encircling rays. For a thick dielectric coating, the attenuation rate

[1] The authors express their thanks to Professor Jack Richmond of The Ohio State University for his subroutine used in calculating Bessel functions.

TABLE I
ν_p AND L_p FOR $k_0 b = 20$, $\epsilon_1 = 4\epsilon_0$

d/λ_0	ν_1	$|L_1|$	$\angle L_1$ (deg.)
0.10	24.10 + 10.117	0.309	83.3
0.20	32.09 + 10.	0.0700	90.0
0.30	34.52 + 10.	0.0218	90.0
0.40	34.93 + 10.	0.0119	90.0
0.50	34.77 + 10.	0.00888	90.0

d/λ_0	ν_2	$|L_2|$	$\angle L_2$ (deg.)
0.10	23.43 + 15.270	0.0601	8.3
0.20	20.81 + 14.182	0.139	-51.9
0.30	20.87 + 11.820	0.226	28.1
0.40	22.87 + 10.271	0.217	78.2
0.50	26.55 + 10.002	0.0951	90.0
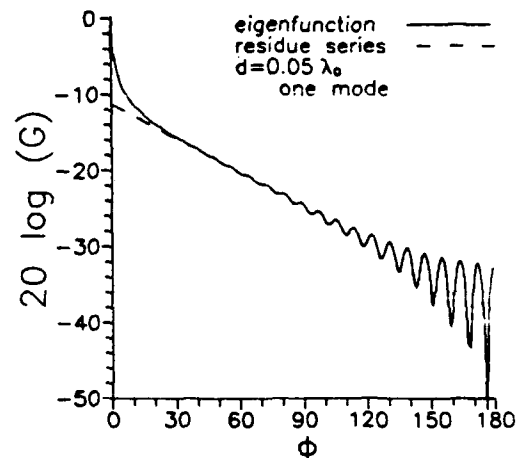
Fig. 3. Eigenfunction and one mode creeping wave solution, $d/\lambda_0 = 0.05$.

(prescribed in Im (ν)) can be quite small. For such a case, it is important to add up all the ray encirclements by using the geometric series

$$\sum_{n=-\infty}^{\infty}{}' e^{i\nu|\phi + 2n\pi|} = \frac{e^{i\nu\phi} + e^{-i\nu\phi}}{e^{-i2\pi\nu} - 1}.$$

The prime denotes exclusion of $n = 0$ from the summation.

C. Numerical Results and Discussion

All cases shown use the parameters $k_0 b = 20$, $\epsilon_1 = 4\epsilon_0$. Table I contains some representative values of ν_p and L_p for the creeping waves. The roots ν_p have already been discussed in [7].

Figs. 3–6 compare the computed Green's function, using (1) and (2). It was found that when $d/\lambda_0 \geqslant 0.25$, the creeping wave solution required both the $p = 1$ and $p = 2$ modes, whereas for thinner coatings the $p = 1$ mode alone was sufficient. A typical case, $d/\lambda_0 = 0.30$ is shown in Fig. 7 to illustrate the behavior of the individual modes which form a two-mode solution.
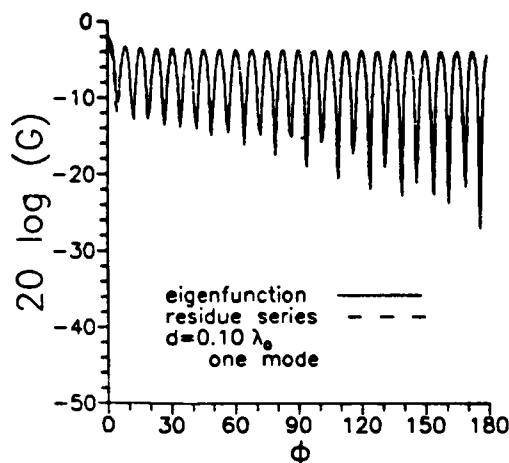
Fig. 4.   Eigenfunction and one mode creeping wave solution, $d/\lambda_0 = 0.10$.
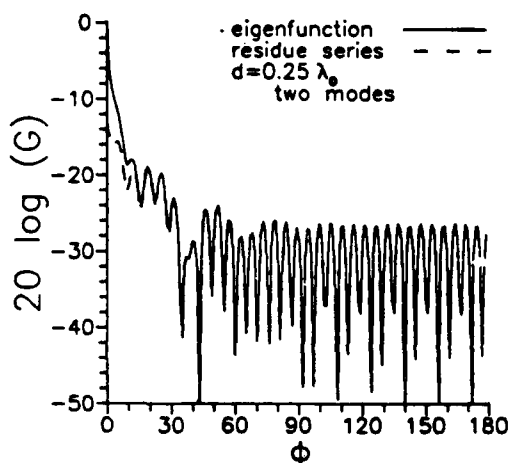
Fig. 5.   Eigenfunction and two mode creeping wave solution, $d/\lambda_0 = 0.25$.
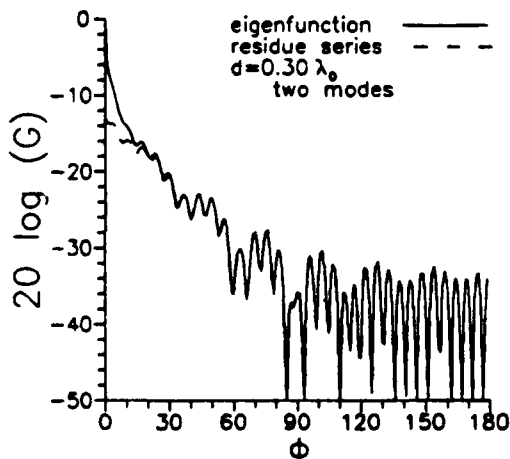
Fig. 6.   Eigenfunction and two mode creeping wave solution, $d/\lambda_0 = 0.30$.

Fig. 7.   Individual modes for $d/\lambda_0 = 0.30$.

REFERENCES

[1]   R. D. Kodis, "The scattering cross section of a composite cylinder, geometric optics," *IEEE Trans. Antennas Propagat.*, vol. AP-11, pp. 86–93, 1963.
[2]   R. D. Kodis and T. T. Wu, "The optical model of scattering by a composite cylinder," *IEEE Trans. Antennas Propagat.*, vol. AP-11, pp. 703–705, 1963.
[3]   T. C. K. Rao and M. A. K. Hamid, "GTD analysis of scattering from a dielectric coated conducting cylinder," *Proc. Inst. Elec. Eng.*, vol. 127, pt. H, no. 3, June 1980.
[4]   N. Wang, "Electromagnetic scattering from a dielectric coated circular cylinder," *IEEE Trans. Antennas Propagat.*, vol. AP-33, pp. 960–963, 1985.
[5]   R. E. Collin, *Field Theory of Guided Waves.*   New York: McGraw-Hill, 1960.
[6]   J. J. Bowman, T. B. A. Senior, and P. L. E. Ushlenghi, *Electromagnetic and Acoustic Scattering by Simple Shapes.*   Amsterdam: North Holland, 1969.
[7]   R. Paknys and N. Wang, "Creeping wave propagation constants and modal impedance for a dielectric coated circular cylinder," *IEEE Trans. Antennas Propagat.*, vol. AP-34, pp. 674–680, 1986.

Comparison Between Two Asymptotic Methods

ROBERTO G. ROJAS

Abstract—Two complete asymptotic expansions of an integral with many simple pole singularities and a first-order, isolated, saddle point evaluated by two different methods are compared. It is shown that both expansions are exactly the same (term by term) inside and outside the transition regions.

I. INTRODUCTION

It is common to express the solution of electromagnetic diffraction problems in terms of an integral, which, in general, cannot be evaluated in closed form. However, it is possible to obtain its complete asymptotic expansion for large values of a parameter. There

CONCLUSION

The surface fields on a circular cylinder with a dielectric coating are computed from both an eigenfunction series and a residue series. It is found that as the coating thickness is increased, the surface field on the dielectric-air interface exhibits a distinctive beat pattern resulting from the interaction between two creeping-wave modes.

Wiener-Hopf Analysis of the EM Diffraction by an Impedance Discontinuity in a Planar Surface and by an Impedance Half-Plane

Roberto G. Rojas

Wiener–Hopf Analysis of the EM Diffraction by an Impedance Discontinuity in a Planar Surface and by an Impedance Half-Plane

ROBERTO G. ROJAS

Abstract—The electromagnetic diffraction of a plane wave by a planar surface with a discontinuity in impedance and by an impedance half-plane is studied. The plane wave of arbitrary polarization is obliquely incident to the axis of the two-dimensional structures. The solutions obtained here are based on the Wiener–Hopf technique and they are cast in a matrix notation which is useful for diffraction problems. The exact formal solutions are expressed in terms of integrals which can be asymptotically evaluated. Uniform asymptotic expressions are obtained where the presence of the geometrical optics (GO) poles as well as the surface wave poles near the saddle point are fully taken into account. Several numerical examples are presented and it is shown that the solutions are continuous across the shadow boundaries of the GO and surface wave fields.

INTRODUCTION

IT IS WELL KNOWN that the scattering properties of a body are functions of both its geometrical and material properties. In the last few years, there has been a renewed interest in understanding the effect of the material properties of a body on its scattering behavior. In particular, the edge diffraction by dihedral structures, whose surfaces can be modeled by the Leontovich (impedance) boundary condition, has been studied by several authors for both acoustic and electromagnetic waves [1]–[22].

For this class of problems, where the surfaces of the wedge-shaped structures satisfy the Leontovich boundary condition, there are two basic methods of analysis. The first method, which is the most general of the two, is that of Maliuzhinets [1]. Bucci and Franceschetti [8] extended Maliuzhinets' solution to formally solve the scattering problem by a half-plane with different face impedances. However, they did not asymptotically evaluate their formal solution. Vacarro [11], [12] has generalized the Maliuzhinets method, which he refers to as the generalized reflection method, to treat the case of oblique incidence on a wedge. The uniform asymptotic evaluation of [11], [12] was obtained by the present author [17] including the case of surface wave incidence.

The second method that is available to solve problems involving the diffraction from the junction of semi-infinite planes is the Wiener–Hopf technique [23], [24] which was introduced around 1931 to solve certain types of integral

equations. Copson [25] was one of the first to apply this method to solve diffraction problems by formulating the diffraction of sound waves by a perfectly reflecting half-plane in terms of an integral equation. A more general method based on the Wiener–Hopf technique also exists. This method, known as the Wiener–Hopf Hilbert technique, was introduced by Hurd [26]. However, as with the Wiener–Hopf technique, in general it cannot be used to treat wedge-shaped objects. Pathak and Rojas [18] have obtained UTD solutions based on the Wiener–Hopf technique for the scattering of plane, cylindrical, and surface wave fields normally incident to the z-axis (no z-dependence) of the two-part impedance surface depicted in Fig. 1, except that in [18], $Z_1 = 0$ or $Z_1 = \infty$. The scattering of a surface wave field by the two-part surface shown in Fig. 1 has also been solved by Kay [5]; however, as in [18], all the fields in [5] have no z-dependence. Furthermore, it is assumed in [5] that Z_1 and Z_2 are purely imaginary, i.e., lossless case. Senior has solved a number of half-plane diffraction problems using the Wiener–Hopf method [2]–[4]. In a recent paper, Volakis [21] modified Senior's Wiener–Hopf solution [3] for the EM diffraction by a half-plane with equal impedances on both sides. The solution in [3] is not bounded at the incident and reflection shadow boundaries; whereas, the modified solution in [21] is uniform (bounded) across these boundaries. However, the solution in [21] does not take into account the presence of the surface wave fields excited at the edge of the half-plane.

In this paper, the Wiener–Hopf technique is used to solve two canonical problems. The first problem considered is the electromagnetic diffraction by a planar surface with an impedance discontinuity (two-part surface) as shown in Fig. 1. Note that each half-plane ($x \gtrless 0$, $y = 0$) is homogeneous and isotropic, i.e., Z_1 and Z_2 are scalar constants. The incident field is assumed to be a plane wave of arbitrary polarization obliquely incident to the z-axis as depicted in Fig. 1.

The starting point of the analysis is to define, as was done in [11], [17], a two element column vector $\bar{f}_z$ whose elements are the z-components of the electric and magnetic fields. It is then sufficient to obtain the solution for this column vector since it plays the role of a vector potential. In other words, all the other field components can be determined in terms of $\bar{f}_z$. In contrast to the case of normal incidence to the z-axis where the elements of $\bar{f}_z$ are decoupled [18], the Leontovich boundary condition couples the elements of $\bar{f}_z$ for the case of oblique incidence. However, as shown in [16], the normal components
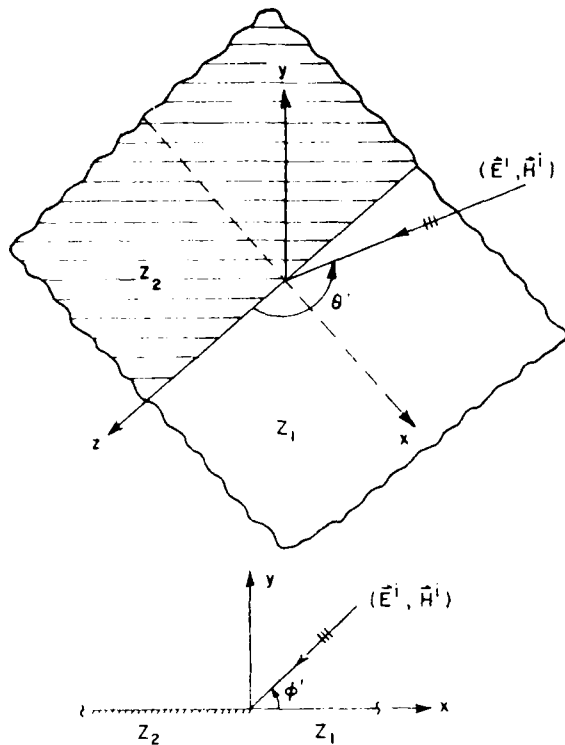
Fig. 1   Planar surface with an impedance discontinuity.

of the fields, i.e., E_ι and H_ι, are decoupled. Therefore, the two element vector $\bar{f}_v$, whose elements are E_v and $\eta_0 H_v$, is also introduced. The Wiener–Hopf equation is then obtained in terms of the column vector $\bar{f}_v$ by following Jones' method [23], [27]. As expected, the Wiener–Hopf equation is simpler when the normal fields E_v and H_v are used instead of E_z and H_z.

The solution of the Wiener–Hopf equation requires the factorization and decomposition of two-by-two diagonal matrices. The factorization procedure employed here is based on Weinstein's work [28]. There is also a formal procedure to decompose a function; however, in this paper it is done by inspection. After applying the radiation and edge conditions, the Wiener–Hopf equation is finally solved yielding an expression for the column vector $\bar{f}_v$ in the Fourier-transformed domain. This expression contains two nonzero arbitrary constants which must be determined in order to have a unique solution. Before these unknown constants are determined, the solution for $\bar{f}_z$ is obtained in the Fourier-transformed domain in terms of $\bar{f}_v$ by means of a transformation matrix. It turns out that the expression for $\bar{f}_z$ contains poles which give rise to fields that have no physical interpretation. Thus, the unknown constants are properly adjusted to remove the unwanted poles yielding a unique solution for $\bar{f}_z(x, y, z)$ in the form of an integral. The asymptotic evaluation of the integral is then performed, where the presence of the geometrical optics (GO) poles, as well as the surface wave poles near the saddle point, is fully taken into account. This results in a uniform expression across the shadow boundaries for the GO and surface wave fields.

The second problem considered in this paper is the EM diffraction by a half-plane with equal impedances on both sides. The solution for the half-plane problem is obtained by appropriately combining two special cases of the two-part problem; namely, the solutions corresponding to the cases where $Z_2 = 0$ and $Z_2 = \infty$, respectively. Finally, several numerical examples are presented for both problems considered here with a brief discussion of their applications to practical problems. It is noted that all the fields in the following discussion have the $e^{-i\omega t}$ time dependence.

STATEMENT OF THE PROBLEM

As stated in the introduction, the first canonical problem to be considered is the analysis of the diffraction by a two-part impedance plane depicted in Fig. 1, where Z_1 and Z_2 are scalar constants. The total field $(\bar{E}, \bar{H})$, which will be determined everywhere in the half-space $y \geq 0$, satisfies the impedance (Leontovich) boundary condition, namely

$$\bar{E} - (\hat{y} \cdot \bar{E})\hat{y} = Z_{\frac{1}{2}}\hat{y} \times \bar{H}; \qquad x \gtrless 0, \, y = 0 \qquad (1)$$

where $\bar{E}$ and $\bar{H}$ are the electric and magnetic fields, respectively. Let us consider a plane wave of arbitrary polarization which is obliquely incident to the z-axis of the infinite plane as shown in Fig. 1. Since the infinite plane is a two-dimensional geometry, all the fields will have the same z-dependence as the incident field, namely

$$\bar{E} = \bar{E}(x, y)e^{ik'_z z}; \qquad \bar{H} = \bar{H}(x, y)e^{ik'_z z} \qquad (2)$$

where $k'_z = -k \cos \theta'$. Therefore, all the field components can be expressed in terms of E_z and H_z (the z-components of the electric and magnetic fields, respectively), that is

$$\bar{E} = \nabla \times [\nabla \times (\hat{z}E_z) + ik\hat{z}(\eta_0 H_z)]/K^2$$

$$\eta_0 \bar{H} = \nabla \times [\nabla \times \hat{z}(\eta_0 H_z) - ik\hat{z}E_z]/K^2 \qquad (3)$$

where

$$\nabla = \nabla_t + \hat{z}ik'_z; \quad \nabla_t = \hat{x}\frac{\partial}{\partial x} + \hat{y}\frac{\partial}{\partial y} \qquad (4a)$$

and

$$K = K_1 + iK_2 = k \sin \theta' = (k_1 + ik_2) \sin \theta'; \qquad k_1, k_2 > 0$$

$$0 < \theta' < \pi. \qquad (4b)$$

The constant η_0 is the free space intrinsic impedance and k is the free space wavenumber which is temporarily allowed to have a small imaginary part for convenience of analysis.

Next, let us define the column vectors $\bar{f}_z$ and $\bar{f}_v$ as follows:

$$\bar{f}_z = \begin{bmatrix} E_z \\ \eta_0 H_z \end{bmatrix}; \bar{f}_v = \begin{bmatrix} \eta_0 H_v \\ E_v \end{bmatrix} = \begin{bmatrix} ik\dfrac{\partial}{\partial x} & ik'_z\dfrac{\partial}{\partial y} \\ ik'_z\dfrac{\partial}{\partial y} & -ik\dfrac{\partial}{\partial x} \end{bmatrix} \dfrac{\bar{f}_z}{K^2}$$

$$(5)$$

where both $\bar{f}_v$ and $\bar{f}_z$ satisfy Helmholtz's differential equation:

$$(\nabla_t^2 + K^2)\bar{f}_l = \bar{0} - \begin{bmatrix} 0 \\ 0 \end{bmatrix}; \qquad l = v, z, \quad y \geq 0. \qquad (6)$$

Since all the field components of $\bar{E}$ and $\bar{H}$ can be determined

from $\vec{f}_z$, the incident plane wave field can be completely defined in terms of $\vec{f}_z^i$, namely

$$\vec{f}_z^i = \vec{F}_{0z} \exp (ik_x' x - ik_y' y + ik_z' z); \qquad \vec{F}_{0z} = \begin{bmatrix} E_{0z} \\ \eta_0 H_{0z} \end{bmatrix} \quad (7)$$

where E_{0z} and H_{0z} are arbitrary constants (the magnitudes of E_z^i and H_z^i, respectively, at $x = y = z = 0$) and

$$k_x' = -K \cos \phi', \quad k_y' = K \sin \phi'; \qquad 0 < \phi' < \pi. \quad (8)$$

The column vector $\vec{f}_y$ was introduced because it satisfies the following boundary condition:

$$\left(I \frac{\partial}{\partial y} + iK \sin \bar{\nu}_{\frac{1}{2}} \right) \vec{f}_y = \vec{0}; \qquad x \geqslant 0, \quad y = 0 \quad (9)$$

where

$$I = \begin{bmatrix} 1 & 0 \\ 0 & 1 \end{bmatrix}; \quad \sin \bar{\nu}_{\frac{1}{2}} = \begin{bmatrix} \sin \nu_{\frac{1}{2}}^e & 0 \\ 0 & \sin \nu_{\frac{1}{2}}^h \end{bmatrix}$$

$$= \begin{bmatrix} \dfrac{\eta_0}{Z_{\frac{1}{2}} \sin \theta'} & 0 \\ 0 & \dfrac{Z_{\frac{1}{2}}}{\eta_0 \sin \theta'} \end{bmatrix}. \quad (10)$$

Since it is assumed that Real $(Z_{\frac{1}{2}}) \geqslant 0$, the real part of ν is restricted to the interval $0 \leqslant \text{Real}(\nu) \leqslant \pi/2$. It is important to note that the fields E_y and H_y are decoupled in (9).

SOLUTION

Because of the simplicity of (9), the Wiener–Hopf equation will be obtained in terms of $\vec{f}_y$ instead of $\vec{f}_z$. For analysis purposes, it is convenient to express the solution as

$$\vec{f}_y = \vec{f}_y^u + \vec{f}_y^s, \qquad y \geqslant 0 \quad (11)$$

where $\vec{f}_y^u$, which will be referred to as the unperturbed solution, is the field that would exist if the whole plane in Fig. 1 were a surface with impedance Z_2. Thus, $\vec{f}_y^s$ will represent the effect of the impedance discontinuity at $x = y = 0$. The unperturbed field $\vec{f}_y^u$ satisfies (6) and

$$\left(I \frac{\partial}{\partial y} + iK \sin \bar{\nu}_2 \right) \vec{f}_y^u = \vec{0}; \qquad |x| < \infty, \quad y = 0. \quad (12)$$

The incident field $\vec{f}_y^i$ is given by

$$\vec{f}_y^i = \vec{F}_{0y} \exp (i(k_x' x - k_y' y + k_z' z));$$

$$\vec{F}_{0y} = \frac{1}{K^2} \begin{bmatrix} -kk_x' & k_z' k_y' \\ k_y' k_z' & kk_x' \end{bmatrix} \vec{F}_{0z}. \quad (13)$$

It follows from the definition of $\vec{f}_y^u$ that

$$\vec{f}_y^u = \vec{f}_y^i + \bar{\Lambda}_2(\phi') \vec{F}_{0y} \exp (i(k_x' x + k_y' y + k_z' z)); \qquad y \geqslant 0 \quad (14a)$$

where

$$\bar{\Lambda}_2(\phi') = \begin{bmatrix} R_2^e(\phi') & 0 \\ 0 & R_2^h(\phi') \end{bmatrix};$$

$$R(\phi') = \frac{\sin \phi' - \sin \nu}{\sin \phi' + \sin \nu}; \quad 0 < \phi' < \pi. \quad (14b)$$

By means of (9), (11), and (12), it can be shown that $\vec{f}_y^s$ satisfies (6) and the following boundary conditions:

$$\left(I \frac{\partial}{\partial y} + iK \sin \bar{\nu}_2 \right) \vec{f}_y^s = \vec{0}; \qquad y = 0 \quad x < 0 \quad (15a)$$

$$\left(I \frac{\partial}{\partial y} + iK \sin \bar{\nu}_1 \right) (\vec{f}_y^s + \vec{f}_y^u) = \vec{0}; \qquad y = 0 \quad x > 0. \quad (15b)$$

In order to simplify the notation, the factor $e^{ik_z' z}$ is dropped at this stage of the analysis; however, it will be reintroduced once the Wiener–Hopf equation is solved. As in [18], it is convenient at this point to introduce the half-range functions $\vec{f}_{y\pm}$. Let

$$\vec{f}_y = \vec{f}_{y+} + \vec{f}_{y-} \quad (16a)$$

where

$$\vec{f}_{y+} = \begin{cases} \vec{f}_y & x > 0 \\ 0 & x < 0 \end{cases}; \quad \vec{f}_{y-} = \begin{cases} 0 & x > 0 \\ \vec{f}_y & x < 0 \end{cases}. \quad (16b)$$

If s is a complex variable, i.e., $s = \sigma + i\tau$, where σ and τ are real variables, one can define one-sided Fourier transforms of $\vec{f}_{y\pm}$, (provided they satisfy certain conditions [23], [24]) which will be denoted by $\bar{F}_{y\pm}(s, y)$. The functions $\bar{F}_{y+}(s, y)$ and $\bar{F}_{y-}(s, y)$, which are carefully defined in Appendix I, are regular in the upper half-s-plane $\text{Im}(s) > \tau_-$ and lower half-s-plane $\text{Im}(s) < \tau_+$, respectively. The constants τ_- and τ_+ ($\tau_- < \tau_+$) are also defined in Appendix I. In terms of the one-sided Fourier transforms $\bar{F}_{y+}(s, y)$ and $\bar{F}_{y-}(s, y)$, the two-sided Fourier transform of $\vec{f}_y$ is given by

$$\bar{F}_y(s, y) = \bar{F}_{y+}(s, y) + \bar{F}_{y-}(s, y); \qquad y \geqslant 0, \quad \tau_- < \tau < \tau_+ \quad (17)$$

where $\bar{F}_y$ is regular in the strip defined by $\tau_- < \tau < \tau_+$. Thus, taking the two-sided Fourier transform of (6), keeping in mind that the unperturbed field $\vec{f}_z^u(x, y)$ satisfies (6), yields

$$\left(\frac{\partial}{\partial y^2} + \beta^2 \right) \bar{F}_y^s = \vec{0}; \qquad y \geqslant 0, \quad \tau_- < \tau < \tau_+ \quad (18)$$

where (18) holds true within the strip defined by $\tau_- < \tau < \tau_+$ and

$$\beta = (K^2 - s^2)^{1/2}; \qquad \text{Im}(\beta) > 0. \quad (19)$$

It is noted that in addition to the boundary conditions, $\bar{F}_y^s$ must also satisfy the radiation condition as $y \to \infty$ for the exp $(-i\omega t)$ time dependence. Furthermore, the branch cuts of β are chosen such that $\text{Im}(\beta) > 0$ in the proper (top) sheet. Therefore, a solution of (18) which satisfies the radiation

condition is

$$\bar{F}_y^s(s, y) = \bar{A}(s)e^{i\beta y}; \qquad \tau_- < \tau < \tau_+, \quad y \geq 0 \quad (20a)$$

where

$$\bar{A}(s) = \bar{F}_{y_+}^s(s, 0) + \bar{F}_{y_-}^s(s, 0); \qquad \tau_- < \tau < \tau_+, \quad y = 0. \quad (20b)$$

The column vector $\bar{A}(s)$, also regular in the strip $\tau_- < \tau < \tau_+$, is an unknown function of s that will be determined via the Wiener–Hopf procedure. Following Jones' method [27], the first step is to take the Fourier transform of the boundary conditions given in (15), which yields

$$\left(\bar{I}\frac{\partial}{\partial y} + iK \sin \bar{\nu}_2\right) \bar{F}_{y_-}^s(s, y) = 0; \qquad y = 0,$$

$$\tau < \tau_+ = \text{Im}(K) = K_2 \quad (21a)$$

and

$$\left(\bar{I}\frac{\partial}{\partial y} + iK \sin \bar{\nu}_1\right) (\bar{F}_{y_-}^s(s, y) + \bar{F}_{y_+}^u(s, y)) = \bar{0};$$

$$y = 0, \quad \tau > \tau_-. \quad (21b)$$

The function $\bar{F}_{y_+}^u$ can easily be obtained by taking the one-sided Fourier transform of (14a), i.e.,

$$\bar{F}_{y_+}^u(s, y) = \frac{i}{\sqrt{2\pi}} (\bar{I} \exp(-ik_y' y) + \bar{\Lambda}_2(\phi')$$

$$\cdot \exp(ik_y' y))\bar{F}_{0y}/(s + k_x'); \quad \tau > \tau_- = K_2 \cos \phi'. \quad (22)$$

Incorporating (20b) and (22) into (21) and after some simplification yields the Wiener–Hopf equation which holds in the strip $\tau_- < \tau < \tau_+$, namely

$$\bar{G}_2(s)\bar{F}_{\setminus_-}^s(s, 0) + \bar{G}_1(s)\bar{F}_{\setminus}^s(s, 0) = \bar{G}_1(s)\bar{G}_2(s)\bar{D}/(s + k_x');$$

$$\tau_- < \tau < \tau_+ \quad (23a)$$

where

$$\bar{G}_{1,2}(s) = \begin{bmatrix} g_{1,2}^e(s) & 0 \\ 0 & g_{1,2}^h(s) \end{bmatrix}; \qquad g(s) = \frac{K}{\beta + K \sin \nu}$$

$$(23b)$$

and

$$\bar{D} = i\,[\sin \bar{\nu}_1(\bar{I} + \bar{\Lambda}_2(\phi')) - k_y'(\bar{I} - \bar{\Lambda}_2(\phi'))/K]\bar{F}_{0y}/\sqrt{2\pi}. \quad (23c)$$

In (23a), the functions $\bar{F}_{y_-}^s$ and $\bar{F}_{\setminus}^s$ are both unknown while $\bar{G}_2(s)$, $\bar{G}_1(s)$ and $\bar{D}$ are known functions. The first step to solve the Wiener–Hopf equation is the factorization of the diagonal matrix $\bar{G}_{1,2}(s)$ into two matrices which are regular in the upper and lower half-spaces defined by $\text{Im}(s) > -K_2$ and $\text{Im}(s) < K_2$, respectively. Since $\bar{G}(s)$ is a diagonal matrix, its factorization reduces to the factorization of its individual elements, i.e.,

$g^h(s)$ and $g^e(s)$. The lengthy details of this procedure will not be presented here, because they can be found elsewhere in the literature [16], [23], [24], [28]. Instead, the main results of the factorization of $\bar{G}(s)$, which are based on Weinstein's work [28], are summarized in Appendix II. Thus, using the results of Appendix II, the factorization of $\bar{G}(s)$ is defined by

$$\bar{G}(s) = \bar{G}_+(s)\bar{G}_-(s). \quad (24)$$

Substituting (24) into (23a) yields

$$\bar{G}_{1+}^{-1}(s)\bar{G}_{2+}(s)\bar{F}_{y_+}^s(s, 0) + \bar{G}_{2-}^{-1}(s)\bar{G}_{1-}(s)\bar{F}_{y_-}^s(s, 0)$$

$$= \bar{X}(s)\bar{D}; \qquad \tau_- < \tau < \tau_+ \quad (25a)$$

where

$$\bar{X}(s) = \bar{G}_{1-}(s)\bar{G}_{2+}(s)/(s + k_x'). \quad (25b)$$

The next step in this procedure is to decompose $\bar{X}(s)$ into

$$\bar{X}(s) = \bar{X}_+(s) + \bar{X}_-(s) \quad (26)$$

where $\bar{X}_+(s)$ is regular in the upper half-space defined by $\text{Im}(s) > \tau_-$ and $\bar{X}_-(s)$ is regular in the lower half-space $\text{Im}(s) < \tau_+$. As was the case for $\bar{G}(s)$, the matrix $\bar{X}(s)$ is also diagonal. Thus, its decomposition reduces to the decomposition of its elements. For the problem being considered here, the decomposition of $\bar{X}(s)$ can be found by inspection. Therefore, only the final results of the decomposition of $\bar{X}(s)$ are given in Appendix II. By means of (26), (25a) reduces to

$$\bar{G}_{1+}^{-1}(s)\bar{G}_{2+}(s)\bar{F}_{y_+}^s(s, 0) - \bar{X}_+(s)\bar{D} = \bar{X}_-(s)$$

$$\cdot \bar{D} - \bar{G}_{2-}^{-1}(s)\bar{G}_{1-}(s)\bar{F}_{y_-}^s(s, 0); \qquad \tau_- < \tau < \tau_+. \quad (27)$$

After a careful examination of (27), one concludes that all the functions on the left side of (27) are regular in the upper half-s-plane defined by $\tau > \tau_-$. On the other hand, the functions on the right side of (27) are regular in the lower half-s-plane defined by $\tau < \tau_+$. Since both half-s-planes have a common overlapping region described by $\tau_- < \tau < \tau_+$, it follows by analytic continuation [23], [24] that both sides are equal to an entire function $\bar{M}(s)$ (regular on the entire s-plane). Due to the edge conditions that the fields must satisfy near the impedance discontinuity, the asymptotic behavior of both sides of (27) is algebraic rather than exponential [24]. It then follows from the extended form of Liouville's theorem [24] that $\bar{M}(s)$ is a polynomial in s. Furthermore, for this particular problem, the edge conditions require that the tangential components of E_z and H_z be bounded across the impedance discontinuity [11], [16]. It can be shown [16], that due to both the constraints on E_z and H_z across the impedance discontinuity, and the asymptotic behavior of $\bar{G}_{1+}(s)$, $\bar{G}_{2+}(s)$ and $\bar{X}_+(s)$ as $|s| \to \infty$ for $\tau \geq \tau_+$, $\bar{M}(s)$ is at most a constant, namely

$$\bar{M}(s) = \bar{M} = \begin{bmatrix} m_1 \\ m_2 \end{bmatrix}, \qquad \text{for all } s \quad (28)$$

where m_1 and m_2 are arbitrary unknown constants at this stage of the analysis. Finally, solving for $\bar{F}_{y_+}^s(s, 0)$ and $\bar{F}_{y_-}^s(s, 0)$ in

(27) and substituting the resulting expressions into (20b), yields

$$\bar{A}_y(s) = \bar{G}_{1+}(s)\bar{G}_{2-}(s)\frac{\bar{Z}(\nu)}{K}$$

$$\cdot \left[\frac{\bar{G}_{1+}(k_x')\bar{G}_{2-}(k_x')ik_y'\bar{F}_{0y}}{(s+k_x')\sqrt{2\pi}} + \frac{\bar{M}}{2}\right], \quad \text{for all } s$$

(29a)

where

$$\bar{Z}(\nu) = 2 (\sin \bar{\nu}_2 - \sin \bar{\nu}_1).$$ (29b)

As expected, when $Z_1 = Z_2$, $\bar{A}_y(s)$ is equal to zero. Note that the expression for $\bar{A}_y$ still contains the unknown constant $\bar{M}$. In order to evaluate $\bar{M}$ and thus obtain a unique solution, it is necessary to first find the expression for $\bar{F}_z^s(s, y)$. Taking the two-sided Fourier transform of (5) and solving for $\bar{F}_z^s$, one obtains

$$\bar{F}_z^s(s, y) = \bar{C}^{-1}(s)\bar{F}_y^s(s, y) = \bar{C}^{-1}(s)\bar{A}_y(s)e^{i\beta y}; \quad y \geq 0$$

(30a)

where

$$\bar{C}(s) = \frac{1}{K^2}\begin{bmatrix} ks & -k_z'\beta \\ -k_z'\beta & -ks \end{bmatrix}.$$ (30b)

The expression in (30a), due to the matrix $\bar{C}^{-1}(s)$, has two poles at $s = \pm ik_z'$ whose residues introduce fields which do not have a physical interpretation [16]. Therefore, the constant $\bar{M}$ has to be adjusted in such a way that these two poles are suppressed. It follows from (30) that

$$\bar{V}^{\pm}\bar{A}_y(\mp ik_z') = 0; \quad \bar{V}^{\pm} = [\pm i, 1]$$ (31)

where $\bar{V}^{\pm}$ is a row vector. Before (31) is solved, it is convenient to first obtain the expression for $\bar{J}_z^s(x, y, z)$. This is accomplished by taking the inverse Fourier transform of $\bar{F}_z^s(s, y)$ and reintroducing the factor $e^{ik_z'z}$, namely

$$\bar{J}_z^s(x, y, z) = \frac{\exp(ik_z'z)}{\sqrt{2\pi}}\int_{-\infty}^{\infty}\bar{F}_z^s(s, y)$$

$$\cdot \exp(-isx) \, ds; \quad y \geq 0 \quad (32)$$

where the path of integration is shown in Fig. 2 and k_2 has been set equal to zero. The next step in the analysis is to introduce a change of variables via the transformation

$$s = -K \cos w; \quad \beta = K \sin w$$ (33)

where w is a complex variable and $K = K_1$, $k = k_1$, i.e., $k_2 = 0$. Replacing x and y by $\rho \cos \phi$ and $\rho \sin \phi$, respectively, (32) can be written in the w-domain as follows:

$$\bar{J}_z^s(\rho, \phi, z) = \frac{\exp(-ikz \cos \theta')}{2\pi i}\int_{\Gamma_w}\bar{A}_z(w)$$

$$\cdot \exp(iK\rho \cos(w-\phi)) \, dw; \quad \rho \geq 0,$$

$$0 \leq \phi \leq \pi$$

(34)

Fig. 2. Path of integration in (32).
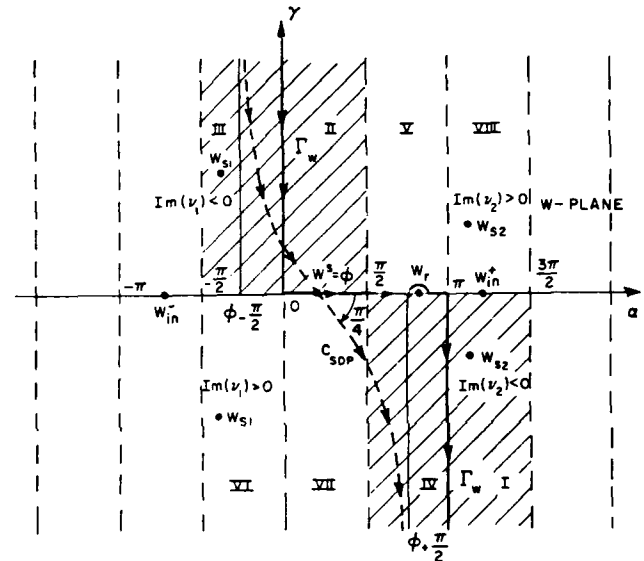
Fig. 3. Integration paths Γ_w and C_{SDP} in the periodic w-plane for $k = k_1$ (real). The singularities of the function $A_z(w)$ are also depicted.

where $\rho = \sqrt{x^2 + y^2}$ and the new integration path Γ_w in the w-domain is shown in Fig. 3. The expression for $\bar{A}_z$ is given by

$$\bar{A}_z(w) = \bar{C}^{-1}(w)\bar{\psi}(w) \sin w \left[\frac{\bar{I}}{\cos w + \cos \phi'} + \bar{B}\right]$$

$$\cdot \sin \phi' \bar{\psi}(\phi')\bar{Z}(\nu)\bar{C}(\pi+\phi')\bar{F}_{0z} \quad (35a)$$

where

$$\bar{C}(w) = \frac{1}{\sin \theta'}\begin{bmatrix} -\cos w & \sin w \cos \theta' \\ \sin w \cos \theta' & \cos w \end{bmatrix};$$

$$\bar{\psi}(w) = \begin{bmatrix} g_{1+}^e(w) & g_{2-}^e(w) & 0 \\ 0 & g_{1+}^h(w) & g_{2-}^h(w) \end{bmatrix} \quad (35b)$$

and

$$\bar{B} = -\bar{N}^{-1}(\bar{w}_0)\bar{T}^{-1}(w_0)\bar{N}(w_0).$$ (35c)

The expressions for $g_{1+}(w)$ and $g_{2-}(w)$ are given in Appendix II and they will not be repeated here. The constant matrix $\bar{B}$ is evaluated by solving (31) in the w-domain. In other words, $\bar{B}$ is adjusted in such a way that the nonphysical poles introduced

by $\bar{C}^{-1}$ are suppressed. The details of the solution of (31) and the expressions for $\bar{N}(w_0)$ and $\bar{T}(w_0)$ are given in Appendix III.

ASYMPTOTIC ANALYSIS

As shown in the previous section, the formal solution to the canonical problem of Fig. 1 has been obtained in terms of an integral. In general, this type of integral cannot be evaluated in closed form. Fortunately, in diffraction problems one is interested in the solutions for large $K\rho$ which can be obtained by applying asymptotic integration techniques. Here, the steepest descents method will be used to obtain the leading term of $\bar{f}_z^s$ for large $K\rho$.

The exponential function in (34), i.e., $\exp(iK\rho \cos(w - \phi))$, possesses an isolated, simple saddle point at $w = \phi$. Furthermore, the function $\bar{A}_z$ is analytic everywhere, except that it has the following simple real poles in the vicinity of the saddle point $w = \phi$:

$$w = \pi - \phi', \quad w = \pi + \phi', \quad w = -\pi + \phi'; \quad 0 < \phi' < \pi. \quad (36)$$

In addition to these real poles, $\bar{A}_z(w)$ also has four complex poles (see Fig. 3) whose residues can be interpreted as surface waves departing from the impedance jump:

$$w_{s1}^{e,h} = -\nu_1^{e,h}; \quad w_{s2}^{e,h} = \pi + \nu_2^{e,h} \quad (37)$$

where $0 \leq \text{Real}(\nu_{1,2}) \leq \pi/2$.

When the contour Γ_w is deformed into the steepest descent path C_{SDP}, the poles of $\bar{A}_z$ may be crossed. If this is the case, then the poles are captured and their residue contributions must be included. Note that $w_{s1}^{e,h}$ and $w_{s2}^{e,h}$, which are the poles of $\bar{\psi}(w)$, can be captured only when $\text{Im}(\nu_{1,2}) < 0$. It follows from (10) that $\text{Im}(\nu_{1,2}^h) \gtrless 0$ and $\text{Im}(\nu_{1,2}^e) \lessgtr 0$ when $\text{Im}(Z_{1,2}) \gtrless 0$. Therefore, for given values of $Z_{1,2}$, only two of these four poles can be captured. Furthermore, since $0 \leq \phi \leq \pi$ and $0 < \phi' < \pi$, the poles $w = \mp\pi + \phi'$ will not be captured for the two-part impedance problem. Thus, deforming the contour Γ_w into C_{SDP} in (34) and adding the unperturbed field $\bar{f}_z^u$ yields the following expression for the total field $\bar{f}_z$:

$$\bar{f}_z = \bar{f}_z^i + \bar{f}_z^r + \bar{f}_{z1}^{sw} + \bar{f}_{z2}^{sw} + \bar{f}_z^d \quad (38)$$

where $\bar{f}_z^i$ is the incident field defined in (7), and $\bar{f}_z^r$ is the reflected field given by

$$\bar{f}_z^r = \bar{C}^{-1}(\pi - \phi')\{\bar{\Lambda}_1(\phi')U(\pi - \phi' - \phi)$$
$$+ \bar{\Lambda}_2(\phi')U(\phi - \pi + \phi')\}\bar{C}(\pi + \phi')\bar{F}_{0z}$$
$$\exp((-iK\rho \cos(\phi + \phi'))\exp(-ikz \cos\theta') \quad (39)$$

where U is the unit step function. The fields $\bar{f}_{z1}^{sw}$ and $\bar{f}_{z2}^{sw}$ are the surface wave fields which exist in the half-planes $x > 0$, $y = 0$ and $x < 0$, $y = 0$, respectively. They can easily be obtained by computing the residues of the integrand in (34) at the poles defined in (37). That is,

$$\bar{f}_{z1}^{sw} = \mp \bar{r}_{sw}(w_{s1}) \exp(iK\rho \cos(w_{s1} - \phi))$$
$$\cdot \exp(-ikz \cos\theta')U_1 \quad (40a)$$

where

$$U_1 = U(\phi_{s1} - \phi); \quad \phi_{s1} = -\nu_{r1} + \arccos\left(\frac{1}{\cos \nu h_{I1}}\right)$$

$$U_2 = U(\phi - \phi_{s2}); \quad \phi_{s2} = \pi + \nu_{r2} - \arccos\left(\frac{1}{\cos \nu h_{I2}}\right)$$

(40b)

and

$$w_{sl} = w_{sl}^h, \quad \nu_l = \nu_l^h, \quad \text{if } \text{Im}(Z_l) < 0, \quad l = 1, 2 \quad (40c)$$

or

$$w_{sl} = w_{sl}^e, \quad \nu_l = \nu_l^e, \quad \text{if } \text{Im}(Z_l) > 0, \quad l = 1, 2. \quad (40d)$$

The constants ν_{rl} and ν_{Il} in (40b) are the real and imaginary parts of ν_l, respectively. Furthermore, $\bar{r}_{sw}(w_{s1,s2})$, which is the residue of $\bar{A}_z(w)$ at $w_{s1,s2}$, can be written as follows:

$$\bar{r}_{sw}(w_{sl}^{e,h}) = \bar{C}^{-1}(w_{sl}^{e,h})\bar{P}_l(w_{sl}^{e,h})\left[\frac{\bar{I}}{\cos w_{sl}^{e,h} + \cos \phi'} + \bar{B}\right]$$

$$\cdot \sin\phi'\bar{\psi}(\phi')\bar{Z}(\nu)\bar{C}(\pi + \phi')\bar{F}_{0z}; \quad l = 1, 2 \quad (41)$$

where $\bar{P}_l(w_{sl}^{e,h})$ is the residue of $\bar{\psi}(w) \sin w$ at $w_{sl}^{e,h}$, namely

$$\bar{P}_1(w_{s1}^h) = \begin{bmatrix} 0 & 0 \\ 0 & \tan(w_{s1}^h)\dfrac{g_{2-}^h(w_{s1}^h)}{g_{1-}^h(w_{s1}^h)} \end{bmatrix};$$

$$\bar{P}_2(w_{s2}^h) = \begin{bmatrix} 0 & 0 \\ 0 & \tan(w_{s2}^h)\dfrac{g_{1+}^h(w_{s2}^h)}{g_{2+}^h(w_{s2}^h)} \end{bmatrix}; \quad (42a)$$

and

$$\bar{P}_1(w_{s1}^e) = \begin{bmatrix} \tan(w_{s1}^e)\dfrac{g_{2-}^e(w_{s1}^e)}{g_{1-}^e(w_{s1}^e)} & 0 \\ 0 & 0 \end{bmatrix};$$

$$\bar{P}_2(w_{s2}^e) = \begin{bmatrix} \tan(w_{s2}^e)\dfrac{g_{1+}^e(w_{s2}^e)}{g_{2+}^e(w_{s2}^e)} & 0 \\ 0 & 0 \end{bmatrix}. \quad (42b)$$

The last term in (38), i.e., $\bar{f}_z^d$, which in this paper is referred to as the diffracted field, is given by

$$\bar{f}_z^d(\rho, \phi, z) = \frac{\exp(-ikz \cos\theta')}{2\pi i} \int_{C_{SDP}} \bar{A}_z(w)$$

$$\cdot \exp(iK\rho \cos(w - \phi)) \, dw;$$

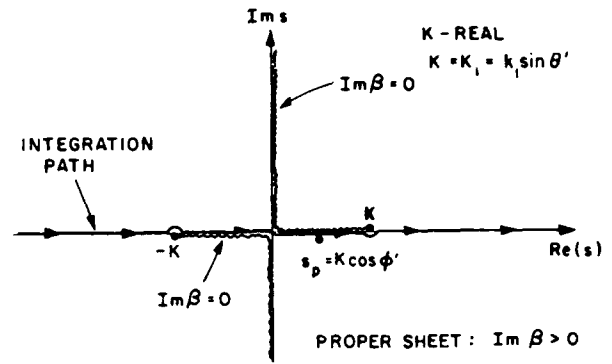$$\rho > 0, \quad 0 \leq \phi \leq \pi. \quad (43)$$

The asymptotic evaluation of (43) was carried out following a

procedure similar to that proposed by Gennarelli [29]. Without going over the details, taking into account the presence of the poles of $\bar{A}_z(w)$ (real and complex) near the saddle point ϕ, and keeping only the leading term of order $(K\rho)^{-1/2}$, the asymptotic evaluation of (43) is given by

$$\bar{f}_z^d(\rho, \phi, z) \sim \frac{-e^{i\pi/4}}{\sqrt{2\pi K\rho}} \exp (iK\rho - ikz \cos \theta')$$

$$\cdot \left\{ \bar{A}_z(\phi) + \sum_{l=1}^{5} \bar{r}_l \frac{[1 - \mathfrak{F}(iK\rho s_l^2)]}{2 \sin \left(\dfrac{w_l - \phi}{2} \right)} \right\} \quad (44a)$$

where

$$s_l = \sqrt{2} e^{i\pi/4} \sin \left(\frac{w_l - \phi}{2} \right) ;$$

$$w_1 = \pi - \phi', \quad w_2 = w_{s1}^h, \quad w_3 = w_{s2}^h, \quad w_4 = w_{s1}^e, \quad w_5 = w_{s2}^e.$$

(44b)

The residues $\bar{r}_l$ contributed by the poles listed in (44b) are given by

$$\bar{r}_1 = -\bar{C}^{-1}(\pi - \phi')(\bar{\Lambda}_1(\phi') - \bar{\Lambda}_2(\phi'))\bar{C}(\pi + \phi')\bar{F}_{0z} \quad (45a)$$

$$\bar{r}_2 = \bar{r}_{sw}(w_{s1}^h), \quad \bar{r}_3 = \bar{r}_{sw}(w_{s2}^h), \quad \bar{r}_4 = \bar{r}_{sw}(w_{s1}^e), \text{ and } \bar{r}_5 = \bar{r}_{sw}(w_{s2}^e).$$

(45b)

As mentioned before, only two of the four surface wave poles w_2 through w_6 can be captured for given values of Z_1 and Z_2. The function $\mathfrak{F}(x)$ is the well-known transition function [30], that is

$$\mathfrak{F}(x) = 2i\sqrt{x} e^{ix} \int_{\sqrt{x}}^{\infty} e^{-it^2} dt; \quad \frac{-3\pi}{2} < \arg (x) < \frac{\pi}{2} \quad (45c)$$

where x can be complex due to the surface wave poles. In order for $\mathfrak{F}(x)$ to converge, the argument of x is restricted to the domain $-3\pi/2 < \text{Arg}(x) < \pi/2$ in the complex x-plane. In other words, the branch cut in the complex x-plane runs from the origin to infinity along the positive imaginary axis. It is noted that when the magnitude of x is large, the transition function $\mathfrak{F}(x)$ approaches one. Hence, when the poles of $\bar{A}_z(w)$ are far from the saddle point, the only nonzero term within the brackets in (44a) is $\bar{A}_z(\phi)$.

As mentioned before, when the original path of integration is deformed into C_{SDP}, the poles of $\bar{A}_z(w)$ at $w = \pi + \phi'$, $w = -\pi + \phi'$ and $w = 3\pi - \phi'$ will not be captured. However, when the half-plane problem is considered and the range of ϕ' and ϕ is extended to 2π, these poles can be captured. Therefore, it is convenient at this point to evaluate these residues, namely

$$\bar{r} = \begin{cases} -\bar{F}_{0z} + \bar{C}^{-1}(\pi + \phi')\bar{\Lambda}_2(2\pi - \phi')\bar{\Lambda}_1(\phi') \\ \quad \cdot \bar{C}(\pi + \phi')\bar{F}_{0z}; \quad \text{residue at } w = \pi + \phi' \\ \bar{F}_{0z} - \bar{C}^{-1}(\pi + \phi')\bar{\Lambda}_2(\phi')\bar{\Lambda}_1(2\pi - \phi') \\ \quad \cdot \bar{C}(\pi + \phi')\bar{F}_{0z}; \quad \text{residue at } w = -\pi + \phi' \\ -\bar{C}^{-1}(\pi - \phi')\{\bar{I} - \bar{\Lambda}_2(\phi')\bar{\Lambda}_1(2\pi - \phi')\}\bar{\Lambda}_2(\phi') \\ \quad \cdot \bar{C}(\pi + \phi')\bar{F}_{0z}; \quad \text{residue at } w = 3\pi - \phi' \end{cases} \quad (46)$$

HALF-PLANE SOLUTION

The solution for a half-plane having the same impedance Z_1 on both sides can easily be obtained from the solution of the two-part problem discussed in the previous sections. This can be accomplished by first expressing the incident plane wave field as the superposition of four incident plane wave fields as depicted in Fig. 4(a). That is, the incident field is decomposed into symmetrical and asymmetrical components. Equivalent configurations to those shown in Fig. 4(a) are easily obtained by taking advantage of the symmetric/asymmetric properties of the incident field. The equivalent configurations, which are shown in Fig. 4(b), are simply special cases ($Z_2 \to 0$, $Z_2 \to \infty$) of the two two-part problem that has already been solved. Thus, the next step in the analysis of the half-plane problem is to evaluate $\bar{A}_z$ and $\bar{\Lambda}_2$ when $Z_2 \to 0$ and $Z_2 \to \infty$, respectively. In order to avoid any confusion, the superscripts "c" and "m" will be added to the solutions of the two-part problem when $Z_2 \to 0$ and $Z_2 \to \infty$, respectively.

Case 1: $Z_2 \to 0 \Rightarrow \nu_2^h \to 0; \nu_2^e \to \pi/2 - i\infty$

$$\bar{\Lambda}_2^c(\phi') = \begin{bmatrix} -1 & 0 \\ 0 & 1 \end{bmatrix} \quad (47a)$$

$$\bar{A}_z^c(\phi) = \bar{C}^{-1}(\phi)\bar{\Psi}^c(\phi) \left[\frac{\bar{I}}{\cos \phi + \cos \phi'} + \bar{B}^c \right]$$

$$\cdot \bar{\Psi}^c(\phi')\bar{Z}^c(\nu)\bar{C}(\pi + \phi')\bar{F}_{0z} \quad (47b)$$

$$\bar{\Psi}^c(\phi) = \begin{bmatrix} g_{1+}^e(\phi) \sin \phi & 0 \\ 0 & \sqrt{2} \sin \left(\dfrac{\phi}{2} \right) g_{1+}^h(\phi) \end{bmatrix} ;$$

$$\bar{Z}^c(\nu) = 2 \begin{bmatrix} 1 & 0 \\ 0 & -\sin \nu_1^h \end{bmatrix} . \quad (47c)$$

Since $Z_2 \to 0$, the residues $\bar{r}_{sw}(w_{s2}^{e,h})$ are equal to zero, i.e., $\bar{r}_{sw}(w_{s2}^{e,h}) = \begin{bmatrix} 0 \\ 0 \end{bmatrix}$. The function $\bar{B}^c$ which is the limit of $\bar{B}$ as $Z_2 \to 0$, is defined in Appendix III.

Case 2: $Z_2 \to \infty \Rightarrow \nu_2^h \to \pi/2 - i\infty, \nu_2^e \to 0$

$$\bar{\Lambda}_2^m(\phi') = -\bar{\Lambda}_2^c(\phi') \quad (48a)$$

$$\bar{A}_z^m(\phi) = \bar{C}^{-1}(\phi)\bar{\Psi}^m(\phi) \left[\frac{\bar{I}}{\cos \phi + \cos \phi'} + \bar{B}^m \right]$$

$$\cdot \bar{\Psi}^m(\phi')\bar{Z}^m(\nu)\bar{C}(\pi + \phi')\bar{F}_{0z} \quad (48b)$$

$$\bar{\Psi}^m(\phi) = \begin{bmatrix} \sqrt{2} \sin \left(\dfrac{\phi}{2} \right) g_{1+}^e(\phi) & 0 \\ 0 & \sin \phi g_{1+}^h(\phi) \end{bmatrix} ;$$

$$\bar{Z}^m(\nu) = 2 \begin{bmatrix} -\sin \nu_1^e & 0 \\ 0 & 1 \end{bmatrix} . \quad (48c)$$

As in Case 1, when $Z_2 \to \infty$, $\bar{r}_{s2}^{e,h} = \begin{bmatrix} 0 \\ 0 \end{bmatrix}$ and $\bar{B}^m$, which is given in Appendix III, is the limit of $\bar{B}$ as $Z_2 \to \infty$.

It is noted that the two-part problem with $Z_2 \to 0(\infty)$ corresponds to the configuration of Fig. 4(a) where E_z and H_z have asymmetric (symmetric) and symmetric (asymmetric)
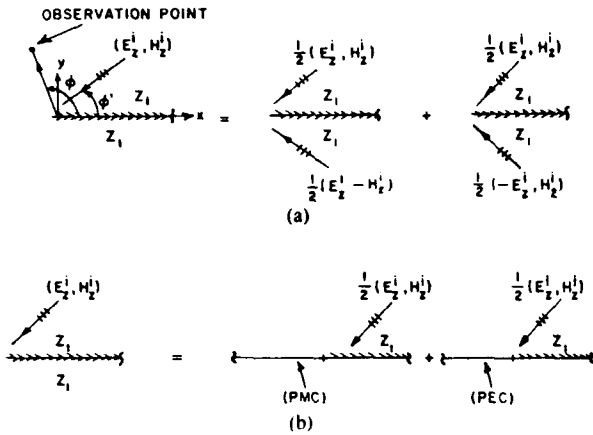
Fig. 4.   Relation between the two-part problem and the impedance half-plane problem.

excitations, respectively. This can be checked by examining (47) and (48), and by noting that $g_+(w)$ satisfies the identity $g_+(2\pi - w) = g_+(w)$. Thus, the range of the angles ϕ' and ϕ, for the two-part solutions can be extended to 2π. The solution of the half-plane problem is then obtained by superposing (see Fig. 4(b)) the two-part solutions with $Z_2 \to 0$ and $Z_2 \to \infty$, respectively, and keeping in mind that the poles of $\bar{A}_z^{c,m}(w)$ at $w = \pi + \phi'$, $w = -\pi + \phi'$, $w = 3\pi - \phi'$ can be captured, namely

$$\bar{J}_{zp} = \bar{J}_{zp}^i + \bar{J}_{zp}^r + \bar{J}_{zp}^{sw} + \bar{J}_{zp}^d; \qquad 0 \leqslant \phi \leqslant 2\pi, \quad 0 < \phi' < 2\pi$$

$$\tag{49}$$

where

$$\bar{J}_{zp}^i = \bar{F}_{0z} \exp \left(-iK\rho \cos (\phi - \phi') - ikz \cos \theta' \right)$$

$$\cdot \, [U(\phi - \phi' + \pi) - U(\phi - \phi' - \pi)] \tag{50}$$

in the incident field and

$$\bar{J}_{zp}^r = \bar{C}^{-1}(\pi - \phi')[\bar{\Lambda}_1(\phi') U(\pi - \phi' - \phi)$$

$$+ \bar{\Lambda}_1(2\pi - \phi') U(\phi - 3\pi + \phi')] \bar{C}(\pi + \phi') \bar{F}_{0z}$$

$$\cdot \, \exp \left(-iK\rho \cos (\phi + \phi') - ikz \cos \theta' \right) \tag{51}$$

is the reflected field. The diffracted field is given by

$$\bar{J}_{zp}^d \sim \frac{-e^{i\pi/4}}{2\sqrt{2\pi K\rho}} \exp \left(iK\rho - ikz \cos \theta' \right)$$

$$\cdot \left\{ \bar{A}_z^c(\phi) + \bar{A}_z^m(\phi) + \sum_{l=1}^{2} \frac{\bar{F}_l^p[1 - \mathcal{F}(iK\rho s_l^2)]}{\sin \left(\dfrac{w_l - \phi}{2} \right)} \right.$$

$$\left. + \sum_{l=3}^{4} \frac{\bar{F}_l^p[1 - \mathcal{F}(iK\rho a_l^2)]}{\sin \left(\dfrac{w_l - \phi}{2} \right)} \right\} \tag{52a}$$

where

$$\bar{F}_1^p = -\bar{C}^{-1}(\pi - \phi')\bar{\Lambda}\bar{C}(\pi + \phi')\bar{F}_{0z}; \qquad r_2^p = -\bar{F}_{0z} \tag{52b}$$

and

$$\bar{\Lambda} = \begin{cases} \bar{\Lambda}_1(\phi'), & \text{for } 0 < \phi' < \pi \\ \bar{\Lambda}_1(2\pi - \phi'), & \text{for } \pi < \phi' < 2\pi \end{cases};$$

$$w_1 = \pi - \phi'; \quad w_2 = \pi + \phi'. \tag{52c}$$

The function a_l introduced in (52a) is defined as follows:

$$a_l = \sqrt{2} e^{i\pi/4} \sin \left(\frac{w_l - \phi}{2} \right);$$

$$l = 3, 4, \quad \phi = \begin{cases} \phi & \text{for } 0 \leqslant \phi \leqslant \pi \\ 2\pi - \phi & \text{for } \pi < \phi \leqslant 2\pi \end{cases} \tag{52d}$$

and

$$\bar{F}_l^p = \begin{cases} \bar{F}_l^p; & l = 3, 4, \quad \text{for } 0 \leqslant \phi < \pi \\ -\bar{F}_{l+2}^p; & l = 3, 4, \quad \text{for } \pi < \phi \leqslant 2\pi. \end{cases} \tag{52e}$$

Furthermore, $\bar{F}_3^p$ through $\bar{F}_6^p$ are given by

$$\bar{F}_l^p = \frac{1}{2} \bar{F}_{sw}^c(w_l) + \frac{1}{2} \bar{F}_{sw}^m(w_l); \tag{52f}$$

where $w_3 = w_{s1}^h$, $w_4 = w_{s1}^e$, $w_5 = 2\pi - w_{s1}^h$, and $w_6 = 2\pi - w_{s1}^e$. The residues $r_{s1}^{ch}(w_l)$ and $\bar{F}_{sw}^m(w_l)$, are given in (41), except that the functions ($\bar{B}$, $\sin \phi \bar{\psi}(\phi')$, $\bar{P}_1(w_l)$, $\bar{Z}(\nu)$) are replaced by ($\bar{B}^c$, $\bar{\psi}^c(\phi')$, $\bar{P}_1^c(w_l)$, $\bar{Z}^c(\nu)$) for Case 1, and by ($\bar{B}^m$, $\bar{\psi}^m(\phi')$, $\bar{P}_1^m(w_l)$, $\bar{Z}^m(\nu)$) for Case 2. All these new functions were already defined, except for $\bar{P}_1^c(w_l)$ and $\bar{P}_1^m(w_l)$, which are the residues of $\bar{\psi}^c(w)$ and $\bar{\psi}^m(w)$, respectively, at $w = w_l$, namely

$$\bar{P}_1^c(w_{s1}^h) = \begin{bmatrix} 0 & 0 \\ 0 & \dfrac{\sqrt{2} \sin (w_{s1}^h/2)}{\cos (w_{s1}^h) g_{1-}^h (w_{s1}^h)} \end{bmatrix};$$

$$\bar{P}_1^m(w_{s1}^h) = \begin{bmatrix} 0 & 0 \\ 0 & \dfrac{\tan (w_{s1}^h)}{g_{1-}^h (w_{s1}^h)} \end{bmatrix} \tag{53a}$$

$$\bar{P}_1^c(w_{s1}^e) = \begin{bmatrix} \dfrac{\tan (w_{s1}^e)}{g_{1-}^e (w_{s1}^e)} & 0 \\ 0 & 0 \end{bmatrix};$$

$$\bar{P}_1^m(w_{s1}^e) = \begin{bmatrix} \dfrac{\sqrt{2} \sin (w_{s1}^e/2)}{\cos (w_{s1}^e) g_{1-}^e (w_{s1}^e)} & 0 \\ 0 & 0 \end{bmatrix} \tag{53b}$$

$$\bar{P}_1^c(2\pi - w_{s1}^h) = -\bar{P}_1^c(w_{s1}^h), \quad \bar{P}_1^m(2\pi - w_{s1}^h) = \bar{P}_1^m(w_{s1}^h),$$

$$\bar{P}_1^c(2\pi - w_{s1}^e) = \bar{P}_1^c(w_{s1}^e), \qquad \bar{P}_1^m(2\pi - w_{s1}^e) = -\bar{P}_1^m(w_{s1}^e).$$

$$\tag{53c}$$

The surface wave field for the half-plane, given by $\bar{J}_{zp}^{sw}$, can also be obtained from the two-part problem. Without showing
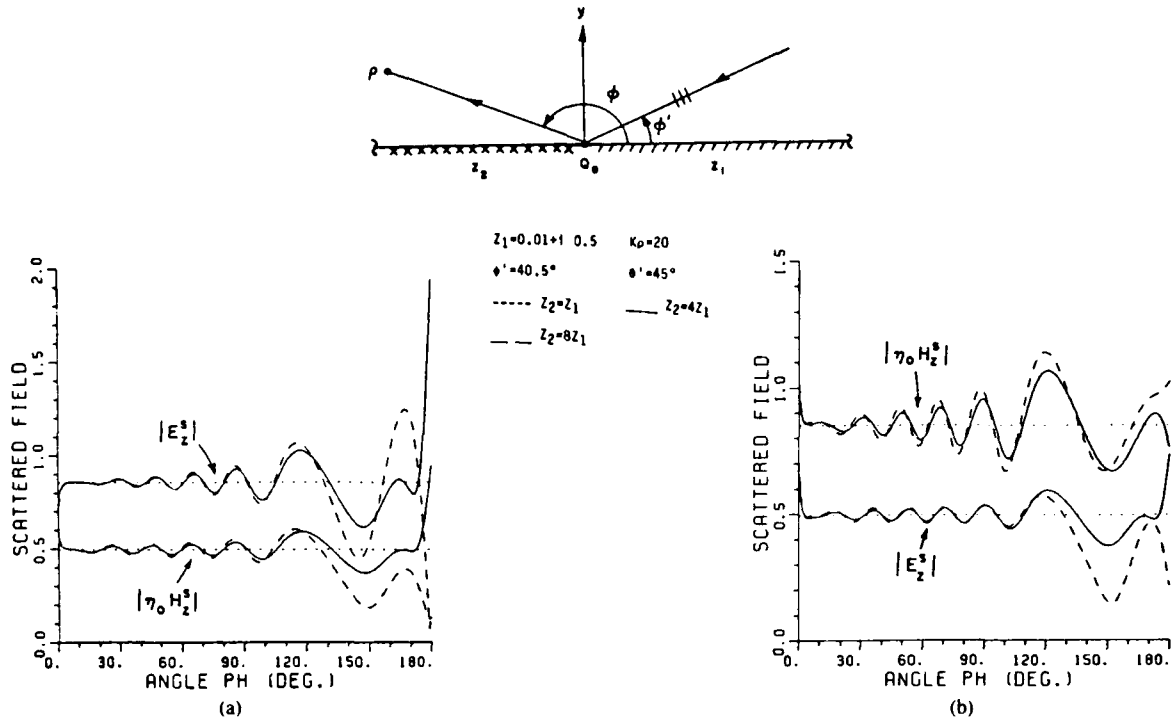
Fig. 5. Field scattered by the two-part impedance plane for an obliquely incident plane wave. (a) TM_z polarization: $E_{0z} = 1$, $\eta_0 H_{0z} = 0$. (b) TE_z polarization: $E_{0z} = 0$, $\eta_0 H_{0z} = 1$.

any details,

$$\bar{f}^{sw}_{zp} = -\bar{f}^{sw}_1 \exp\left(iK\rho \cos\left(w_{s1} - \phi\right) - ikz \cos\theta'\right)U(\phi_{s1} - \phi)$$

$$+ \bar{f}^{sw}_2 \exp\left(iK\rho \cos\left(w_{s1} + \phi\right) - ikz \cos\theta'\right)U(\phi - 2\pi + \phi_{s1})$$

$$(54)$$

where ϕ_{s1} was defined in (40b). Note that in (54), $\bar{f}^{sw}_1 = \bar{f}^p_3$, $\bar{f}^{sw}_2$ = $\bar{f}^p_5$ and $w_{s1} = w^h_{s1}$ if $\text{Im}(Z_1) < 0$. On the other hand, if $\text{Im}(Z_1) > 0$, $\bar{f}^{sw}_1 = \bar{f}^p_4$, $\bar{f}^{sw}_2 = \bar{f}^p_6$ and $w_{s1} = w^e_{s1}$.

NUMERICAL RESULTS

Most of the expressions presented in the previous sections are simple functions which are amenable for numerical calculations. The only expression that requires a simple numerical integration is $I(w, v)$ defined in (62b). This function can be efficiently computed with a 12-point Gaussian integration algorithm. In Fig. 5, the field scattered by the two-part surface is depicted for three-different values of Z_2, while Z_1 is kept constant. The incident field is an obliquely incident plane wave $(\theta' = 45°)$ with two different polarizations. In Fig. 5(a), the incident field is TM_z polarized $(E_{0z} = 1, H_{0z} = 0)$, while in Fig. 5(b) it is a TE_z polarized $(E_{0z} = 0, H_{0z} = 1)$ plane wave. As expected, when $Z_2 = Z_1$, the diffracted field is zero and the scattered field is just the reflected field. As Z_2 changes, the diffracted field becomes more important and it begins to interact with the reflected field. As a result of this interaction, the magnitude of the scattered field is no longer a constant, but fluctuates as depicted in Fig. 5. In addition to the diffracted and reflected fields, the surface wave fields also contribute to the scattered field. It is seen in Fig. 5 that the surface wave fields are significant around $0°$ and $180°$. It is

also important to mention that an obliquely incident plane wave which is TM_z or TE_z polarized, excites a scattered field that has both polarizations as shown in Fig. 5. However, it must be noted that the TE_z and TM_z field components become decoupled for a normally incident $(\theta' = 90°)$ field.

The results in Fig. 6 illustrate the effect of the angle θ' on the scattered fields. When $\theta' = 30°$, both fields E_z and $\eta_0 H_z$ are equally important. However, when $\theta' = 80°$, the cross-polarized field becomes less significant. For example, in Fig. 6(a), where the incident field is TM_z polarized, the scattered field $\eta_0 H_z$ becomes very small as θ' changes from $\theta' = 30°$ to $\theta' = 80°$. On the other hand, in Fig. 6(b), where the incident field is TE_z polarized, the field E_z becomes much smaller in relation to the $\eta_0 H_z$ field when θ' changes from $30°$ to $80°$. It is easy to show that if $\theta' = 90°$, the cross-polarized scattered field is identically equal to zero.

The other canonical problem that was considered here is the half-plane with equal impedances on both sides. In Fig. 7, the total field is shown for a lossless impedance half-plane excited by an obliquely incident plane wave. In order to show the effect of the surface waves excited at the edge of the half-plane, two cases are considered. First, the impedance Z_1 is allowed to have a large reactance $(Z_1 = i4\eta_0)$. For this value of Z_1, the effect of the surface wave can clearly be seen in Fig. 7 from $\phi = 340°$ to $\phi = 360°$ where the total field starts to increase in magnitude due to the surface wave field. When $Z_1 = i0.2\eta_0$, the surface waves become weaker and the total field decreases monotonically for $\phi > 316°$, except around $\phi = 360°$, where the presence of the surface wave field is still observed. The incident plane wave field in Fig. 7, is obliquely incident $(\theta' = 45°)$ to the axis of the half-plane, which excites a scattered field with both TM_z and TE_z polarized components.
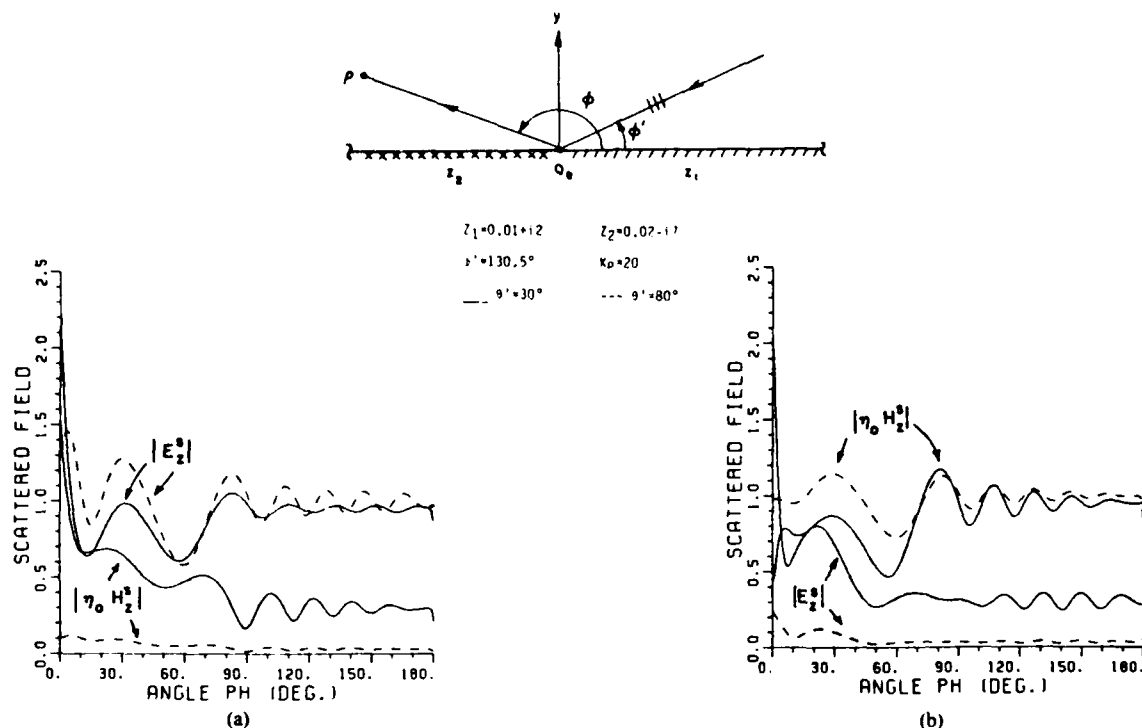
Fig. 6.   Field scattered by the two-part impedance plane for two different values of θ': 30°, 80°. (a) TM$_z$ polarization: $E_{0z} = 1$, $\eta_0 H_{0z} = 0$. (b) TE$_z$ polarization: $E_{0z} = 0$, $\eta_0 H_{0z} = 1$.

Fig. 7.   Total field excited by a plane wave obliquely incident on a lossless impedance half-plane. (a) TM$_z$ polarization: $E_{0z} = 1$, $\eta_0 H_{0z} = 0$. (b) TE$_z$ polarization: $E_{0z} = 0$, $\eta_0 H_{0z} = 1$.

In Fig. 7(a), the incident field is TM$_z$ polarized, while in Fig. 7(b) it is a TE$_z$ polarized plane wave.

The last example considered here is depicted in Fig. 8 where the total field was calculated for two values of θ'. In Fig. 8(a), the incident field is TM$_z$ polarized, while in Fig. 8(b), the incident field is TE$_z$ polarized. As expected, when θ' is small ($\theta' = 25°$), both fields E_z and $\eta_0 H_z$ are significant.

However, as θ' gets closer to 90° ($\theta' = 80°$), the cross-polarized component of the scattered field approaches zero.

CONCLUSION

The electromagnetic diffraction of a plane wave by a two-part surface and by an impedance half-plane was studied in detail. The incident field was assumed to be a plane wave of

Fig. 8. Total field excited by a plane wave obliquely incident on an impedance half-plane for two different values of θ': 25°, 80°. (a) TM$_z$ polarization: $E_{0z} = 1$, $\eta_0 H_{0z} = 0$. (b) TE$_z$ polarization: $E_{0z} = 0$, $\eta_0 H_{0z} = 1$.
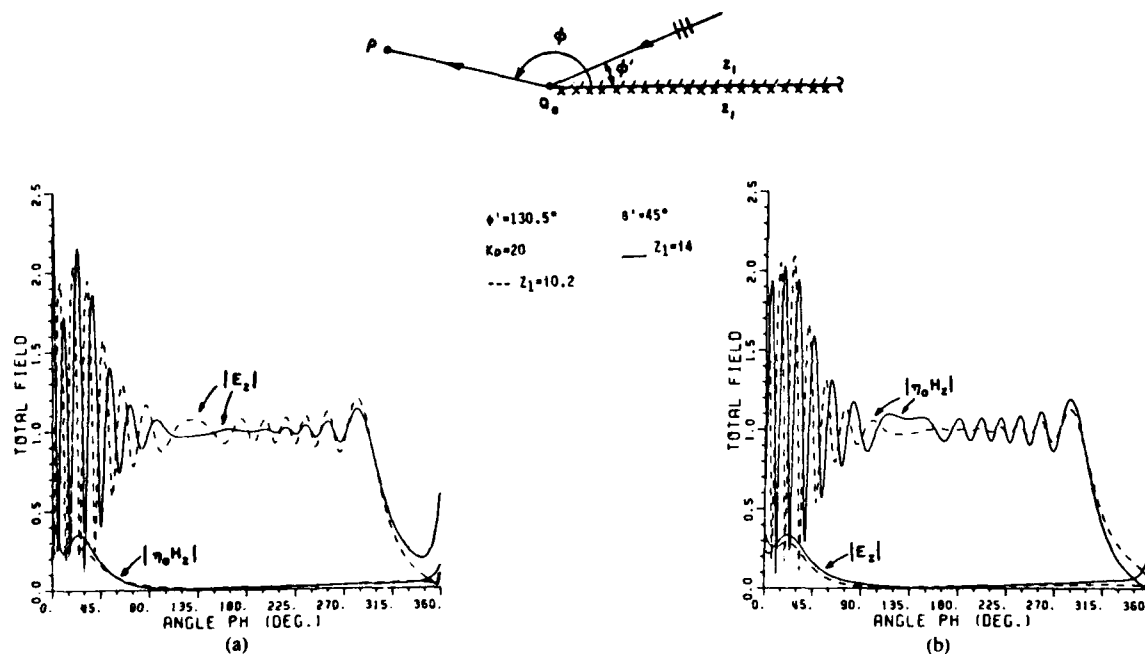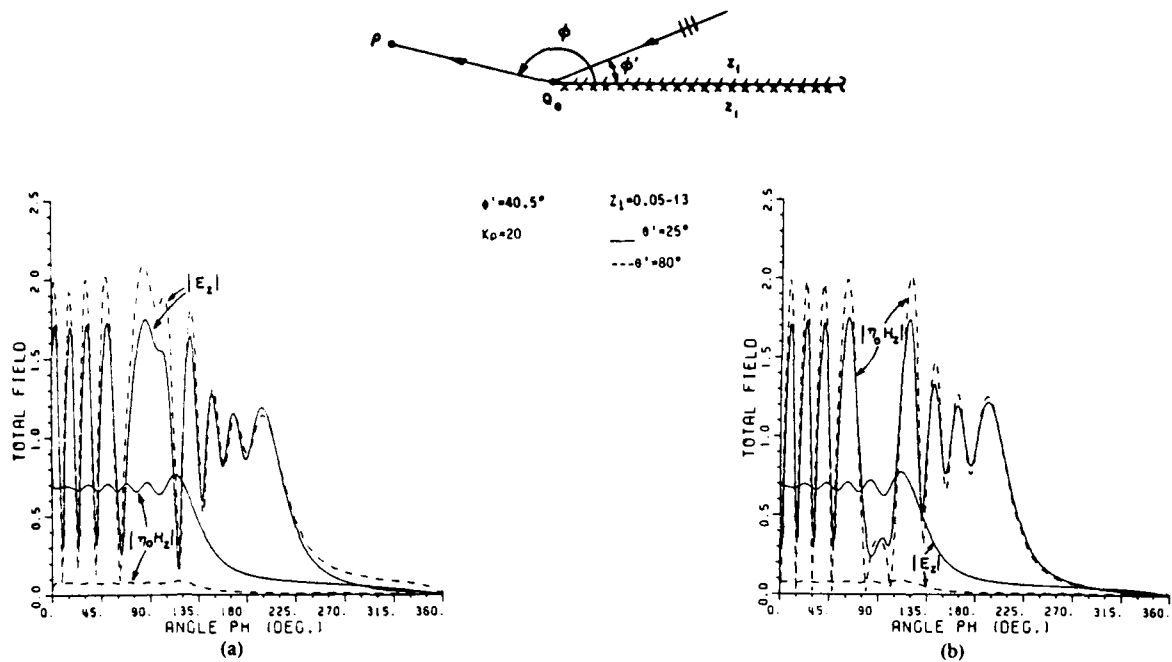
arbitrary polarization, obliquely incident to the axis of the two-dimensional structures. The exact solutions for these canonical problems were developed in terms of integrals which can not be evaluated in closed form. Thus, uniform asymptotic solutions, valid for large $(K\rho)$, were obtained by applying the method of steepest descents. These uniform solutions are valid for any angles of incidence and observation for both TM$_z$ and TE$_z$ polarizations, however, special care must be taken for the cases of grazing incidence and/or when $Z_{1,2}$ goes to zero or infinity. For these special cases, where two or more poles may coalesce to the saddle point, the procedure described by Gennarelli [29] can be followed to obtain a valid solution.

The uniform asymptotic solutions presented here were obtained by taking into account the presence of the geometrical optics poles (real poles) as well as the surface wave poles (complex poles) in the vicinity of the saddle point. The diffracted field was derived by keeping only the leading term of order $(K\rho)^{-1/2}$ with respect to the incident field. Thus, if a more accurate description of the diffracted field is necessary, e.g., the diffracted field propagating on the impedance surface, it is necessary to include the next term of order $(K\rho)^{-3/2}$.

As indicated in [18], one possible application of the present work is the prediction of the EM scattering by a metallic surface which is partly covered by a thin material coating. Another application would be a study of the scattering by a conducting half-plane covered on both sides by a thin coating. These problems can be treated with the solutions developed here. Furthermore, the results obtained here play an important role in the development of a solution for the problem of EM diffraction by the edge of a thin dielectric/ferrite half-plane [16], [31].

The solution for f_z was written in a very compact matrix notation which is especially useful when treating the more

general wedge problem [11], [17]. Furthermore, the elements of the diffracted fields f_z^d and f_{zp}^d, i.e., E_z^d and $\eta_0 H_z^d$, are proportional to the field components E_β and E_ϕ of the ray-fixed coordinate system defined in [30]. Thus, in the treatment of canonical diffraction problems, it is convenient to express the diffracted fields in terms of f_z^d.

To conclude, it is important to keep in mind that for the case of oblique incidence, the normal components E_y^{sw} and H_y^{sw} of the surface wave field are decoupled. That is, for a given value of surface impedance Z, only one of these field components E_y^{sw} or H_y^{sw}) will be excited. However, when E_z^{sw} and H_z^{sw} are computed, both can be nonzero because the matrix $\bar{C}^{-1}(w)$ is not diagonal.

Appendix I

In this Appendix, the most important properties of the Fourier transform that are relevant to the Wiener-Hopf technique are summarized. A detailed discussion of this topic can be found in many excellent textbooks, one being Tichmarsh [32]. Let the function $\tilde{f}(x)$ (see (16a)) be expressed in terms of the half-range functions $\tilde{f}_+$ and $\tilde{f}_-$ which were introduced in (16b). Note that the subscript $(+)$ in the function $\tilde{f}_+(x)$ signifies that this function is identically zero for $x < 0$, and the subscript $(-)$ in the function $\tilde{f}_-$ means that the second function is identically zero for $x > 0$. Next, assume that $\tilde{f}_+(x)$ and $\tilde{f}_-(x)$ have the following asymptotic behavior:

$$\tilde{f}_+(x) \sim \begin{bmatrix} 1 \\ 1 \end{bmatrix} e^{\tau_- x}, \quad \text{as } x \to \infty;$$

$$\tilde{f}_-(x) \sim \begin{bmatrix} 1 \\ 1 \end{bmatrix} e^{\tau_+ x}, \quad \text{as } x \to -\infty. \quad (55)$$

The Fourier transform of $\tilde{f}_+(x)$, provided $\tilde{f}_+(x)$ satisfies

certain conditions [23], [24], is defined as

$$\bar{F}_+(s) = \frac{1}{\sqrt{2\pi}} \int_0^\infty \bar{f}_+(x)e^{isx}\,dx \qquad (56)$$

where $\bar{F}_+(s)$ is regular in the upper half-s-plane defined by $\tau > \tau_-$ [23], [24]. Similarly, the Fourier transform of $\bar{f}_-(x)$ is defined by

$$\bar{F}_-(s) = \frac{1}{\sqrt{2\pi}} \int_{-\infty}^0 \bar{f}_-(x)e^{isx}\,dx \qquad (57)$$

where $\bar{F}_-(s)$ is regular in the lower half-s-plane defined by $\tau < \tau_+$. Finally, the two-sided Fourier transform $\bar{f}(x)$ can be written by combining (56) and (57), namely

$$\bar{F}(s) = \frac{1}{\sqrt{2\pi}} \int_{-\infty}^\infty \bar{f}(x)e^{isx}\,dx \qquad (58)$$

where $\bar{F}(s)$ is regular in the strip defined by $\tau_- < \tau < \tau_+$. The inverse Fourier transform of $\bar{F}(s)$ is then given by

$$\bar{f}(x) = \frac{1}{\sqrt{2\pi}} \int_{-\infty+ia}^{\infty+ia} \bar{F}(s)e^{-isx}\,ds; \qquad \tau_- < a < \tau_+. \quad (59)$$

APPENDIX II

The factorization of the function $g(s)$ (an even function of s) defined in (23b), which is regular and free of zeros in the strip $-K_2 < \tau < K_2$, means that $g(s)$ can be expressed as the product of two functions such that

$$g(s) = g_+(s)g_-(s);$$

$$g(s) = g(-s); \quad g_+(\pm s) = g_-(\mp s) \quad (60)$$

where $g_+(s)$ and $g_-(s)$ are regular and free of zeros in the upper and lower half-s-planes $\text{Im}(s) > -K_2$ and $\text{Im}(s) < K_2$, respectively. There is a formal procedure for obtaining $g_+(s)$ and $g_-(s)$. All the details of this procedure can be found in [24], [28]. As stated before, the factorization of $g(s)$ is based on Weinstein's work [28]. It is easier to carry out the factorization in the w-plane by introducing the change of variables given in (33). Thus, on the w-plane, the functions g, g_+, and g_- can be expressed as follows:

$$g(w) = \frac{1}{\sin w + \sin \nu} \qquad (61)$$

$$g_-(w) = \frac{\exp(I(w,\nu)/2\pi)}{[\cos \nu + \cos w]^{1/2}};$$

$$g_+(w) = \frac{\exp[I(\pi-w,\nu)/2\pi]}{[\cos \nu - \cos w]^{1/2}} \qquad (62a)$$

where

$$I(w,\nu) = \int_{w+\nu}^{w-\nu} \frac{t}{\sin t}\,dt. \qquad (62b)$$

It follows from (62) that $g_+(w) = g_-(\pi - w)$, $g_-(w) = g_+(\pi - w)$, and $g_+(2\pi - w) = g_+(w)$. Another important step in the Wiener–Hopf procedure is the decomposition of the function $\bar{X}(s)$ into the sum of the functions $\bar{X}_+(s)$ and $\bar{X}_-(s)$

as indicated in (26). There is also a formal procedure to decompose the function $\bar{X}(s)$; however, in this case it can be done by inspection. Without showing the details, $\bar{X}_+(s)$ and $\bar{X}_-(s)$ can be expressed as follows:

$$\bar{X}_+(s) = \frac{2\bar{Z}^{-1}(\nu)}{(s+k_x')}[\bar{G}_{1-}(-k_x')\bar{G}_{2-}^{-1}(-k_x') - \bar{G}_{2+}(s)\bar{G}_{1+}^{-1}(s)] \qquad (63a)$$

$$\bar{X}_-(s) = \frac{2\bar{Z}^{-1}(\nu)}{(s+k_x')}[\bar{G}_{1-}(s)\bar{G}_{2-}^{-1}(s) - \bar{G}_{1-}(-k_x')\bar{G}_{2-}^{-1}(-k_x')] \qquad (63b)$$

where $\bar{X}_+(s)$ and $\bar{X}_-(s)$ are regular in the upper and lower half-s-planes defined by $\text{Im}(s) > K_2 \cos \phi'$ and $\text{Im}(s) < K_2$, respectively.

APPENDIX III

In the w-domain, (31) can be written as follows:

$$V^\pm \bar{A}_y(w_0^\pm) = 0 = V^\pm \bar{\psi}(w_0^\pm)\left[\frac{\bar{I}}{\cos w_0^\pm + \cos \phi'} + \bar{B}\right]$$

$$\cdot \bar{\psi}(\phi')\bar{Z}(\nu) \sin \phi' \bar{F}_{0y} = 0 \quad (64)$$

where $V^\pm$ is a row vector defined in (31) and

$$w_0^\pm = \frac{\pi}{2} \pm i\beta_0; \quad \beta_0 = \ln\left(\frac{1+\cos \theta'}{\sin \theta'}\right). \qquad (65)$$

Let

$$\bar{T}(w_0) = \cos \phi' \bar{I} - \cos w_0^- \bar{L}; \quad \bar{N}(w_0) = \begin{bmatrix} V^+ \bar{\psi}(w_0^+) \\ V^- \bar{\psi}(w_0^-) \end{bmatrix} \qquad (66a)$$

where

$$\bar{L} = \begin{bmatrix} 1 & 0 \\ 0 & -1 \end{bmatrix}. \qquad (66b)$$

By means of (66), (64) can be rewritten using a more compact notation, namely

$$[\bar{T}^{-1}(w_0)\bar{N}(w_0) + \bar{N}(w_0)\bar{B}]\bar{\psi}(\phi')\bar{Z}(\nu) \sin \phi' \bar{F}_{0y} = \bar{0}. \qquad (67)$$

The expression outside the brackets in (67) is not identically zero, which implies that the expression inside the brackets must be zero. Solving for $\bar{B}$, one obtains

$$\bar{B} = -\bar{N}^{-1}(w_0)\bar{T}^{-1}(w_0)\bar{N}(w_0). \qquad (68)$$

In the half-plane problem, the expressions for $\bar{B}^c$ and $\bar{B}^m$ are needed. They are given by

$$\bar{B}^c = -(\bar{N}^c(w_0))^{-1}\bar{T}^{-1}(w_0)\bar{N}^c(w_0);$$

$$\bar{B}^m = -(\bar{N}^m(w_0))^{-1}\bar{T}^{-1}(w_0)\bar{N}^m(w_0) \qquad (69a)$$

where

$$\bar{N}^{c,m}(w_0) = \begin{bmatrix} \bar{V}^+ \bar{\psi}^{c,m}(w_0^+) \\ \bar{V}^- \bar{\psi}^{c,m}(w_0^-) \end{bmatrix} . \tag{69b}$$

Note that $\bar{\psi}^c$ and $\bar{\psi}^m$ were defined in (47c) and (48c), respectively.

REFERENCES

[1] G. D. Maliuzhinets, "Excitation, reflection and emission of surface waves from a wedge with given face impedances," *Sov. Phys. Dokl.*, vol. 3, pp. 752-755, 1959.

[2] T. B. A. Senior, "Diffraction by an imperfectly conducting half-plane at oblique incidence," *Appl. Sci. Res.*, sec. B, vol. 8, pp. 35-61, 1959.

[3] ———, "Diffraction tensors for imperfectly conducting edges," *Radio Sci.*, vol. 10, no. 10, pp. 911-919, Oct. 1975.

[4] ———, "Half-plane diffraction," *Radio Sci.*, vol. 10, no. 6, pp. 645-650, June 1975.

[5] A. F. Kay, "Scattering of a surface wave by a discontinuity in reactance," *IRE Trans. Antennas Propagat.*, vol. AP-7, pp. 22-31, 1959.

[6] G. Tyras, *Radiation and Propagation of Electromagnetic Waves.* New York: Academic, London, 1969.

[7] J. Bazer and S. N. Karp, "Propagation of plane electromagnetic waves past a shoreline," *J. Res. Nat. Bureau Stand.*, D. Radio Propagation, Vol. 66D, No. 3, pp. 319-334, May-June 1962.

[8] O. M. Bucci and G. Franceschetti, "Electromagnetic scattering by a half-plane with two face impedances," *Radio Sci.*, vol. 11, no. 1, pp. 49-59, Jan. 1976.

[9] ———, "Rim loaded reflector antennas," *IEEE Trans. Antennas Propagat.*, vol. 28, pp. 297-305, May 1980.

[10] J. J. Bowman, "High Frequency Backscattering from an Absorbing Infinite Strip with Arbitrary Face Impedances," *Canadian Journal of Physics*, Vol. 45, pp. 2409-2430, 1967.

[11] V. G. Vaccaro, "The generalized reflection method in electromagnetism, *AEU*, vol. 34, pp. 493-500, 1980.

[12] V. G. Vaccaro, "Electromagnetic diffraction from a right-angled wedge with soft conditions on one face," *Opt. Acta*, vol. 28, pp. 293-311, Mar. 1981.

[13] R. Tiberio, F. Bessi, G. Manara, and G. Pelosi, "Scattering by a strip with two face impedances at edge-on incidence," *Radio Sci.*, vol. 17, no. 5, pp. 1199-1210, Sept.-Oct. 1982.

[14] R. Tiberio and G. Pelosi, "High-frequency scattering from the edges of impedance discontinuities on a flat plane," *IEEE Trans. Antennas Propagat.*, vol. AP-31, no. 4, pp. 590-596, July 1983.

[15] R. Tiberio, G. Pelosi, and G. Manara, "A uniform GTD formulation for the diffraction by a wedge with impedance faces," *IEEE Trans. Antennas Propagat.*, vol. AP-33, pp. 867-873, Aug. 1985.

[16] R. G. Rojas, "A uniform GTD analysis of the EM diffraction by a thin dielectric/ferrite half-plane and related configurations," Ph.D. dissertation, Dept. Elec. Eng., Ohio State Univ., Columbus, OH, 1985.

[17] ———, "A uniform formulation for the EM diffraction by a wedge with impedance faces and with included angles equal to 0, $\pi/2$ and π (oblique incidence)," presented at IEEE Antennas Propagat. Soc. Symp. Nat. Radio Sci. Meet., Philadelphia, PA, June 1986.

[18] P. H. Pathak and R. G. Rojas, "A UTD analysis of the EM diffraction by an impedance discontinuity in a planar surface," *J. Wave-Material Interaction*, vol. 1, pp. 16-33, Jan. 1986.

[19] P. H. Pathak, "A GTD analysis of the radiation from slots in planar and cylindrical perfectly-conducting structures with a surface impedance patch." ElectroSci. Lab. Rep. 4396-2, pp. 46-54, Feb. 1977.

[20] Y. M. Hwang, "The diffraction at the edge of a uniform impedance surface," Ph.D. dissertation, Dept. Elec. Eng., Ohio State Univ., 1973.

[21] J. L. Volakis, "A uniform geometrical theory of diffraction for an imperfectly conducting-half-plane," *IEEE Trans. Antennas Propagat.*, vol. AP-34, pp. 172-180, Feb. 1986.

[22] T. B. A. Senior and J. L. Volakis, "Scattering by an imperfect right-angled wedge," *IEEE Trans. Antennas Propagat.*, vol. AP-34, pp. 681-689, May 1986.

[23] B. Nobel, *Methods Based on the Wiener-Hopf Technique.* Elmsford, NY: Pergamon, 1958.

[24] R. Mittra and S. W. Lee, *Analytical Techniques in the Theory of Guided Waves.* New York: MacMillan, 1971.

[25] E. T. Copson, "On an integral equation arising in the theory of diffraction," *Quart. J. Math*, vol. 17, pp. 19-34, 1946.

[26] R. A. Hurd, "The Wiener-Hopf-Hilbert method for diffraction problems," *Canadian J. Phys.*, vol. 54, pp. 775-780, 1976.

[27] D. S. Jones, "A simplifying technique in the solution of a class of diffraction problems," *Quart. J. Math.*, pp. 189-196, 1952.

[28] Lev A. Weinstein, *The Theory of Diffraction and the Factorization Method.* Boulder, CO: Golem, 1969.

[29] C. Gennarelli and L. Palumbo, "A uniform asymptotic expansion of a typical diffraction integral with many coalescing simple pole singularities and a first-order saddle point," *IEEE Trans. Antennas Propagat.*, vol. AP-32, pp. 1122-1124, Oct. 1984.

[30] R. G. Kouyoumjian and P. H. Pathak, "A uniform geometrical theory of diffraction for an edge in a perfectly conducting surface," *Proc. IEEE*, vol. 62, no. 11, pp. 1448-1461, Nov. 1974.

[31] R. G. Rojas and P. H. Pathak, "A UTD analysis of the diffraction by a thin dielectric/ferrite half-plane (oblique incidence), presented at IEEE Antennas Propagat. Soc. Symp. Nat. Radio Sci. Meet., Vancouver, Canada, June 1985.

[32] E. C. Titchmarsh, *Theory of Fourier Integrals.* New York: Oxford Univ. Press, 1937.

Roberto G. Rojas was born in Potosi, Bolivia, on March 15, 1957. He received the B.S.E.E. degree from New Mexico State University, in 1979, and the M.Sc. and Ph.D. degrees in electrical engineering from The Ohio State University, Columbus, in 1981 and 1985, respectively.

Since 1979 he has been with The Ohio State University ElectroScience Laboratory, initially as a Graduate Research Associate, later as a Post-Doctoral Researcher. He currently holds the position of Senior Research Associate. His current research interests are in electromagnetic scattering, high frequency techniques and antennas.

Dr. Rojas serves as Vice-Chairman of the Columbus, OH chapter of the IEEE Antennas and Propagation and Microwave and Techniques Societies. He is a member of Sigma Xi, Tau Beta Pi, Eta Kappa Nu, and Phi Kappa Phi.

The Bandwidth Performance of a Two-Element Adaptive

Array with Tapped Delay-Line Processing

R. T. Compton, Jr.

The Bandwidth Performance of a Two-Element Adaptive Array with Tapped Delay-Line Processing

R. T. COMPTON, JR., FELLOW, IEEE

Abstract—The bandwidth performance of a two-element adaptive array with a tapped delay-line behind each element is examined. It is shown how the number of taps and the delay between taps affect the bandwidth performance of the array. It is shown that an array with two weights and one delay behind each element yields optimal performance (equal to that obtained with continuous wave (CW) interference) for any value of intertap delay between zero and T_{90}/B, where T_{90} is a quarter wavelength delay and B is the fractional signal bandwidth. Delays less than T_{90} yield optimal performance but result in large array weights. Delays larger than T_{90}/B yield suboptimal signal-to-interference-plus-noise ratio (SINR) when each element has only two weights. For delays between T_{90}/B and $4T_{90}/B$, the performance is suboptimal with only two taps but approaches the optimal if more taps are added to each element. Delays larger than $4T_{90}/B$ result in suboptimal performance regardless of the number of taps used.

I. INTRODUCTION

IT IS WELL KNOWN that the ability of an adaptive array to null interference deteriorates rapidly as the interference bandwidth increases [1]-[4]. However, using tapped delay-lines behind the elements improves the bandwidth performance. The purpose of this paper is to examine how the improvement depends on the number of taps and the amount of delay between taps for a simple two-element array.

The use of tapped delay lines in an adaptive array was first suggested by Widrow *et al.* [1] and has since been studied by several others. In one study, Rodgers and Compton [2] compared the performance of a two-element array with two-, three- and five-tap delay-lines using real weights to that of an array with a single complex weight behind each element. In another work, Mayhan, Simmons, and Cummings [3] presented a mathematical analysis of how the number of elements and the number of delay-line taps affect the interference cancellation ratio as a function of bandwidth. Finally, White [4] has studied the trade-off between the number of interfering signals and the required number of auxiliary elements and delay-line taps in an Applebaum array.

In spite of these contributions, there still appears to be no simple explanation in the literature for how the number of taps and the amount of delay between taps should be chosen in an adaptive array to achieve a given bandwidth performance. The

purpose of this paper is to address this question. In Section II, we formulate the equations needed to calculate the output signal-to-interference-plus-noise ratio (SINR) from an array with M elements and K delay-line taps behind each element. Then, in Section III, we use these equations to determine the bandwidth performance of a two-element array. We show how the performance depends on the number of taps behind each element and the amount of delay between taps. Section IV contains our conclusions.

II. FORMULATION

Consider an adaptive array with M elements, as shown in Fig. 1. Let the elements be isotropic and a half-wavelength apart at the signal frequency ω_0. Assume each element is followed by a tapped delay-line with K taps and a delay of T_0 seconds between taps. The output of the first tap behind each element is the element signal itself, with no delay. Let $\tilde{x}_{mk}(t)$ denote the analytic signal from element m at tap k. Thus, $\tilde{x}_{11}(t)$ is the signal received on element 1, $\tilde{x}_{21}(t)$ is the signal on element 2, $\tilde{x}_{12}(t) = \tilde{x}_{11}(t - T_0)$, $\tilde{x}_{1k}(t) = \tilde{x}_{11}(t - [k - 1]T_0)$, and so forth.

We assume the tap signals are combined by an adaptive processor. This processor multiplies each $\tilde{x}_{mk}(t)$ by a complex weight w_{mk} and then sums the signals to produce the array output $\tilde{s}(t)$, as shown in Fig. 1. The adaptive processor could consist of a set of analog least mean square (LMS) or Applebaum loops [1], [5], or it could be a digital controller based on the sample matrix inverse method [6] or some other algorithm. All such processors attempt to adjust the array weights to their optimal values, which are known variously as the Wiener weights, the LMS weights, the Applebaum weights, or the maximum SINR weights. In this paper, we shall not be concerned with the specific form of the adaptive processor, but shall simply assume that this processor adjusts the weights to their optimal values for any given set of incident signals.

For a given set of tap signals $\tilde{x}_{mk}(t)$, the optimal weights may be found as follows. Let X_m and W_m be column vectors containing the signals and weights at the K taps behind element m, i.e.,

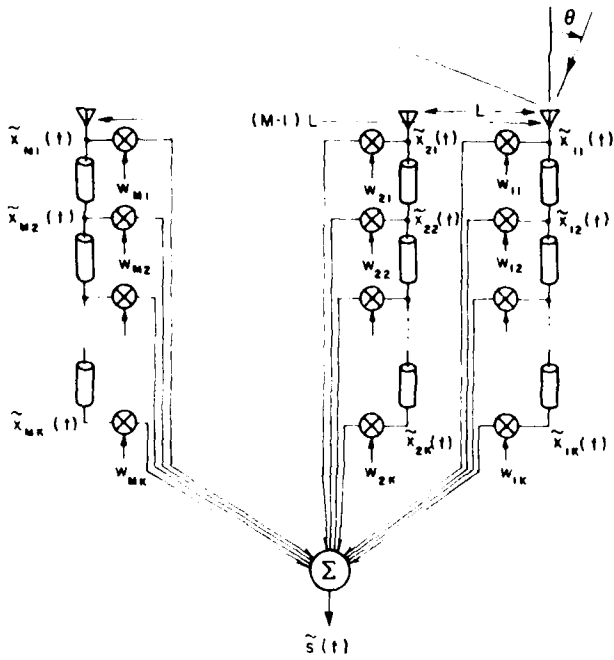$$X_m = [\tilde{x}_{m1}(t), \tilde{x}_{m2}(t), \cdots, \tilde{x}_{mK}(t)]^T, \tag{1}$$

and

$$W_m = [w_{m1}, w_{m2}, \cdots, w_{mK}]^T. \tag{2}$$

Fig. 1. An M-element adaptive array with tapped delay lines.

(Superscript T denotes transpose.) We shall call X_m the *element* signal vector and W_m the *element* weight vector. Then let X and W be the *total* signal and weight vectors for the entire array

$$X = \begin{bmatrix} X_2 \\ -- \\ X_2 \\ -- \\ \vdots \\ -- \\ X_M \end{bmatrix}, \qquad (3)$$

and

$$W = \begin{bmatrix} W_1 \\ -- \\ W_2 \\ -- \\ \vdots \\ -- \\ W_M \end{bmatrix}, \qquad (4)$$

where we use a partitioned vector notation. The optimal weight vector in the array is then given by [1], [5]

$$W = \Phi^{-1} S, \qquad (5)$$

where Φ is the signal covariance matrix,

$$\Phi = E[X^* X^T], \qquad (6)$$

and S is the steering vector (or reference correlation vector),

$$S = E[X^* \tilde{d}_0(t)]. \qquad (7)$$

In these equations, the asterisk denotes complex conjugate and

$\tilde{d}_0(t)$ is a normalized replica of the desired signal to be received by the array. ($\tilde{d}_0(t)$ is defined below in (14).) For narrow-band signals, the weight vector W satisfying (5) yields maximum SINR at the array output [5], [7].

The $\tilde{x}_{mk}(t)$ may be determined from the signals incident on the array. For this study, we shall assume the array receives a desired signal and an interference signal, and that each element signal also contains an independent thermal noise voltage, as would be contributed by a front-end preamplifier or mixer. Thus, the signal at tap k behind element m has the form

$$\tilde{x}_{mk}(t) = \tilde{d}_{mk}(t) + \tilde{i}_{mk}(t) + \tilde{n}_{mk}(t), \qquad (8)$$

where $\tilde{d}_{mk}(t)$, $\tilde{i}_{mk}(t)$, and $\tilde{n}_{mk}(t)$ are the desired, interference, and noise components, respectively. The element signal vectors X_m and the total signal vector X may then be split in a similar way,

$$X_m = X_{dm} + X_{im} + X_{nm}, \qquad (9)$$

and

$$X = X_d + X_i + X_n. \qquad (10)$$

$\tilde{d}_{mk}(t)$, $\tilde{i}_{mk}(t)$, and $\tilde{n}_{mk}(t)$ may be determined as follows.

First, suppose the desired signal arrives from angle θ_d. (θ is defined in Fig. 1.) Let $\tilde{d}(t)$ be the desired signal waveform as received on element 1. The desired signal at an arbitrary tap is then

$$\tilde{d}_{mk}(t) = \tilde{d}(t - [k-1]T_0 - [m-1]T_d), \qquad (11)$$

where T_0 is the delay between taps and T_d is the desired signal spatial propagation delay between elements,

$$T_d = \frac{L}{c} \sin(\theta_d), \qquad (12)$$

with L the element separation (see Fig. 1) and c the velocity of propagation. We assume $\tilde{d}(t)$ is a zero-mean, stationary, random process with average power p_d,

$$p_d = E[|\tilde{d}(t)|^2]. \qquad (13)$$

The signal $\tilde{d}_0(t)$ in (7) is identical to $\tilde{d}(t)$ except normalized to have unit power,

$$\tilde{d}_0(t) = \frac{1}{\sqrt{p_d}} \tilde{d}(t). \qquad (14)$$

Next, assume the interference arrives from angle θ_i and has waveform $\tilde{i}(t)$ at element 1. The interference signal at an arbitrary tap is then

$$\tilde{i}_{mk}(t) = \tilde{i}(t - [k-1]T_0 - [m-1]T_i), \qquad (15)$$

where T_i is the interference propagation delay between elements,

$$T_i = \frac{L}{c} \sin(\theta_i). \qquad (16)$$

We assume $\tilde{i}(t)$ is also a zero-mean, stationary, random process, statistically independent of $\tilde{d}(t)$, with power p_i,

$$p_i = E[|\tilde{i}(t)|^2]. \tag{17}$$

Finally, assume each element signal contains a zero-mean thermal noise voltage $\tilde{n}_{m1}(t)$ of power σ^2, statistically independent between elements. Thus,

$$E[\tilde{n}_{j1}^*(t)\tilde{n}_{m1}(t)] = \sigma^2\delta_{jm}, \qquad 1 \leq j, \, m \leq M, \tag{18}$$

where δ_{jm} is the Kronecker delta. The noise signal at an arbitrary tap is just a delayed version of the noise on that element.

$$\tilde{n}_{mk}(t) = \tilde{n}_{m1}(t - [k - 1]T_0). \tag{19}$$

The $\tilde{n}_{m1}(t)$ are assumed independent of $\tilde{d}(t)$ and $\tilde{i}(t)$.

With these definitions, we may determine Φ and S in (6) and (7). Because the desired, interference and thermal noise terms are mutually independent and zero-mean, Φ splits into desired, interference, and thermal noise terms,

$$\Phi = \Phi_d + \Phi_i + \Phi_n. \tag{20}$$

Consider Φ_d first. In partitioned form, Φ_d is

$$\Phi_d = \begin{pmatrix} \Phi_{d_{11}} & \vdots & \Phi_{d_{12}} & \vdots & \cdots & \vdots & \Phi_{d_{1M}} \\ -- & \vdots & -- & \vdots & -- & \vdots & -- \\ \Phi_{d_{21}} & \vdots & \Phi_{d_{22}} & \vdots & & \vdots & \\ -- & \vdots & -- & \vdots & -- & \vdots & -- \\ \vdots & & \vdots & & \ddots & & \vdots \\ -- & \vdots & -- & \vdots & -- & \vdots & -- \\ \Phi_{d_{M1}} & \vdots & & \vdots & & \vdots & \Phi_{d_{MM}} \end{pmatrix}, \tag{21}$$

where each $K \times K$ submatrix $\Phi_{d_{mn}}$ is the desired signal covariance matrix associated with a pair of element signal vectors X_{dm} and X_{dn},

$$\Phi_{d_{mn}} = E[X_{dm}^* X_{dn}^T]. \tag{22}$$

$\Phi_{d_{mn}}$ may be found by substituting $\tilde{d}_{mk}(t)$ of (11) into (22). The jkth term of $\Phi_{d_{mn}}$ (the element in the jth row and kth column of $\Phi_{d_{mn}}$) is found to be

$$[\Phi_{d_{mn}}]_{jk} = R_d[(j - k)T_0 + (m - n)T_d], \tag{23}$$

where $R_d(\tau)$ is the autocorrelation function of the desired signal $\tilde{d}(t)$,

$$R_d(\tau) = E[\tilde{d}^*(t)\tilde{d}(t + \tau)]. \tag{24}$$

To have a specific case to use for calculations below, we shall assume $\tilde{d}(t)$ has a flat, bandlimited power spectral density $S_d(\omega)$ equal to $2\pi p_d/\Delta\omega_d$ over a bandwidth $\Delta\omega_d$ centered at frequency ω_0, as shown in Fig. 2(a). $R_d(\tau)$ is then the inverse Fourier transform of $S_d(\omega)$, or

$$R_d(\tau) = p_d \, \text{sinc}\left(\frac{\Delta\omega_d\tau}{2}\right) e^{j\omega_0\tau}. \tag{25}$$
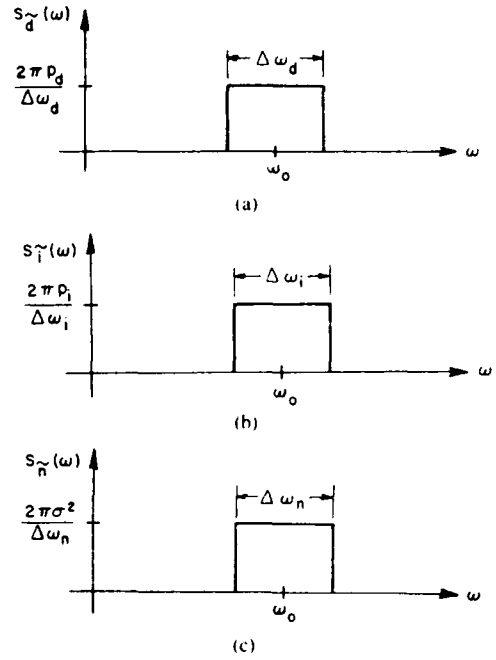

Fig. 2. Power spectral densities. (a) Desired signal. (b) Interference. (c) Thermal noise.

p_d is the desired signal power received per array element, as defined in (13), and $\text{sinc}(x)$ denotes $\sin(x)/x$.

For a specific arrival angle θ_d and tap delay T_0, the matrix Φ_d in (21) can be determined by substituting (25) into (23). Before doing that, it is helpful to write the autocorrelation function in (23) in normalized form. From (25), we have

$$R_d[(j - k)T_0 + (m - n)T_d] = p_d \, \text{sinc}\left\{\frac{\Delta\omega_d}{2}[(j - k)T_0 + (m - n)T_d]\right\} e^{j\omega_0[(j - k)T_0 + (m - n)T_d]}. \tag{26}$$

Note first that the product $\Delta\omega_d T_d$ may be written

$$\Delta\omega_d T_d = \frac{\Delta\omega_d}{\omega_0}(\omega_0 T_d) = B_d\phi_d, \tag{27}$$

where B_d is the desired signal relative bandwidth,

$$B_d = \frac{\Delta\omega_d}{\omega_0}, \tag{28}$$

and ϕ_d is the interelement phase shift at the carrier frequency ω_0,

$$\phi_d = \omega_0 T_d = \frac{\omega_0 L}{c}\sin(\theta_d). \tag{29}$$

In addition, it is helpful to write T_0, the time delay between taps, in normalized form. Because earlier papers have often assumed a quarter wavelength delay between taps [2], we shall arbitrarily normalize T_0 to the time delay associated with a quarter wavelength delay. The time delay required to produce a 90° phase shift at frequency ω_0 is

$$T_{90} = \frac{\pi}{2\omega_0}. \tag{30}$$

Therefore we write T_0 in the form

$$T_0 = r T_{90} = \frac{\pi r}{2\omega_0}, \tag{31}$$

where r is the number of quarter-wave delays in T_0 at frequency ω_0. Then we also have

$$\Delta\omega_d T_0 = \Delta\omega_d \frac{\pi r}{2\omega_0} = \frac{\pi}{2} r B_d. \tag{32}$$

In terms of the normalized parameters B_d, ϕ_d and r, the jkth element of $\Phi_{d_{mn}}$ is

$$[\Phi_{d_{mn}}]_{jk} = p_d \text{ sinc } \left\{ \frac{B_d}{2} \left[\frac{\pi}{2} (j-k)r + (m-n)\phi_d \right] \right\}$$
$$\cdot e^{j[\pi/2(j-k)r + (m-n)\phi_d]}. \tag{33}$$

The interference matrix Φ_i in (20) may be found in the same way. Φ_i is

$$\Phi_d = \begin{pmatrix} \Phi_{i_{11}} & \Phi_{i_{12}} & \cdots & \Phi_{i_{1M}} \\ \Phi_{i_{21}} & \Phi_{i_{22}} & & \\ & & & \\ \vdots & & \ddots & \\ \Phi_{i_{M1}} & & & \Phi_{i_{MM}} \end{pmatrix}, \tag{34}$$

where each $K \times K$ submatrix $\Phi_{i_{mn}}$ is the covariance matrix for the element signal vectors X_{i_m} and X_{i_n},

$$\Phi_{i_{mn}} = E[X_{i_m}^* X_{i_n}^T]. \tag{35}$$

The jkth element of $\Phi_{i_{mn}}$ is

$$[\Phi_{i_{mn}}]_{jk} = R_i[(j-k)T_0 + (m-n)T_i], \tag{36}$$

where $R_i(\tau)$ is the autocorrelation function of the interference,

$$R_i(\tau) = E[\bar{i}^*(t)\bar{i}(t+\tau)]. \tag{37}$$

We shall assume the interference also has a flat, bandlimited power spectral density $S_i(\omega)$ equal to $2\pi p_i/\Delta\omega_i$ over bandwidth $\Delta\omega_i$, as shown in Fig. 2(b). p_i is the interference power received per element. $R_i(\tau)$ is then

$$R_i(\tau) = p_i \text{ sinc } \left(\frac{\Delta\omega_i \tau}{2} \right) e^{j\omega_0 \tau}. \tag{38}$$

Substituting T_0 and T_i in (35) and normalizing as in (32) gives

$$[\Phi_{i_{mn}}]_{jk} = p_i \text{ sinc } \left\{ \frac{B_i}{2} \left[\frac{\pi}{2} (j-k)r + (m-n)\phi_i \right] \right\}$$
$$\cdot e^{j[\pi/2(j-k)r + (m-n)\phi_i]}. \tag{39}$$

where B_i is the relative bandwidth of the interference,

$$B_i = \frac{\Delta\omega_i}{\omega_0}, \tag{40}$$

and ϕ_i is the interelement phase shift for the interference at carrier frequency ω_0,

$$\phi_i = \omega_0 T_i = \frac{\omega_0 L}{c} \sin(\theta_i). \tag{41}$$

The noise matrix Φ_n in (20) is slightly different because the noise is independent between elements, so the noise cross products are zero except for those associated with the same element. We have

$$\Phi_n = \begin{pmatrix} \Phi_{n_{11}} & 0 & \cdots & 0 \\ 0 & \Phi_{n_{22}} & & \\ & & & \\ \vdots & & \ddots & \\ 0 & & & \Phi_{n_{MM}} \end{pmatrix}. \tag{42}$$

We assume the noise power spectral density $S_n(\omega)$ is equal to $2\pi\sigma^2/\Delta\omega_n$ over a bandwidth $\Delta\omega_n$, as shown in Fig. 2(c). The jkth element of $\Phi_{n_{mm}}$ is then

$$[\Phi_{n_{mm}}]_{jk} = \sigma^2 \text{ sinc } \left[\frac{B_n}{4} (j-k)r\pi \right] e^{j(\pi/2)(j-k)r}, \tag{43}$$

where B_n is the relative noise bandwidth,

$$B_n = \frac{\Delta\omega_n}{\omega_0}. \tag{44}$$

We have now obtained all terms in the matrix Φ of (6).

Next, consider the reference correlation vector S in (7). Because the interference and noise vectors X_i and X_n are independent of $\bar{d}(t)$, the only term that contributes to S is X_d,

$$S = E[X^* \bar{d}_0(t)] = E[X_d^* \bar{d}_0(t)]. \tag{45}$$

Substituting for X_d and using (14) gives

$$S = [s_{11}, s_{12}, \cdots, s_{1K}, s_{21}, s_{22}, \cdots, s_{2K}, \cdots,$$
$$s_{M1}, s_{M2}, \cdots, s_{MK}]^T, \tag{46}$$

where

$$s_{mk} = \sqrt{p_d} \text{ sinc } \left\{ \frac{B_d}{2} \left[\frac{\pi}{2} (k-1)r + (m-1)\phi_d \right] \right\}$$
$$\cdot e^{j[\pi/2(k-1)r + (m-1)\phi_d]}. \tag{47}$$

From Φ and S, the optimal array weight vector may be computed from (5).

In solving (5), it is helpful to make one more normalization. Every element of the matrix Φ_d contains the constant p_d, every element of Φ_i contains p_i, and every element of Φ_n contains σ^2. If we divide the entire set of equations by σ^2, the solution for W will then depend on the normalized parameters

$$\xi_d = \frac{p_d}{\sigma^2} = \text{desired signal-to-noise ratio (SNR) per element,}$$
$$\tag{48}$$

and

$$\xi_i = \frac{p_i}{\sigma^2} = \text{interference-to-noise ratio (INR) per element.} \quad (49)$$

From the optimal weight vector W, we may compute the output SINR at the array output. For a given W, the array output signal $\tilde{s}(t)$ is

$$\tilde{s}(t) = W^T X, \quad (50)$$

where X is the signal vector in (3). By writing X as in (10), we may split $\tilde{s}(t)$ into its desired, interference, and noise components,

$$\tilde{s}(t) = \tilde{s}_d(t) + \tilde{s}_i(t) + \tilde{s}_n(t), \quad (51)$$

where

$$\tilde{s}_d(t) = W^T X_d, \quad (52)$$

$$\tilde{s}_i(t) = W^T X_i, \quad (53)$$

and

$$\tilde{s}_n(t) = W^T X_n. \quad (54)$$

The output desired signal power is then

$$P_d = \frac{1}{2} E[|\tilde{s}_d(t)|^2]$$

$$= \frac{1}{2} E[W^\dagger X_d^* X_d^T W]$$

$$= \frac{1}{2} W^\dagger \Phi_d W, \quad (55)$$

where the dagger denotes the conjugate transpose. Similarly, the output interference and thermal noise powers are

$$P_i = \frac{1}{2} W^\dagger \Phi_i W, \quad (56)$$

and

$$P_n = \frac{1}{2} W^\dagger \Phi_n W. \quad (57)$$

Finally, the output SINR is

$$SINR = \frac{P_d}{P_i + P_n}. \quad (58)$$

In the next section, we apply these equations to a two-element array.

III. The Performance of a Two-Element Array

Now let us consider the bandwidth performance of a simple two-element array with tapped delay-lines and see how this performance depends on the delay line parameters.

First, for later comparison, we show in Fig. 3 the SINR of a two-element array with a single complex weight (and no delay)
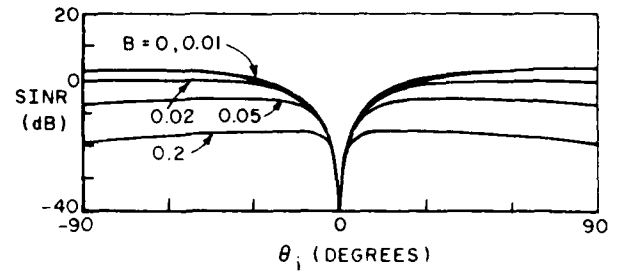

Fig. 3. SINR versus θ_i: $M = 2$, $K = 1$, $\theta_d = 0°$, $\xi_d = 0$ dB, $\xi_i = 40$ dB.

behind each element. In this figure, the desired signal arrives from broadside ($\theta_d = 0°$) and the interference from an arbitrary angle θ_i. The SINR is plotted as a function of θ_i. The desired, interference and noise signals are all assumed to have the same bandwidth B, and Fig. 3 shows the SINR for $B = 0$, 0.01, 0.02, 0.05 and 0.2. ξ_d, the SNR per element, is 0 dB and ξ_i, the INR per element, is 40 dB for all curves.

Fig. 3 shows that when $B = 0.02$ the output SINR has dropped about 3 dB below its value with CW (zero bandwidth) signals. Larger bandwidths quickly reduce the SINR more. For $B = 0.2$, the largest value we show, there is as much as 22 dB degradation for some θ_i.[1] For such large bandwidths, the array performance is clearly unsuitable.

Now suppose we add a single quarter wavelength delay and one extra tap behind each element. (In the equations above, we let $K = 2$ and $r = 1$.) Fig. 4 shows the output SINR that results for this case with $B = 0.2$ and with all other parameters the same as in Fig. 3. We see that the array now performs essentially as well as the simple array in Fig. 3 with CW signals. Thus, adding a single extra tap to each element, with a quarter wavelength between taps, has fully overcome the bandwidth degradation.

Figs. 3 and 4 were computed for $\theta_d = 0°$. However, the results are similar for other values of θ_d. In general, when the array has a single weight behind each element, the SINR for $B = 0.2$ is much poorer than for $B = 0$. But if a single quarter wave delay and one extra tap are added to each element, the performance is fully restored.

Now consider what happens if we change the amount of delay between taps. The curve in Fig. 4 was computed for a one-quarter wavelength delay between taps ($r = 1$), an arbitrary amount. When other values of r are used, one finds an interesting result: the array output SINR is hardly affected by r! On the one hand, if r is reduced below 1, even to arbitrarily small value, the SINR is not noticeably different from that for $r = 1$. A plot of SINR versus θ_i for $r = 10^{-4}$, for example, looks identical to Fig. 4. On the other hand, if r is raised above 1, there is also very little change in SINR, until the delay exceeds about two wavelengths. For example, Fig. 5 shows the SINR versus θ_i for $r = 5$, 10, 15, 20 and 25 and for all parameters the same as in Fig. 4. Note that when $r = 5$ the SINR still achieves the optimal value shown in Fig. 4. When $r = 10$ the SINR has dropped about 1 dB below optimal. ($r =$

---

[1] In general, the amount of degradation for a given bandwidth is strongly influenced by the INR. The larger the INR, the more sensitive the array is to interference bandwidth. In this discussion, we shall simply present results for an INR of 40 dB.
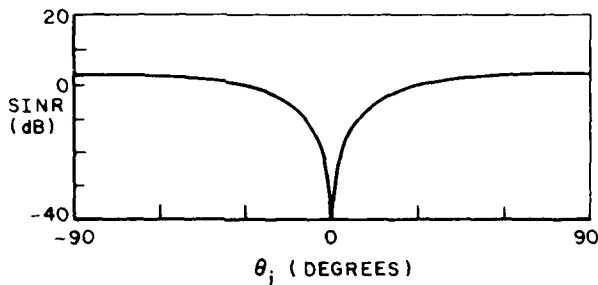
Fig. 4. SINR versus θ_i: $M = 2$, $r = 1$, $K = 2$, $B = 0.2$, $\theta_d = 0°$, $\xi_d = 0$ dB, $\xi_i = 40$ dB.
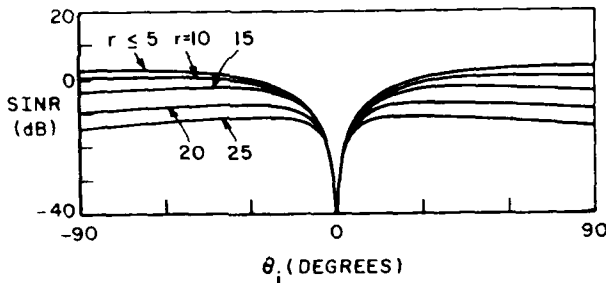

Fig. 5. SINR versus θ_i: $M = 2$, $K = 2$, $B = 0.2$, $\theta_d = 0°$, $\xi_d = 0$ dB, $\xi_i = 40$ dB.

10 corresponds to 2.5 wavelengths of delay between taps.) For $r = 15$ and above, the degradation is more serious, particularly for θ_i near $\pm 90°$.

Thus, the array performance is rather insensitive to r. Any value of r in the range $0 < r < 5$ yields essentially the same SINR. At first glance, this results seems puzzling, especially the fact that the SINR is unaffected when r approaches zero. Intuitively, it appears that a tapped delay-line should become equivalent to a single weight when the delay is very small. However, this is not the case, as we shall see below.

To understand the effect of r on the array performance, we consider the transfer function of the array as seen by the interference. Let $H_m(\omega)$ be the transfer function of the delay line behind element m in Fig. 1. In general, with K taps and $K - 1$ delays behind element m, $H_m(\omega)$ is

$$H_m(\omega) = w_{m1} + w_{m2}e^{-j\omega T_0} + \cdots + w_{mK}e^{-j\omega(K-1)T_0}. \quad (59)$$

The transfer function of the entire array as seen by the interference $H_i(\omega)$ is then

$$H_i(\omega) = \sum_{m=1}^{M} H_m(\omega)e^{-j\omega(m-1)T_i}, \quad (60)$$

where T_i is given in (16). To null an interference signal completely, $H_i(\omega)$ must be zero over the interference bandwidth. For the special case of a two-element array, as considered in Figs. 3 and 4, $H_i(\omega)$ will be zero if

$$H_1(\omega) = -H_2(\omega)e^{-j\omega T_i}. \quad (61)$$

The physical meaning of (61) is easy to see. An interference signal from angle θ_i arrives at element 2 a time T_i later than at element 1. When the interference has nonzero bandwidth, this delay reduces the correlation between the signals on the two

elements and makes it difficult to null the interference by subtracting one element signal from another. However, if the filters $H_1(\omega)$ and $H_2(\omega)$ satisfy (61), the factor $e^{-j\omega T_i}$ in (61) will delay the interference an additional time T_i in element 1 to restore its correlation with the interference on element 2. The minus sign in (61) will then make the interference cancel at the array output.

Before considering what happens as r is varied, let us see how well (61) is satisfied by the arrays considered in Figs. 3–5. Note that to satisfy (61), the transfer functions $H_1(\omega)$ and $H_2(\omega)$ must have identical amplitudes,

$$|H_1(\omega)| = |H_2(\omega)|, \quad (62)$$

and phases whose difference varies linearly with frequency,

$$\angle H_1(\omega) = \angle H_2(\omega) - \pi - \omega T_i, \quad (63)$$

over the signal bandwidth. For the array in Fig. 3, we assumed one weight and no delays behind each element. For this case $H_m(\omega)$ is simply

$$H_m(\omega) = w_{m1}, \quad (64)$$

which is a constant independent of frequency. With such an $H_m(\omega)$, it is possible to satisfy (61) at one frequency, but not over a band of frequencies. For the array in Fig. 4, however, we assumed two weights and one delay behind each element. In this case each $H_m(\omega)$ has the form

$$H_m(\omega) = w_{m1} + w_{m2}e^{-j\omega T_0}. \quad (65)$$

Because of the term $e^{-j\omega T_0}$, the $H_m(\omega)$ can now vary with frequency. This capability allows $H_1(\omega)$ and $H_2(\omega)$ to do a better job of satisfying (61) over the signal bandwidth and hence improves the array bandwidth performance, as Fig. 4 shows.

Examination of the $H_1(\omega)$ and $H_2(\omega)$ that actually result when each element has two weights and one delay confirm that the processor does attempt to satisfy (61). For example, Fig. 6 shows $|H_1(\omega)/H_2(\omega)|$ and $\angle H_1(\omega) - \angle H_2(\omega)$ versus ω for the same parameters as in Fig. 4: $\theta_d = 0°$, $\xi_d = 0$ dB, $\xi_i = 40$ dB, $r = 1$ and $B = 0.2$, and for $\theta_i = 20°$. It may be seen how $|H_1(\omega)/H_2(\omega)| = 0$ dB and $\angle H_1(\omega) - \angle H_2(\omega)$ varies linearly with frequency over the signal bandwidth. The slope of $\angle H_1(\omega) - \angle H_2(\omega)$ has the proper value to satisfy (61).

Now consider how the delay between taps affects the performance. First, suppose we let r approach zero. For very small r (small T_0), $H_m(\omega)$ in (65) becomes

$$H_m(\omega) = w_{m1} + w_{m2} \cos \omega T_0 - j w_{m2} \sin \omega T_0$$
$$\approx w_{m1} + w_{m2} - j w_{m2}\omega T_0. \quad (66)$$

We observe that no matter how small T_0 is (as long as $T_0 \neq 0$), the array can always realize any given linear slope for $\angle H_1(\omega) - \angle H_2(\omega)$ by making the weights suficiently large. Calculations show that that is what happens. As r is reduced toward zero, the weights obtained from (5) increase without bound. Fig. 7 illustrates this behavior. It shows Re (w_{11}) and Im (w_{11}) as functions of r for $\theta_d = 0°$, $\theta_i = 20°$, $\xi_d = 0$ dB, ξ_i
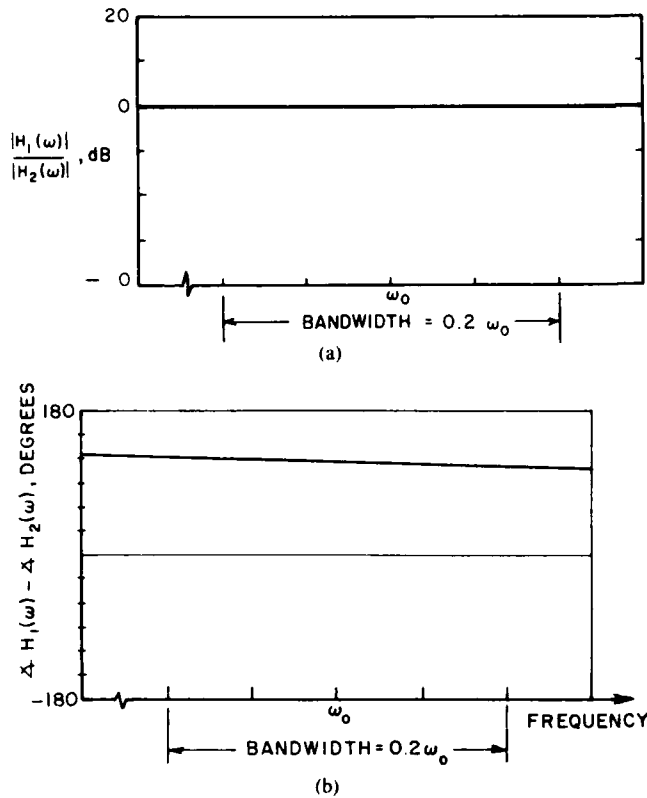
Fig. 6. The transfer functions $H_1(\omega)$ and $H_2(\omega)$: $r = 1$, $K = 2$, $B = 0.2$, $\theta_d = 0°$, $\theta_i = 20°$, $\xi_d = 0$ dB, $\xi_i = 40$ dB. (a) $|H_1(\omega)|/|H_2(\omega)|$ versus ω (b) $\angle H_1(\omega) - \angle H_2(\omega)$ versus ω.
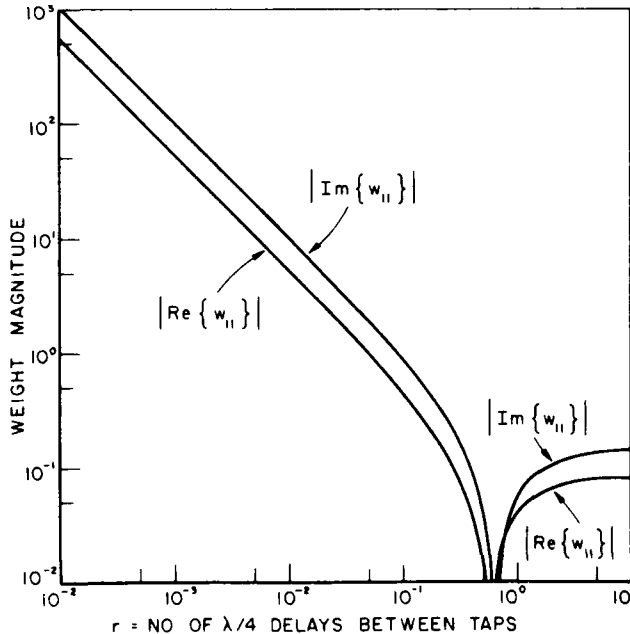

Fig. 7. w_{11} versus r: $\theta_d = 0°$, $\theta_i = 20°$, $\xi_d = 0$ dB, $\xi_i = 40$ dB, $B = 0.2$.

$= 40$ dB and $B = 0.2$, the same parameters as above. The other weights behave similarly as $r \to 0$.

Thus, by increasing the weights, the array can satisfy (61) regardless of how small r becomes (as long as $r \neq 0$). This is the reason an array with two weights and one delay behind each element does not become equivalent to an array with a

single weight behind each element as $r \to 0$. With two weights and one delay, the SINR obtained versus θ_i does not change significantly from that in Fig. 4 as $r \to 0$.

The unbounded increase in the weights as $r \to 0$ is understandable if we also note that the covariance matrix in (6) becomes singular when r goes to zero. As $r \to 0$, the signal $\tilde{x}_{m2}(t)$ at the second tap becomes equal to $\tilde{x}_{m1}(t)$, the signal at the first tap. In the limit, when two tap signals are equal, the covariance matrix in (6) will have two identical columns (or rows) and hence will be singular. Thus we should expect the weight vector W satisfying (5) to exhibit unusual behavior as $r \to 0$.

In a hardware array, there is always a limit to how large the weights can actually become, of course. With analog weights, the circuits always saturate at some point. With digital weights, finite register lengths limit the maximum attainable weight values. Because the weights cannot increase indefinitely in a real array, there will be some minimum value of r for which the array can maintain the SINR. Below this minimum r, the SINR will drop.[2]

Now consider what happens if we increase r. We showed in Fig. 5 that when r is increased, the array performance is unaffected at first. But finally, for large values of r, the performance begins to drop. The explanation for this behavior may again be found by considering the $H_m(\omega)$.

For any value of r, nulling the interference requires the transfer functions $H_1(\omega)$ and $H_2(\omega)$ in a two-element array to satisfy (61) over the interference bandwidth. However, note that $H_m(\omega)$ in (59) is a periodic function of frequency. (It is a finite Fourier series). The period of $H_m(\omega)$ is

$$\Omega_0 = \frac{2\pi}{T_0} = \frac{4\omega_0}{r}. \tag{67}$$

For small r, this period is much larger than the signal bandwidth. But when r is increased, the period drops. Ω_0 will equal the signal bandwidth when

$$r = \frac{4}{B}. \tag{68}$$

When r is small and the period is much larger than the bandwidth, $\angle H_1(\omega) - \angle H_2(\omega)$ can easily approximate a linear function of frequency over the signal bandwidth (as seen in Fig. 6 for example). But if r is large enough, the period Ω_0 becomes comparable to the signal bandwidth. Because the $H_m(\omega)$ are periodic, it then becomes difficult for the $H_m(\omega)$ to satisfy (61) over the whole bandwidth. In particular, when $r > 4/B$, $\angle H_1(\omega) - \angle H_2(\omega)$ cannot vary linearly over the entire bandwidth, because its value must repeat periodically within the bandwidth. This is the reason array performance drops when r becomes too large.

Fig. 5, computed for $B = 0.2$, illustrates this point. For $B = 0.2$, the period Ω_0 will equal the signal bandwidth when $r = 20$. One finds that there is no drop in SINR for r up to about five (which is $1/B$). Beyond five, the SINR drops as r

[2] There will also be convergence difficulties for most weight control algorithms as $r \to 0$, because the eigenvalue spread of Φ becomes infinite.

approaches and then passes 20. We find the same general result for all values of B (up to $B = 0.5$): *when the array has two weights and one delay behind each element, the SINR is unaffected by r as long as r is in the range* $0 < r < 1/B$.

The performance degradation for large r may also be understood from a time domain point of view. Signals with nonzero bandwidth remain correlated with themselves for time shifts up to approximately the reciprocal of the bandwidth. Hence, one would expect that adding an extra delay and tap to each element will be effective only if the delays are short compared with the reciprocal of the bandwidth. If the delays are too large, the signals on different taps become decorrelated, and the array cannot null the interference by subtracting one tap signal from another.

The curves in Figs. 4 and 5 assumed two weights and one delay behind each element. Let us now consider what happens if we add extra taps (extra delays and weights) behind each element in the two-element array.

We observe first that adding extra taps can help the performance only for a limited range of r. On the other hand, when $r < 1/B$, the array is already capable of nulling a wideband interference signal. Hence for $r < 1/B$ there appears to be no point in adding extra taps. On the other hand, if $r > 4/B$, the period Ω_0 of the $H_m(\omega)$ is less than the signal bandwidth. In this case the $H_m(\omega)$ cannot satisfy (61) over the signal bandwidth, regardless of how many taps are used, because $\angle H_1(\omega) - \angle H_2(\omega)$ must repeat periodically within the signal bandwidth. Hence the only case where extra taps may be useful is when $1/B < r < 4/B$. In this range, the period of $H_m(\omega)$, although larger than the bandwidth, is small enough that with only two weights and one delay $\angle H_1(\omega) - \angle H_2(\omega)$ does not vary linearly with frequency. However, adding more Fourier terms in (59) will allow $\angle H_1(\omega) - \angle H_2(\omega)$ to approximate a linear behavior more accurately.

Let us illustrate this behavior for $B = 0.2$. First, for $r < (1/B) = 5$, no extra taps are needed. An array with one delay and two weights already has optimal performance, as may be seen in Fig. 4. Next, for $5 < r < 20$, we find that with only two weights and one delay, the SINR is reduced from that in Fig. 4. Fig. 5 shows this behavior. However, for this range of r, the performance will improve if we increase the number of taps. Fig. 8 shows the SINR versus θ_i for $r = 15$ and for $K = 2, 4, 8$ and 16 taps. As may be seen, for this r the perfomance is ir roved by increasing K. The reason for this improvement is s(1 in Fig. 9, which shows $\angle H_1(\omega) - \angle H_2(\omega)$ versus ω for the same values of K and for $\theta_i = 80°$. $\angle H_1(\omega) - \angle H_2(\omega)$ becomes more nearly linear with ω over the signal bandwidth as K increases. ($|H_1(\omega)/H_2(\omega)|$ is unity over the bandwidth for all four values of K.)

Finally, when $r > (4/B) = 20$, we expect poor nulling performance no matter how many extra taps are added, because $\angle H_1(\psi) - \angle H_2(\omega)$ is periodic with a period smaller than the bandwidth. Fig. 10 shows such a case. It shows the SINR versus θ_i for $r = 22$, (with $B = 0.2$, $\theta_d = 0°$, $\xi_d = 0$ dB, $\xi_i = 40$ dB) and for $K = 2, 4, 8$ and 16. As may be seen, the SINR improves somewhat with K but never achieves the value in Fig. 4. Fig. 11 shows $|H_1(\omega)/H_2(\omega)|$ and $\angle H_1(\omega) - \angle H_2(\omega)$ for this case with $\theta_i = 80°$. Note how $|H_1(\omega)/H_2(\omega)|$

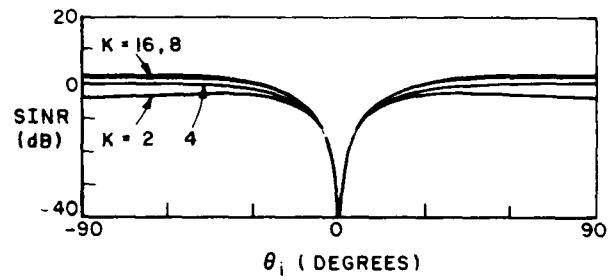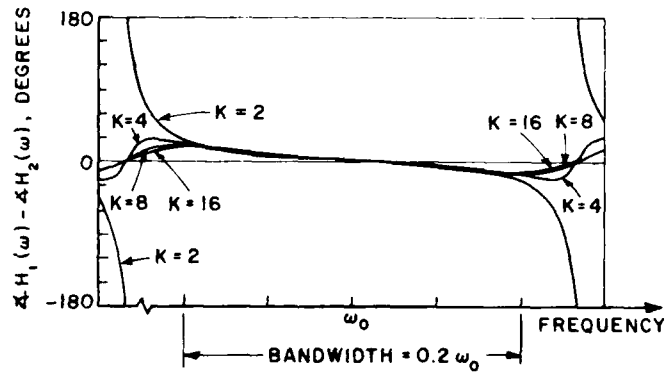Fig. 8.   SINR versus θ_i: $r = 15$, $B = 0.2$, $\theta_d = 0°$, $\xi_d = 0$ dB, $\xi_i = 40$ dB.

Fig. 9. $\angle H_1(\omega) - \angle H_2(\omega)$ versus ω: $r = 15$, $B = 0.2$, $\theta_d = 0°$, $\theta_i = 80°$, $\xi_d = 0$ dB, $\xi_i = 40$ dB.
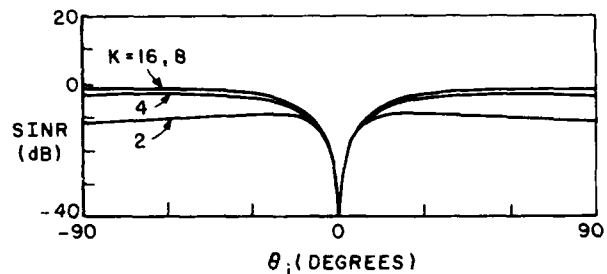

Fig. 10.   SINR versus θ_i: $r = 22$, $B = 0.2$, $\theta_d = 0°$, $\xi_d = 0$ dB, $\xi_i = 40$ dB.

and $\angle H_1(\omega) - \angle H_2(\omega)$ repeat periodically within the signal bandwidth. Also, $|H_1(\omega)/H_2(\omega)| \neq 1$ at some frequencies within the bandwidth, and $\angle H_1(\omega) - \angle H_2(\omega)$ is not linear across the bandwidth, regardless of how many Fourier series terms are used in the $H_m(\omega)$.

Whether an adaptive array should be operated with r in the range $1/B < r < 4/B$ and with a large value of K depends on how the array is to be implemented. For an array with analog control loops, there is no reason to use such a large r. For one thing, it is difficult to implement long time delays between taps. For another, each weight in an adaptive processor adds cost and complexity to the processor. To obtain good bandwidth performance from the array, it is simpler just to use a small value of r, such as $r = 1$, and to use only two weights and one delay per element.

For an array with digital weight control, on the other hand, an A/D converter will be used behind each element. In this case it may be useful to have a large value of r, since a large r corresponds to a low sampling rate. However, if r is large enough, more weights will be needed, as discussed above.
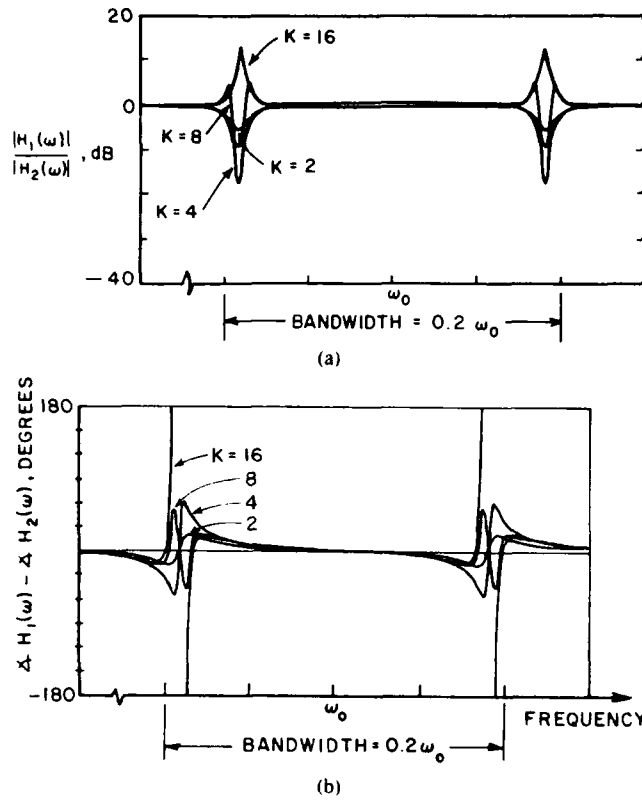
Fig. 11. The transfer functions $H_1(\omega)$ and $H_2(\omega)$: $r = 22$, $B = 0.2$, $\theta_d = 0°$, $\theta_i = 80°$, $\xi_d = 0$:3, $\xi_i = 40$ dB. (a) $|H_1(\omega)|/|H_2(\omega)|$ versus ω. (b) $\angle H_1(\omega) - \angle H_2(\omega)$ versus ω.

Fig. 12. The transfer function $H_d(\omega)$: $r = 15$, $B = 0.2$, $\theta_d = 0°$, $\theta_i = 80°$, $\xi_d = 0$ dB, $\xi_i = 40$ dB. (a) $|H_d(\omega)|$ versus ω. (b) $\angle H_d(\omega)$ versus ω.

Increasing the number of weights may be easier than in an analog array, but will still add to the complexity of the weight control algorithm.[3]

Another factor that must be considered when r is large is the effect of the array on the desired signal. In general, an M-element array presents a transfer function

$$H_d(\omega) = \sum_{m=1}^{M} H_m(\omega) e^{-j\omega(m-1)T_d} \qquad (69)$$

to the desired signal, where T_d is given in (12) and $H_m(\omega)$ in (59). If $H_d(\omega)$ has anything other than a constant amplitude and a linear phase slope over the desired signal bandwidth, the desired signal waveform will be distorted in passing through the array. Whether this is a problem or not depends on the desired signal waveform and the application. However, for many communication systems, it is difficult to accommodate a desired signal whose waveform changes as the array adapts.

Because the array responds to the incoming signals, $H_d(\omega)$ depends in general on all the signal parameters: the desired signal power and arrival angle and the interference power and arrival angle. However, for the two-element array considered above, calculations show that when r is small ($r < 1/B$), $|H_d(\omega)|$ is constant and $\angle H_d(\omega)$ varies linearly with frequency. But when $r > 1/B$, $H_d(\omega)$ can vary substantially over the desired signal bandwidth. For r in the range $1/B < r < 4/$

---

[1] For the discrete LMS algorithm [1], the computational burden increases linearly with the number of weights. For the sample matrix inverse method [6], it increases with the cube of the number of weights.
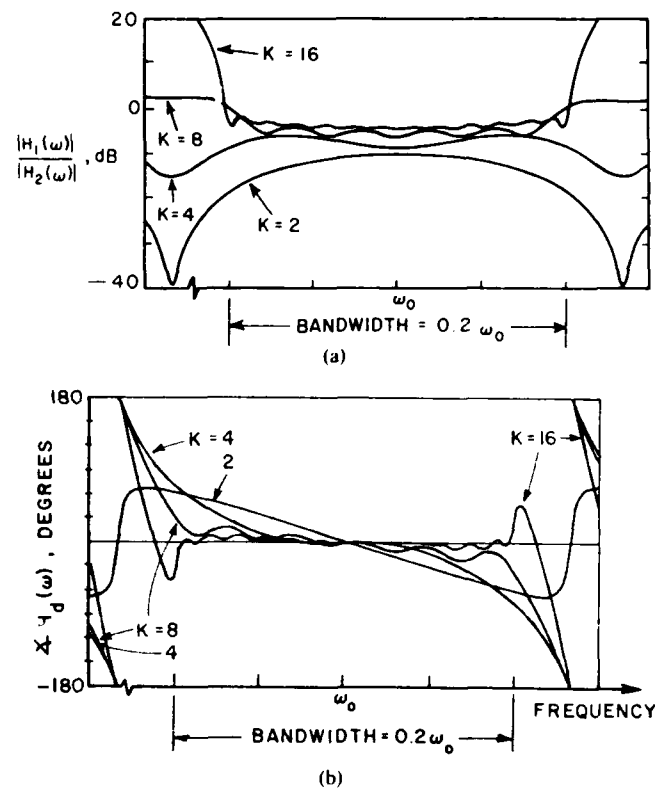
B, one finds that $|H_d(\omega)|$ becomes more nearly constant and $\angle H_d(\omega)$ becomes more nearly linear with frequency as the number of weights K is increased. Fig. 12 shows a typical case. It shows $|H_d(\omega)|$ and $\angle H_d(\omega)$ over the signal bandwidth for $r = 15$ and $K = 2, 4, 8$ and 16, with all other parameters the same as in Figs. 8 and 9. Note how the behavior of $H_d(\omega)$ improves as k increases. On the other hand, for $r > 4/B$, $H_d(\omega)$ cannot have the required behavior over the signal bandwidth, because the Fourier series period is less than the signal bandwidth. In this case, there is always at least some desired signal distortion, no matter how large K. It is clear that a designer must take the behavior of $H_d(\omega)$ into account when a large value of r is used.

IV. CONCLUSION

This paper has considered the bandwidth performance of a two-element adaptive array with tapped delay-lines behind the elements. Section II presented the equations needed to compute the output SINR for an array with an arbitrary number of elements and taps. Section III described how the number of taps and the amount of delay between taps affect the SINR for a two-element array.

An array with two weights and one delay behind each element yields optimal performance (equal to that obtained with CW interference) for any value of delay greater than zero and less than T_{90}/B, where T_{90} is the time delay for a 90° carrier phase shift and B is the fractional signal bandwidth. Delays less than T_{90} yield optimal performance but result in large array weights. Delays larger than T_{90}/B yield suboptimal SINR when each element has only two weights.

For delays between T_{90}/B and $4T_{90}/B$, the performance is suboptimal with only two weights but approaches optimal if more delay-line sections and weights are added to each element. Delays larger than $4T_{90}/B$ result in suboptimal performance regardless of the number of delays and weights used.

ACKNOWLEDGMENT

REFERENCES

[1] B. Widrow, P. E. Mantey, L. J. Griffiths and B. B. Goode, "Adaptive antenna systems," *Proc. IEEE*, vol. 55, no. 12, pp. 2143-2159, Dec. 1967.

[2] W. E. Rodgers and R. T. Compton, Jr., "Adaptive array bandwidth with tapped delay-line processing," *IEEE Trans. Aerospace Electron. Syst.*, vol. AES-15, no. 1, pp. 21-27, Jan. 1979.

[3] J. T. Mayhan, A. J. Simmons and W. C. Cummings, "Wideband adaptive antenna nulling using tapped delay-lines," *IEEE Trans. Antennas Propagat.*, vol. AP-29, no. 6, pp. 923-936, Nov. 1981.

[4] W. D. White, "Wideband interference cancellation in adaptive sidelobe cancellers," *IEEE Trans. Aerospace Electron. Syst.*, vol. AES-19, no. 6, pp. 915-925, Nov. 1983.

[5] S. P. Applebaum, "Adaptive arrays," *IEEE Trans. Antennas Propagat.*, vol. AP-24, no. 5, pp. 585-598, Sept. 1976.

[6] I. S. Reed, J. D. Mallett, and L. E. Brennan, "Rapid convergence rate in adaptive arrays," *IEEE Trans. Aerospace Electron. Syst.*, vol. AES-10, no. 6, pp. 853-863, Nov. 1974.

[7] C. A. Baird, Jr., and C. L. Zahm, "Performance criteria for narrowband array processing," presented at 1971 IEEE Conf. Decision and Control, Miami Beach, FL, Dec. 15-17, 1971.

R. T. Compton, Jr. (S'58-M'59-M'81-SM'82-F'84) was born in St. Louis, MO, on July 26, 1935. He received the S.B. degree from Massachusetts Institute of Technology, Cambridge, in 1958 and the M.Sc. and Ph.D. degrees from the The Ohio State University, Columbus, in 1961 and 1964, all in electrical engineering.

From 1965 to 1967, he was an Assistant Professor of Engineering at Case Institute of Technology, Cleveland, OH, and from 1967 to 1968 he was an NSF Postdoctoral Fellow at The Technische Hochschule, Munich, Germany. He spent the 1983-1984 academic year at the Naval Research Laboratory, Washington, DC. He is a Professor of Electrical Engineering at The Ohio State University.

Dr. Compton is a member of Sigma Xi and Pi Mu Epsilon. He received the M. Barry Carlton Award for best paper from the IEEE Aerospace and Electronic Systems Society in 1983.

A Selective Modal Scheme for the Analysis of EM Coupling Into or Radiation from Large Open-Ended Waveguides

Ayhan Altintas

Prabhakar H. Pathak

Ming-Cheng Liang

A Selective Modal Scheme for the Analysis of EM Coupling Into or Radiation from Large Open-Ended Waveguides

AYHAN ALTINTAŞ, PRABHAKAR H. PATHAK, FELLOW, IEEE, AND MING-CHENG LIANG

Abstract—The problem of electromagnetic (EM) coupling into or radiation from open-ended waveguides is addressed here. Of particular interest is the high-frequency range where a large number of propagating waveguide modes can be excited and conventional procedures requiring a summation over a large number of propagating modes can become cumbersome and inefficient. A selective modal scheme is proposed based on the observation that the modes which contribute most significantly to the fields coupled into the waveguide are those whose modal ray directions are most nearly parallel to the incident wave direction. This concept is illustrated by calculating the EM radiation and backscattering from open-ended parallel-plate, rectangular, circular, and sectoral waveguide geometries. The calculations employ the usual geometrical optics, aperture field, and Ufimtsev edge current techniques. Also included are some measured results which further verify the accuracy of the above computations.

I. INTRODUCTION

A SELECTIVE modal scheme is proposed in this paper to efficiently analyze the problem of high-frequency (HF) electromagnetic (EM) coupling/penetration into or radiation from open-ended waveguides. This scheme is based on the phenomenon that at sufficiently high frequencies, the modes which contribute most significantly to the fields coupled into the waveguide are those whose modal ray directions are most nearly parallel to the incident wave direction [1]. Even though the transmission of EM energy at HF into semi-infinite open-ended waveguides has been discussed extensively in the literature [2]–[6], the above mentioned fact does not appear to have been exploited previously. This observation applies equally well to the reciprocal problem of EM radiation from the open end where only those modes whose modal ray angles are most nearly parallel to the desired radiation direction contribute strongly to the radiated field. This fact is especially useful at high frequencies where a direct modal analysis becomes cumbersome and inefficient due to the existence of a large number of propagating modes inside the waveguide cavity region.

The present approach is based on the ray optical characterization of the waveguide modes in terms of a set of equivalent modal rays, either directly or through asymptotic approximations to the modal field expressions. Some examples of modal rays are illustrated in Fig. 1. Each set of modal rays exhibits a linear or almost linear phase distribution in the waveguide aperture. Using a Kirchhoff-type approximation in the aperture integration (AI), the far field radiated into the exterior by such aperture distributions consists of patterns which have beam maxima in directions perpendicular to the wavefronts of the corresponding set of modal rays in the aperture. Therefore, for a given observation direction, only those sets of modal rays in the aperture which radiate beam maxima closest to this direction contribute significantly; other modes (modal rays) radiate sidelobes in that direction and generally yield a relatively small contribution. It is known that the edge effects included in the Kirchhoff-based AI are not as complete as those predicted by the geometrical theory of diffraction (GTD) [7] especially for wide-angle radiation; thus the Kirchhoff approximation is improved via a modification of Ufimtsev's physical theory of diffraction (PTD) [8] presented in [9] to get the generally small correction to the edge effects predicted by the Kirchhoff-based AI [10]. The additional correction resulting from the multiple-edge diffraction of modal rays across the aperture is assumed to be negligible for large waveguides, and it is thus ignored.

Section II discusses the Kirchhoff-based AI and the Ufimtsev-type contributions to the modal radiation from semi-infinite, perfectly conducting parallel-plate, rectangular, circular, and sectoral waveguide geometries as shown in Fig. 1. In all of these geometries the modes will be classified as transverse electric (TE) or transverse magnetic (TM) to the z-direction. The explicit expressions for the modal radiation are presented in the Appendix. The EM fields coupled into these open-ended waveguides illuminated by a plane wave can be found directly from the solutions to the above radiation problems via reciprocity. It is noted that the Kirchhoff-based aperture integral (AI), which essentially constitutes a physical optics (PO) approximation, gives results which satisfy reciprocity only in the main beam direction. However, when the Ufimtsev correction to the PO approximation is included, it then tends to restore reciprocity in directions away from the main beam as well. The results of Section II are then employed in Section III to analyze the more general problem of EM plane-wave backscattering from open-ended waveguide cavities. In particular, the two cases treated in Section III are those

MODAL RAY DIRECTIONS

$$\mp \left(\frac{n\pi}{ka}\right)\hat{x} \mp \left(\frac{m\pi}{kb}\right)\hat{y} + \frac{\beta_{nm}}{k}\hat{z}$$
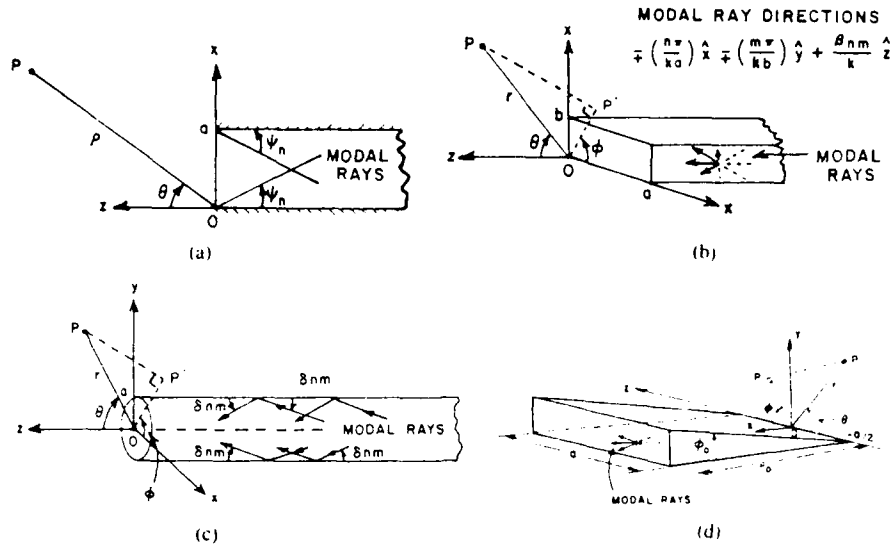

Fig. 1.   Radiation from (a) the parallel plate waveguide; (b) the rectangular waveguide; (c) the circular waveguide; (d) the sectoral waveguide.

pertaining to the EM backscatter by open-ended circular, and nonuniform (piecewise linearly tapered) waveguide cavities with an interior planar short-circuit termination. Again, it is observed that only a few selected ones out of a large number of propagating modes contribute strongly to the backscattered field for each backscatter direction, and a good comparison is obtained between the calculated results and corresponding measurements on actual models. Finally, some conclusions are given in Section IV.

An $e^{j\omega t}$ time convention is assumed and suppressed for the field expressions. k refers to the free-space wavenumber, and $Z_0 = Y_0^{-1}$ is the intrinsic impedance of free space.

II. MODAL RADIATION FROM SOME WAVEGUIDE GEOMETRIES

In this section, the far-zone modal radiation from open-ended parallel-plate, rectangular, circular, and sectoral waveguides is discussed. As indicated earlier, these radiation problems are directly related to the problems of the coupling of an incident plane-wave field into the waveguide modal fields via reciprocity [10] as mentioned in Section I. Thus the coupling problem will not be explicitly discussed here.

A. The Parallel-Plate Waveguide

The geometry of an open-ended parallel-plate waveguide is depicted in Fig. 1(a). The expressions for the modal fields and the modal radiation are given in the Appendix.

Each component of the nth modal field can be decomposed into the fields associated with two characteristic plane waves (which propagate along modal rays). The modal rays associated with the propagation of these modal plane waves make a fixed angle ψ_n with the waveguide walls. Specifically, ψ_n is given by [10]

$$\psi_n = \cos^{-1}\left(\frac{\beta_n}{k}\right) \tag{1}$$

as illustrated in Fig. 1(a) where β_n is the propagation constant for the nth mode as given in (9). For the radiation, the incident

and reflection shadow boundary (ISB and RSB) directions correspond to this modal ray direction. The field pattern of each mode is composed of two $\sin(\xi)/\xi$ functions with their peaks in the modal ray shadow boundary (SB) directions (see Fig. 2). It is also noted that if one considers the radiation only from the nth odd (or even) mode, the peak radiation occurs at $\sin\theta = n\pi/ka$. In this shadow boundary direction the other odd (or even) modes have a null in their pattern. Therefore, around this direction only the nth mode and the two neighboring even modes are mainly responsible for the radiation. The contributions from other modes interfere mostly destructively especially in the case of a large waveguide where there are many propagating modes. In comparison with the exact Wiener–Hopf result [11], it is known that the Kirchhoff-based AI approximation result is reasonably accurate for frequencies exceeding the cutoff frequency by 5 percent. It is also known that the Kirchhoff-based AI approximation gives exact radiation in the modal ray angle directions [11].

The modal radiation patterns obtained from (13) of the Appendix are compared with the first-order GTD results for nonstaggered and staggered waveguide geometries. In order to show the effect of Ufimtsev correction, the mode chosen is very close to the cutoff frequency for some small waveguides. The radiation patterns from these waveguides are shown in Figs. 3 and 4. The results indicate that the Ufimtsev contribution improves the AI approximation primarily away from the direction of the AI beam maximum so that it becomes indistinguishable from the GTD result which is known to be accurate.

As mentioned earlier in the Introduction, the Ufimtsev contribution to the radiated field is generally quite weak in comparison with the AI contribution for large waveguides, as observed in Fig. 5.

B. The Rectangular Waveguide

From the expressions in (20) and (21) of the Appendix, each component of the nmth modal field in a rectangular wave-
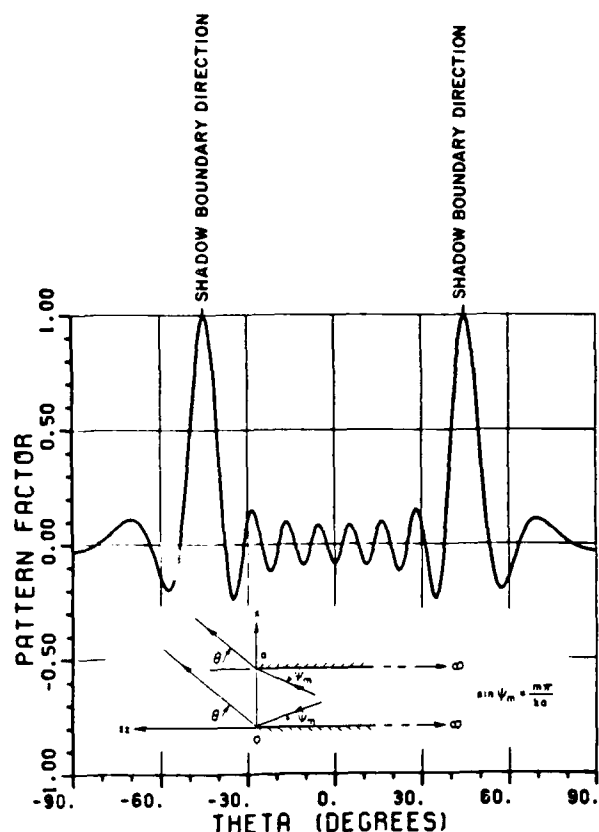
Fig. 2. The modal radiation pattern for a TMy mode from an open-ended, parallel-plate waveguide using AI. Mode index: $m = 15$, modal ray angle $= 45°$.
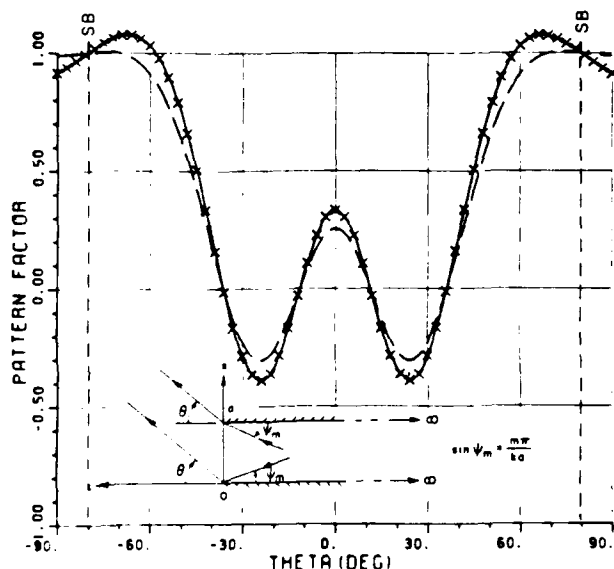
Fig. 3. Comparison of far zone modal radiation patterns for a TM$_v$ mode from an open-ended, parallel-plate waveguide. Mode index: $m = 5$, modal ray angle $= 80°$, ——— : GTD; ———: AI; xxxx: modified PTD.

Fig. 4. Comparison of far zone modal radiation patterns for a TM$_y$ mode from an open-ended, parallel-plate waveguide. Mode index: $m = 3$, modal ray angle $= 50°$, staggering angle: $t_o = 60°$, ——— : GTD; ———: AI; xxxx: modified PTD.
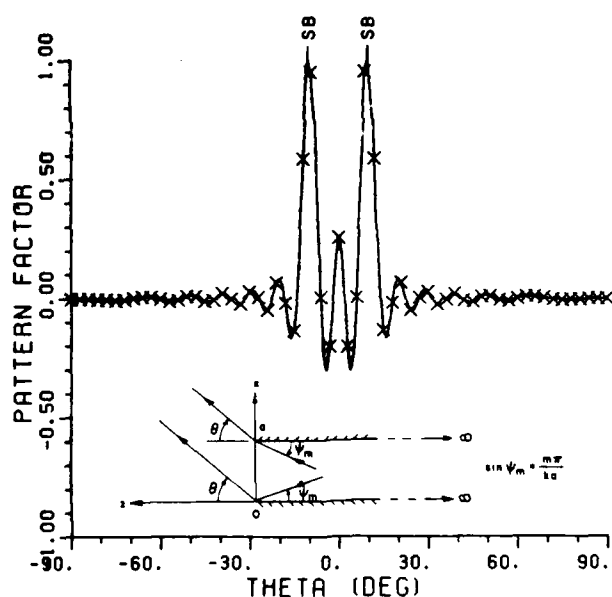
Fig. 5. Comparison of far zone modal radiation patterns for a TM$_v$ mode from an open-ended parallel-plate waveguide. Mode index: $m = 5$, modal ray angle $= 10°$, ——— : GTD; ———: AI; xxxx: modified PTD.

guide can be decomposed into fields which are associated with four characteristic plane waves that propagate along modal ray paths as shown in Fig. 1(b).

From the results given in (22)–(26) of the Appendix, it is seen that the radiation pattern has a sin ξ/ξ type behavior in both the $\hat{\theta}$ and $\hat{\phi}$ directions. There are four different sin ξ/ξ forms, each of which is due to the integration of a plane-wave

component of the mode. Therefore, each sin ξ/ξ exhibits a peak at the corresponding plane-wave direction. Also, as the waveguide becomes electrically larger, the main peaks get sharper. As a result, only a few modes contribute strongly to the radiation for a given direction of observation at high frequencies.

C. The Circular Waveguide

The far-zone radiation due to the nmth modal fields in the circular waveguide geometry of Fig. 1(c) is given by expressions in (50)–(61) of the Appendix.
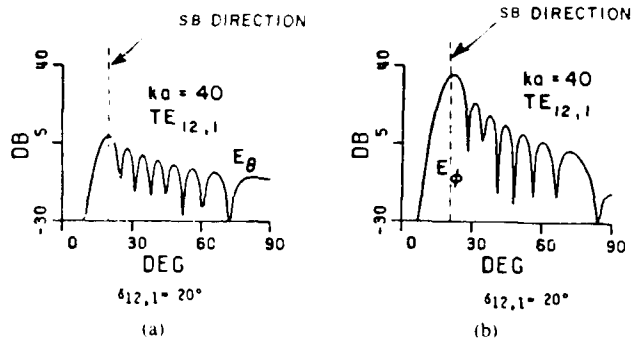
Fig. 6   Modal radiation from an open ended circular waveguide, as a function of elevation angle.

The modal ray representation can be obtained by applying the large argument approximation to the Bessel functions and each mode consists of two conical modal rays which converge onto and diverge from the axis of the waveguide [10]. The modal ray angle corresponding to the nmth mode is represented by δ_{nm} in Fig. 1(c). The expression for δ_{nm} is given in (57) of the Appendix.

A typical modal radiation pattern is shown in Fig. 6 based on the expressions given in (51) and (52) of the Appendix. The modal ray shadow boundary direction is also indicated in the figure and it is seen that modal radiation has a beam maximum in the modal ray direction.

D. The Sectoral Waveguide

The geometry of the sectoral waveguide is shown in Fig. 1(d). The nmth TE modal field expressions can be generated from the z-component of the magnetic field of that nmth mode which is given by [12]

$$H_z = \frac{1}{jkZ_0} k_t^2 \sin\left[\frac{n\pi}{a}\left(z+\frac{a}{2}\right)\right]$$

$$\cdot \cos\left[\frac{m\pi}{\phi_0}\left(\phi+\frac{\phi_0}{2}\right)\right] H_{m\pi/\phi_0}^{(2)}(k_t\rho) \quad (2)$$

where

$$k_t = \sqrt{k^2 - \left(\frac{n\pi}{a}\right)^2} \quad (3)$$

and similarly the nmth TM modal fields can be obtained from the z-component of the electric field of that nmth mode which is likewise given by [12]

$$E_z = \frac{1}{jk} k_t^2 \cos\left[\frac{n\pi}{a}\left(z+\frac{a}{2}\right)\right]$$

$$\cdot \sin\left[\frac{m\pi}{\phi_0}\left(\phi+\frac{\phi_0}{2}\right)\right] H_{m\pi/\phi_0}^{(2)}(k_t\rho) \quad (4)$$

where $H_\nu^{(2)}(k_t\rho)$ denotes a cylindrical Hankel function of the second kind of order ν ($= m\pi/\phi_0$ in this case) and of argument $k_t\rho$.

Using the Debye asymptotic form for the Hankel function in the region $k_t\rho > m\pi/\phi_0$, each mode can be decomposed into four ray-optical parts which follow zig-zag paths inside the sectoral waveguide [10].

The projection of the ray trajectories are depicted in Fig. 7, and they are tangent to the circular cylindrical modal ray caustic and oblique to the parallel walls of the waveguide. The radius of the circular modal ray caustic is given by

$$R = \frac{n\pi}{k\rho_0}. \quad (5)$$

Typical results of the numerical integration of the Kirchhoff-based aperture fields on the planar aperture of Fig. 1(d) are shown in Figs. 8 and 9. Fig. 8 is the modal radiation of the TE_{70} mode in the x-z plane. The modal ray shadow boundary directions of the TE_{70} mode in the x-z plane are also sketched in Fig. 8. As indicated in the figure, the peak of the radiation pattern coincides with the modal ray direction. Fig. 9 shows the modal radiation of the TM_{05} mode in the x-y plane. The TM_{05} modal ray shadow boundary directions in the x-y plane are also shown in Fig. 9. It is noted that due to the existence of nonparallel walls, the shadow boundaries of the modal rays are not parallel. Therefore, in this case, the dominant modal radiation beam is not too sharp and it smears out over the region corresponding to the angular separation between the incident shadow boundary (ISB) direction of one edge and the reflection shadow boundary (RSB) of the other (opposite) edge. Hence, the efficiency of the selective modal scheme is slightly reduced in the strongly tapered case as compared to the rectangular waveguide geometry which exhibits sharper modal radiation beams. The sharper the modal radiation beam, the less the number of modes required in the selective modal scheme.

It is also noted that a Ufimtsev-type correction to the AI can be obtained in a manner similar to that done for the case of rectangular waveguide; hence, these details are omitted here for the sake of brevity.

III. ELECTROMAGNETIC BACKSCATTERING FROM A CIRCULAR AND A WEAKLY TAPERED WAVEGUIDE CAVITY MODEL

In this section, the EM backscatter results are presented for a waveguide cavity model, and for a semi-infinite terminated circular waveguide. The backscatter returns have two main contributions. The energy coupled into the open-ended waveguide from the externally incident plane wave is reflected at an interior termination to radiate out of the open end; this constitutes the interior cavity contribution to the scattered field. The other contribution to the scattered field comes directly from the exterior diffraction of the incident wave by the rim edge at the open end. The interior radiation contribution to the scattered field is calculated through the analytical expressions developed in Section II; whereas, the rim scattering is calculated via the equivalent current method used in conjunction with the GTD [13]. For the short-circuited interior termination considered here, the interior cavity contribution to the scattered field is generally more significant; in this case, the rim scattering may be important when the cavity contribution exhibits a pattern minima.

The backscatter results obtained from a selective modal

$$\cos \psi_h = \left[\frac{k^2 - (\frac{n\pi}{a})^2 - (\frac{m\pi}{\rho_0 \phi_0})^2}{k^2 - (\frac{n\pi}{a})^2} \right]^{1/2}$$

MODAL RAY CAUSTIC

(a)

$$\cos \psi_v = \left[\frac{k^2 - (\frac{n\pi}{a})^2 - (\frac{m\pi}{\rho_0 \phi_0})^2}{k^2 - (\frac{m\pi}{\rho_0 \phi_0})^2} \right]^{1/2}$$

(b)
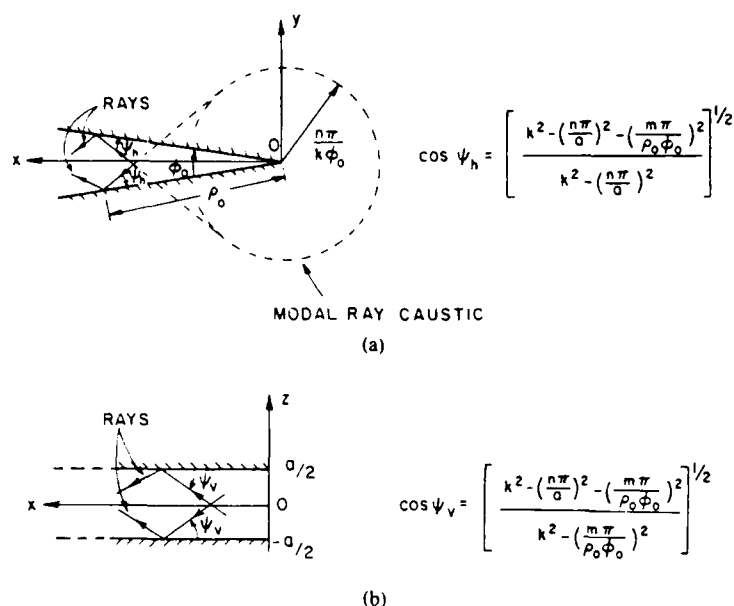
Fig. 7.   The projection of ray trajectories in a sectoral waveguide of Fig. 1(d). (a) Projection onto $x - y$ plane. (b) Projection onto $x - z$ plane.
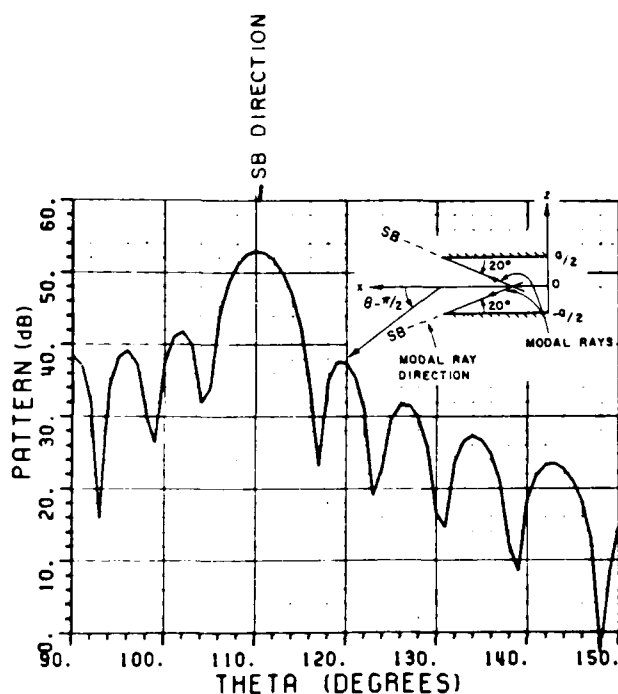
Fig. 8.   Modal radiation of TE$_{70}$ mode from the open end of a linearly tapered waveguide in the horizontal plane. $a = 10\lambda$, $\phi_0 = 20°$ and $\rho_0 = 14.4\lambda$

Fig. 9.   Modal radiation of TM$_{05}$ mode from the open end of a linearly tapered waveguide in the vertical plane. $a = 10\lambda$, $\phi_0 = 20°$, and $\rho_0 = 14.4\lambda$.

scheme approach are tested against the contribution of all modes. The numerical calculations on the cavity model is compared with the experimental results.

A. EM Backscattering from a Terminated Semi-Infinite Circular Waveguide

The calculations are presented in Figs. 10 and 11 for the EM backscattering from an open-ended semi-infinite perfectly conducting circular waveguide. The interior of the waveguide is terminated with a planar perfectly conducting short circuit.

The termination is placed ten free-space wavelengths away from the open end, as shown in Figs. 10 and 11; therefore, the effect of evanescent modes can be neglected. The radius of the waveguide is 3.34 free-space wavelengths which allows 115 modes to propagate. Figs. 10 and 11 illustrate the comparison of the backscattered field by including the contributions of all propagating modes versus those based on including only the modes whose modal ray angles are inside a 10° neighborhood of the observation direction.

In the graphs of Figs. 10 and 11, the effect of the multiple wave interactions between the open end and the termination are included in the calculations via the generalized scattering matrix technique (GSMT) [10], [14] with the use of modal reflection coefficients from the open end given in [10], and it
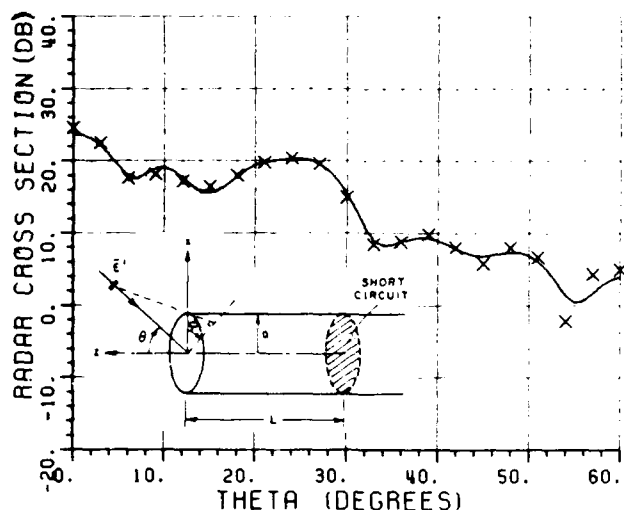
Fig. 10. Calculated backscattered field from a circular waveguide cavity in the $\phi = 0°$ plane cut as a function of the angle from the axis with the waveguide radius $a = 3.24\lambda$, termination position $L = 10\lambda$, $\bar{E}^i = \hat{\phi}E^i$. ——: all propagating modes included; xxxx: only modes with modal ray angles closer than 10° are included (normalized to πa^2).
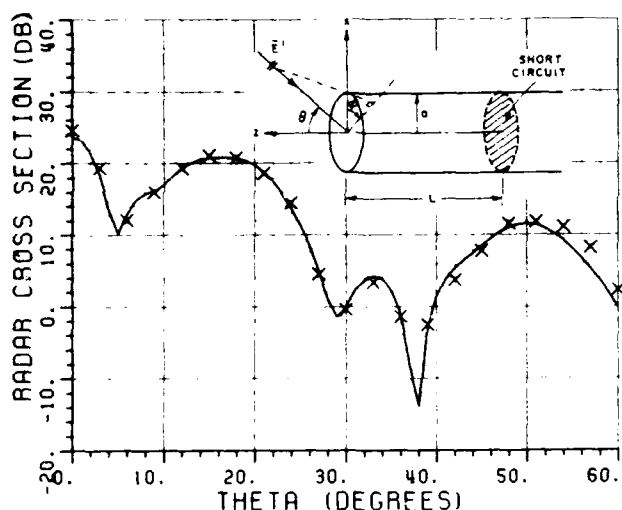
Fig. 11. Calculated backscattered field from a circular waveguide cavity in the $\phi = 0°$ plane cut as a function of the angle from the axis with the waveguide radius $a = 3.34\lambda$, termination position $L = 10\lambda$, $\bar{E}^i = \hat{\theta}E^i$. ——: All propagating modes included; xxxx: only modes with modal ray angles closer than 10° are included (normalized to πa^2).

Fig. 12. The geometry of the cavity model

is observed that the effect of all the higher order interactions between the open end and the terminations is small in comparison with the first-order interaction. Only for sufficiently smaller waveguides, the modal reflection from the open end is relatively strong in comparison with the aperture radiation; in such cases, the multiple interactions are expected to be stronger and hence they have been included via the GSMT in our computer code.
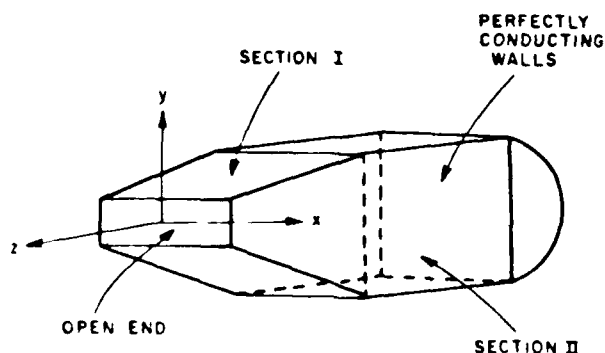
It is clear from these plots in Figs. 10 and 11 that by including only the few significant modes, one can substantially reduce the amount of calculations without seriously reducing the accuracy.

B. Electromagnetic Backscattering from a Weakly Tapered Waveguide Cavity Model

The tapered waveguide model is shown in Fig. 12. It is basically an open-ended cavity composed of two waveguide sections. The first section is part of a sectoral waveguide with one end open, whereas the other end of this section is connected to a second section which is a uniform waveguide with a planar termination at its far end. The exterior of the second section is curved at the back end to minimize the scattering coming from the exterior features of the structure. The model is made of wood and then coated with a conductive paint. The dimensions of the cavity are shown in Fig. 13. The length "L" is long enough for the effects of evanescent modes to be negligible.

The GTD-based equivalent current analysis for the rim scattering is compared with a set of measurements on the model. In order to remove the interior cavity effects, the inner surface of the back wall of the cavity is covered with absorbing material. The radar cross section (RCS) patterns in the $\phi = 0°$ and $\phi = 90°$ planes are shown in Figs. 14 and 15.

The interior cavity contribution to the scattered field is calculated using the modal coupling and radiation expressions of Section II. At 10 GHz, the first or the sectoral waveguide section containing the open end can accommodate 152 propagating modes. The analytical expression for these modes can be approximated to yield a propagation constant

$$\beta_{nm} = \sqrt{k^2 - \left(\frac{n\pi}{a}\right)^2 - \left(\frac{m\pi}{\rho\phi_0}\right)^2} \qquad (6)$$

inside the slightly tapered waveguide. In the uniform rectangular second section, these modes propagate with a propagation constant given by the dimensions of that section. The mode conversion due to the small discontinuity between two waveguide sections is ignored. From the time-domain results obtained from the swept frequency measurement in the 8–12-GHz band, the multiple interactions between the open end and the termination are determined to be small enough to be neglected here. Since the modal reflection from the open end (which is formed by half-planes) is expected to be much stronger than the modal reflection and coupling due to the join between the two sections (which forms a edge with wedge angle very close to 180°), the negligibility of these multiple interactions also implies that modal conversion is very weak. A 1-dB bounce energy loss for the modal rays is assumed to
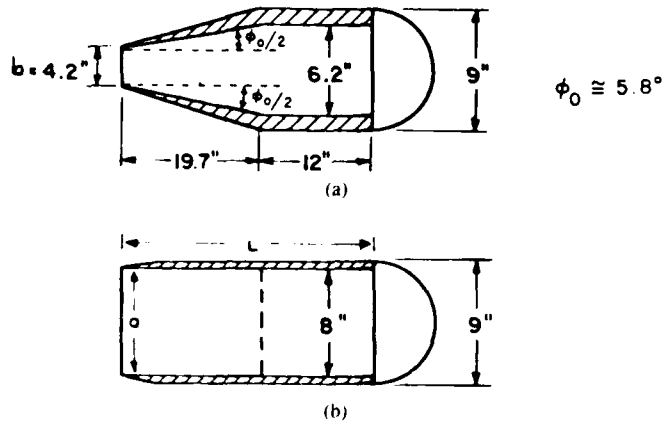
Fig. 13. Cavity model. (a) Side view. (b) Top view.
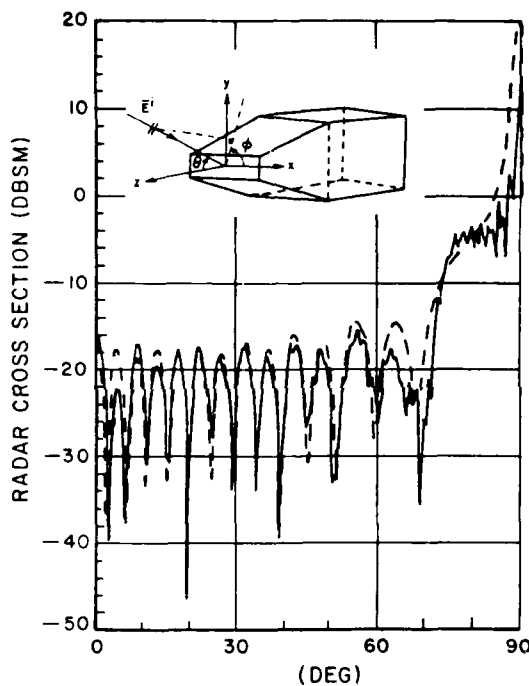
Fig. 14. Radar cross section pattern due to only the front end rim of the cavity structure at f = 9.98 GHz, $\bar{E}^i$ = $\hat{\phi}E^i$, ϕ = 0° plane. ———: measured; ———: calculated.

Fig. 15. Radar cross section pattern due to only the front end rim of the cavity structure at f = 9.98 GHz, $\bar{E}^i$ = $\hat{\phi}E^i$, ϕ = 90° plane. ———: measured; ———: calculated.

Fig. 16. Radar cross section pattern of the cavity structure at f = 10.00 GHz, $\bar{E}^i$ = $\hat{\phi}E^i$, ϕ = 0 plane. ———: measured; ———: calculated.

model the finite conductivity of the cavity model used in the measurements. The measured and calculated RCS patterns at 10 GHz are shown in Figs. 16 and 18 for the scans in ϕ = 0° and ϕ = 90° planes. The agreement between the measured and calculated results is poorer in the ϕ = 90° plane where the sectoral waveguide modes are excited for which the modal rays bounce from the tapered walls. The approximation to the propagation constant in the tapered waveguide gets worse especially for higher order modes. Also, in Figs. 17 and 19, the numerical calculations are compared by including the contributions of all modes versus only three selected modes. The modal ray directions of these three modes are closest to the backscattering direction. As explained earlier, selecting only three modes is a weaker approximation in the ψ = 90° plane than ϕ = 0° plane, because of the effect of the taper; the approximation can, of course, be improved by including just a
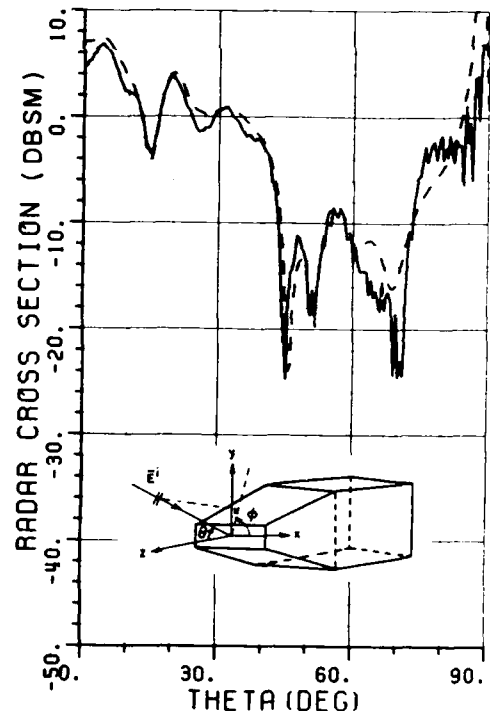
few more modes. Comparable accuracy is obtained at 8 and 12 GHz and for other polarizations.

Since this new selective modal scheme proved to be so valuable in the principal plane; namely, ϕ = 0 and ϕ = 90° planes, it is next applied to ϕ = 45° plane to ascertain its

Fig. 17.   Radar cross section pattern of the cavity structure at $f = 10.00$ GHZ. $\hat{E}^i = \hat{\phi}E^i$, $\phi = 0°$ plane. ——: all modes are included; xxxx: only three modes are included.
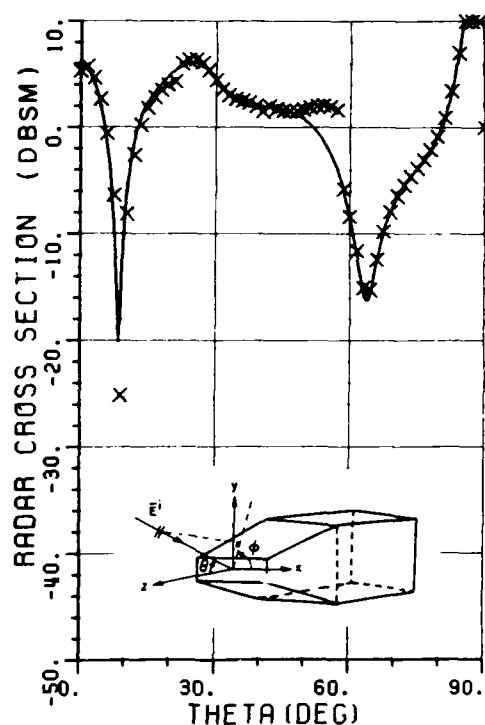
Fig. 19.   Calculated RCS pattern corresponding to Fig. 18. ——: all modes are included; xxxx: only three modes are included.
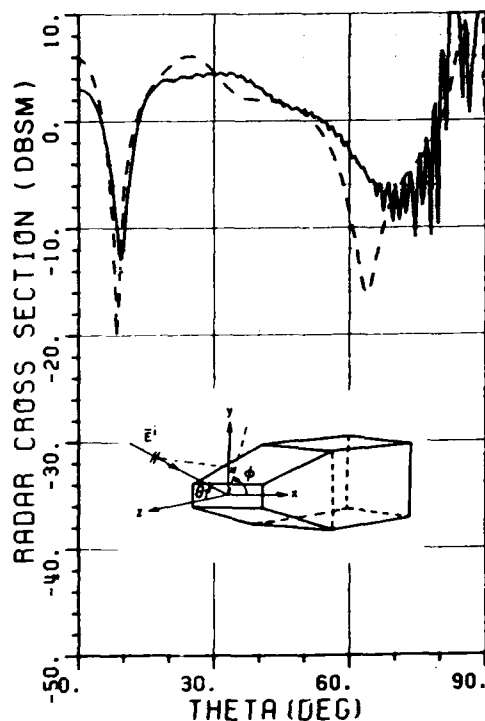
Fig. 18.   Radar cross section pattern at $f = 10.01$ GHz, $\hat{E}^i = \hat{\phi}E^i$, $\phi = 90°$ plane. ——: measured; ———: calculated.

Fig. 20.   Radar cross section pattern of the cavity structure at $f = 10.00$ GHz, $\hat{E}^i = \hat{\phi}E^i$, $\phi = 45°$ plane. ——: all 152 modes are included (86 TE, 66 TM modes); xxxx: only 18 modes are included (9 TE, 9 TM).

efficiency when the incident plane-wave direction is not aligned with the structural symmetry. The aspect angle scan is calculated in the $\phi = 45°$ plane for both the θ and ϕ polarized incident fields. The results are shown in Figs. 20 and 21. In this case, the 18 preselected modes are compared with the 152
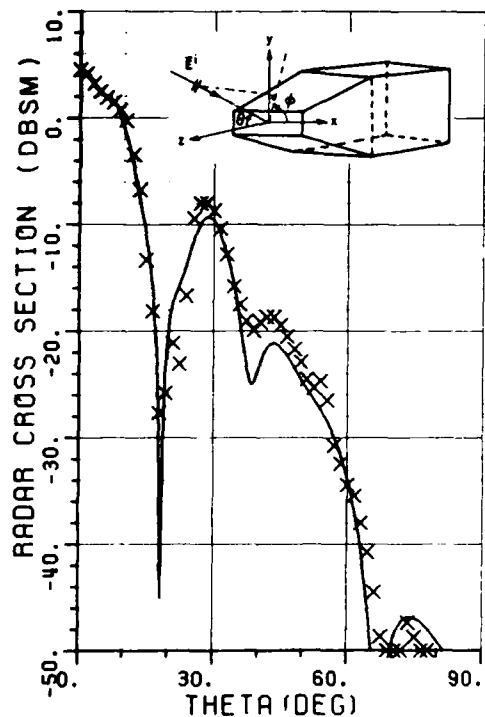
modes as shown in each figure. Note that more modes are needed in this general case as indicated by the results shown in Fig. 22 where the 6-mode result is compared with the one including 152 modes. Even so it is clear that one can use far fewer modes than the complete set of all the propagating modes.
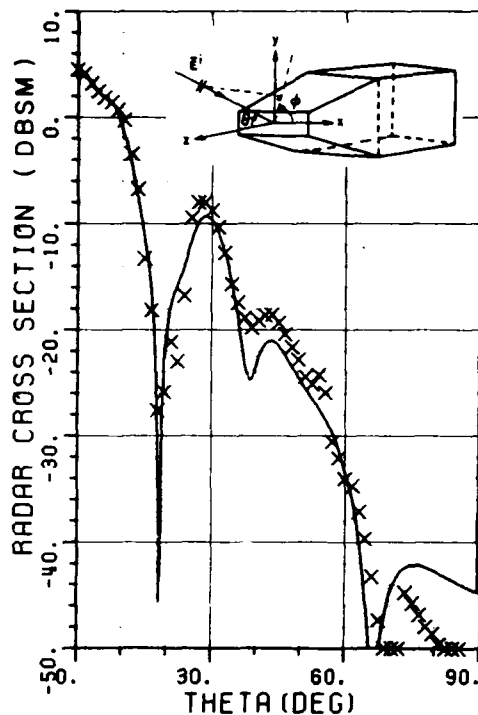
Fig. 21. Radar cross section pattern of the cavity structure at $f = 10.00$ GHz, $E^i = \theta E^i$, $\phi = 45°$ plane. ——: all 152 modes are included (86 TE, 66 TM modes); xxxx: only 18 modes are included (9 TE, 9 TM).
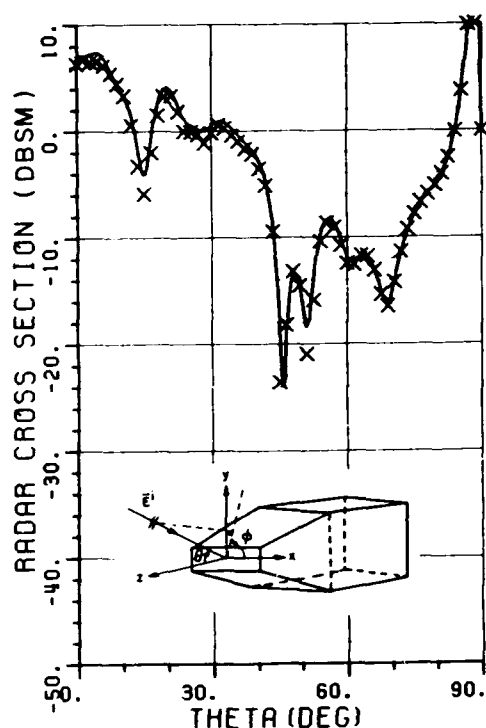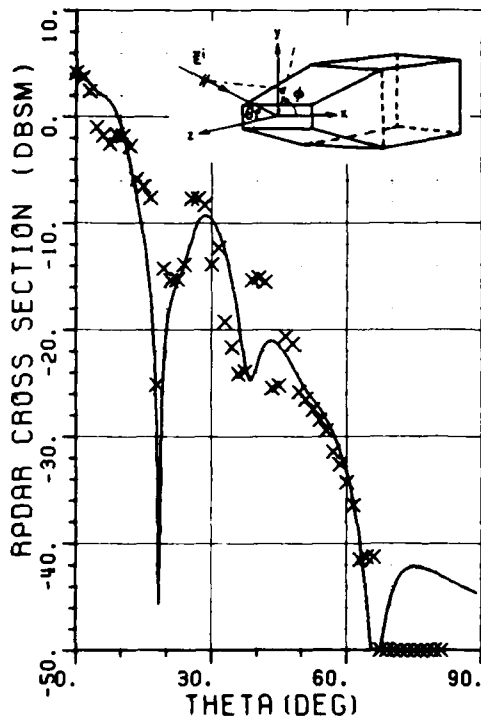

Fig. 22. Radar cross section pattern of the cavity structure at $f = 10.00$ GHz, $E^i = \theta E^i$, $\phi = 45°$ plane. ——: all 152 modes are included (86 TE, 66 TM modes); xxxx: only 6 modes are included (3 TE, 3 TM).

IV. CONCLUSION

It is shown here that an equivalent ray-optical representation of waveguide modes in terms of modal rays has an important implication which may be utilized to efficiently analyze the far-zone EM scattering by large open-ended waveguide

cavities. The procedure is to select and include in the analysis only those modes whose modal ray directions are closest to the incoming plane-wave illumination direction in the coupling problem. Analogously, in the radiation problem only those modes whose modal ray directions are closest to the observation direction are selected. The approach is illustrated on uniform waveguides such as parallel-plate, rectangular, and circular geometries as well as a nonuniform sectoral waveguide. In the case of uniform waveguides, the incident and reflection shadow boundary directions of modal rays shrink into a single direction which results in a sharper modal radiation beam. Generally, nonuniform waveguides require somewhat more modes to be included in the analysis as compared to the uniform case because of the existence of nonvanishing angular separation between the incident and reflection shadow boundary directions due to the taper. The procedure is especially useful at high frequencies where the usual modal analysis which includes all the propagating modes becomes cumbersome and inefficient, and where the existing rigorous and exact solutions are difficult to apply. Also, the procedure can be applied to the waveguide cavities formed by different waveguide sections. The discontinuities inside the waveguides may cause intermodal coupling as well as scattering. The multiple scattering effects can be taken into account using a GSMT approach. For backscattering problems, the interior cavity radiation contribution to the scattered field is still mainly dictated by the modes most strongly coupled into the waveguide. For bistatic scattering, the modes coupled most strongly into the waveguide are those whose modal ray angles are close to the angle of incidence; whereas, the modes which radiate most strongly from the interior cavity are those whose modal ray angles are close to the bistatic scattering aspect. Only in those special situations where the intermodal coupling at some interior termination or discontinuity is such that the reflection of the modes whose modal ray angles are close to the monostatic (bistatic) scattering aspect is very weak, then the interior cavity contribution to the scattered field from the other modes which are strongly excited by the discontinuity could become significant in the monostatic (bistatic) scattering direction, and hence their effect should be included.

APPENDIX

The Kirchhoff-based aperture integration approximation together with the Ufimtsev corrections for the far-zone modal radiation from the open-ended parallel-plate, rectangular and circular waveguides are given below. The waveguide geometries are depicted in Fig. 1. The normalized modal fields propagate in $+z$-direction in all cases. The Kirchhoff approximation to the radiated field is denoted by the subscript "k" and the Ufimtsev correction is shown by the subscript "u."

A. The Parallel-Plate Waveguide

The nth modal fields can be generated from the y-component of the fields of that nth mode which is given by

$$E_y = -N_n \sin\left(\frac{n\pi}{a} x\right) e^{-j\beta_n z}, \qquad \text{for TE modes} \quad (7)$$

$$H_y = N_n Y_n \cos\left(\frac{n\pi}{a} x\right) e^{-j\beta_n z}, \quad \text{for TM modes} \quad (8)$$

where

$$\beta_n = \left(k^2 - \left(\frac{n\pi}{a}\right)^2\right)^{1/2} \quad (9)$$

$$N_n = \frac{2}{(\epsilon_{0n} a Y_n)^{1/2}} \quad (10)$$

$$\epsilon_{0n} = \begin{cases} 2, & \text{for } n = 0 \\ 1, & \text{for } n \neq 0 \end{cases} \quad (11)$$

$$Y_n = \begin{cases} Y_0 \dfrac{\beta_n}{k}, & \text{for TE modes} \\[2ex] Y_0 \dfrac{k}{\beta_n}, & \text{for TM modes.} \end{cases} \quad (12)$$

The total far-zone radiated field is given by

$$\bar{E} = \bar{E}_k + \bar{E}_u \quad (13)$$

where the Kichhoff-based AI approximation is given by

$$\bar{E}_k = -\hat{y}(j)^n \frac{N_n e^{-j\pi/4}}{\sqrt{8\pi k\rho}} \left(\cos\theta + \frac{Y_n}{Y_0}\right)$$
$$\cdot [A_+ - (-1)^n A_-] e^{-jk(\rho - (a/2)\sin\theta)}, \quad \text{for TE modes} \quad (14)$$

$$\bar{E}_k = \hat{\theta}(j)^n \frac{N_n Y_0 e^{-j\pi/4}}{\sqrt{8\pi k\rho}} \left(1 + \frac{Y_n}{Y_0}\cos\theta\right)$$
$$\cdot [A_+ + (-1)^n A_-] e^{-jk(\rho - (a/2)\sin\theta)}, \quad \text{for TM modes} \quad (15)$$

in which

$$A_\pm = \frac{\sin\left[\dfrac{ka}{2}\left(\sin\theta \pm \dfrac{n\pi}{ka}\right)\right]}{\sin\theta \pm \dfrac{n\pi}{ka}}. \quad (16)$$

The Ufimtsev edge current contribution is given by

$$\bar{E}_u = -\hat{y}\frac{N_n}{2} e^{-j\pi/2}[D_s^u(\psi_n, \pi+\theta) - (-1)^n$$
$$\cdot D_s^u(\psi_n, \pi-\theta)e^{-jka\sin\theta}]\frac{e^{-jk\rho}}{\sqrt{\rho}}, \quad \text{for TE modes} \quad (17)$$

$$\bar{E}_u = \hat{\theta}\frac{N_n}{2}\frac{Y_n}{Y_0}[D_h^u(\psi_n, \pi+\theta) + (-1)^n$$
$$\cdot D_h^u(\psi_n, \pi-\theta)e^{-jka\sin\theta}]\frac{e^{-jk\rho}}{\sqrt{\rho}}, \quad \text{for TM modes} \quad (18)$$

where $D_{s \atop h}^u$ are the soft and hard Ufimtsev diffraction coefficients and in this case are the same as those obtained by subtracting the physical optics diffraction coefficients from the GTD diffraction coefficients for the case of a half-plane illuminated by a plane wave; namely,

$$D_{s \atop h}^u(\psi, \psi') = \frac{2e^{-j\pi/4}}{\sqrt{2\pi k}}\frac{\sin\dfrac{\psi}{2} - \cos\dfrac{\psi'}{2}}{\cos\psi + \cos\psi'}\begin{Bmatrix}\sin\dfrac{\psi'}{2} \\[2ex] \cos\dfrac{\psi}{2}\end{Bmatrix} \quad (19)$$

where the angle of incidence (ψ') and diffraction (ψ) are as shown in Fig. 23. The ψ' and ψ in the above expressions of (17) and (18) are measured from the interior of the waveguide for both half-planes.

B. The Rectangular Waveguide

The nmth modal fields of the rectangular waveguide can be obtained from the z-component of the fields of that nmth mode which is given by

$$H_z = N_{nm} Y_{nm} \frac{\left(\dfrac{n\pi}{a}\right)^2 + \left(\dfrac{m\pi}{b}\right)^2}{j\beta_{nm}}$$
$$\cdot \cos\left(\frac{n\pi}{a}x\right)\cos\left(\frac{m\pi}{b}y\right)e^{-j\beta_{nm}z} \quad (20)$$

for the TE modes and

$$E_z = -N_{nm} \frac{\left(\dfrac{n\pi}{a}\right)^2 + \left(\dfrac{m\pi}{b}\right)^2}{j\beta_{nm}}$$
$$\cdot \sin\left(\frac{n\pi}{a}x\right)\sin\left(\frac{m\pi}{b}y\right)e^{-j\beta_{nm}z} \quad (21)$$

for the TM modes.

The total far-zone radiated field is given by

$$\bar{E} = \hat{\theta}E_\theta + \hat{\phi}E_\phi \quad (22)$$

where

$$E_\theta = E_{\theta k} + E_{\theta u} \quad (23)$$

and

$$E_\phi = E_{\phi k} + E_{\phi u}. \quad (24)$$

The contribution from the AI approximation is given by [15]

$$E_{\theta k} = \frac{j^{n+m} N_{nm}}{4\pi kab}\frac{e^{-jkr}}{r}e^{(jk/2)(a\cos\phi b\sin\phi)\sin\theta}$$
$$\cdot \left\{u\cos\phi\left(1 + \frac{Y_{nm}}{Y_0}\cos\theta\right)\right.$$
$$\cdot [A_+ + (-1)^n A_-][B_+ - (-1)^m B_-]$$
$$- v\sin\phi\left(1 + \frac{Y_{nm}}{Y_0}\cos\theta\right)$$
$$\cdot [A_+ - (-1)^n A_-][B_+ + (-1)^m B_-]\bigg\} \quad (25)$$
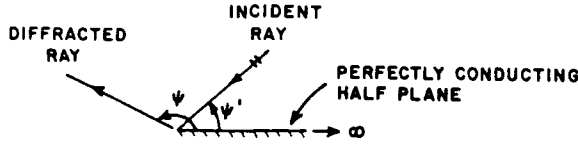
Fig. 23. Angle of incidence (ψ') and diffraction (ψ') for the half-plane geometry.

and

$$E_{\phi k} = \frac{j^{n+m} N_{nm}}{4\pi kab} \frac{e^{-jkr}}{r} e^{(jk/2)(a\cos\phi b\sin\phi)\sin\theta}$$

$$\cdot \left\{ -u\sin\phi \left(\cos\theta + \frac{Y_{nm}}{Y_0} \right) \right.$$

$$\cdot [A_+ + (-1)^n A_-][B_+ - (-1)^m B_-]$$

$$- v\cos\phi \left(\cos\theta + \frac{Y_{nm}}{Y_0} \right)$$

$$\left. \cdot [A_+ - (-1)^n A_-][B_+ + (-1)^m B_-] \right\} \quad (26)$$

in which

$$A_\pm = \frac{\sin\left[\frac{ka}{2} \left(\sin\theta\cos\phi \pm \frac{n\pi}{ka} \right) \right]}{\sin\theta\cos\phi \pm \frac{n\pi}{ka}} \quad (27)$$

$$B_\pm = \frac{\sin\left[\frac{kb}{2} \left(\sin\theta\sin\phi \pm \frac{m\pi}{kb} \right) \right]}{\sin\theta\sin\phi \pm \frac{m\pi}{kb}} \quad (28)$$

$$N_{nm} = 4 \left[2\epsilon_{0n}\epsilon_{0m} Y_{nm} ab \left\{ \left(\frac{n\pi}{a} \right)^2 + \left(\frac{m\pi}{b} \right)^2 \right\} \right]^{-1/2} \quad (29)$$

$$\beta_{nm} = \sqrt{ k^2 - \left(\frac{n\pi}{a} \right)^2 - \left(\frac{m\pi}{b} \right)^2 } \quad (30)$$

$$Y_{nm} = \begin{cases} Y_0 \dfrac{\beta_{nm}}{k}, & \text{for TE modes} \\[2mm] Y_0 \dfrac{k}{\beta_{nm}}, & \text{for TM modes} \end{cases} \quad (31)$$

$$u = \begin{cases} \dfrac{m\pi}{b}, & \text{for TE modes} \\[2mm] \dfrac{n\pi}{a}, & \text{for TM modes} \end{cases} \quad (32)$$

$$v = \begin{cases} \dfrac{n\pi}{a}, & \text{for TE modes} \\[2mm] -\dfrac{m\pi}{b}, & \text{for TM modes} \end{cases} \quad (33)$$

and ϵ_{0n} is as in (11). Likewise, the contributions to the radiated field from the equivalent Ufimtsev edge currents are given by [15]

$$E_{\theta u} = \frac{1}{\sqrt{8\pi jk}} N_{nm} \frac{e^{-jkr}}{kabr} e^{(jk/2)(a\cos\phi b\sin\phi)\sin\theta}$$

$$\cdot \theta \left\{ \frac{j^n}{\sin\beta_{0h}\sin\beta_h} [e^{-(jk/2)b\sin\theta\sin\phi} \right.$$

$$- (-1)^m e^{(jk/2)b\sin\theta\sin\phi}]$$

$$\cdot \left[D_s^u(\psi_h, \psi_h')u(A_+ + (-1)^n A_-)\cos\theta\cos\phi \right.$$

$$\left. - \frac{Y_{nm}}{Y_0} D_h^u(\psi_h, \psi_h')v(A_+ - (-1)^n A_-)\sin\phi \right]$$

$$+ \frac{j^m}{\sin\beta_{0v}\sin\beta_v} [e^{-(jk/2)a\sin\theta\cos\phi}$$

$$- (-1)^n e^{(jk/2)a\sin\theta\cos\phi}]$$

$$\cdot \left[-D_s^u(\psi_v, \psi_v')v(B_+ + (-1)^m B_-)\cos\theta\sin\phi \right.$$

$$\left. \left. + \frac{Y_{nm}}{Y_0} D_h^u(\psi_v, \psi_v')u(B_+ - (-1)^m B_-)\cos\phi \right] \right\} \quad (34)$$

and

$$E_{\phi u} = \frac{1}{\sqrt{8\pi jk}} N_{nm} \frac{e^{-jkr}}{kabr} e^{(jk/2)(a\cos\phi b\sin\phi)\sin\phi}$$

$$\cdot \left\{ \frac{-j^n}{\sin\beta_{0h}\sin\beta_h} [e^{-(jk/2)b\sin\theta\sin\phi} \right.$$

$$- (-1)^m e^{(jk/2)b\sin\theta\sin\phi}]$$

$$\cdot \left[D_s^u(\psi_h, \psi_h')u(A_+ + (-1)^n A_-)\sin\phi \right.$$

$$\left. + \frac{Y_{nm}}{Y_0} D_h^u(\psi_h, \psi_h')v(A_+ - (-1)^n A_-)\cos\theta\cos\phi \right]$$

$$- \frac{j^m}{\sin\beta_{0v}\sin\beta_v} [e^{-(jk/2)a\sin\theta\cos\phi}$$

$$- (-1)^n e^{(jk/2)a\sin\theta\cos\phi}]$$

$$\cdot \left[D_\zeta^u(\psi_v, \psi_v')v(B_+ + (-1)^m B_-)\cos\phi \right.$$

$$\left. \left. + \frac{Y_{nm}}{Y_0} D_h^u(\psi_v, \psi_v')u(B_+ - (-1)^m B_-)\cos\theta\sin\phi \right] \right\} \quad (35)$$

where u, v, $A_\pm$, $B_\pm$ are defined as before, and $D_{s_h}^u$ is given in (19), and

$$\cos\psi_h' = \frac{\beta_{nm}/k}{\sin\beta_{0h}} \quad (36)$$

$$\cos \psi_h = -\frac{\cos \theta}{\sin \beta_h} \tag{37}$$

$$\sin \beta_{0h} = [1 - (n\pi/ka)^2]^{1/2} \tag{38}$$

$$\sin \beta_h = (1 - \sin^2 \theta \cos^2 \phi)^{1/2} \tag{39}$$

$$\cos \psi_v' = \frac{\beta_{nm}/k}{\sin \beta_{0v}} \tag{40}$$

$$\cos \psi_v = -\frac{\cos \theta}{\sin \beta_v} \tag{41}$$

$$\sin \beta_{0v} = [1 - (m\pi/kb)^2]^{1/2} \tag{42}$$

$$\sin \beta_v = [1 - \sin^2 \theta \sin^2 \phi]^{1/2}. \tag{43}$$

C. The Circular Waveguide

The *nm*th modal fields of the circular waveguide can be obtained from the *z*-component of the fields of that mode which is given by

$$H_z = jN_{nm}' \left(\frac{p_{nm}'}{a}\right)^2 J_n\left(\frac{p_{nm}'\rho}{a}\right) \begin{Bmatrix} \cos n\phi \\ \sin n\phi \end{Bmatrix} e^{-j\beta_{nm}z},$$

for the TE modes (44)

and

$$E_z = jN_{nm} \left(\frac{p_{nm}}{a}\right)^2 J_n\left(\frac{p_{nm}\rho}{a}\right) \begin{Bmatrix} -\sin n\phi \\ \cos n\phi \end{Bmatrix} e^{-j\beta_{nm}z},$$

for the TM modes. (45)

In (44) and (45), $J_n(x)$ is the Bessel function of order n and $J_n'(x)$ is its derivative with respect to the argument x. The eigenvalues p_{nm} and p'_{nm} are the mth root of the equations

$$J_n(x) = 0 \tag{46}$$

and

$$J_n'(x) = 0 \tag{47}$$

respectively. The expressions for the propagation constants β_{nm} are

$$\beta_{nm} = \begin{cases} \sqrt{k^2 - \left(\frac{p_{nm}'}{a}\right)^2}, & \text{for TE modes} \\ \sqrt{k^2 - \left(\frac{p_{nm}}{a}\right)^2}, & \text{for TM modes.} \end{cases} \tag{48}$$

The normalization constants are given by

$$N_{nm} = \begin{cases} \dfrac{2}{J_n(p_{nm}')\sqrt{\pi k Z_0 \beta_{nm}(p_{nm}'^2 - n^2)}}, & \text{for TE modes} \\ \dfrac{2}{p_{nm}J_n'(p_{nm})\sqrt{\pi k Y_0 \beta_{nm}\epsilon_{0n}}}, & \text{for TM modes} \end{cases} \tag{49}$$

wit'ı ϵ_{0n} as in (11).

The far-zone radiated electric field $\vec{E}$ can be written as

$$\vec{E} = \left[\hat{\theta}E_\theta \begin{pmatrix} -\sin n\phi \\ \cos n\phi \end{pmatrix} + \hat{\phi}E_\phi \begin{pmatrix} \cos n\phi \\ \sin n\phi \end{pmatrix} \right] \frac{e^{-jkr}}{r} \tag{50}$$

where E_θ and E_ϕ can be further separated as

$$E_\theta = E_{\theta k} + E_{\theta u} \tag{51}$$

and

$$E_\phi = E_{\phi k} + E_{\phi u}. \tag{52}$$

The contribution from the Kirchhoff-based AI approximation becomes [16]

$$E_{\theta k} = j^n k Z_0 N_{nm} n \frac{1 + \cos \theta \cos \delta_{nm}}{2 \sin \theta} J_n(p_{nm}') J_n(ka \sin \theta) \tag{53}$$

$$E_{\phi k} = j^n k Z_0 N_{nm} p_{nm}' \frac{\sin \delta_{nm}}{2(\cos \delta_{nm} - \cos \theta)} J_n(p_{nm}') J_n'(ka \sin \theta) \tag{54}$$

for the TE modes, and

$$E_{\theta k} = j^n k N_{nm} p_{nm} \frac{\sin \theta}{2(\cos \delta_{nm} - \cos \theta)} J_n'(p_{nm}) J_n(ka \sin \theta) \tag{55}$$

$$E_{\phi k} = 0 \tag{56}$$

for the TM modes. In (53)–(55), δ_{nm} is the modal ray angle and is given by

$$\delta_{nm} = \cos^{-1}(\beta_{nm}/k). \tag{57}$$

The contribution from the equivalent Ufimtsev edge currents can be approximated in the following form [16]:

$$E_{\theta u} = j^n Z_0 N_{nm} n f(\theta, \delta_{nm}) J_n(p_{nm}')$$

$$\cdot \left[\beta_{nm} \sin\left(\frac{\theta}{2}\right) J_n''(ka \sin \theta) \right.$$

$$\left. - k p_{nm}' \sin\left(\frac{\delta_{nm}}{2}\right) \frac{\cos \theta}{ka \sin \theta} J_n(ka \sin \theta) \right] \tag{58}$$

$$E_{\phi u} = j^n Z_0 N_{nm} n f(\theta, \delta_{nm}) J_n(p_{nm}')$$

$$\cdot \left\{ k p_{nm}' \sin\left(\frac{\delta_{nm}}{2}\right) J_n'(ka \sin \theta) \right.$$

$$- n^2 \beta_{nm} \sin\left(\frac{\theta}{2}\right) \frac{\cos \theta}{ka \sin \theta} \left[J_n'(ka \sin \theta) \right.$$

$$\left. \left. - \frac{J_n(ka \sin \theta)}{ka \sin \theta} \right] \right\} \tag{59}$$

for the TE modes and

$$E_{\theta u} = j^n N_{nm} f(\theta, \delta_{nm}) J_n'(p_{nm})$$

$$\cdot \left[n^2 \beta_{nm} \sin\left(\frac{\delta_{nm}}{2}\right) \frac{\cos\theta}{ka\sin\theta} J_n(ka\sin\theta) \right.$$

$$\left. + kp_{nm} \sin\left(\frac{\theta}{2}\right) J_n''(ka\sin\theta) \right] \qquad (60)$$

$$E_{\phi u} = -j^n N_{nm} n f(\theta, \delta_{nm}) J_n'(P_{nm})$$

$$\cdot \left\{ \beta_{nm} \sin\left(\frac{\delta_{nm}}{2}\right) J_n'(ka\sin\theta) \right.$$

$$+ kp_{nm} \sin\left(\frac{\theta}{2}\right) \frac{\cos\theta}{ka\sin\theta} \left[J_n'(ka\sin\theta) \right.$$

$$\left. \left. - \frac{J_n(ka\sin\theta)}{ka\sin\theta} \right] \right\} \qquad (61)$$

for the TM modes, where

$$f(\theta, \delta_{nm}) = \frac{\cos\left(\frac{\theta}{2}\right) - \cos\left(\frac{\delta_{nm}}{2}\right)}{\cos\delta_{nm} - \cos\theta} \qquad (62)$$

for both the TE and TM cases.

ACKNOWLEDGMENT

REFERENCES

[1] P. H. Pathak and A. Altıntaş, "An efficient approach for analyzing the EM coupling into large open-ended waveguide cavities," presented at URSI North Am. Radio Sci. Meet., Vancouver, Canada, June 1985.

[2] L. Grun and S. W. Lee, "Transmission into staggered parallel-plate waveguides," IEEE Trans. Antennas Propagat., vol. AP-30, no. 1, pp. 35–43, Jan. 1982.

[3] H. Y. Yee, L. B. Felsen, and J. B. Keller, "Ray theory of reflection from the open end of a waveguide," SIAM J. App. Math., vol. 16, no. 2, pp. 268–300, 1968.

[4] S. W. Lee, "Ray theory of diffraction by open ended waveguides I. fields in waveguides," J. Math. Phys., vol. 11, no. 9, pp. 2830–2850, Sept. 1970.

[5] —, "Ray theory of diffraction by open-ended waveguides, II. Applications," J. Math. Phys., vol. 13, no. 5, pp. 656–664, May 1972.

[6] S. W. Lee and J. Boersma, "Ray-optical analysis of fields on shadow boundaries of two parallel plates," J. Math., Phys., vol. 16, no. 9, pp. 1746–1764, Sept. 1975.

[7] J. B. Keller, "Geometrical theory of diffraction," J. Opt. Soc. Am., vol. 52, pp. 116–130, 1962.

[8] P. Ya Ufimtsev, "Method of edge waves in the physical theory of diffraction," (from the Russian "Method krayevykh voin v frizicheskoy teorii diffraksii," Izd-Vo Sov. Radio, pp. 1–243, 1962) translation prepared by the U.S. Air Force Foreign Technology Division, Wright-Patterson AFB, Ohio; released for public distribution, Sept. 7, 1971.

[9] P. H. Pathak, "Techniques for high frequency problems," in Handbook of Antenna Theory and Design, Y. T. Lo and S. W. Lee, Eds. New York: Van Norstrand Reinhold, to appear.

[10] A. Altıntaş, "Electromagnetic Scattering from a Class of Open-Ended Waveguide Discontinuities," Ph.D. dissertation, Dept. Elec. Eng., Ohio State Univ., Columbus, Mar. 1986.

[11] L. A. Weinstein, The Theory and Diffraction and the Factorization Method. Boulder, CO: Golem, 1969.

[12] R. F. Harrington, Time Harmonic Electromagnetic Fields. New York: McGraw-Hill, 1961.

[13] C. E. Ryan and L. Peters, Jr., "Evaluation of edge-diffracted fields including equivalent currents for the caustic regions," IEEE Trans. Antennas Propagat., vol. AP-17, no. 3, pp. 292–299, May 1969.

[14] R. Mittra and S. W. Lee, Analytical Techniques in the Theory of Guided Waves. New York: Macmillan, 1971.

[15] P. H. Pathak, C. W. Chuang, and M. C. Liang, "Inlet modeling studies," ElectroSci. Lab., Ohio State Univ., for Naval Weapons Center, China Lake, CA, Contract N60530-85-C-0249, Final Rep. 717674-1, Oct. 1986.

[16] P. H. Pathak and C. W. Chuang, "Continuation of work on near and far field scattering by rectangular and circular inlet configurations with an impedance surface termination," Dept. Navy, Naval Weapons Center, China Lake, CA, Contract N60530-84-C-0143, Final Rep. 715979-1, Aug. 1985.

Ayhan Altıntaş received the B.S. and M.S. degrees in from the Middle East Technical University, Ankara, Turkey in 1979 and 1981, respectively, and the Ph.D. degree in from The Ohio State University, Columbus, in 1986, all in electrical engineering.

From 1981 to 1986, he was a graduate research associate with ElectroScience Laboratory, the Department of Electrical Engineering, The Ohio State University, and from March 1986 to February 1987 he continued to work there as a post-doctoral researcher. He was a post-doctoral researcher in the Department of Applied Mathematics at the Australian National University, Canberra, Australia, until January 1988, and is now at the Bilkent University, Ankara, Turkey. His current interests are in the mathematical modeling and analysis of electromagnetic radiation and scattering problems using both, high and low frequency methods.

Dr. Altıntaş is a member of Sigma Xi and Phi Kappa Phi.

Prabhakar H. Pathak (M'76–SM'81–F'86), for a photograph and biography please see page 4 of this issue.

Ming-Cheng Liang, for a photograph and biography please see page 286 of the March 1987 issue of this transaction.

The Relationship Between Tapped Delay-Line and FFT

Processing in Adaptive Arrays

R. T. Compton, Jr.

The Relationship Between Tapped Delay-Line and FFT Processing in Adaptive Arrays

R. T. COMPTON, JR., FELLOW, IEEE

Abstract—The use of fast Fourier transform (FFT) processing behind the elements in adaptive arrays is often considered as a means of improving the nulling bandwidth of such arrays. However, it is shown here that the output signal-to-interference-plus-noise ratio (SINR) obtained from an adaptive array with FFT's behind the elements is identical to that of an equivalent adaptive array with tapped delay-line processing. The equivalent tapped delay-line array has the same number of taps in each delay-line as the number of time samples in the FFT's, and has a delay between taps equal to the delay between samples in the FFT's. Thus, while the bandwidth performance of an adaptive array can be improved by using time delayed samples of each element signal, no further improvement results from taking FFT's of these sampled signals. The same bandwidth performance is obtained by simply weighting and combining the time domain samples directly.

I. INTRODUCTION

AN IMPORTANT PROBLEM with adaptive arrays [1], [2] is that their performance deteriorates with interference bandwidth. The wider the bandwidth of an interference signal, the more difficult it is for an adaptive array to null it [3]-[7].

Fig. 1 illustrates this problem. It shows the output signal-to-interference-plus-noise ratio (SINR) achieved by a two element adaptive array when an interference signal arrives from angle θ_i measured from broadside. The figure is calculated for two isotropic elements a half-wavelength apart, a desired signal with 0 dB signal-to-noise ratio (SNR) per element arriving from broadside ($\theta_d = 0^\circ$), and interference with a 40 dB interference-to-noise ratio (INR) per element. The SINR is shown for several values of relative bandwidth B, the ratio of the absolute bandwidth to the center frequency. As may be seen, for $B = 0.02$ the output SINR has dropped about 3 dB below its value for $B = 0$. Larger bandwidths cause increasingly more degradation.

When the bandwidth performance of an adaptive array is inadequate, three methods exist for improving its performance:

1) using more elements in the array,
2) using tapped delay-lines behind the elements, and
3) using fast Fourier transforms (FFT's) behind the elements.
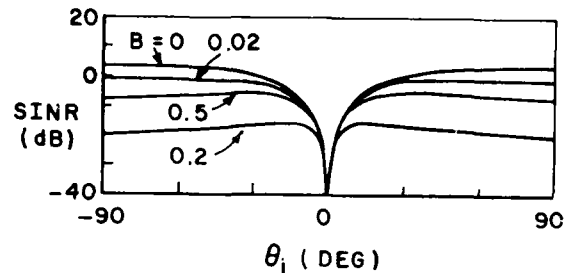
Fig. 1. SINR versus θ_i: two-element array, one weight per element, $\theta_d = 0^\circ$, SNR = 0 dB, INR = 40 dB.

Let us compare the performance obtained with each of these approaches.

First, suppose we add more elements to the array. Fig. 2 shows the SINR for arrays with three, five, ten, or twenty elements, instead of two as in Figs. 1. (Each array is a linear array with half-wavelength spacing between elements. All other parameters are the same as in Fig. 1.) For each array, the SINR is shown for $B = 0$ and $B = 0.2$. As may be seen by comparing Figs. 1 and 2, adding elements does improve the SINR. However, it is interesting that no matter how many elements are used, there is always a region for θ_i near θ_d where the SINR for $B = 0.2$ is poorer than for $B = 0$.

The second way to improve bandwidth performance is to use a tapped delay-line behind each element. (For Figs. 1 and 2, a single complex weight was assumed behind each element.) Fig. 3 shows a two-element array with a two-tap delay line behind each element. Fig. 4 shows the output SINR versus θ_i achieved by this array for $B = 0.2$ when each delay is a quarter wavelength. (The other parameters are the same as in Fig. 1.) Comparing Fig. 4 with Fig. 1 shows that the delay lines have fully overcome the bandwidth degradation. The performance for $B = 0.2$ in Fig. 4 is just as good as that for $B = 0$ in Fig. 1.

A third method for improving bandwidth performance is to use an FFT behind each element of the array, with a separate weight on each frequency bin. This approach is shown in Fig. 5. At the output of each element, and A/D converter takes samples of the received signal. When K samples are available from each element, these samples are transformed with an FFT. The FFT produces K frequency domain samples of each element output. Each frequency domain sample is multiplied by a weight and then added to the corresponding frequency samples from other elements. Finally, the inverse FFT (IFFT) is taken of the frequency domain samples to obtain the time-domain array output samples.
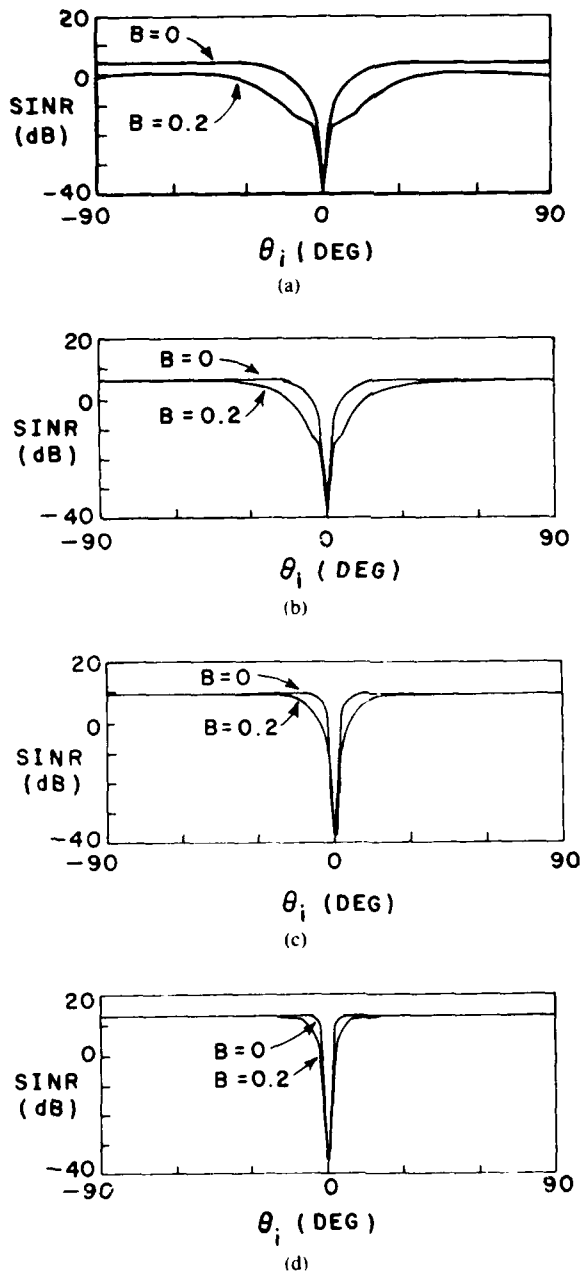
Fig. 2. SINR versus θ_i: One weight per element, $\theta_d = 0°$, SINR = 0 dB, INR = 40 dB. (a) Three elements. (b) Five elements. (c) Ten elements. (d) Twenty elements.

Fig. 3. A two-element array with two-tap delay lines.

Fig. 4. SINR versus θ_i: two-element array, two-taps per element, $\theta_d = 0°$, SNR = 0 dB, INR = 40 dB.

Fig. 5. An array with FFT processing.

The use of FFT's behind the elements has a certain intuitive appeal as a method of improving array bandwidth performance. In effect, the FFT divides the signal bandwidth into smaller subbands. (For this reason, this technique is sometimes called *frequency subbanding*.) With a separate weight on each frequency bin, the array can compensate differently in each frequency subband.

Unfortunately, calculations of array output SINR for FFT processing often show poorer performance than that obtained with tapped delay lines. Fig. 6 shows a typical set of results. It shows the output SINR from the same two-element array as in Fig. 1, but with a K-point FFT behind each element. The curves are computed for the same bandwidth, $B = 0.2$, and for a sampling interval that makes one period of the FFT

frequency response equal to the signal bandwidth. The SINR is shown for K = two, four, eight and sixteen samples in the FFT's. As may be seen, the performance does improve with K, but even for $K = 16$ it is not as good as the performance for tapped delay lines with only two taps, as seen in Fig. 3. Thus, in spite of the intuitive appeal of FFT's, their performance can be disappointing.

The present study was done in an effort to understand the relationship between tapped delay-line and FFT processing in
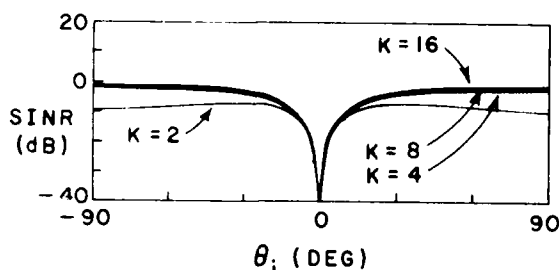
Fig. 6. SINR versus θ_i; two-element array. K-point FFTS. $B = 0.2$, $\theta_d = 0°$, SNR = 0 dB, INR = 40 dB.

adaptive arrays. The study was motivated by the fact that there seemed to be no apparent reason why FFT performance should be poorer than tapped delay-line performance.

What we shall show is that inserting an FFT between the delay-line taps and the weights in an adaptive array in fact has *no effect* on the output SINR. The performance differences noted above between the two approaches are simply due to the use of different time delays between samples or different numbers of samples in each case. When a tapped delay-line array and an FFT array use *the same time between samples and the same number of samples*, their performance is identical.

We proceed as follows. In Section II, we show that inserting any linear, invertible transformation between the delay-line taps and the weights in an adaptive array has no effect on either the output signal or the output SINR. We prove this result for both the least mean square (LMS) array and the Applebaum array. (For the Applebaum array, the proof holds only if the steering vector is transformed in the appropriate way.) Then in Section III, we show that using FFT's in an array simply inserts a linear invertible transformation between the delay-line taps and the weights. Taken together, these results show that the performance of FFT processing is identical to that of tapped delay-line processing. Finally, in Section IV we consider some related questions: the effect of FFT processing on the array weights and the covariance matrix eigenvalue spread. We also discuss how tapped delay-line and FFT parameters are usually chosen, and point out how these choices result in the performance differences between the two methods noted above. Section V contains our conclusions.

II. A SIMPLE PROPERTY OF ADAPTIVE ARRAYS

In this section we show that inserting an arbitrary invertible linear transformation between the delay line taps and the weights in an adaptive array has no effect on either the output signal or the output SINR. We prove this result for LMS arrays in Section II-A and for Applebaum arrays in Section II-B. For Applebaum arrays, the steering vector must be transformed in the proper way along with the signals for the theorem to hold.

A. The LMS Array

Consider an adaptive array with M elements, as shown in Fig. 7. Assume each element is followed by a tapped delay-line with K taps and a delay of T_0 seconds between taps. The output of the first tap behind each element is the element signal
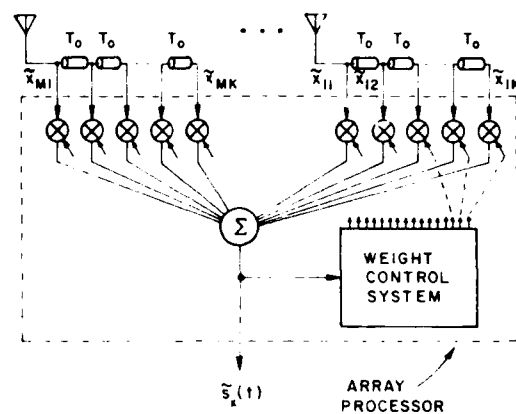
Fig. 7. An M-element array.

itself, with no delay. Let $\tilde{x}_{mk}(t)$ denote the (analytic) signal from element m at tap k. Then $\tilde{x}_{m1}(t)$ is the signal received on element m, and

$$\tilde{x}_{mk}(t) = \tilde{x}_{m1}(t - [k-1]T_0). \qquad (1)$$

We suppose the $\tilde{x}_{mk}(t)$ are used as inputs to an LMS adaptive array processor [1]. This processor multiplies each $\tilde{x}_{mk}(t)$ by a complex weight w_{mk} and then adds the weighted signals to produce the array output $\tilde{s}_x(t)$, as shown in Fig. 7. The processor uses LMS feedback loops [1] or an equivalent technique [8] to set the weights to their optimal values. These weights maximize SINR at the array output [9].

For a given set of tap signals $\tilde{x}_{mk}(t)$, the optimal weights may be calculated as follows. Let $X_m(t)$ and W_m (with $1 \le m \le M$) be column vectors containing the signals and weights at the K taps behind element m.

$$X_m(t) = [\tilde{x}_{m1}(t), \tilde{x}_{m2}(t), \cdots, \tilde{x}_{mK}(t)]^T, \qquad (2)$$

and

$$W_m = [w_{m1}, w_{m2}, \cdots, w_{mK}]^T. \qquad (3)$$

(Superscript T denotes transpose.) We refer to $X_m(t)$ as the element signal vector and to W_m as the element weight vector. Then let $X(t)$ and W be the *total* signal and weight vectors for the entire array,

$$X(t) = \begin{bmatrix} X_1(t) \\ -- \\ X_2(t) \\ -- \\ \vdots \\ -- \\ X_M(t) \end{bmatrix}. \qquad (4)$$

and

$$W = \begin{bmatrix} W_1 \\ -- \\ W_2 \\ -- \\ \vdots \\ -- \\ W_M \end{bmatrix}, \qquad (5)$$

where we use a partitioned vector notation. The optimal weight vector in the array is then given by [1], [2]

$$W = \Phi_x^{-1} S_x, \tag{6}$$

where Φ_x is the signal covariance matrix,

$$\Phi_x = E[X^* X^T], \tag{7}$$

and S_x is the reference correlation vector,

$$S_x = E[X^* \tilde{r}(t)]. \tag{8}$$

In these equations, the asterisk denotes complex conjugate and $\tilde{r}(t)$ is the reference signal [1]. We assume the signals $\tilde{x}_{mk}(t)$ as well as $\tilde{r}(t)$ are all jointly stationary random processes, so Φ_x and S_x do not depend on t. With the weight vector W given by (6), the array output signal is

$$\tilde{s}_x(t) = X^T(t) W = X^T(t) \Phi_x^{-1} S_x. \tag{9}$$

Now consider the following alternative situation. Suppose that, instead of using the signals $\tilde{x}_{mk}(t)$ as inputs to the processor, we first combine them in some manner to produce a new set of signals $\tilde{y}_{mk}(t)$, where $1 \leq m \leq M$ and $1 \leq k \leq K$. Specifically, suppose Y_m is the K-component vector

$$Y_m = [\tilde{y}_{m1}(t), \tilde{y}_{m2}(t), \cdots, \tilde{y}_{mK}(t)]^T, \tag{10}$$

and Y is the MK-component vector,

$$Y(t) = \begin{bmatrix} Y_1 \\ -- \\ Y_2 \\ -- \\ \vdots \\ -- \\ Y_M \end{bmatrix}. \tag{11}$$

Then let us assume that

$$Y(t) = TX(t), \tag{12}$$

where T is an $MK \times MK$ matrix of constants. Thus, each $\tilde{y}_{mk}(t)$ is a linear combination of the $\tilde{x}_{mk}(t)$. Now let us use the $\tilde{y}_{mk}(t)$ as inputs to the same LMS processor as before. Fig. 8 shows the new arrangement with transformation T between the $\tilde{x}_{mk}(t)$ and the $\tilde{y}_{mk}(t)$. For this case, we denote the mkth array weight by u_{mk}, to distinguish it from w_{mk} in Fig. 7.

With the signals $\tilde{y}_{mk}(t)$ as inputs, the LMS processor will produce optimal weights given by

$$U = \Phi_y^{-1} S_y, \tag{13}$$

where U is the new weight vector,

$$U = [u_{11}, u_{12}, \cdots, u_{21}, \cdots, u_{MK}]^T, \tag{14}$$

Φ_y is the covariance matrix associated with the signals $\tilde{y}_{mk}(t)$,

$$\Phi_y = E[Y^*(t) Y^T(t)], \tag{15}$$

and S_y is the reference correlation vector for the signals $\tilde{y}_{mk}(t)$,

$$S_y = E[Y^*(t) \tilde{r}(t)]. \tag{16}$$
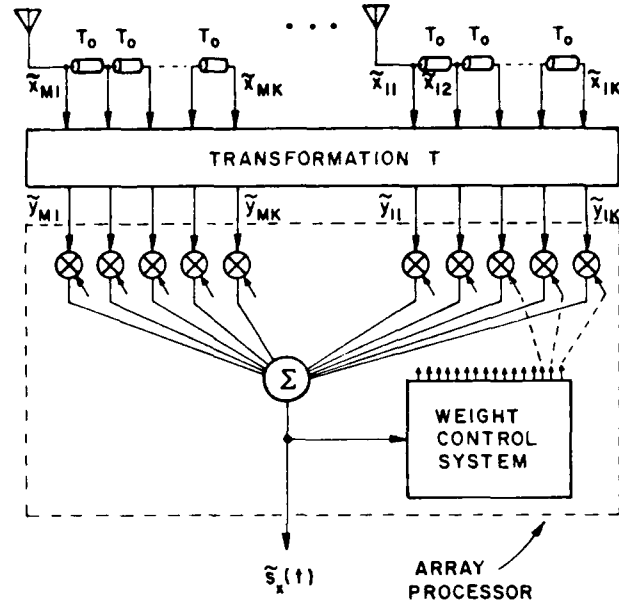
Fig. 8. A tapped delay-line array with transformation T.

$\tilde{r}(t)$ is the same reference signal as in (8). The array output signal for this case $\tilde{s}_y(t)$ is

$$\tilde{s}_y(t) = Y^T(t) U = Y^T(t) \Phi_y^{-1} S_y. \tag{17}$$

Now it is easy to show that if T is invertible $\tilde{s}_y(t)$ and $\tilde{s}_x(t)$ are in fact identical signals. Substituting (12) into (15) and (16), and using (7) and (8), we find

$$\Phi_y = E[Y^*(t) Y^T(t)] = E[T^* X^*(t) X^T(t) T^T] = T^* \Phi_x T^T, \tag{18}$$

and

$$S_y = E[Y^*(t) \tilde{r}(t)] = E[T^* X^*(t) \tilde{r}(t)] = T^* S_x. \tag{19}$$

If T is invertible (i.e., nonsingular), $\tilde{s}_y(t)$ in (17) reduces to

$$\begin{aligned} \tilde{s}_y(t) &= Y^T(t) \Phi_y^{-1} S_y \\ &= X^T(t) T^T [T^* \Phi_x T^T]^{-1} T^* S_x \\ &= X^T(t) \Phi_x^{-1} S_x \\ &= \tilde{s}_x(t). \end{aligned} \tag{20}$$

Furthermore, the output SINR is the same for the two arrays. Substituting (18) and (19) into (13) shows that the weight vectors U and W are related by

$$\begin{aligned} U &= [T^* \Phi_x T^T]^{-1} T^* S_x \\ &= [T^T]^{-1} \Phi_x^{-1} S_x \\ &= [T^T]^{-1} W. \end{aligned} \tag{21}$$

Consider, for example, the output desired signal. Suppose $X_d(t)$ is the desired signal part of signal vector $X(t)$ and $Y_d(t)$ is the desired signal part of $Y(t)$. Then

$$Y_d(t) = TX_d(t). \tag{22}$$

The array output desired signal in Fig. 7 is

$$\tilde{s}_{x_d}(t) = X_d^T(t) W,\qquad (23)$$

whereas the output desired signal in Fig. 8 is

$$\tilde{s}_{y_d}(t) = Y_d^T U.\qquad (24)$$

However, using (21) and (22) in (24) gives

$$\tilde{s}_{y_d}(t) = [TX_d(t)]^T [T^T]^{-1} W = \tilde{s}_{x_d}(t).\qquad (25)$$

Thus, the arrays in Figs. 7 and 8 have identical output desired signals, and hence identical output desired signal powers. A similar argument shows that the output interference and thermal noise powers are also identical for the two arrays. From this it follows that the output SINR is the same in Figs. 7 and 8.

Thus, inserting a linear transformation T between the elements and the processor, as in Fig. 8, has no effect on the output signal or the output SINR. The only requirement for this result to hold is that the transformation be invertible.

B. The Applebaum Array

Now suppose the array processor in Fig. 7 uses Applebaum control loops [2] or an equivalent technique [8] to set the weights w_{mk}. Applebaum control loops use a steering vector instead of a reference signal to point the array beam at the desired signal. With Applebaum loops, the steady-state weight vector in the array will be [2]

$$W = \mu \Phi_x^{-1} V\qquad (26)$$

where μ is an arbitrary (nonzero) gain constant and V is the steering vector. The array output signal will be

$$\tilde{s}_x(t) = X^T W = \mu X^T(t) \Phi_x^{-1} V.\qquad (27)$$

Now suppose a transformation T is inserted between the signals $\tilde{x}_{mk}(t)$ and the Applebaum processor, as in Fig. 8. Let the processor now have a new steering vector Q. The steady-state weight vector in this case is

$$U = \mu \Phi_y^{-1} Q.\qquad (28)$$

If (18) is substituted for Φ_y, (28) becomes

$$U = \mu [T^T]^{-1} \Phi_x^{-1} [T^*]^{-1} Q,\qquad (29)$$

so the array output signal is

$$\tilde{s}_y(t) = Y^T(t) U$$

$$= \mu X^T(t) T^T [T^T]^{-1} \Phi_x^{-1} [T^*]^{-1} Q$$

$$= \mu X^T(t) \Phi_x^{-1} [T^*]^{-1} Q.\qquad (30)$$

Comparing (30) with (27) shows that $\tilde{s}_x(t)$ and $\tilde{s}_y(t)$ will be the same if

$$V = [T^*]^{-1} Q,\qquad (31)$$

i.e., if

$$Q = T^* V.\qquad (32)$$

Thus, inserting the transformation T between the elements and the processor has no effect on the output signal (or, as with the LMS array, on the output SINR), if the steering vector is transformed according to (32).

We have now shown that placing an invertible transformation T between the delay-line taps and the adaptive processor has no effect on the output signal or the output SINR. This result holds for the LMS array and also for the Applebaum array if the steering vector is properly transformed.

It is important to note what this result says about array bandwidth performance. Since the transformation T has no effect on the output signal or SINR of an array, *it also can have no effect on the bandwidth performance of an array*. In other words, the theorem applies no matter what signals are present in the array. Whatever the signal bandwidths, the array SINR will be the same with or without the transformation T. Thus, there is no invertible transformation T that one can insert between the delay-line taps and the weights that will improve the bandwidth performance.

III. AN ARRAY WITH FFT PROCESSING

Now consider an array with FFT processing. Such an array was shown in Fig. 5. An A/D converter behind each element samples the signal from that element every T_s s. The samples from each element are collected in the input buffer of a K-point FFT [10]. When K samples have been stored, the FFT is taken. This process generates K frequency domain samples from each element. These samples are multiplied by weights and then added in corresponding frequency bins to the weighted samples from other elements. The result is a set of K frequency domain samples of the array output. Finally, the inverse FFT is taken to obtain K time domain samples of the array output. This entire process is repeated every K samples.

The process described above is called block processing, since the input time samples are handled in blocks of K samples. After each block of K input samples is collected, a block of K array output time samples is generated by the inverse FFT. Each FFT cycle involves a block of K entirely new samples.

The FFT processing can also be done in a sliding window mode. In this case, the FFTs are recomputed after each new time sample, using always the most recent K time samples in each FFT input buffer. As we shall see below, with this approach it is not necessary to do the inverse FFT to obtain the time domain array output. The time domain output is simply the sum of the weighted-frequency domain samples.

Block processing has the advantage over sliding window processing that the FFT's need be computed only once per block, instead of once per sample. However, sliding window processing has the advantage that no inverse FFT is required to obtain the array output. In this section we shall consider both forms of processing.

We first define notation for the sampled signals. To make the notation here consistent with that in Section II, we denote the signal on the mth element of the array by $\tilde{x}_{m1}(t)$. Let us concentrate on a particular set of K contiguous samples in each FFT input buffer in Fig. 5. Suppose that, of these K samples, the most recent was taken at $t = t_0$. Then the latest sample of

$\tilde{x}_{m1}(t)$ in the mth FFT input buffer is $\tilde{x}_{m1}(t_0)$. The previous sample in that buffer is $\tilde{x}_{m1}(t_0 - T_s)$, and the earliest sample is $\tilde{x}_{m1}(t_0 - [K - 1]T_s)$. If we define the signal $\tilde{x}_{mk}(t)$ to be[1]

$$\tilde{x}_{mk}(t) = \tilde{x}_{m1}(t - [k - 1]T_s), \qquad (33)$$

we may write these samples as

$$\tilde{x}_{m1}(t_0) = \tilde{x}_{m1}(t_0),$$

$$\tilde{x}_{m1}(t_0 - T_s) = \tilde{x}_{m2}(t_0),$$

$$\cdots$$

$$\tilde{x}_{m1}(t_0 - [K - 1]T_s) = \tilde{x}_{mK}(t_0). \qquad (34)$$

Now consider the FFT obtained from these samples. Let the K frequency domain samples produced by the FFT behind element m be denoted by $\tilde{y}_{m1}, \tilde{y}_{m2}, \cdots, \tilde{y}_{mK}$. These $\tilde{y}_{mn}$ are given by[2]

$$\tilde{y}_{mn} = \sum_{k=1}^{K} \tilde{x}_{mk}(t_0) E_K^{(k-1)(n-1)}, \qquad 1 \le n \le K, \qquad (35)$$

where

$$E_K = e^{-j(2\pi/K)}. \qquad (36)$$

The array processor multiplies each frequency domain sample $\tilde{y}_{mn}$ by a complex weight u_{mn}. We assume these weights are set to their optimum values, which maximize SINR at the array output. (The weights can be controlled with an LMS processor, an Applebaum processor, or any other equivalent processor.) The weighted samples are then combined, in one of two ways, to produce the array output. The method used to combine the samples depends on whether block processing or sliding window processing is used.

If block processing is used, the weighted frequency domain samples from each element are added in corresponding frequency bins, as shown in Fig. 5. This step produces array output frequency domain samples $\tilde{f}_n$, given by

$$\tilde{f}_n = \sum_{m=1}^{M} u_{mn}\tilde{y}_{mn}. \qquad (37)$$

Then the inverse FFT of the $\tilde{f}_n$ is taken to obtain the time domain samples of the array output. If we denote the array output signal by $\tilde{s}(t)$, and its samples by $\tilde{s}_k(t)$,

$$\tilde{s}_k(t) = \tilde{s}(t_0 - [k - 1]T_s), \qquad 1 \le k \le K, \qquad (38)$$

[1] Equation (33) has the same form as (1) of Section II, with T_0 replaced by T_s.

[2] It is common in the FFT literature [10] to denote the time domain samples by $x_0, x_1, \cdots, x_{K-1}$ and the frequency domain samples by $X_0, X_1, \cdots, X_{K-1}$. In this case the FFT is usually written

$$X_n = \sum_{k=0}^{K-1} x_k E_K^{kn}, \qquad 0 \le n \le K-1.$$

and the IFFT is

$$x_k = \frac{1}{K} \sum_{n=0}^{K-1} X_n E_K^{-kn}, \qquad 0 \le k \le K-1.$$

However, to make our FFT notation correspond to that in Section II, we instead write the FFT as in (35) and allow the indices k, n to vary from 1 to K.

then the inverse FFT of the $\tilde{f}_n$ produces the following time samples of $\tilde{s}(t)$,

$$\tilde{s}_k(t_0) = \frac{1}{K} \sum_{n=1}^{K} \tilde{f}_n E_K^{-(k-1)(n-1)}, \qquad 1 \le k \le K. \qquad (39)$$

In a practical array, the factor $1/K$ in (39) may be omitted. This factor is simply a gain constant in the array output signal, and it has no effect on the output SINR.[3] Hence we assume the array output is actually obtained from

$$\tilde{s}_k(t_G) = \sum_{n=1}^{K} \tilde{f}_n E_K^{-(k-1)(n-1)}, \qquad 1 \le k \le K. \qquad (40)$$

Thus, with block processing, a block of K input samples is used in this manner to produce a block of K array output time samples. The entire process is repeated every KT_s s, using for each cycle an entirely new set of K samples from each element.

If sliding window processing is used, on the other hand, it is not necessary to perform the IFFT in (40). Note that the most recent sample of $\tilde{s}(t)$, $\tilde{s}(t_0)$, is given by (40) with $k = 1$,

$$\tilde{s}(t_0) = \tilde{s}_1(t_0) = \sum_{n=1}^{K} \tilde{f}_n. \qquad (41)$$

Thus $\tilde{s}(t_0)$ is just the sum of the $\tilde{f}_n$. With sliding window processing, the other samples of $\tilde{s}(t)$ that could be found from (40) are not needed, because an entire FFT cycle is performed for each new input time sample. Successive samples of the array output are obtained simply by repeating (41) at each sample time. Hence the total array processing in this case is as shown in Fig. 9.

Note that the optimal weights u_{mn} in the processor are the same regardless of whether block processing or sliding window processing is used. The optimal weights maximize SINR. defined by

$$\text{SINR} = \frac{P_d}{P_i + P_n}, \qquad (42)$$

where P_d, P_i, and P_n are the average desired, interference and thermal noise powers at the array output, respectively. If $\tilde{s}_d(t_j)$, $\tilde{s}_i(t_j)$ and $\tilde{s}_n(t_j)$ denote the desired, interference and thermal noise signals at the array output at a particular sample time t_j, then these powers are given by

$$P_d = E[|\tilde{s}_d(t_j)|^2], \qquad (43)$$

$$P_i = E[|\tilde{s}_i(t_j)|^2], \qquad (44)$$

and

$$P_n = E[|\tilde{s}_n(t_j)|^2]. \qquad (45)$$

Because we assume the signals $\tilde{x}_{mk}(t)$ are stationary, the array output time samples are also stationary. Hence each of the

[3] An LMS processor adjusts the weights so the array output matches the reference signal. Omitting the factor $1/K$ just results in weights smaller by a factor $1/K$ than they would have been. For an Applebaum processor, the optimal weights contain an arbitrary gain constant anyway, such as μ in (26).
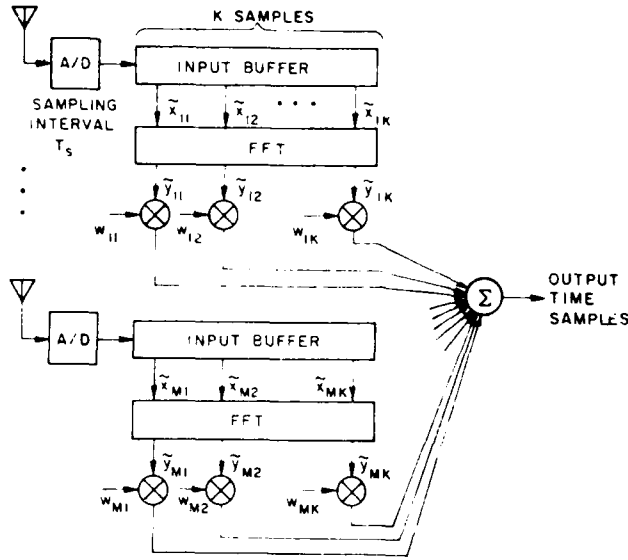
Fig. 9. Sliding window FFT processing.

Fig. 10. An equivalent tapped delay-line array.

Fig. 11. A simpler equivalent tapped delay-line array.

powers in (43)–(45) has the same value at every sample time t_j. Therefore the weights that maximize SINR at one sample time also maximize it at every other sample time.

To see that the optimal weights with sliding window processing are the same as those with block processing, it suffices to note that the array output for sliding window processing in (41) is the same as the array output for block processing in (40) when $k = 1$. Hence the weights that maximize the SINR at the $k = 1$ sample for block processing also maximize if for sliding window processing.

Since the optimal weights are the same for either type of processing, and since these weights produce the same output SINR in either case, we shall simplify the discussion below by considering only sliding window processing.

Now let us consider the relationship between FFT processing and tapped delay-line processing. First, we note that (33) for the time samples in the FFT processor has the same form as (1) for the signals in a tapped delay-line processor, except that the intertap delay T_0 in (1) is replaced by the sampling time T, in (33). Hence, for mathematical purposes, we may view the samples in the FFT processor as having been obtained from tapped delay-lines as shown in Fig. 10. If the delay between taps in Fig. 10 is T_s, and if every tap is sampled simultaneously at $t = t_0$, the same set of K samples will be obtained from the tapped delay-lines as from a single A/D converter behind each element as in Fig. 9.

Second, we note that the frequency domain samples $\tilde{y}_{mn}$ are each a linear combination of the input samples $\tilde{x}_{mk}(t_0)$. The linear combination is just the FFT in (35). Third, we have shown that the array output (for sliding window processing) is just the sum of the weighted frequency domain samples as in (41). Hence, an array with FFT processing is mathematically equivalent to an array with tapped delay-lines, followed by a linear transformation of the signals, followed by weighting and summing, as shown in Fig. 10.

Moreover, note that the A/D converters at the delay-line taps in Fig. 10 play no fundamental role in the operation of the array. The same array output samples would be produced by
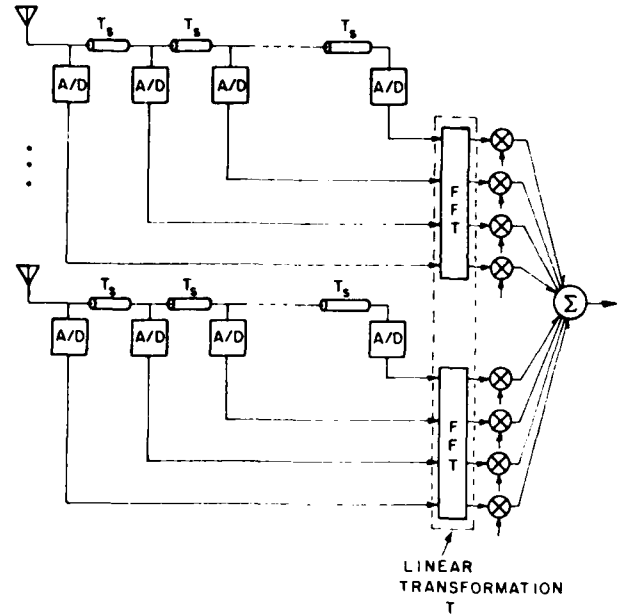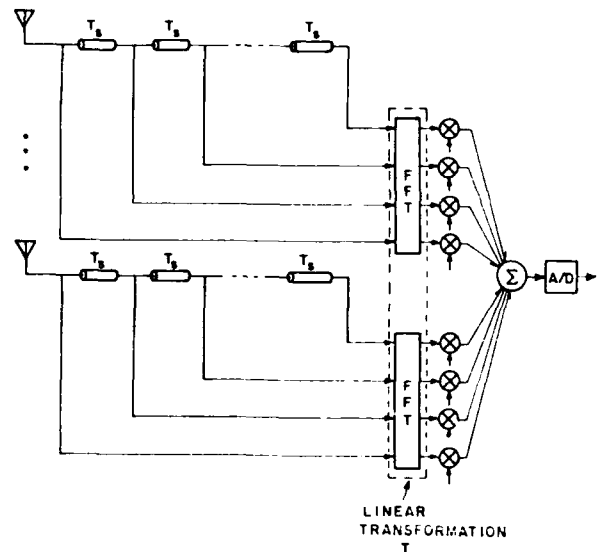
eliminating the A/D converters in Fig. 10 and instead putting a single A/D converter at the array output as in Fig. 11. The array is then an analog adaptive array with tapped delay-lines, followed by an A/D converter at the array output. The A/D converter in Fig. 11 serves only to discretize the array output, but has no effect on the output SINR of the array.

The transformation between the $\tilde{x}_{mk}(t_0)$ and the $\tilde{y}_{mn}$ in (35) may be expressed in matrix form as in Section II, of course. Let $X_m(t_0)$ be the element signal vector at time t_0,

$$X_m(t_0) = [\tilde{x}_{m1}(t_0), \tilde{x}_{m2}(t_0), \cdots, \tilde{x}_{mK}(t_0)]^T. \quad (46)$$

Then $X_m(t_0)$ contains the FFT input samples from element m used in (35). Also, let Y_m be a vector containing the frequency domain FFT samples from element m,

$$Y_m = [\tilde{y}_{m1}, \tilde{y}_{m2}, \cdots, \tilde{y}_{mK}]^T. \quad (47)$$

Then Y_m and X_m are related by

$$Y_m = EX_m,$$ (48)

where, from (35), E is the matrix

$$E = \begin{bmatrix} E_K^0 & E_K^0 & E_K^0 & \cdots & E_K^0 \\ E_K^0 & E_K^1 & E_K^2 & \cdots & E_K^{K-1} \\ E_K^0 & E_K^2 & E_K^4 & \cdots & E_K^{2(K-1)} \\ \vdots & \vdots & \vdots & & \vdots \\ E_K^0 & E_K^{K-1} & E_K^{2(K-1)} & \cdots & E_K^{(K-1)^2} \end{bmatrix}$$ (49)

$$= \begin{bmatrix} 1 & 1 & \cdots & 1 \\ 1 & e^{-j2\pi(1/K)} & \cdots & e^{-j2\pi(K-1/K)} \\ 1 & e^{-j2\pi(2/K)} & \cdots & e^{-j2\pi(2(K-1)/K)} \\ \vdots & \vdots & & \vdots \\ 1 & e^{-j2\pi(K-1/K)} & \cdots & e^{-j2\pi((K-1)^2/K)} \end{bmatrix}.$$

If $X(t_0)$ is the complete signal vector for the entire array,

$$X(t_0) = \begin{bmatrix} X_1(t_0) \\ -- \\ X_2(t_0) \\ -- \\ \vdots \\ -- \\ X_M(t_0) \end{bmatrix},$$ (50)

and Y is the vector containing all the frequency domain samples,

$$Y = \begin{bmatrix} Y_1 \\ -- \\ Y_2 \\ -- \\ \vdots \\ -- \\ Y_M \end{bmatrix},$$ (51)

then Y and X are related by

$$Y = TX(t_0),$$ (52)

$$T = \begin{bmatrix} E & | & 0 & | & \cdots & | & 0 \\ -- & | & -- & | & -- & | & -- \\ 0 & | & E & | & \cdots & | & 0 \\ -- & | & -- & | & -- & | & -- \\ \vdots & | & \vdots & | & \ddots & | & \vdots \\ -- & | & -- & | & -- & | & -- \\ 0 & | & 0 & | & \cdots & | & E \end{bmatrix}.$$ (53)

Note that T is a block diagonal matrix. It has this form because each FFT uses time samples from only one array element.

T is an invertible matrix, of course. The inverse of E in (49)

is just the inverse FFT in matrix form,

$$E^{-1} = \frac{1}{K} \begin{bmatrix} E_K^0 & E_K^0 & \cdots & E_K^0 \\ E_K^0 & E_K^{-1} & \cdots & E_K^{-(K-1)} \\ E_K^0 & E_K^{-2} & \cdots & E_K^{-2(K-1)} \\ \vdots & \vdots & & \vdots \\ E_K^0 & E_K^{-(K-1)} & \cdots & E_K^{-(K-1)^2} \end{bmatrix}$$ (54)

$$= \frac{1}{K} E^*.$$

The inverse of T is then just

$$T^{-1} = \frac{1}{K} \begin{bmatrix} E^* & | & 0 & | & \cdots & | & 0 \\ -- & | & -- & | & -- & | & -- \\ 0 & | & E^* & | & \cdots & | & 0 \\ -- & | & -- & | & -- & | & -- \\ \vdots & | & \vdots & | & \ddots & | & \vdots \\ -- & | & -- & | & -- & | & -- \\ 0 & | & 0 & | & \cdots & | & E^* \end{bmatrix}$$ (55)

$$= \frac{1}{K} T^*.$$

Thus, an array with FFT processing is mathematically equivalent to a tapped delay-line array with a linear invertible transformation between the taps and the weights. The equivalent tapped delay-line array has the same number of taps in each delay-line as the number of samples in the FFT's, and has an intertap delay T_0 equal to the sampling time T_s. It then follows from the theorem in Section II that an array with FFT processing will produce the same output SINR as the corresponding array with tapped delay-lines. The FFT's can be inserted or omitted with no change in performance.

An important conclusion that follows from this result is that FFT processing in and of itself does not offer any improvement in array bandwidth performance. The same bandwidth performance can be obtained simply by storing K samples of each element signal and then weighting these samples directly. Including the FFT's between the samples and the weights merely adds to the computational burden, but does nothing for the bandwidth performance.

IV. ADDITIONAL COMMENTS ON FFT PROCESSING

In this section we discuss a few additional points of interest concerning FFT processing.

A. Optimal Weights With and Without FFT Processing

First, we consider how the optimal weights with FFT processing compare to those with tapped delay-line processing. Let U and W be the optimal weight vectors with and without the FFT transformation T in the array, respectively. Then, from (21), U and W are related by

$$U = [T^*]^{-1} W.$$ (56)

However, the matrix T in (53) is symmetrical, because E in (49) is symmetrical. Hence (56) simplifies to

$$U = T^{-1} W. \qquad (57)$$

Moreover, U and W may each be expressed in terms of element weight vectors U_m and W_m as in (5). Equation (57) then reduces to

$$U_m = E^{-1} W_m, \qquad 1 \le m \le M. \qquad (58)$$

Hence the *optimal weight vector behind each element with FFT's is just the inverse FFT of the optimal weight vector without FFT's*. Note that because (57) holds, the same array output signal is obtained with or without the FFT's,

$$Y^T U = [TX]^T [T^{-1} W] = X^T W, \qquad (59)$$

as the theorem of Section II requires.

B. Covariance Matrix Eigenvalues

Next, we consider the eigenvalues of the covariance matrix seen by the adaptive array processor with and without the FFT's. These eigenvalues are of interest because they control the transient behavior or convergence properties of the algorithm used to adapt the weights [11]. Without the FFT's, the signal vector is X and the covariance matrix is

$$\Phi_x = E[X^* X^T]. \qquad (60)$$

Suppose Φ_x has orthonormal eigenvectors e_{x_i} and eigenvalues[4] λ_{x_i}

$$\Phi_x e_{x_i} = \lambda_{x_i} e_{x_i}, \qquad 1 \le i \le KM. \qquad (61)$$

The eigenvectors e_{x_i} satisfy

$$e_{x_i}^\dagger e_{x_j} = \delta_{ij}, \qquad 1 \le i, j \le KM \qquad (62)$$

where the superscript dagger denotes conjugate transpose and δ_{ij} is the Kronecker delta.

Now define new vectors

$$e_{y_i} = \sqrt{K} T^{-1} e_{x_i}, \qquad 1 \le i \le KM. \qquad (63)$$

These e_{y_i} also form an orthonormal set. From (63), we have

$$e_{y_i}^\dagger e_{y_j} = e_{x_i}^\dagger \sqrt{K} [T^{-1}]^\dagger \sqrt{K} T^{-1} e_{x_j}. \qquad (64)$$

But because T is symmetrical ($T^T = T$) and $T^{-1} = (1/K)T^*$ (see (55)), we have

$$[T^{-1}]^\dagger = \left(\frac{1}{K} T^* \right)^\dagger = \frac{1}{K} T, \qquad (65)$$

so (64) reduces to

$$e_{y_i}^\dagger e_{y_j} = K e_{x_i}^\dagger \frac{1}{K} TT^{-1} e_{x_j}$$

$$= e_{x_i}^\dagger e_{x_j}$$

$$= \delta_{ij}, \qquad 1 \le i, j \le KM. \qquad (66)$$

Now substitute $e_{x_i} = (1/\sqrt{K})Te_{y_i}$ (the inverse of (63)) in (61) and multiply on the left by T^{-1}. This gives

$$T^{-1}\Phi_x Te_{y_i} = \lambda_{x_i} e_{y_i}. \qquad (67)$$

Then replace T^{-1} by $(1/K)T^*$ and T by T^T,

$$[T^*\Phi_x T^T]e_{y_i} = K\lambda_{x_i} e_{y_i}. \qquad (68)$$

Finally, from (18) note that

$$T^*\Phi_x T^T = \Phi_y, \qquad (69)$$

so (68) is just

$$\Phi_y e_{y_i} = K\lambda_{x_i} e_{y_i}, \qquad 1 \le i \le KM. \qquad (70)$$

Equation (70) shows that e_{y_i} and $K\lambda_{x_i}$ are the ith eigenvector and eigenvalue of Φ_y. Thus, each eigenvalue of Φ_y is simply K times the corresponding eigenvalue of Φ_x.

From this it follows that Φ_y and Φ_x have the same eigenvalue *spread*. (The eigenvalue spread is the ratio of the largest to the smallest eigenvalue.) Hence typical problems caused by eigenvalue spread, such as long convergence times, roundoff errors in covariance matrix inversions, etc., will be the same with or without the FFT's.

C. Weight Dynamic Range

Now we consider an issue of practical interest: how FFT processing affects the dynamic range of the weights. We may gain insight into this question as follows.

McClellan and Parks [12] have studied the eigenstructure of the FFT transformation matrix. From their results, it is easily shown that the matrix E in (49) has a complete set of orthonormal eigenvectors e_{E_j}, $1 \le j \le K$, and that every eigenvalue λ_{E_j} of E has one of the four values $\sqrt{K}$, $-\sqrt{K}$, $+j\sqrt{K}$, or $-j\sqrt{K}$. The multiplicity of each eigenvalue varies with K, the order of E.

From the eigenvectors and eigenvalues of E one can obtain the eigenvectors and eigenvalues of T in (53) in an obvious way. Each eigenvector e_{T_j} of T will have $(M - 1)K$ components equal to zero and K components consisting of one eigenvector e_{E_j} of E. The eigenvalues λ_{T_j} of T will be the same as those of E but with multiplicities M times higher.

Suppose W is the optimum weight vector without FFT's and U the optimum weight vector with FFT's. Then from (21) we have

$$U = [T^T]^{-1} W = T^{-1} W. \qquad (71)$$

The optimal weight vector W may be expressed in terms of its components along each of the eigenvectors of T,

$$W = \sum_{j=1}^{MK} \alpha_j e_{T_j} \qquad (72)$$

where each α_j is a scalar constant. Moreover, the matrix T^{-1} may be written in terms of the eigenvectors e_{T_j} and eigenvalues λ_{T_j} of T using the spectral decomposition formula,

$$T^{-1} = \sum_{j=1}^{MK} \frac{1}{\lambda_{T_j}} e_{T_j} e_{T_j}^\dagger. \qquad (73)$$

Substituting (72) and (73) into (71) then gives

$$U = \sum_{j=1}^{MK} \frac{\alpha_j}{\lambda_{T_j}} e_{T_j}. \tag{74}$$

We cannot determine the magnitude of the components of U exactly without considering specific cases, because some λ_{T_j} are real and some are imaginary. But because $|\lambda_{T_j}| = \sqrt{K}$ for every j, (74) shows that the weights with FFT's will generally be smaller than the weights without FFT's by a factor of about $1/\sqrt{K}$. The ratio of the largest to the smallest weight is approximately the same with or without FFT processing.

D. Performance Differences Between Tapped Delay-Line and FFT Processing

Next, let us consider how the delay parameters are usually chosen in tapped delay-line and FFT processors. In the introduction we noted that array performance can be poorer for FFT processing than for tapped delay-line processing. Fig. 6, showing typical results with FFT's, was compared with Fig. 4 for tapped delay-lines.

However, it is clear from the results of Sections II and III that the SINR achieved by an array with FFT's must be identical to that achieved by the *equivalent* tapped delay-line array. The equivalent tapped delay-line array has the same number of taps as the number of samples in the FFT's and has an intertap delay equal to the FFT sampling interval.

The performance difference noted in the Introduction is due entirely to the fact that typical comparisons have assumed different intertap delays or different numbers of taps for the two types of arrays. For a tapped delay-line processor, the intertap delay is often assumed to be a quarter wavelength at the carrier frequency. For an FFT processor, the sampling time is usually chosen so the period of the FFT frequency response approximates the signal bandwidth. These two amounts of delay are usually very different.

Consider a typical case. First, suppose the signal carrier frequency is ω_0. The time delay required to produce a 90° phase shift at the carrier frequency (a quarter-wave delay) is then

$$T_{90} = \frac{\pi}{2\omega_0}. \tag{75}$$

In general, suppose we have

$$T_0 = rT_{90}, \tag{76}$$

where r is the number of quarter-wave delays in T_0. Although there is actually no fundamental reason to do so, with tapped delay-line processing it is common [4] to assume[5] $r = 1$.

Now consider the choice of T_s in an FFT processor. We may view the FFT in (35) as a filter bank. The input to the filter bank is $\tilde{x}_{m1}(t)$ and the outputs are $\tilde{y}_{m1}, \tilde{y}_{m2}, \cdots, \tilde{y}_{mK}$. One filter produces the output $\tilde{y}_{m1}$, another produces the output $\tilde{y}_{m2}$, and so forth. Let us consider the transfer function of each of these filters.

Suppose the input signal $\tilde{x}_{m1}(t)$ is a sinusoid at frequency ω,

$$\tilde{x}_{m1}(t) = e^{j\omega t}. \tag{77}$$

Then, from (33),

$$\tilde{x}_{mk}(t) = e^{j\omega[t-(k-1)T_s]}. \tag{78}$$

For a specific n, the output signal $\tilde{y}_{mn}$ may be found by substituting (78) into (35),

$$\tilde{y}_{mn} = \sum_{k=1}^{K} \tilde{x}_{mk}(t)e^{-j(2\pi/K)(k-1)(n-1)}$$

$$= \sum_{k=1}^{K} e^{-j(k-1)[\omega T_s+(2\pi/K)(n-1)]}e^{j\omega t}. \tag{79}$$

This may be written,

$$\tilde{y}_{mn} = H_n(\omega)e^{j\omega t}, \tag{80}$$

where $H_n(\omega)$, the nth transfer function, is

$$H_n(\omega)$$

$$= \sum_{k=1}^{K} e^{-j(k-1)[\omega T_s+(2\pi/K)(n-1)]}$$

$$= e^{-j(K-1)/2[\omega T_s+(2\pi/K)(n-1)]} \frac{\sin \dfrac{K}{2}\left[\omega T_s+\dfrac{2\pi}{K}(n-1)\right]}{\sin \dfrac{1}{2}\left[\omega T_s+\dfrac{2\pi}{K}(n-1)\right]}. \tag{81}$$

In general, $H_n(\omega)$ is a periodic function of frequency with peaks at frequencies

$$\omega = \frac{2\pi}{T_s}\left[i-\frac{n-1}{K}\right], \qquad i = \cdots, -2, -1, 0, 1, 2, \cdots. \tag{82}$$

For a given n, the peaks of $H_n(\omega)$ occur every $2\pi/T_s$ along the frequency axis. For adjacent n, the peaks are separated by $2\pi/KT_s$. Fig. 12 shows a typical set of $H_1(\omega), \cdots, H_K(\omega)$ over part of the frequency axis.

In studies of FFT processing, it is common to choose T_s so one complete set of K filter passbands approximately covers the signal bandwidth. (This choice seems sensible, since it divides the signal bandwidth into K subbands.) If the signal bandwidth is $\Delta\omega$, we set

$$\frac{2\pi}{T_s} = \Delta\omega, \tag{83}$$

or

$$T_s = \frac{2\pi}{\Delta\omega}. \tag{84}$$

[5] It is shown in [7] that for a two-element array any choice of r in the range $0 < r < 1/B$ will work just as well.
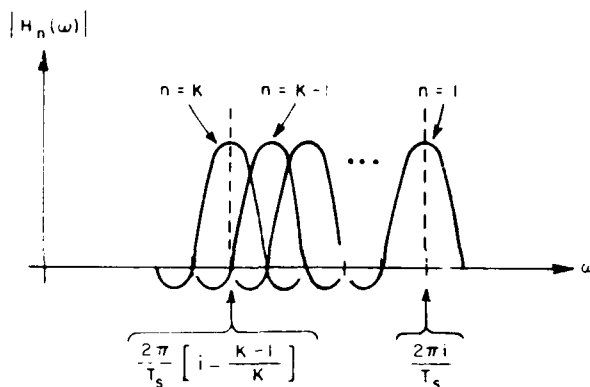
Fig. 12. The transfer functions $H_1(\omega), \cdots, H_K(\omega)$.

However, (84) may be rearranged into the form

$$T_s = 4 \frac{\pi}{2\omega_0} \frac{\omega_0}{\Delta\omega} = \frac{4}{B} T_{90}, \tag{85}$$

where B is the relative bandwidth of the signals,

$$B = \frac{\Delta\omega}{\omega_0}, \tag{86}$$

and T_{90} is given in (75). If, for example, the signal has a 1 percent relative bandwidth, then

$$T_s = 400 T_{90}. \tag{87}$$

Note that this choice corresponds to $r = 400$ in (76), i.e., to an intertap delay of 400 quarter-waves in the equivalent tapped delay-line array!

In Fig. 4, which shows the SINR of a two-element tapped delay-line array, there are two taps per element and one quarter-wave delay between taps. In Fig. 6, which shows the SINR for a two-element array with FFT processing, the sampling time has been selected according to (84). Thus, the tapped delay-line array in Fig. 4 and the FFT array in Fig. 6 are not equivalent. The difference in their performance is due to the difference between T_0 and T_s, as well as K.

In an earlier paper [7], the author discussed in detail how the number of taps and the amount of intertap delay affect the SINR performance of a two-element tapped delay-line array. In particular, it was shown there that setting T_s according to (84) (i.e., setting $r = 4/B$) makes r too large to obtain optimal SINR from the array. For optimal SINR, r must be in the range $0 < r < 1/B$. Thus, although it seems intuitively sensible to choose T_s so the signal bandwidth is divided into K subbands, in fact this choice yields suboptimal SINR. Better performance will be obtained if T_s is chosen so the FFT period is at least four times the signal bandwidth. The reader is referred to [7] for further discussion of this question.

E. An Advantage of FFT Processing

It should be pointed out that even though FFT's do not improve bandwidth performance per se, they may nevertheless be useful for other reasons. For example, when the sample matrix inverse (SMI) technique [8] is used to control the weights, the number of multiplications required for each weight update is proportional to $(KM)^3$, the number of

weights cubed. As a result, the computational burden increases rapidly with the number of weights, and can quickly become prohibitive. However, taking FFT's tends to reduce the correlation between samples in different frequency subbands. In the ideal case in which samples in different subbands are completely decorrelated, the covariance matrix has a block diagonal form and the optimal weights can be computed separately in each subband. In this case one need only compute M weights for each of K subbands, so the total number of multiplications is proportional to KM^3 rather than K^3M^3. For large K the computational savings may more than offset the extra burden of taking the FFT's.

In practice the samples in different frequency subbands are usually not completely decorrelated. (The actual decorrelation depends on the signal spectra and the sampling rate.) However, even with imperfect decorrelation, it may still be advantageous to compute weights in each subband separately. Although the resulting weights are suboptimal, the computational savings may be worth the loss in SINR. Using FFT's in the array makes this trade-off possible. Studies of this approach have been made by Berni and Kretschmer [13], Dillard [14], Gabriel [15], Gerlach [16] and Brennan and Doyle [17].

V. Conclusion

We have shown that the SINR achieved by an adaptive array with FFT processing is identical to that achieved by an adaptive array with the *equivalent* tapped delay-line processing. In the equivalent tapped delay-line processor, the number of taps in the delay-lines is equal to the number of samples used in the FFT's, and the delay between taps is equal to the delay between samples in the FFT's.

In Section II, we showed that inserting a linear invertible transformation between the delay-line taps and the weights in a tapped delay-line array has no effect on the array output signal or SINR. Whatever changes are caused in the signals by the linear transformation are compensated for by corresponding changes in the weights. Then in Section III we showed that using FFT's behind each element is mathematically equivalent to using tapped delay-lines followed by a linear transformation of the signals. The main conclusion follows from the results of Sections II and III.

In Section IV, we considered the effects of FFT's on the optimal weights, the covariance matrix eigenvalues, and the dynamic range of the weights. Finally, we discussed the reasons for the performance differences noted between FFT processing and tapped delay-line processing.

The most important conclusion that follows from these results is that FFT processing in and of itself does not offer any improvement in array bandwidth performance. The same bandwidth performance will be obtained by simply storing K samples from each element signal and then weighting and combining these samples directly.

Acknowledgment

REFERENCES

[1] B. Widrow, P. F. Mantey, L. J. Griffiths and B. B. Goode, "Adaptive antenna systems," *Proc. IEEE*, vol. 55, no. 12, p. 2143, Dec. 1967.

[2] S. P. Applebaum, "Adaptive arrays," *IEEE Trans. Antennas Propagat.*, vol. AP-24, no. 5, p. 585, Sept. 1976.

[3] R. A. Monzingo and T. W. Miller, *Introduction to Adaptive Arrays*. New York: Wiley, 1980.

[4] W. E. Rodgers and R. T. Compton, Jr., "Adaptive array bandwidth with tapped delay-line processing," *IEEE Trans. Aerospace Electron. Syst.*, vol. AES-15, no. 1, p. 21, Jan. 1979.

[5] J. T. Mayhan, A. J. Simmons, and W. C. Cummings, "Wideband adaptive antenna nulling using tapped delay lines," *IEEE Trans. Antennas Propagat.*, vol. AP-29, no. 6, p. 923, Nov. 1981.

[6] W. D. White, "Wideband interference cancellation in adaptive sidelobe cancellers," *IEEE Trans. Aerospace Electron. Syst.*, vol. AES-19, no. 6, p. 915, Nov. 1983.

[7] R. T. Compton, Jr., "The bandwidth performance of a two-element adaptive array with tapped delay-line processing," *IEEE Trans. Antennas Propagat.*, p. 5, this issue.

[8] I. S. Reed, J. D. Mallett, and L. E. Brennan, "Rapid convergence rate in adaptive arrays," *IEEE Trans. Aerospace Electron. Syst.*, vol. AES-10, no. 6, p. 853, Nov. 1974.

[9] C. A. Baird and C. L. Zahm, "Performance criteria for narrowband array processing," presented at 1971 IEEE Conf. Decision Control, Miami Beach, FL, Dec. 15-17, 1971.

[10] A. V. Oppenheim and R. W. Schafer, *Digital Signal Processing*. Englewood Cliffs, NJ: Prentice-Hall, 1975.

[11] R. T. Compton, Jr., *Adaptive Antennas—Concepts and Performance*. Englewood Cliffs, NJ: Prentice-Hall, 1988.

[12] J. H. McClellan and T. W. Parks, "Eigenvalue and eigenvector decomposition of the discrete Fourier transform," *IEEE Trans. Audio Electroacoust.*, vol. AU-20, p. 66, Mar. 1972.

[13] B. L. Lewis and F. F. Kretschmer, Jr., Naval Res. Lab. reports of limited distribution, dating back to Feb. 1974.

[14] G. M. Dillard, "Band-partitioning for coherent sidelobe cancellation," Naval Ocean Syst. Center, San Diego, CA, Rep. NOSC TD 597, May 1983.

[15] W. F. Gabriel, "Adaptive digital processing investigation of DFT subbanding vs transversal filter canceler," Naval Res. Lab., Washington, DC, Rep. 8981, July 28, 1986.

[16] K. Gerlach, "A numerically efficient band-partitioned canceller," Naval Res. Lab., Washington, DC, Rep. 9050, July 1987.

[17] L. E. Brennan and W. L. Doyle, "Sub-banding and transversal filtering for correcting receiver mismatch in adaptive cancellers," Adaptive Sensors, Inc., 216 Pico Blvd., Suite 8, Santa Monica, CA, Tech. Rep., Mar. 1986.

R. T. Compton, Jr. (S'58-M'59-M'81-SM'82-F'84), for a photograph and biography please see page 14 of this issue.

Scattering by an Inhomogeneous Dielectric/Ferrite Cylinder of Arbitrary Cross-Section Shape—Oblique Incidence Case

Roberto G. Rojas

Scattering by an Inhomogeneous Dielectric/Ferrite Cylinder of Arbitrary Cross-Section Shape—Oblique Incidence Case

ROBERTO G. ROJAS

Abstract—A moment method (MM) solution is developed for the fields scattered by an inhomogeneous dielectric/ferrite cylinder of arbitrary cross-section shape. The incident field is assumed to be a plane wave of arbitrary polarization with oblique incidence with respect to the axis of the cylinder. The total electric and magnetic fields are the unknown quantities in two coupled integral equations from which a system of linear equations is obtained. Once the total electric and magnetic fields within the cylinder are computed, the scattered fields at any other point in space are easily calculated. It is noted that for the case of oblique incidence, the scattered field has TE_z and TM_z polarized fields regardless of the polarization (TM_z or TE_z) of the incident field. The echo widths of cylinders and shells of circular, semicircular, and rectangular cross section are calculated for TE_z and TM_z polarized incident fields. Furthermore, it is shown that the results obtained for dielectric/ferrite cylinders and shells of circular cross section with the solutions developed here agree very well with the corresponding exact eigenfunction solutions.

I. INTRODUCTION

THE ELECTROMAGNETIC scattering by dielectric and/or magnetic bodies has been studied by several authors in the past. For objects of arbitrary shape, two formulations have been widely used; namely, volume (surface) and surface (line) integral equations for three-(two-) dimensional objects. These integral equations can then be solved numerically with the method of moments.

The volume integral equations are obtained by replacing the dielectric/ferrite objects, which can be inhomogeneous, by equivalent volumetric polarization currents. This method has been used in [1]-[6] to solve scattering problems from two- and three-dimensional bodies and to study the fields induced inside biological bodies [7]. A different approach is the surface integral formulation in which a homogeneous dielectric object is replaced by equivalent currents along the surface of the scatter. This method, which can also be used to study objects made up of homogeneous layers, is employed in [8]-[11] to solve a variety of problems involving dielectric objects.

In addition to the two methods mentioned earlier, a characteristic mode solution is developed in [12] for two-dimensional dielectric bodies which are replaced by equivalent surface currents. A different approach is followed in [13], where an impedance sheet approximation is used to study the

EM scattering from thin dielectric shells. The unimoment [14] and finite element [15] methods have also been used to calculate the fields scattered by dielectric cylinders. Recently, the conjugate gradient method [16] has been applied to analyze the scattering from two-dimensional dielectric structures.

The problem considered in this paper is the EM scattering by a dielectric/ferrite cylinder of arbitrary cross-section shape [17]. The incident field is a plane wave of arbitrary polarization with oblique incidence with respect to the axis of the cylinder as shown in Fig. 1. The cylinder is assumed to be linear and isotropic; however, it can be inhomogeneous and lossy. By replacing the cylinder with equivalent polarization currents, two coupled integral equations are obtained for the total electric and magnetic fields inside the dielectric/ferrite cylinder. The solution of the integral equations is obtained by following a method similar to that employed by Richmond [1], [2]. That is, the cylinder is divided into square cells which are small enough so that the electric and magnetic fields are nearly constant within each cell, except for the exponential z-dependance of all the fields due to the oblique incidence of the plane wave with respect to the axis of the cylinder which coincides with the z-axis. A system of linear equations is obtained by enforcing the condition that the integral equations must be exactly satisfied at the center of each cell. Unlike [1], [2], this paper considers the general case of dielectric/ferrite cylinders. Furthermore, as mentioned before, the incident plane wave field is obliquely incident to the axis of the cylinder, and it can have arbitrary polarization. Note that all the fields in the following discussion have the conventional $e^{j\omega t}$ time dependence which is suppressed to simplify the notation.

II. FORMULATION OF THE PROBLEM

Assume that $(\vec{E}^i, \vec{H}^i)$ is the incident field in the absence of the dielectric/ferrite cylinder. Without loss of generality, the medium exterior to the scatter is assumed to be free space. Let $(\vec{E}, \vec{H})$ represent the total field; that is, the field excited by the incident field in the presence of the dielectric/ferrite cylinder. The difference between the total and incident fields is usually referred to as the scattered field $(\vec{E}^s, \vec{H}^s)$. Thus,

$$\vec{E} = \vec{E}^i + \vec{E}^s; \qquad \vec{H} = \vec{H}^i + \vec{H}^s. \qquad (1)$$

It follows from Maxwell's equations that the scattered field $(\vec{E}^s, \vec{H}^s)$ may be considered to be the field generated by a set of equivalent electric $\vec{J}$ and magnetic $\vec{M}$ polarization currents
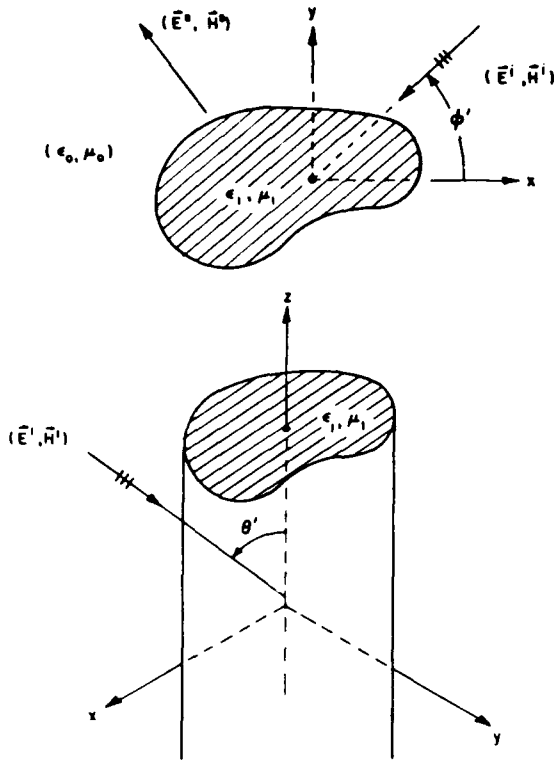
Fig. 1. Geometry for EM scattering by dielectric/ferrite cylinder of arbitrary cross-section shape.

radiating in free space. These currents can be expressed as follows:

$$\vec{J}(\vec{r}) = jk Y_0(\epsilon_r(\vec{\rho}) - 1)\vec{E}(\vec{r})$$

$$\vec{M}(\vec{r}) = jk\eta_0(\mu_r(\vec{\rho}) - 1)\vec{H}(\vec{r}) \quad (2)$$

where η_0 and $Y_0 = 1/\eta_0$ are the free-space impedance and admittance, respectively, and k is the free-space wavenumber. Furthermore,

$$\epsilon_r(\vec{\rho}) = \epsilon_r'(\vec{\rho}) - j\epsilon_r''(\vec{\rho}); \qquad \epsilon_r'(\vec{\rho}) \geqslant 1, \qquad \epsilon_r''(\vec{\rho}) \geqslant 0$$
$$\tag{3a}$$

is the relative permittivity, while

$$\mu_r(\vec{\rho}) = \mu_r'(\vec{\rho}) - j\mu_r''(\vec{\rho}); \qquad \mu_r'(\vec{\rho}) \geqslant 1, \qquad \mu_r''(\vec{\rho}) \geqslant 0$$
$$\tag{3b}$$

is the relative permeability. Also $\vec{r} = \hat{x}x + \hat{y}y + \hat{z}z$ and $\vec{\rho} = \hat{x}x + \hat{y}y$. Note that $\epsilon_r'(\vec{\rho})$, $\epsilon_r''(\vec{\rho})$, $\mu_r'(\vec{\rho})$, and $\mu_r''(\vec{\rho})$ are all real quantities whose values depend on $\vec{\rho}$, but not on z.

Since the cylinder is a two-dimensional object and the incident field is a plane wave, the polarization currents $\vec{J}$ and $\vec{M}$ and all the field components will have the same exponential z dependence as the incident field. It can be shown [18] that if all the field components have the same exponential z-dependence exp $(jkz \cos \theta')$, then, all the fields can be expressed in terms of E_z and H_z as follows:

$$\vec{E}(\vec{r}) = \nabla \times (\nabla \times (\hat{z}E_z(\vec{r})) - jk\eta_0\hat{z}H_z(\vec{r}))/K^2$$

and

$$\vec{H}(\vec{r}) = \nabla \times (\nabla \times (\hat{z}H_z(\vec{r})) + jk Y_0\hat{z}E_z(\vec{r}))/K^2 \quad (4)$$

where $K = k \sin \theta'$ and $0 < \theta' < \pi$. Therefore, the complete solution can be expressed in terms of E_z and H_z only. Thus, assume that the incident field (E_z^i, H_z^i) is given by

$$E_z^i(\vec{r}) = E_{0z} \exp (-jK\vec{\rho} \cdot \hat{p}) \exp (-jk_z'z)$$

and

$$H_z^i(\vec{r}) = H_{0z} \exp (-jK\vec{\rho} \cdot \hat{p}) \exp (-jk_z'z) \quad (5)$$

where E_{0z} and H_{0z} are arbitrary constants, $k_z' = -k \cos \theta'$, and

$$\hat{p} = -\hat{x} \cos \phi' - \hat{y} \sin \phi'. \quad (6)$$

Note that, except for $e^{-jk_z'z}$, this problem is still a two-dimensional problem. To simplify the notation, the z dependance of the fields and currents in the following analysis will not be shown explicitly.

Once the electric and magnetic currents are defined, the scattered fields $(\vec{E}^s, \vec{H}^s)$ can be expressed in terms of the electric and magnetic free-space dyadic Green's functions, namely [19]

$$\vec{E}^s(\vec{\rho}) = -\lim_{\delta \to 0} \int_{A_J - A_\delta} [\bar{g}_m^0(\vec{\rho}, \vec{\rho}') \cdot \vec{M}(\vec{\rho}')$$
$$+ jk\eta_0\bar{g}_e^0(\vec{\rho}, \vec{\rho}') \cdot \vec{J}(\vec{\rho}')] ds' - \frac{\bar{I} \cdot \vec{J}(\vec{\rho})}{jk Y_0} \quad (7)$$

$$\vec{H}^s(\vec{\rho}) = \lim_{\delta \to 0} \int_{A_J - A_\delta} [\bar{g}_m^0(\vec{\rho}, \vec{\rho}') \cdot \vec{J}(\vec{\rho}')$$
$$- jk Y_0\bar{g}_e^0(\vec{\rho}, \vec{\rho}') \cdot \vec{M}(\vec{\rho}')] ds' - \frac{\bar{I} \cdot \vec{M}(\vec{\rho})}{jk\eta_0} \quad (8)$$

where A_J is the area occupied by the equivalent currents and $\vec{\rho}' = \hat{x}x' + \hat{y}y'$ is the source location. The area A_δ, which excludes the singularities of $\bar{g}_e^0$ and $\bar{g}_m^0$, i.e., $\vec{\rho} = \vec{\rho}'$, is called the "principal area" [19]. It becomes infinitesimally small in the limit as its maximum chord length δ approaches zero. Since the value of $\bar{I}$ and the integrals in (7) and (8) depend on the geometry of A_δ, the area A_δ is assumed to be a circular disk. The reasons for choosing this shape will be explained later. The electric free-space dyadic Green's function $\bar{g}_e^0$ is given by

$$\bar{g}_e^0(\vec{\rho}, \vec{\rho}') = \frac{-j}{4} \left(\bar{I} + \frac{\nabla\nabla}{k^2}\right) H_0^{(2)}(K|\vec{\rho} - \vec{\rho}'|); \quad \vec{\rho} \neq \vec{\rho}', \quad (9)$$

while the magnetic free-space dyadic Green's function $\bar{g}_m^0$ can be expressed as follows:

$$\bar{g}_m^0(\vec{\rho}, \vec{\rho}') = \frac{-j}{4} \nabla \times (\bar{I}H_0^{(2)}(K|\vec{\rho} - \vec{\rho}'|)); \quad \vec{\rho} \neq \vec{\rho}' \quad (10a)$$

where

$$\bar{I} = \hat{x}\hat{x} + \hat{y}\hat{y} + \hat{z}\hat{z}$$

$$\nabla = \hat{x}\frac{\partial}{\partial_x} + \hat{y}\frac{\partial}{\partial_y} + \hat{z}jk \cos \theta'$$

$$\bar{I} = \frac{1}{2}(\hat{x}\hat{x} + \hat{y}\hat{y}) \quad (10b)$$

and $H_0^{(2)}$ is the Hankel function of the second kind of zeroth order. It is important to point out that even though $\bar{T}$ and the integrals in (7) and (8) depend on the shape of A_δ, their sum does not.

To obtain the integral equations, one enforces (1) inside the dielectric/ferrite object; namely,

$$\bar{E}(\bar{\rho}) + \lim_{\delta \to 0} \int_{A_J - A_\delta} [jk\eta_0[\mu_r(\bar{\rho}') - 1] \bar{g}_m^0(\bar{\rho}, \bar{\rho}')$$

$$\cdot \bar{H}(\bar{\rho}') - k^2[\epsilon_r(\bar{\rho}') - 1] \bar{g}_e^0(\bar{\rho}, \bar{\rho}') \cdot \bar{E}(\bar{\rho}')] \, ds'$$

$$+ [\epsilon_r(\bar{\rho}) - 1] \bar{T} \cdot \bar{E}(\bar{\rho}) = \bar{E}^i(\bar{\rho}) \qquad (11)$$

and

$$\bar{H}(\bar{\rho}) - \lim_{\delta \to 0} \int_{A_J - A_\delta} [jkY_0[\epsilon_r(\bar{\rho}') - 1] \bar{g}_m^0(\bar{\rho}, \bar{\rho}')$$

$$\cdot \bar{E}(\bar{\rho}') + k^2[\mu_r(\bar{\rho}') - 1] \bar{g}_e^0(\bar{\rho}, \bar{\rho}) \cdot \bar{H}(\bar{\rho}')] \, ds'$$

$$+ [\mu_r(\bar{\rho}) - 1] \bar{T} \cdot \bar{H}(\bar{\rho}) = \bar{H}^i(\bar{\rho}). \qquad (12)$$

Note that (11) and (12) are coupled integral equations where the unknowns are the fields $\bar{E}(\bar{\rho})$ and $\bar{H}(\bar{\rho})$.

III. SOLUTION

The solution of the coupled integral equations in (11) and (12) will be obtained in a fashion similar to that followed by Richmond [1], [2]. That is, the integral equations are transformed into a system of linear equations by enforcing (11) and (12) at a number of discrete points. The first step in this procedure is to divide the cylinder into N square cells which are small enough so that the electric and magnetic fields are nearly uniform in each cell. This is equivalent to choosing the pulse functions $\{f_n(\bar{\rho} \cdot)\}_{n=1}^N$ as the basis functions [20]. That is, let

$$E_p(\bar{\rho}') = \sum_{n=1}^N E_{pn} f_n(\bar{\rho}')$$

$$H_p(\bar{\rho}') = \sum_{n=1}^N H_{pn} f_n(\bar{\rho}'); \qquad p = x, y, z \qquad (13)$$

where

$$f_n(\bar{\rho}') = \begin{bmatrix} 1, & \text{in cell } n \text{ of area } c_n^2 \\ 0, & \text{elsewhere} \end{bmatrix} \qquad (14)$$

and $\{E_{pn}, H_{pn}\}_{n=1}^N$ are unknown coefficients that have to be determined. The second and last step in the discretization of (11) and (12) is to define a set of testing functions [20]. Here, the Dirac delta functions $\{\delta(x - x_n)\delta(y - y_n)\}_{n=1}^N$ are chosen as the testing functions, where (x_n, y_n) is the center of cell n. This is equivalent to enforcing (11) and (12) at the center of each cell; i.e., the total field must be equal to the sum of the incident and scattered fields at the center of each cell.

Substituting (13) into (11) and (12), and enforcing (1) at the center of each cell, a set of $6N$ simultaneous equations with $6N$ unknowns is obtained. Note that, in general, there are six unknowns in each cell, i.e., E_x, E_y, E_z, H_x, H_y, and H_z. However, as shown in (4), only two field components; namely, E_z and H_z, are necessary to determine completely the total $\bar{E}$ and $\bar{H}$ fields. However, the expressions for E_x, E_y, H_x, and H_y involve the derivatives (with respect to x and y) of E_z and H_z. Thus, if the derivatives of E_z and H_z are approximated by finite differences, (11) and (12) would become difference equations. Therefore, all six unknowns are kept in each cell to avoid this complication. The resulting set of $6N$ simultaneous equations with $6N$ unknowns can then be written in matrix form as follows:

$$\mathbf{Z}(\epsilon_r, \mu_r) \bar{X} = \bar{Y} \qquad (15)$$

where $\mathbf{Z}(\epsilon_r, \mu_r)$ is a $6N \times 6N$ matrix and $\bar{X}$ and $\bar{Y}$ are $6N \times 1$ column vectors, which are given by

$$\bar{X} = \begin{bmatrix} \bar{E}_x \\ \bar{E}_y \\ \bar{E}_z \\ \eta_0 \bar{H}_x \\ \eta_0 \bar{H}_y \\ \eta_0 \bar{H}_z \end{bmatrix} \qquad \bar{Y} = \begin{bmatrix} \bar{E}_x^i \\ \bar{E}_y^i \\ \bar{E}_z^i \\ \eta_0 \bar{H}_x^i \\ \eta_0 \bar{H}_y^i \\ \eta_0 \bar{H}_z^i \end{bmatrix}. \qquad (16)$$

The vectors $\bar{E}_p$, $\bar{H}_p$, $\bar{E}_p^i$, and $\bar{H}_p^i$ ($p = x, y, z$) are $N \times 1$ column vectors and they can be expressed as follows:

$$\bar{E}_p^i = [E_{p1}^i, E_{p2}^i, \cdots, E_{pn}^i, \cdots, E_{pN}^i]^T$$

$$\bar{E}_p = [E_{p1}, E_{p2}, \cdots, E_{pn}, \cdots, E_{pN}]^T$$

$$\bar{H}_p^i = [H_{p1}^i, H_{p2}^i, \cdots, H_{pn}^i, \cdots, H_{pN}^i]^T$$

$$\bar{H}_p = [H_{p1}, H_{p2}, \cdots, H_{pn}, \cdots, H_{pN}]^T; \qquad p = x, y, z \qquad (17)$$

where E_{pn}^i and H_{pn}^i represent the p components of the incident electric and magnetic fields, respectively, at the center of cell n and T denotes the transpose operation. Note that E_{pn} and H_{pn} were defined in (13). That is, E_{pn} and H_{pn} represent the total electric and magnetic fields, respectively, at the center of cell n.

In calculating the elements of the matrix $\mathbf{Z}(\epsilon_r, \mu_r)$, the following types of surface integrals need to be evaluated:

$$I_m = \lim_{\delta \to 0} \int_{A_{Jm} - A_{\delta m}} \frac{\partial^2}{\partial x_1, \partial x_2} H_0^{(2)}(K|\bar{\rho} - \bar{\rho}'|) \, ds'$$

$$\bar{I}_m = \lim_{\delta \to 0} \int_{A_{Jm} - A_{\delta m}} H_0^{(2)}(K|\bar{\rho} - \bar{\rho}'|) \, ds'$$

$$\tilde{I}_m = \lim_{\delta \to 0} \int_{A_{Jm} - A_{\delta m}} \frac{\partial}{\partial x_1} H_0^{(2)}(K|\bar{\rho} - \bar{\rho}'|) \, ds', \quad \begin{matrix} x_1 = x \text{ or } y \\ x_2 = x \text{ or } y \end{matrix}$$

$$(18)$$

where A_{Jm} is the area of the mth cell and $A_{\delta m}$ is the principal area located at the center of the mth cell. In general, these integrals cannot be evaluated in closed form, except for some special geometries, e.g., circular disks. Thus, some sort of numerical integration algorithm must be used to evaluate these integrals, keeping in mind that care should be exercised when the observation point is within the mth cell. The expressions given in (18), where the singularity of the integrand is isolated

by $A_{\delta m}$ as the limit $\delta \to 0$ is taken, are, in general, not suitable for practical numerical calculations. This is due to the fact that one does not know *a priori* how small $A_{\delta m}$ should be to obtain a result with a preselected accuracy. There are alternative expressions given in [19], [21] where $A_{\delta m}$ is a finite-sized pricipal area. These alternative expressions are more suitable when (18) has to be evaluated numerically.

As already mentioned, when A_{Jm} is a circular disk, the integrals in (18) can be evaluated in closed form [1], [2]. Thus, to simplify the evaluation of the elements of the matrix $Z(\epsilon_r, \mu_r)$, the square cells are replaced by circular disks of the same cross-sectional area. Furthermore, as indicated before, the principal area $A_{\delta m}$ is also assumed to be a circular disk which allows the closed-form evaluation of the integrals in (18). It is shown in the next section that this approximation, which greatly simplifies the evaluation of the elements of $Z(\epsilon_r, \mu_r)$, gives good numerical results.

The matrix $Z(\epsilon_r, \mu_r)$ in (15), which is partitioned into submatrix blocks, is then given by

$$Z(\epsilon_r, \mu_r) = \left[\begin{array}{c|c} Z_1(\epsilon_r) & Z_2(\mu_r) \\ \hline -Z_2(\epsilon_r) & Z_1(\mu_r) \end{array}\right] \quad (19)$$

where Z_1 and Z_2 are $3N \times 3N$ matrices and can also be partitioned into submatrix blocks, namely,

$$Z_1(\epsilon_r) = \left[\begin{array}{c|c|c} A & B & C \\ \hline B & I & J \\ \hline C & J & P \end{array}\right] \qquad Z_2(\mu_r) = \left[\begin{array}{c|c|c} 0 & D & F \\ \hline -D & 0 & L \\ \hline -F & -L & 0 \end{array}\right]$$

$$(20)$$

where 0 is the null $N \times N$ matrix. The matrices $A, B, C, I, J,$ $P, D, F,$ and L are $N \times N$ matrices whose elements are given by the following expressions:

A. $m \neq n$; $n, m = 1, 2, \cdots, N$

$$A_{mn} = \frac{-(\epsilon_{rn} - 1)\pi Ka_n J_1(Ka_n)}{2j} \left[k_z'^2 H_0^{(2)}(K\rho_{mn})/K^2 \right.$$

$$+ \frac{-1}{(K\rho_{mn})^3} \left[-K^3 \rho_{mn}(y_m - y_n)^2 H_0^{(2)}(K\rho_{mn}) \right.$$

$$+ \left[(y_m - y_n)^2 - (x_m - x_n)^2 \right] K^2 H_1^{(2)}(K\rho_{mn}) \right] \quad (21)$$

$$B_{mn} = \frac{-(\epsilon_{rn} - 1)\pi Ka_n J_1(Ka_n)K^2(x_m - x_n)(y_m - y_n)}{2j(K\rho_{mn})^3}$$

$$\cdot \left[2H_1^{(2)}(K\rho_{mn}) - K\rho_{mn}H_0^{(2)}(K\rho_{mn}) \right] \quad (22)$$

$$C_{mn} = -(\epsilon_{rn} - 1)\frac{\pi Ka_n}{2} J_1(Ka_n)\frac{k_z'}{K}\frac{K(x_m - x_n)}{(K\rho_{mn})} H_1^{(2)}(K\rho_{mn})$$

$$(23)$$

$$I_{mn}(x_m, x_n, y_m, y_n) = A_{mn}(y_m, y_n, x_m, x_n) \quad (24)$$

$$J_{mn}(x_m, x_n, y_m, y_n) = C_{mn}(y_m, y_n, x_m, x_n) \quad (25)$$

$$P_{mn} = -(\epsilon_{rn} - 1)\frac{\pi Ka_n}{2j} J_1(Ka_n) \; H_0^{(2)}(K\rho_{mn}) \quad (26)$$

$$D_{mn} = \frac{j\pi}{2}(Ka_n)J_1(Ka_n)(\mu_{rn} - 1)\frac{kk_z'}{K^2} H_0^{(2)}(K\rho_{mn}) \quad (27)$$

$$F_{mn} = -\frac{\pi Ka_n}{2} J_1(Ka_n)(\mu_{rn} - 1)K(y_m - y_n)\frac{k}{K}\frac{H_1^{(2)}(K\rho_{mn})}{K\rho_{mn}}$$

$$(28)$$

$$L_{mn}(x_m, x_n, y_m, y_n) = -F_{mn}(y_m, y_n, x_m, x_n) \quad (29)$$

where

$$\rho_{mn} = ((x_m - x_n)^2 + (y_m - y_n)^2)^{1/2}.$$

B. $n = m$

$$B_{mm} = C_{mm} = J_{mm} = L_{mm} = F_{mm} = 0 \quad (30)$$

$$A_{mm} = I_{mm} = 1 - \frac{(\epsilon_{rm} - 1)}{2jK^2} k_z'^2 [\pi Ka_m H_1^{(2)}(Ka_m) - 2j]$$

$$+ \frac{j(\epsilon_{rm} - 1)}{4} [\pi Ka_m H_1^{(2)}(Ka_m) - 4j] \quad (31)$$

$$P_{mm} = 1 + \frac{j}{2}(\epsilon_{rm} - 1)[\pi Ka_m H_1^{(2)}(Ka_m) - 2j] \quad (32)$$

$$D_{mm} = \frac{jkk_z'}{2K^2}(\mu_{rm} - 1)[\pi Ka_m H_1^{(2)}(Ka_m) - 2j] \quad (33)$$

where ϵ_{rn} and μ_{rn} are the relative permittivity and permeability of cell n, respectively, and the radius of the nth circular cell, denoted by a_n, is equal to $c_n/\sqrt{\pi}$. Thus, (21)-(33) completely define the matrices $Z_1(\epsilon_r)$ and $Z_2(\mu_r)$. The expressions for the elements of $Z_1(\mu_r)$ and $Z_2(\epsilon_r)$ can be easily obtained by replacing ϵ_{rn} and μ_{rn} by μ_{rn} and ϵ_{rn}, respectively, in (21)-(33). Note that by inserting the appropriate equations for the incident field, one can obtain solutions for any two-dimensional source, i.e., line source, array of line sources, etc.

Assuming that the simultaneous equations have been solved, i.e., the total E_z and H_z fields have been determined at the center of each cell, the scattered fields E_z^s and H_z^s can easily be obtained at any point outside the dielectric/ferrite body. Thus, after reintroducing the function $e^{-ik_z'z}$, the expressions for E_z^s and H_z^s are given by

$$E_z^s(x, y, z) = \frac{\pi}{2} \sum_{n=1}^{N} \frac{ka_n J_1(Ka_n)(\mu_{rn} - 1)}{\rho_n} H_1^{(2)}(K\rho_n)$$

$$\cdot \{\eta_0 H_{yn}(x - x_n) - \eta_0 H_{xn}(y - y_n)\} e^{-jk_z'z}$$

$$+ \frac{\pi}{2Kj} \sum_{n=1}^{N} a_n J_1(Ka_n)(\epsilon_{rn} - 1) \left[K^2 H_0^{(2)}(K\rho_n) \right.$$

$$\cdot E_{zn} + jk_z'\frac{K}{\rho_n} H_1^{(2)}(K\rho_n)\{E_{xn}(x - x_n)$$
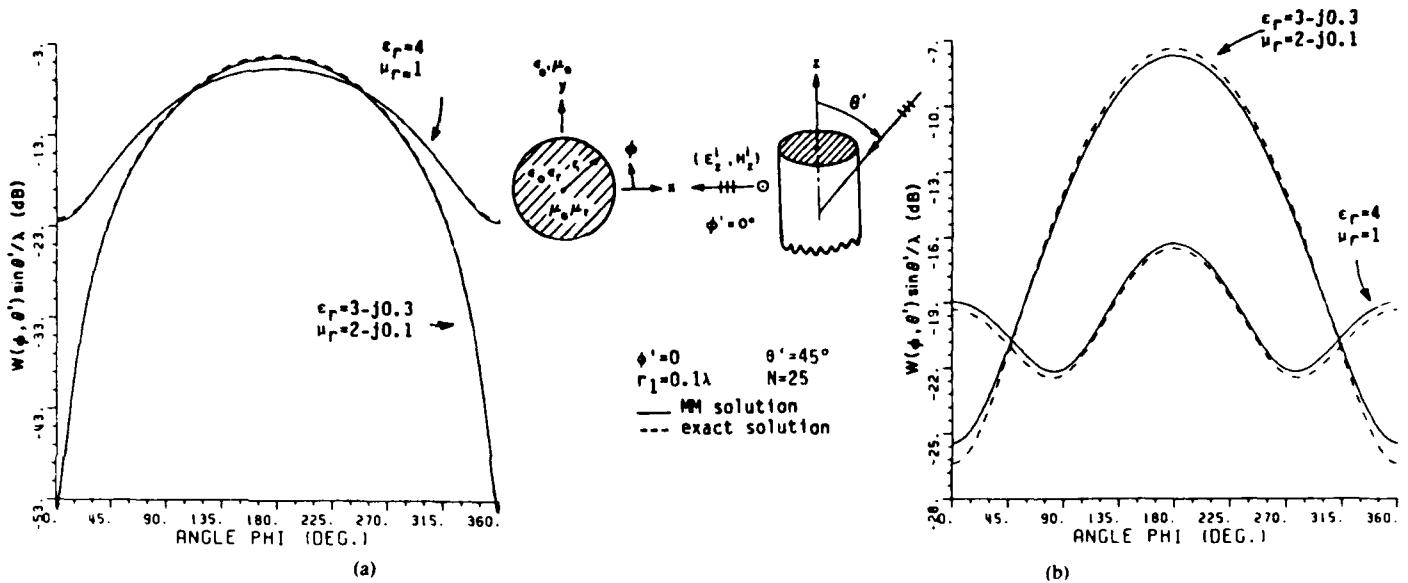
$$+ E_{yn}(y - y_n)\} \right] e^{-jk_z'z} \quad (34)$$

Fig. 2. $W(\phi, \theta')$ sin θ'/λ of circular cylinder for obliquely incident plane wave ($\theta' = 45°$). (a) TM$_z$ polarization: $E_{0z} = 1$, $\eta_0 H_{0z} = 0$. (b) TE$_z$ polarization: $E_{0z} = 0$, $\eta_0 H_{0z} = 1$.

$$\eta_0 H_z^s(x, y, z, x_n, y_n, -E_{xn}, -E_{yn},$$

$$\eta_0 H_{xn}, \eta_0 H_{yn}, \eta_0 H_{zn}, \epsilon_{rn}, \mu_{rn})$$

$$= E_z^s(x, y, z, x_n, y_n, \eta_0 H_{xn}, \eta_0 H_{yn},$$

$$E_{xn}, E_{yn}, E_{zn}, \mu_{rn}, \epsilon_{rn}) \tag{35}$$

where

$$\rho_n = [(x - x_n)^2 + (y - y_n)^2]^{1/2}.$$

The far-zone scattered fields are obtained by employing the asymptotic form of the Hankel function (large argument form) and by approximating ρ_n as follows:

$$\rho_n \sim \rho_0 - x_n \cos \phi - y_n \sin \phi; \quad \frac{1}{\rho_n} \sim \frac{1}{\rho_0} \tag{36}$$

where $\rho_0 = (x^2 + y^2)^{1/2}$. The expression for E_z^s in the far zone becomes

$$E_z^s(\rho_0, \phi, z) \sim j \frac{\pi}{2} \sqrt{\frac{2j}{\pi}} \sum_{n=1}^{N} (Ka_n) J_1(Ka_n)$$

$$\cdot \left[\frac{k}{K} (\mu_{rn} - 1)[\eta_0 H_{yn} \cos \phi - \eta_0 H_{xn} \sin \phi] \right.$$

$$\left. - (\epsilon_{rn} - 1)[E_{zn} - \frac{k_z'}{K} (\cos \phi E_{xn} + \sin \phi E_{yn})] \right]$$

$$\cdot e^{jK(x_n \cos \phi + y_n \sin \phi)} \frac{e^{jK\rho_0}}{\sqrt{K\rho_0}} e^{-jk_z'z} \tag{37}$$

and H_z^s is obtained by substituting (37) into (35).

The scattering properties of a two-dimensional body can be expressed in terms of its echo width. The echo width $W(\phi, \theta')$ is defined as follows [18]:

$$W(\phi, \theta') = \lim_{\rho_0 \to \infty} 2\pi\rho_0 \frac{|\vec{E}^s(\rho, \phi, \theta')|^2}{|\vec{E}^i|^2}. \tag{38}$$

Substituting (4), (5), (35), and (37) into (38) yields the following expression for the echo width per wavelength:

$$\frac{W(\phi, \theta')}{\lambda} = \lim_{\rho_0 \to \infty} k\rho_0 \frac{|E_z^s|^2 + |\eta_0 H_z^s|^2}{|E_{0z}|^2 + |\eta_0 H_{0z}|^2} \tag{39}$$

where λ is the free-space wavelength.

Note that for the case of oblique incidence, the scattered field will have both TM$_z$ and TE$_z$ polarized fields regardless of the polarization of the incident plane wave field. In the next section, $W(\phi, \theta')$ sin θ'/λ will be calculated for various geometries for a TM$_z$ and TE$_z$ polarized incident plane wave field, respectively.

IV. NUMERICAL RESULTS

The results obtained in Section III have been implemented with a Fortran program on a VAX 11/780 computer. Using (35), (37), and (39), numerical results were obtained for the following geometries.

A. Cylinder of Circular Cross Section

Figs. 2(a) and 2(b) depict the echo width of a circular cylinder of radius 0.1λ for obliquely incident ($\theta' = 45°$) TM$_z$ ($E_{0z} = 1$, $H_{0z} = 0$) and TE$_z$ polarized ($E_{0z} = 0$, $\eta_0 H_{0z} = 1$) plane wave fields, respectively. For each polarization, two sets of values of (ϵ_r, μ_r) are considered to illustrate the effect of ϵ_r and μ_r on the echo width. As indicated in the previous sections, the circular cylinder is divided into cells whose cross-sectional areas must be as close to squares as possible. It is known from experience [1], [2] that, to obtain good numerical results, c must satisfy the inequality

$$\frac{c}{\lambda} \le \frac{0.1}{\sqrt{\epsilon_r \mu_r}}$$

where c is the length of one side of the square cell. In other words, c should be less than or equal to one-tenth the wavelength inside the dielectric cylinder. The cylinder in Fig.

Fig. 3. $W(\phi, \theta')\sin\theta'/\lambda$ of cylindrical shell of circular cross-section shape. (a) TM_z polarization: $E_{0z} = 1$, $\eta_0 H_{0z} = 0$. (b) TE_z polarization: $E_{0z} = 0$, $\eta_0 H_{0z} = 1$.
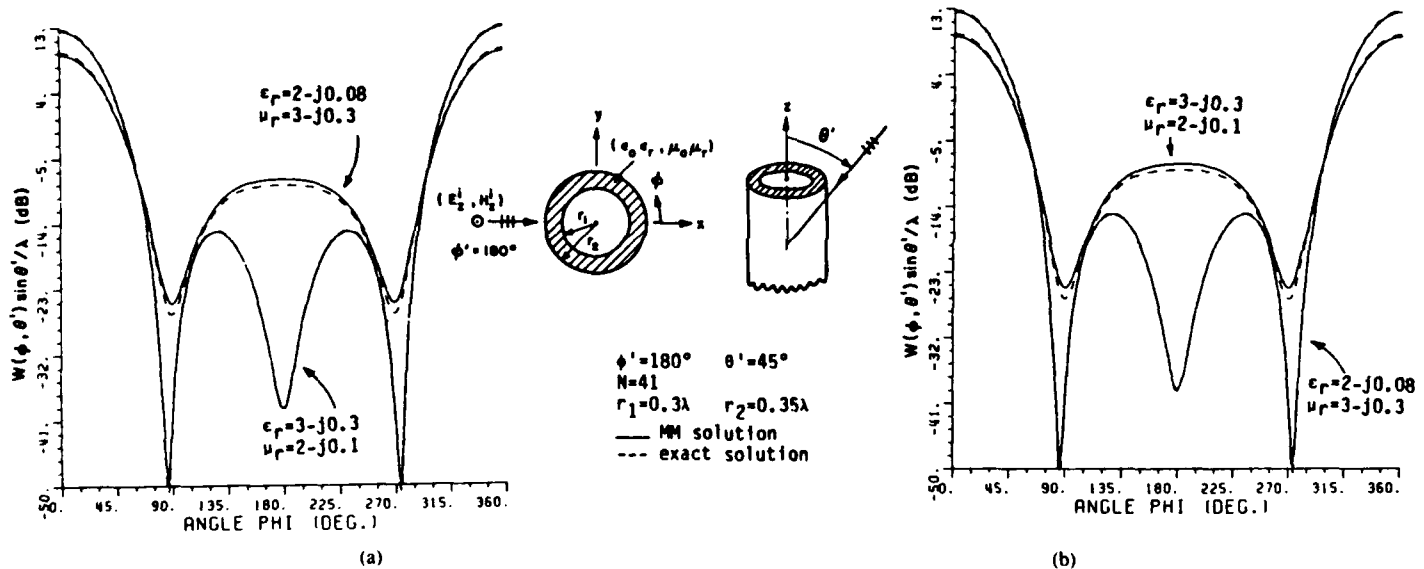
Fig. 4. $W(\phi, \theta')\sin\theta'/\lambda$ of cylindrical shell of circular cross-section shape for obliquely incident plane wave ($\theta' = 45°$). (a) TM_z polarization: $E_{0z} = 1$, $\eta_0 H_{0z} = 0$. (b) TE_z polarization: $E_{0z} = 0$, $\eta_0 H_{0z} = 1$.

2 was divided into 25 square cells ($N = 25$) of the same cross-sectional area, i.e., $(3.54 \times 10^{-2}\lambda)^2$. The moment method solutions for the circular cylinder shown in Fig. 2 are compared with the exact eigenfunction solutions which consist of infinite series involving Bessel and Hankel functions [22]. Note that the agreement between these two independent solutions is very good.

B. Cylindrical Shell of Circular Cross Section

In Figs. 3(a) and 3(b), the echo width of a circular cylindrical shell is depicted for a TM_z and TE_z incident plane wave, respectively. In both cases, the shell was divided into 66 cells ($N = 66$) and the solutions for a normally and obliquely incident plane wave are depicted. In Fig. 4 a shell with different dimensions was considered. The angle θ' was set to 45° and the parameters ϵ_r and μ_r were changed to illustrate the effect of these parameters on the echo width. Note that for the

TM_z case, the echo width in the backscattered direction ($\phi = 180°$) is significantly reduced when the values of ϵ_r and μ_r are changed from $\epsilon_r = 2 - j0.08$, $\mu_r = 3 - j0.3$ to $\epsilon_r = 3 - j0.3$, $\mu_r = 2 - j0.1$. The opposite effect is observed for the TE_z case as shown in Fig. 4(b). The shell was divided into 41 cells ($N = 41$) which means that a system of 246 simultaneous equations was solved. It took about 3 min of CPU time on a VAX 11/780 computer to obtain the moment method solution for each polarization considered in Fig. 4. As in the case for the circular cylinder, the moment method solutions for the circular shell are compared with the exact eigenfunction solutions. The agreement between the two solutions is very good as illustrated in Figs. 3 and 4.

C. Semicircular Shell

Figs. 5(a) and 5(b) show the echo width of a semicircular shell which was divided into 20 cells of the same cross-
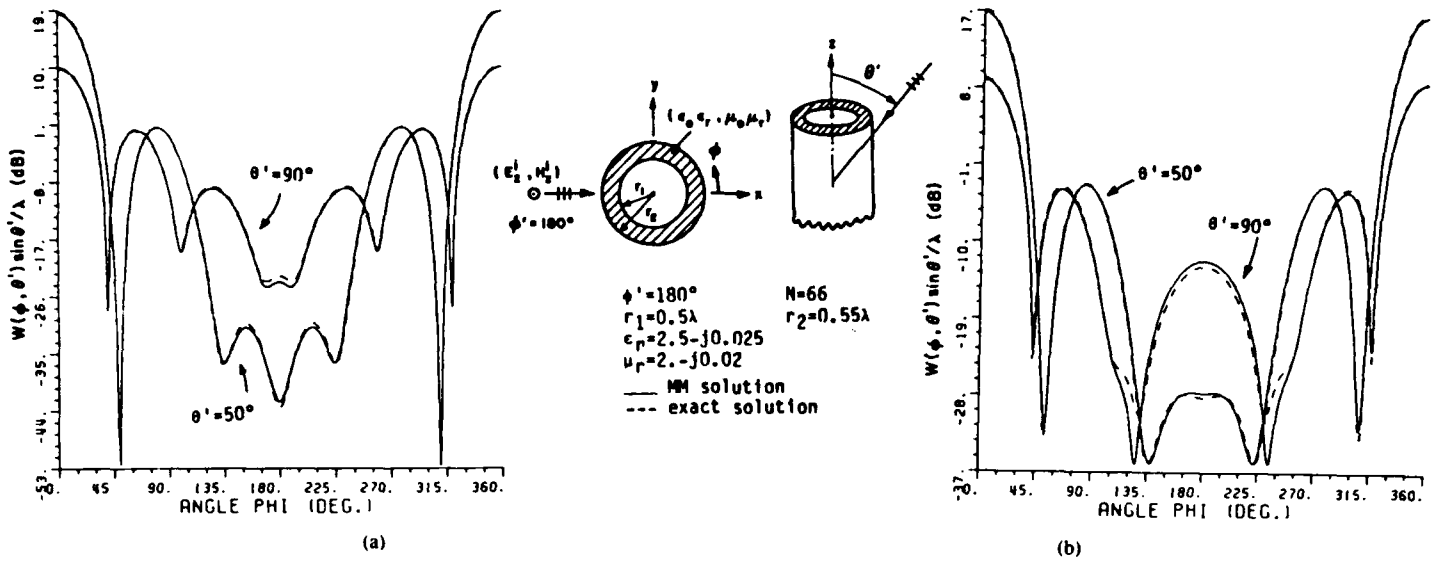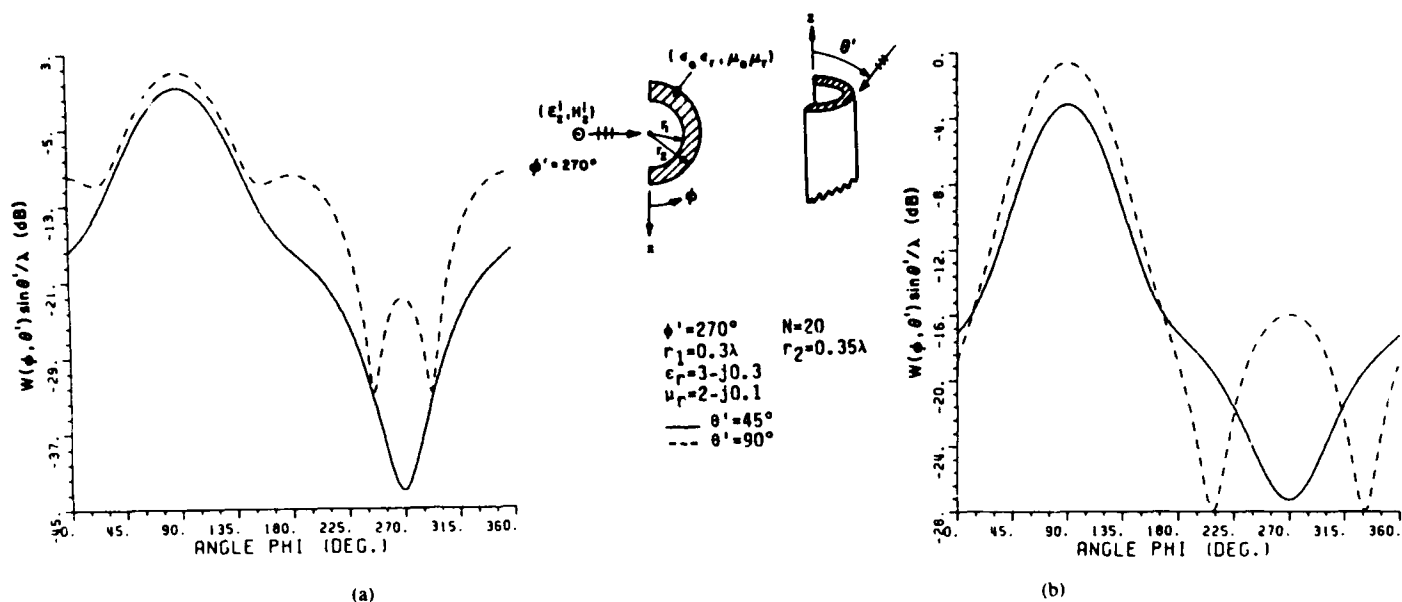
Fig. 5. $W(\phi, \theta')$ sin θ'/λ of cylindrical shell of semicircular cross-section shape. (a) TM$_z$ polarization: $E_{0z} = 1$, $\eta_0 H_{0z} = 0$. (b) TE$_z$ polarization: $E_{0z} = 0$, $\eta_0 H_{0z} = 1$.
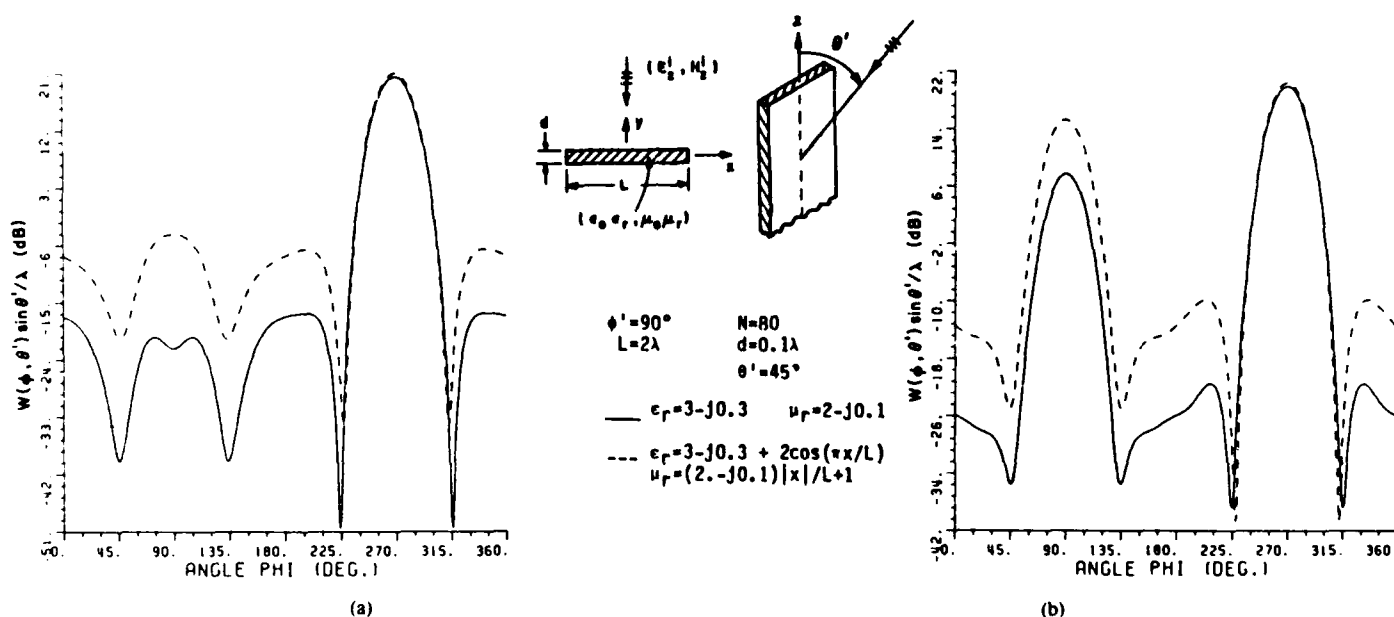

Fig. 6. $W(\phi, \theta')$ sin θ'/λ of cylinder of rectangular cross-section shape excited by broadside incident plane wave. (a) TM$_z$ polarization: $E_{0z} = 1$, $\eta_0 H_{0z} = 0$. (b) TE$_z$ polarization: $E_{0z} = 0$, $\eta_0 H_{0z} = 1$.

sectional area. Both the TM$_z$ and TE$_z$ polarizations are considered; however, no exact solution is available for this geometry to compare with the solutions obtained here. To study the effect of the angle θ' on the echo width, Fig. 5 shows the echo width calculated for a normally and obliquely incident plane wave, respectively.

D. Cylinder of Rectangular Cross Section

Finally, in Figs. 6 and 7, the echo width of a cylinder of rectangular cross section is considered. In Fig. 6, the angle of incidence is $\phi' = 90°$ (broadside), while in Fig. 7, the case of grazing incidence is considered ($\phi' = 0°$). Note that in both cases $\theta' = 45°$ and unlike the previous examples, the cylinder

is allowed to be inhomogeneous. First, the echo width of a homogeneous rectangular slab is calculated for $\epsilon_r = 3. - j0.3$ and $\mu_r = 2. - j0.1$. Next, the same slab is assumed to be inhomogeneous (in x), namely,

$$\epsilon_r(x) = 3. - j0.3 + 2 \cos (\pi x/L)$$

$$\mu_r(x) = (2. - j0.1)|x|/L + 1$$

where x varies from $-L/2$ to $L/2$ and L is the width of the rectangular slab. Since the integral equations in (11) and (12) are enforced at the center of each nth cell, ϵ_r and μ_r have to be evaluated at (x_n, y_n). Thus ϵ_{rn} and μ_{rn} can be written as

Fig. 7. $W(\phi, \theta')\sin\theta'/\lambda$ of cylinder of rectangular cross-section shape excited by plane wave having grazing incidence. (a) TM_z polarization: $E_{0z} = 1$, $\eta_0 H_{0z} = 0$. (b) TE_z polarization: $E_{0z} = 0$, $\eta_0 H_{0z} = 1$.
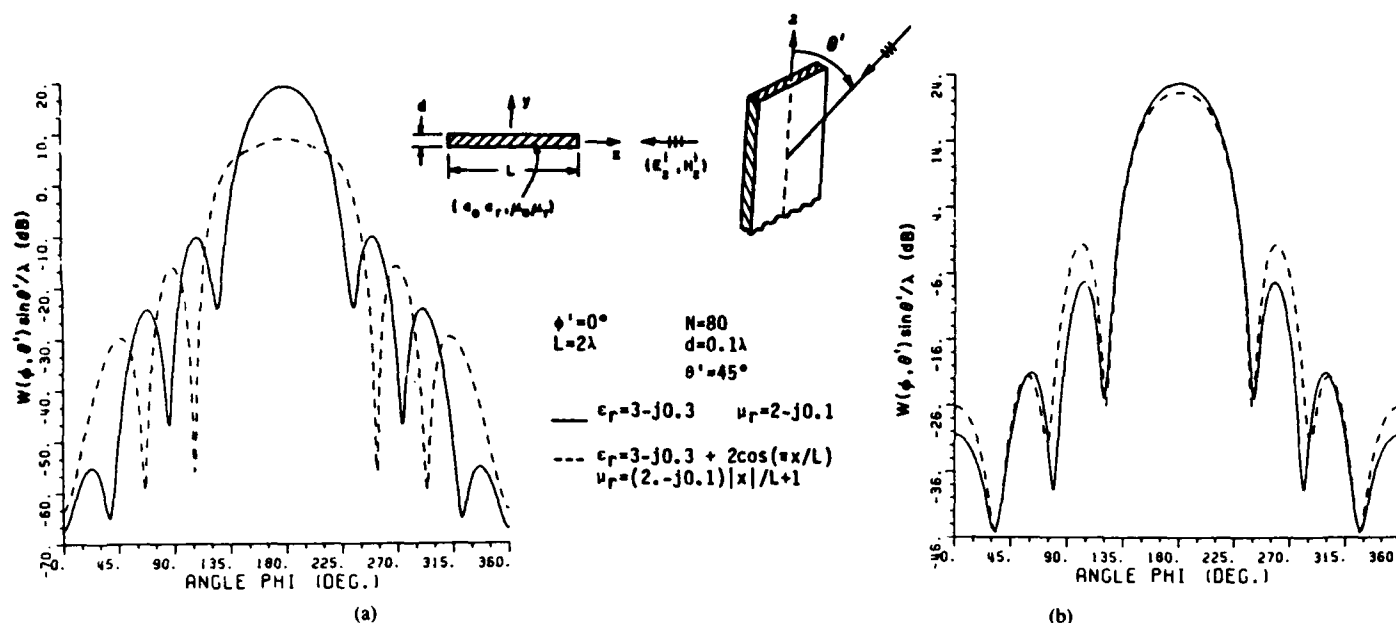
follows:

$$\epsilon_{rn}(x_n) = 3. - j0.3 + 2\cos(\pi x_n/L)$$

$$\mu_{rn}(x_n) = (2 - j0.1)|x_n|/L + 1.$$

Since the cylinder was divided into 80 identical square cells, a system of 480 simultaneous equations was solved. As in the case for the semicircular shell, no exact solution is available for the cylinder of rectangular cross section.

V. CONCLUSION

A moment method solution has been developed to calculate the scattering by a dielectric/ferrite cylinder of arbitrary cross-section shape. Even though the cylinder is assumed to be linear and isotropic, it can be inhomogeneous and lossy. It is noted that for the problems considered here, the integral equations for the electric and magnetic fields are coupled. The solution of this pair of integral equations was obtained by transforming them into a system of simultaneous linear equations by choosing appropriate basis and testing functions. In this paper, pulse and Dirac delta functions were chosen for the basis and testing functions, respectively.

It is possible to improve the accuracy of the solutions presented here by evaluating the integrals in (18) numerically over the square cells; however, this obviously will increase the CPU time. An alternative approach is to follow the procedure described in [23] where the square cells are still approximated by circular disks, but a new set of basis functions is used which takes into account the variation of the fields within each cell. This method, as shown in [23], allows the use of larger cells resulting in a smaller matrix. However, the calculation of each element of the matrix is more difficult than in the method followed here. It is noted that, in the solutions presented here, their sensitivity to errors in the calculation of the elements of the matrix Z can be checked by computing the condition

number of Z. Unfortunately, as pointed out in [24], the condition number will not indicate whether the best expansion functions are being used. Finally, several numerical examples were presented and compared with the exact eigenfunction solutions when they were available. The agreement between the independent MM and exact solutions was shown to be very good for the cases considered here. An interesting feature of the case of oblique incidence in problems involving dielectric/ferrite cylinders, which does not hold for the special case of normal incidence, is that the scattered field has TE_z and TM_z polarized components regardless of the polarization (TM_z or TE_z) of the incident field.

REFERENCES

[1] J. H. Richmond, "Scattering by a dielectric cylinder of arbitrary cross section shape," IEEE Trans. Antennas Propagat., vol. AP-13, pp. 334-341, May 1965.

[2] ——, "TE-wave scattering by a dielectric cylinder of arbitrary cross-section shape," IEEE Trans. Antennas Propagat., vol. AP-14, pp. 460-464, July 1966.

[3] E. H. Newman, "TM scattering by a dielectric cylinder in the presence of a half-plane," IEEE Trans. Antennas Propagat., vol. AP-33, pp. 773-782, July 1985.

[4] ——, "TM and TE scattering by a dielectric/ferrite cylinder in the presence of a half-plane," IEEE Trans. Antennas Propagat., vol. AP-34, pp. 804-813, June 1986.

[5] K. M. Chen, D. E. Livesay, and B. S. Guru, "Induced current in and scattered field from a finite cylinder with arbitrary conductivity and permittivity," IEEE Trans. Antennas Propagat., vol. AP-24, pp. 330-336, May 1976.

[6] D. H. Schaubert, D. R. Wilton, and A. W. Glisson, "A tetrahedral modelling method for electromagnetic scattering by arbitrarily shaped inhomogeneous dielectric bodies," IEEE Trans. Antennas Propagat., vol. AP-32, pp. 77-85, Jan. 1984.

[7] D. E. Livesay and K. M. Chen, "Electromagnetic fields induced inside arbitrarily shaped biological bodies," IEEE Trans. Microwave Theory Tech., vol. MTT-22, pp. 1273-1280, Dec 1974.

[8] N. Morita, "Surface integral representations for electromagnetic scattering from dielectric cylinders," IEEE Trans. Antennas Propagat., vol. AP-26, pp. 261-266, Mar. 1978.

[9] K. Umashankar, A. Taflove, and S. M. Rao, "Electromagnetic scattering by arbitrary shaped three-dimensional homogeneous lossy

An Overview of the Hybrid MM/Green's Function

Method in Electromagnetics

Edward H. Newman

An Overview of the Hybrid MM/Green's Function Method in Electromagnetics

EDWARD H. NEWMAN, SENIOR MEMBER, IEEE

This paper presents an overview of a hybrid technique for solving electromagnetic radiation and scattering problems by combining the method of moments (MM) with a special Green's function. The method, commonly referred to as an MM/Green's function solution combines the ability of MM solutions to treat geometrically complex bodies with the accuracy and computational efficiency of Green's function solutions. As compared to a standard MM solution, the MM/Green's function solution reduces the number of unknowns, and thus reduces the computer storage requirements. In most, but not all cases, the CPU time for the MM/Green's function solution is considerably less than that for a standard MM solution. The basic formalism of the MM/Green's function solution is presented and contrasted to that of the standard MM solution. The example problem of TM scattering by a semicircular strip in the presence of a circular cylinder is solved by the MM, and by the MM/Green's function technique with a matrix, exact eigenfunction, and high-frequency Green's function.

I. INTRODUCTION

This paper will present an overview of a technique which combines the method of moments (MM) [1]-[3] and a Green's function [4] in the solution of electromagnetic radiation and scattering problems. The technique is termed an MM/Green's function solution and combines the flexibility of MM solutions for treating scatterers of complex geometry with the accuracy and computational efficiency of Green's function solutions.

A general problem in electromagnetics is that of finding the fields of known or impressed currents radiating in a vacuum or homogeneous medium in which is present one or more inhomogeneities or scatterers. Traditionally these problems have been solved by what can be called Green's function techniques. That is, one attempts to find either exact or approximate explicit formulas, known as Green's functions, for the fields of an infinitesimal current element radiating in the presence of the scatterers and/or boundaries. The fields of the known impressed current are then found by superposition, that is by integrating through the

region of the current the vector dot product of the current distribution and the dyadic Green's function. Green's functions tend to be highly accurate and, as compared to MM solutions, in many cases they are computationally efficient in that they can be evaluated with a minimum of effort. The main limitation of Green's function solutions is that, except for a few simple shapes [4]-[6], the Green's functions are difficult to obtain, with each new geometry requiring a new analysis.

With the widespread availability of high-speed digital computers in the mid-1960s, a numerical technique known as the method of moments (MM) [1]-[3] began to gain popularity. Consider the standard MM solution for a problem involving two scatterers, which we term Scatterer 1 and Scatterer 2. The first step is to use the surface and/or volume equivalence theorems [1], [7] to replace both scatterers by free-space and equivalent currents. An exact integral equation for the equivalent currents is then formulated and involves the relatively simple free-space Green's function in its kernel. The unknown equivalent currents are then expanded as a finite sum of N_1 basis or expansion functions on Scatterer 1 and N_2 basis functions on Scatterer 2. N_1 and N_2 weighted averages of the integral equation are enforced on Scatterers 1 and 2, respectively. This transforms the integral equation into an order $N_1 + N_2$ matrix equation, which can be solved for the $N_1 + N_2$ coefficients in the expansion for the equivalent currents. The total fields radiated by the impressed currents in the presence of the two scatterers is the sum of the free-space fields of the impressed currents and the equivalent currents on Scatterers 1 and 2. The main advantages of the MM approach are that it is accurate and extremely versatile as to the geometries which it can treat. For example, while the exact Green's function solution for scattering by a dielectric cylinder appears only to be possible for the circular cross section [6], MM solutions are available for the scattering by dielectric cylinders of essentially arbitrary cross section [8], [9]. However, as compared to Green's function techniques, MM solutions usually require more computational effort.

In an MM/Green's function solution to the same two scatterer problem described above, Scatterer 1, but not Scatterer 2, is replaced by free-space and equivalent currents. An exact integral equation for the equivalent currents representing Scatterer 1 is formulated and will involve the rel-

atively complicated Scatterer 2 (as compared to the free-space) Green's function in its kernel. The unknown equivalent currents on Scatterer 1 are expanded as a finite sum of N_1 basis functions. N_1 weighted averages of the integral equation are enforced on Scatterer 1. This transforms the integral equation into an order N_1 matrix equation, which can be solved for the N_1 coefficients in the expansion for the current on Scatterer 1. The total fields radiated by the impressed currents in the presence of the two scatterers is the sum of the fields of the impressed currents and the equivalent currents on Scatterer 1, both radiating in the presence of Scatterer 2.

As compared with the Green's function technique, the MM/Green's function method has the advantage that it is applicable to a much wider class of geometries. This is because the MM/Green's function method requires that we know the Green's function for either Scatterer 1 or 2, while the Green's function method requires that we can find the Green's function for the combination of Scatterer 1 in the presence of Scatterer 2. As compared to a standard MM solution, the MM/Green's function method has the advantages that the number of unknowns in the matrix equation is reduced from $N_1 + N_2$ to N_1, thus reducing the required computer storage. The disadvantages of the MM/Green's function technique is that since the kernel of its integral equation involves the relatively complicated Scatterer 2 Green's function, the evaluation of a typical element in the MM/Green's function matrix equation is more difficult and time-consuming than that in a standard MM solution. However, if Scatterer 2 is substantially larger than Scatterer 1, then $N_2 \gg N_1$, and the CPU time for the MM/Green's function solution is almost always considerably less than that of the standard MM solution.

Probably the most common use of MM/Green's function solutions has been for problems involving antennas in the presence of a plane dielectric interface, such as a flat earth. In this case, the antenna is Scatterer 1 and the dielectric half space, representing the earth, is Scatterer 2. Of the many papers in this area we mention the work of the group at Lawrence Livermore Laboratory [10]-[13], much of which has been incorporated into a user-oriented computer code [14], the solution of Chang and Wait for a vertical wire over the earth [15], the use of ray methods by Tiberio et al. to represent the energy reflected from the earth [16], and the use by Parhami and Mittra of an approximate but highly accurate representation of the exact half space Green's function [17]. Solutions for obstacles other than wires in the presence of a flat earth have also been presented in [18]-[20]. A closely related problem is that of printed circuit antennas. Here the printed circuit antenna is Scatterer 1 and the dielectric substrate is Scatterer 2. Again, there are a large number of papers, and we mention MM/Green's function solutions for microstrip antennas by Pozar [21], [22], Newman and Forrai [23], and Bailey and Deschamps [24]. In addition, Alexopoulos et al. have published several papers on printed circuit dipoles [25], [26]. A second related area is that of periodic arrays in multilayered dielectric slabs of which [27], [28] are representative.

Another popular use of MM/Green's function solutions has been for problems involving antennas or other obstacles in waveguides and cavities. In these cases, Scatterer 1 was the antenna and Scatterer 2 was the waveguide or cavity. Possibly the first MM/Green's function solution was

Rao's [29], [30] analysis of a two-element Yagi array in a parallel plate waveguide in 1965. It is interesting that this work was done before Harrington [2] published his description of the MM in 1967. Other work involving wires in waveguides or cavities include Taylor's [31] and Tesche's [32] solutions for a wire in a parallel plate waveguide, and Seidel's [33] solution for a wire in a cavity. MM/Green's function solutions for posts in waveguides have been done by Leviatan et al. [34], Auda and Harrington [35], and Jarem [36]. Material bodies in waveguides have been analyzed by Wang [37], Omar and Schunemann [38], and Hsu and Auda [39]. Khac and Carson [40] have analyzed a slot in a waveguide and Thong [41] has analyzed waveguide discontinuities.

Several MM/Green's function solutions have been obtained for cases in which Scatterer 2 is one of the classical shapes which fits into a separable coordinate system, and thus has a well-known Green's function. Solutions for wires in the presence of spheres have been presented by Tesche, Neureuther, and Stovall [42]-[44] and by Butler and Keshavamurthy [45]. MM/Green's function solutions involving circular cylinders have been done by Misra and Chen [46], Steyskal [47], Karunaratne et al. [48], and Lamensedorf and Ting [49]. Wire antennas near the edge of a half-plane or a wedge have been analyzed by Pozar and Newman [50], [51]. Newman has analyzed a material cylinder of arbitrary cross section in the presence of a half-plane [52], [53], and Newman and Blanchard [54] have analyzed an impedance sheet in the presence of a parabolic cylinder. Section III of this paper presents an analysis for a semicircular strip in the presence of a circular cylinder.

Most of the above referenced works were natural MM/Green's function solutions in that Scatterer 2 was one of the few shapes for which an exact Green's function was known. Thiele and Newhouse [55] greatly expanded the range of problems which could be solved via the MM/Green's function technique by recognizing that the geometrical theory of diffraction (GTD) [56] could be used to obtain the asymptotic or high-frequency Green's function for a large class of electrically large bodies (Scatterer 2). This important special case of the MM/Green's function technique, where the GTD is used to evaluate the Green's function, is referred to as an MM/GTD solution. For problems involving electrically small and large parts, MM/GTD solutions are ideal since the MM can efficiently treat the electrically small part of the problem (Scatterer 1), while the GTD can efficiently treat the electrically large part (Scatterer 2). The earliest use of the MM with an asymptotic Green's function appears to be that of Green [57] for a monopole on the base of a large cone. Other applications include that by Awadalla and Maclean [58], [59] and by Marin and Catedra [60] to analyze a monopole on a plate. MM/GTD solutions for wires on curved surfaces have been presented by Ekelman and Thiele [61] and by Henderson and Thiele [62], [63]. Thiele and Chan [64] have used the MM/GTD to efficiently generate large amounts of frequency domain data so that the Fourier transform could be used to obtain time domain results. Also, Ko and Mittra [65] have developed an iterative MM/GTD solution which allows for a check as to how well the solution satisfies the boundary conditions.

Harrington and Mautz [66] and Glisson and Butler [67] showed that for a Scatterer 2 geometry which is so complex that it is not feasible to obtain a functional expression for its Green's function, an MM/Green's function solution is

still possible. This is done using a numerical Green's function which is evaluated by an MM solution of Scatterer 2. Harrington and Mautz used the MM to find the numerical Green's function for a body of revolution. Glisson and Butler applied the MM/Green's function technique, with numerical Green's function, to the problem of a wire (Scatterer 1) in the presence of a body of revolution (Scatterer 2). The concept of a numerical Green's function is similar to Harker's [68] matrix partitioning method and to the matrix Green's function discussed in the next section.

There are several hybrid techniques, related to the MM/Green's function technique, which will not be treated in this paper. In particular, we mention the so-called GTD/MM technique which uses the MM to numerically evaluate an unknown diffraction coefficient [69]-[71]. Thiele et al. have developed a hybrid theory of diffraction (HTD) which uses a high-frequency approximation for the current on a portion of the body and the MM on the remainder [72], [73]. In a related technique, Mitschang and Wang incorporate the high-frequency currents into the MM solution for scattering by a body of revolution [74]. Azarbar and Shafai [75] efficiently analyzed large reflector antennas by employing an MM solution which solved for the difference between the actual and the physical optics currents on the surface of the reflector. Finally, Richmond [76] has developed a physical basis technique for an MM solution of a wide dielectric strip which involves only three basis functions.

Section II of this paper presents the basic formalism for a standard MM solution and an MM/Green's function solution. The two methods are compared and the concept of of a matrix Green's function is introduced. Section III solves the example problem of TM scattering by a perfectly conducting semicircular strip in the presence of a perfectly conducting circular cylinder by a standard MM solution, and by the MM/Green's function method using a matrix, exact eigenfunction, and GTD Green's function. Section IV briefly summarizes the main points of this paper.

II. MM AND MM/GREEN'S FUNCTION FORMULATIONS

A. Problem Geometry

This section will outline the MM and MM/Green's function solution for the scattering by two perfectly conducting scatterers. The basic geometry is shown in Fig. 1(a). Here we have the impressed currents, (J^i, M^i), radiating in the presence of two perfectly conducting obstacles, termed Scatterers 1 and 2, and producing the total fields (E, H). In free-space the impressed currents radiate the incident fields (E^{i0}, H^{i0}). Scatterer 1 is enclosed by the surface S_1 which has outward unit normal $\hat{n}_1$, and similar definitions apply to Scatterer 2. The ambient medium is free-space with permeability and permittivity (μ_0, ϵ_0). All fields and currents are time harmonic, with the $e^{i\omega t}$ time dependence suppressed. Here $\omega = 2\pi f$ is the radian frequency, λ denotes the free-space wavelength, and $k = 2\pi/\lambda$. For simplicity, we present the MM and MM/Green's function solution for perfectly conducting obstacles, and unless specifically noted, all general remarks apply equally well to problems involving penetrable scatterers.

The MM and MM/Green's function solutions can be notationally complex, involving many quantities, some of which differ only slightly in their meaning. To minimize confusions we introduce a notation based upon subscripts and
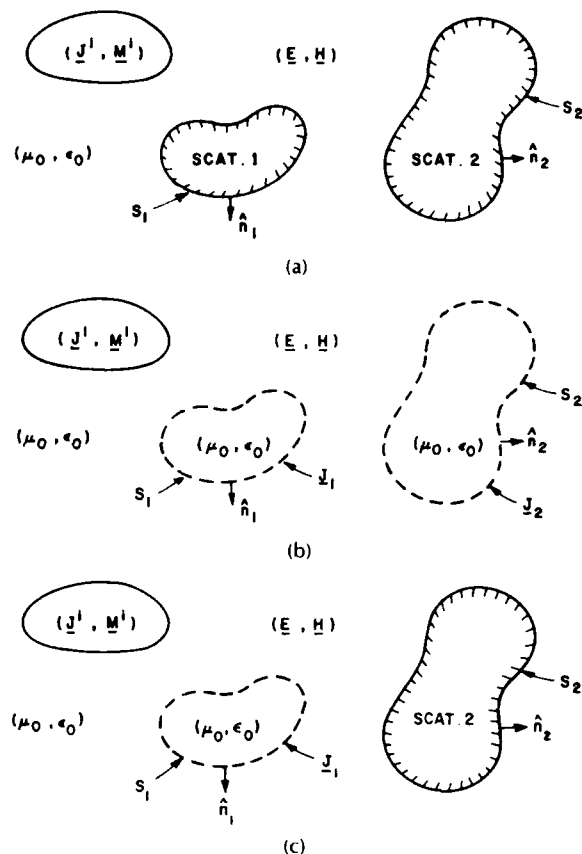
Fig. 1. (a) In the original problem the impressed currents radiate in the presence of two perfectly conducting scatterers. (b) In the standard MM solution, both scatterers are replaced by free-space and equivalent currents. (c) In the MM/Green's function solution, only Scatterer 1 is replaced by free-space and equivalent currents.

superscripts. For example, we use the notation of the superscripts $^0, ^2$, or ^{S2}, to indicate a quantity computed from the fields of a current in free-space, in the presence of Scatterer 2, or the fields scattered from Scatterer 2, respectively. The subscripts $_1$ or $_2$ will be used to denote a quantity associated with Scatterers 1 or 2, respectively. The integer subscripts $_m$ and $_n$ are used to refer to MM basis function numbers, while the integer subscript $_p$ refers to term p in a cylindrical eigenfunction expansion. Finally, the superscript $'$ denotes a quantity associated with the impressed currents. This notation is summarized in Table 1.

Table 1 Summary of Superscript and Subscript Notation

Notation	Implies a Quantity Associated with . . .
Superscript 0	the free-space fields of a current
Superscript 2	the fields in the presence of Scatterer 2
Superscript S2	the fields scattered from Scatterer 2
Subscript 1	Scatterer 1 or the N_1 modes on Scatterer 1
Subsript 2	Scatterer 2 or the N_2 modes on Scatterer 2
Superscript i	the impressed currents (J^i, M^i)
Subscript m or n	MM modes m or n
Subscript p	cylindrical eigenfunction term p

B. MM Solution

As illustrated in Fig. 1(b), the first step in the standard MM solution is to replace all matter, i.e., Scatterers 1 and 2, by

free-space and by the equivalent electric surface current density J where

$$J = \begin{cases} J_1 = \hat{n}_1 \times H & \text{on } S_1 \\ J_2 = \hat{n}_2 \times H & \text{on } S_2. \end{cases} \quad (1)$$

Note that J is unknown since H is unknown, however, J will be found in the MM solution. By definition, the scattered fields are the difference between the total fields and the incident fields. In the equivalent problem of Fig. 1(b), the scattered fields are the free-space fields of J, denoted $(E^0(J), H^0(J))$. In this case, the total fields are

$$E = E^{i0} + E^0(J) \quad (2)$$

$$H = H^{i0} + H^0(J). \quad (3)$$

Note that we use the notation of superscript ^{0} to imply the free-space fields of a current distribution.

An electric field integral equation (EFIE) for J is obtained by enforcing the boundary condition that the total electric field tangential to S_1 and S_2 must vanish on the surfaces S_1 and S_2. Then from (2)

$$-E^0(J) = E^{i0} \text{ tangential components on } S_1 \text{ and } S_2. \quad (4)$$

Equation (4) is an integral equation for J since

$$E^0(J) = \iint_{S_1 + S_2} J \cdot \overline{G}^0 \, ds' \quad (5)$$

where $\overline{G}^0$ is the dyadic free-space Green's function [4]. Basically $\overline{G}^0$ is a 3×3 matrix which gives the free-space vector electric field of an arbitrarily oriented infinitesimal electric current element. For example, in the rectangular coordinate system, the i, j element of $\overline{G}^0$ is the $\hat{x}, \hat{y},$ or $\hat{z}$ polarization (for $j = 1, 2, 3$) of the free-space electric field due to an infinitesimal electric current element with dipole orientation $\hat{x}, \hat{y},$ or $\hat{z}$ (for $i = 1, 2, 3$).

Equation (4) must now be solved for J. The first step is to expand J in terms of an appropriate set of expansion, basis, or interpolating functions. Thus we write

$$J = \sum_{n=1}^{N} I_n J_n \quad (6)$$

where the J_n are a set of N known linearly independent basis functions defined on S_1 and S_2, and the I_n are a set of N unknown coefficients ($n = 1, 2, \cdots, N$). Denoting $E^0(J_n)$ as the free-space electric field of J_n, and substituting (6) into (4) yields

$$-\sum_{n=1}^{N} I_n E^0(J_n) = E^{i0}$$

$$\text{tangential components on } S_1 \text{ and } S_2. \quad (7)$$

Now define a set of N linearly independent vector weighting functions, $w_m (m = 1, 2, \cdots, N)$, on and tangential to the surfaces S_1 and S_2. If in (6) the first N_1 expansion functions are on S_1 and the last N_2 are on $S_2 (N = N_1 + N_2)$, then the first N_1 weighting functions are on S_1 and the last N_2 are on S_2. Taking the inner product of both sides of (7) with each of the N weighting functions converts (7) into an $N \times N$ system of simultaneous linear algebraic equations which can be written in matrix form as

$$[Z^0][I] = [V^0] \quad (8)$$

where $[Z^0]$ is the $N \times N$ impedance matrix, $[V^0]$ is the length N right-hand-side or voltage vector, and $[I]$ is the length N solution or current vector which contains the $N = N_1 + N_2$ coefficients in the original expansion for the current in (6). Typical elements of $[Z^0]$ and $[V^0]$ are given by

$$Z^0_{mn} = -\iint_m E^0(J_n) \cdot w_m \, ds$$

$$= -\iint_m \left[\iint_n J_n \cdot \overline{G}^0 \, ds' \right] \cdot w_m \, ds \quad (9)$$

$$V^0_m = \iint_m E^{i0} \cdot w_m \, ds. \quad (10)$$

As indicated in (9) and (10) the ds integrals are over the surface of the mth weighting function, while the ds' integrals are over the surface of the nth expansion function.

Assuming N_1 basis functions are employed on Scatterer 1, and N_2 basis functions on Scatterer 2, Fig. 2 shows the matrix equation (8) partitioned into blocks, corresponding to the basis functions on Scatterers 1 and 2. Here $[Z^0_{11}]$ is the

$$[Z^0] \qquad [I] = [V^0]$$

Fig. 2. The standard MM matrix equation is partitioned into blocks related to basis functions on Scatterers 1 and 2.

$N_1 \times N_1$ block of $[Z^0]$ which represents coupling between basis functions on Scatterer 1, $[Z^0_{12}]$ is the $N_1 \times N_2$ block of $[Z^0]$ which represents coupling between basis functions on Scatterer 1 and basis functions on Scatterer 2, $[I_1]$ is the first N_1 elements of $[I]$ containing the coefficients of the expansion functions on Scatterer 1, etc. Note that $[Z^0_{11}]$ and $[Z^0_{22}]$ are the MM impedance matrices for isolated Scatterer 1 or Scatterer 2, respectively, in free-space. Similarly, $[V^0_1]$ and $[V^0_2]$ are the voltage vectors for isolated Scatterer 1 or Scatterer 2, respectively, in free-space. As shown in Table 1, the notation being used is that the subscript $_1$ indicates a quantity associated with the first N_1 basis functions on Scatterer 1, while the subscript $_2$ indicates a quantity associated with the N_2 basis functions on Scatterer 2.

Using standard techniques of matrix algebra, (8) can now be solved for the current vector $[I]$ which when substituted into (6) provides an approximation to the current on the scatterers. In principle, as N is increased, a well-formulated MM solution approaches the exact solution. For problems which are formulated in terms of an unknown surface current density, the number of unknowns, N, which must be retained in the MM solution is proportional to the electrical surface area $(S_1 + S_2)/\lambda^2$, with values from 24 to 100 basis functions per λ^2 being typical.

The CPU time necessary to compute $[Z^0]$ is proportional to N^2. The CPU time to solve (8) tends to be proportional to N^2 for small to modest N, but to N^3 for large N. Thus, if N is not too large, the computer CPU time and storage requirements needed to carry out the MM solution vary roughly as N^2 or as f^4. As the frequency is increased N must be increased, and at some point the computer resources needed to solve the problem become prohibitive. For this reason, MM solutions are often referred to as low-frequency solutions, applicable to bodies which are not too large in terms of a wavelength.

C. MM/Green's Function Solution

The fundamental difference between the MM and MM/Green's function solutions is that in the MM/Green's function solution some, but not all, of the matter is replaced by free-space and equivalent currents. In the equivalent problem of Fig. 1(c), Scatterer 1, but not Scatterer 2, is replaced by free-space and equivalent currents. Then, in contrast to (1), the equivalent currents for the MM/Green's function solution are

$$J = J_1 = \hat{n}_1 \times H \text{ on } S_1 \text{ only.} \qquad (11)$$

In Fig. 1(c), the total fields are the superposition of the fields of the impressed currents and J_1, both radiating in the presence of Scatterer 2. Then denoting (E^{i2}, H^{i2}) and $(E^2(J_1), H^2(J_1))$ as the fields of the impressed currents and J_1, respectively, radiating in the presence of Scatterer 2, the total fields are

$$E = E^{i2} + E^2(J_1) \qquad (12)$$

$$H = H^{i2} + H^2(J_1). \qquad (13)$$

As indicated in Table 1, the notation of superscript ^{2} implies the fields of a current distribution in the presence of Scatterer 2. Inherent in the MM/Green's function formulation is that we know (to an acceptable accuracy) the Green's function for Scatterer 2. That is, we know the near zone fields of a current element in the vicinity of Scatterer 2.

The EFIE is obtained by enforcing the boundary condition that the total electric field tangential to S_1 must vanish on the surface S_1. Then from (12)

$$-E^2(J_1) = E^{i2} \text{ tangential components on } S_1 \text{ only.} \qquad (14)$$

Note that it is not necessary to explicitly satisfy the boundary conditions on Scatterer 2, since it is implicit in (14) that all sources radiate in the presence of Scatterer 2, and by definition these fields satisfy the boundary conditions on Scatterer 2. Equation (14) is an integral equation for J_1 since

$$E^2(J_1) = \iint_{S_1} J_1 \cdot \overline{G}^2 \, ds' \qquad (15)$$

where $\overline{G}^2$ is the dyadic Green's function for Scatterer 2. $\overline{G}^2$ is similar to $\overline{G}^0$ in (5), except the electric current element is radiating in the presence of Scatterer 2.

Equation (14) must now be solved for J_1. We begin by expanding J_1 as

$$J_1 = \sum_{n=1}^{N_1} I_n J_n. \qquad (16)$$

This expansion is identical to that in (6), except that we include only the first N_1 basis functions on Scatterer 1. Substituting (16) into (14) yields

$$-\sum_{n=1}^{N_1} I_n E^2(J_n) = E^{i2}$$

tangential components on S_1 only $\qquad (17)$

where $E^2(J_n)$ is the electric field of J_n, located on S_1, and radiating in the presence of Scatterer 2. Taking the inner product of (17) with a set of N_1 weighting functions located on S_1 reduces (17) to the matrix equation

$$[Z^2][I_1] = [V^2] \qquad (18)$$

where $[Z^2]$ is the $N_1 \times N_1$ impedance matrix, $[I_1]$ is the length N_1 current vector containing the unknown coefficients in the expansion for J_1, and $[V^2]$ is the N_1 element voltage vector. Typical terms of $[Z^2]$ and $[V^2]$ are given by

$$Z^2_{mn} = -\iint_m E^2(J_n) \cdot w_m \, ds$$

$$= -\iint_m \left[\iint_n J_n \cdot \overline{G}^2 \, ds' \right] \cdot w_m \, ds \qquad (19)$$

$$V^2_m = \iint_m E^{i2} \cdot w_m \, ds. \qquad (20)$$

The above expressions for the elements in the MM/Green's function matrix equation are identical to those for the standard MM solution (9), (10), except that we replace the free-space fields with the fields in the presence of Scatterer 2

Equation (18) can now be solved for $[I_1]$, which when substituted into (16) provides an approximation to the current on Scatterer 1. The total fields are then found using (12) and (13).

The fields of any current distribution in the presence of Scatterer 2 can always be written as the sum of the free-space fields of the current plus a correction term, corresponding to the fields scattered from Scatterer 2. Thus we can write

$$\overline{G}^2 = \overline{G}^0 + \overline{G}^{S2}$$

$$E^2(J_n) = E^0(J_n) + E^{S2}(J_n)$$

$$E^{i2} = E^{i0} + E^{iS2} \qquad (21)$$

where the superscript ^{S2} implies the fields scattered from Scatterer 2. Using this notation, (18) can split into its free-space and scattered components as

$$([Z^0_{11}] + [Z^{S2}])[I_1] = [V^0_1] + [V^{S2}] \qquad (22)$$

where the $[Z^0_{11}]$ and $[V^0_1]$ are the Scatterer 1 matrix elements in the absence of Scatterer 2 as defined by (9), (10), and Fig. 2. $[Z^{S2}]$ and $[V^{S2}]$ are perturbation terms which account for the fields scattered from Scatterer 2, and are given by (19), (20), with the superscript ^{2} replaced by ^{S2}.

In some cases, it is advantageous to split the impedance matrix into its free-space and scattered components, as shown in (22). This is a result of the fact that it is almost always easier and faster to accurately find the elements of $[Z^0_{11}]$ than those of $[Z^2]$ or $[Z^{S2}]$. In many problems the free-space components will be much larger than the scattered components. In this case, it is computationally efficient to first evaluate the elements of $[Z^0_{11}]$ with high accuracy and relatively little CPU time, and then expend as much CPU time as is reasonable to evaluate the elements of $[Z^{S2}]$. If, for example,

a typical element of $[Z^{52}]$ is about 10 percent as large as the corresponding element in $[Z^0_{11}]$, then a 10-percent error in evaluating that element in $[Z^{52}]$ will result in only about a 1-percent error in the corresponding element in $[Z^2]$. Thus one can save considerable CPU time by requiring only modest accuracy in the computation of those elements of $[Z^2]$. The split shown in (22) is especially advantageous when treating the singularity in the self-impedance (i.e., $m = n$) terms, or other terms where the expansion and weighting functions physically overlap. Since this singularity is entirely in $[Z^0_{11}]$, the split in (22) allows one to analyze the singularity with the relatively simple free-space Green's function, and not the more complex Scatterer 2 Green's function. An exception would be if Scatterers 1 and 2 touch at an edge, or corner of Scatterer 2, in which case $\overline{G}^{52}$ would be singular at the attachment line or point, respectively. Treatment of this singularity in $\overline{G}^{52}$ is highly problem dependent, and is beyond the scope of this tutorial paper. The split shown in (22) is also natural for the MM/GTD method where the ray picture of the Scatterer 2 Green's function expresses the fields as the sum of an incident ray plus several scattered or diffracted rays. A further practical advantage of the split in (22) is that computer programs for the evaluation of $[Z^0_{11}]$ and $[V^0_1]$ may already be available. We caution that there are instances where certain elements of $[Z^0_{11}]$ are almost the negative of the corresponding elements of $[Z^{52}]$, making the split in (22) a numerically unstable method of computing $[Z^2]$ [52], [77].

D. A Comparison Between the MM and MM/Green's Function Solutions

First consider the basic accuracy of the MM and MM/Green's function solutions. The basic integral equations on which the MM and MM/Green's function solutions are based are both exact. If both methods use the same N_1 expansion and weighting functions on Scatterer 1, and the exact Green's function is used in the MM/Green's function solution, then in the limit as N_1 and $N_2 \to \infty$, both solutions should in principle yield the exact result. For the case of finite N_1, but in the limit as $N_2 \to \infty$, both solutions should produce the same approximate result. In particular, the N_1 elements of $[I_1]$ in (18) should be identical to the first N_1 elements of $[I]$ in (8). However, in practice N_1 and N_2 will both be finite, and the two solutions will yield somewhat different results. The most accurate method is the one with the most accurate model of Scatterer 2. The MM solution employs an MM model of Scatterer 2, while the MM/Green's function method employs the Scatterer 2 Green's function. If the exact Scatterer 2 Green's function is used (and we assume that it can be evaluated exactly), then the MM/Green's function solution will be the most accurate. However, if an approximate Green's function is used, then the MM/Green's function solution may not be as accurate as the MM solution. In this case, the relative accuracy will depend upon the accuracy of the approximate Scatterer 2 Green's function and on the number of basis functions N_2 used in the MM model of Scatterer 2.

Next consider the CPU time and storage for the MM and MM/Green's function solutions. The MM solution for the current on Scatterers 1 and 2 involves an order $N = N_1 + N_2$ matrix equation, while the MM/Green's function solution involves an order $N = N_1$ matrix equation. Since N^2

storage locations are required for the impedance matrix ($(N^2 + N)/2$ for a symmetric matrix), the MM/Green's function solution requires less storage, especially if $N_2 \gg N_1$. By the same argument, the matrix solution time is less for the MM/Green's function solution. The CPU time to compute a single element in an MM/Green's function impedance matrix generally requires more CPU time than a corresponding element in a MM impedance matrix. This is because the elements in the MM/Green's function impedance matrix involves the relatively complicated Scatterer 2 Green's function. In both cases, the total CPU time to compute or fill the impedance matrix is proportional to N^2. However, if $N_2 \gg N_1$, then the CPU time to compute the N_1^2 elements in the MM/Green's function impedance matrix will usually be less than the CPU time to compute the $(N_1 + N_2)^2$ elements in the MM impedance matrix.

E. The Matrix Green's Function

As mentioned above, the MM and MM/Green's function solutions produce essentially the same result for $[I_1]$. It follows that there must be a very close relationship between the MM matrix equation (8) and the MM/Green's function matrix equation (18) or (22). We will now obtain this relationship by casting (8) into an order N_1 matrix equation for $[I_1]$, and then comparing the result to (22).

As illustrated in Fig. 2, the MM matrix equation (8) is equivalent to the coupled matrix equations

$$[Z^0_{11}][I_1] + [Z^0_{12}][I_2] = [V^0_1] \tag{23}$$

$$[Z^0_{21}][I_1] + [Z^0_{22}][I_2] = [V^0_2]. \tag{24}$$

Left multiplying (24) by $[Z^0_{12}][Z^0_{22}]^{-1}$ yields

$$[Z^0_{12}][Z^0_{22}]^{-1}[Z^0_{21}][I_1] + [Z^0_{12}][I_2]$$
$$= [Z^0_{12}][Z^0_{22}]^{-1}[V^0_2]. \tag{25}$$

If we now subtract (25) from (23), the $[I_2]$ terms cancel leaving the order N_1 matrix equation for $[I_1]$

$$([Z^0_{11}] - [Z^0_{12}][Z^0_{22}]^{-1}[Z^0_{21}])[I_1] = [V^0_1] - [Z^0_{12}][Z^0_{22}]^{-1}[V^0_2]. \tag{26}$$

After (26) has been solved for $[I_1]$, then $[I_2]$ can be obtained from (24) as

$$[I_2] = [Z^0_{22}]^{-1}[V^0_2] - [Z^0_{22}]^{-1}[Z^0_{21}][I_1]. \tag{27}$$

Comparison with (22) shows that (26) is in the form of an MM/Green's function solution, where the perturbation terms, caused by Scatterer 2, are given by

$$[Z^{52}] = [Z^0_{12}][Z^0_{22}]^{-1}[Z^0_{21}] \tag{28}$$

$$[V^{52}] = [Z^0_{12}][Z^0_{22}]^{-1}[V^0_2]. \tag{29}$$

$[Z^{52}]$ and $[V^{52}]$ in (28), (29) are not identical to those in (22), since different models are being used for Scatterer 2. In principle, they will become identical if the exact Green's function is used to compute $[Z^{52}]$ and $[V^{52}]$ in (22), and if $N_2 \to \infty$ basis functions are used to model Scatterer 2 in the evaluation of (26). For finite N_2, the corresponding elements in these equations will be approximately the same. In either case, (26) can be interpreted as an MM/Green's function solution for the current on Scatterer 1. However, the Green's function is in the form of a matrix rather than a functional expression. Thus, we can loosely refer to $[Z^0_{12}][Z^0_{22}]^{-1}[Z^0_{21}]$ as a matrix Green's function for Scatterer 2, since it is a com-

plete description of the scattering of electromagnetic waves from Scatterer 2 due to the source currents modeling Scatterer 1. The advantage of the matrix Green's function is that it can be obtained for any Scatterer 2 geometry for which a standard MM solution for Scatterer 2 in free-space is available. Employing (26), with the matrix Green's function, is similar to Glisson and Butler's use of a numerical Green's function to analyze a wire antenna in the presence of a body of revolution (BOR) [67] and to Harker's matrix partitioning method [68].

The following physical interpretation can be made for the matrix terms in (26):

- $[Z^0_{21}][I_1]$ is the electric field incident upon Scatterer 2 caused by the current on Scatterer 1 radiating in free-space.
- $[Z^0_{22}]^{-1}[Z^0_{21}][I_1]$ is the current induced on Scatterer 2 by the above incident field.
- $-[Z^{s,2}] = [Z^0_{12}][Z^0_{22}]^{-1}[Z^0_{21}][I_1]$ is the electric field incident upon Scatterer 1 caused by the above current on Scatterer 2 radiating in free-space, i.e., this term accounts for the coupling between the currents on Scatterers 1 and 2.
- $[Z^0_{22}]^{-1}[V^0_2]$ is the current induced on Scatterer 2 by the original incident field, (E^{i0}, H^{i0}).
- $[V^{s,2}] = [Z^0_{12}][Z^0_{22}]^{-1}[V^0_2]$ is the electric field incident upon Scatterer 1 caused by the above current on Scatterer 2, i.e., this term accounts for the perturbation in the electric field incident upon Scatterer 1 caused by the presence of Scatterer 2.

Although the MM and MM/Green's function solution with matrix Green's function are algebraically equivalent, there are times when the MM/matrix Green's function solution can reduce the CPU time. A practical example would be a parameter study to find the length and location of a dipole on an airplane in order to obtain a prescribed input impedance and/or radiation pattern. To solve this design problem we analyze dipoles of various lengths and locations on the airplane, until a length and location is found which meets the pattern and impedance specifications. In the MM model of the dipole and the aircraft, the number of unknowns needed to model the airplane would far exceed that needed for the dipole. If we let the dipole be Scatterer 1 and the airplane Scatterer 2, this problem is an excellent candidate for an MM/Green's function solution since $N_2 \gg N_1$. Using thin wire and surface patch modeling techniques, a standard MM solution for the dipole in the presence of the airplane is available [78]. However, this $(N_1 + N_2)$ basis function MM solution would be time-consuming, especially since it would have to be repeated for many dipole lengths and locations. The MM/Green's function solution, with matrix Green's function, can dramatically reduce the CPU time for the second and subsequent runs in the parameter study by the following four-step procedure:

1) Begin by computing $[Z^0_{22}]$, the MM impedance matrix for the airplane in free-space. Then compute $[Z^0_{22}]^{-1}$ (and store it in the locations originally used for $[Z^0_{22}]$). For large N_2, this can be a very time-consuming process. However, it is only done once, and the remainder of the computation is much faster.

2) Next a dipole location and length is chosen and the matrices $[Z^0_{11}], [Z^0_{12}],$ and $[Z^0_{21}]$ are computed. The CPU time to compute these three matrices will be much less than that to compute $[Z^0_{22}]$, since $N_2 \gg N_1$. The vectors $[V^0_1]$ and $[V^0_2]$ are also computed.

3) Equation (26) is solved for $[I_1]$, which then is inserted

into (27) to find $[I_2]$. These operations are relatively fast, as compared to computing and inverting $[Z^0_{22}]$, since they involve only matrix multiplications and the solution of an order N_1 matrix equation.

4) With the current on the dipole and airplane known, the computation of the dipole input impedance and far-zone radiation patterns is straightforward and fast. If the pattern and input impedance meet specifications, then stop; if not, go back to step 2.

The advantage of the above procedure is that the most time-consuming part, i.e., the computation and inversion of $[Z^0_{22}]$, is done only once, regardless of the number of dipole lengths and locations which are analyzed. Steps 2-4 may be fast enough to be done interactively.

As an aside, if the dipole was a monopole which contacted the aircraft, then the MM model for the monopole on the aircraft would contain an attachment mode at the wire to surface junction point [78], [79]. This attachment mode is used to enforce continuity of current at the wire/surface junction and involves currents on the wire and on the aircraft surface. In the MM/matrix Green's function solution, the attachment mode should be considered as part of the wire or Scatterer 1.

III. MM AND MM/GREEN'S FUNCTION EXAMPLES

This section presents MM and MM/Green's function solutions to the two-dimensional problem of TM scattering by a perfectly conducting semicircular strip in the presence of a perfectly conducting circular cylinder. The strip will be Scatterer 1, and the cylinder will be Scatterer 2. As illustrated in Fig. 3, the cylinder has radius a, and the strip is at radius b and extends over the angular range $-\phi_s < \phi \le \phi_s$.
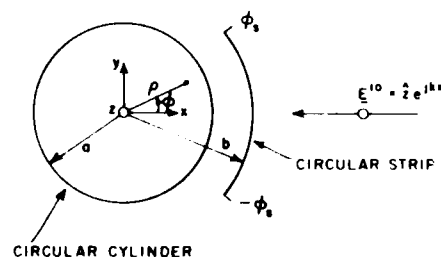
Fig. 3. Geometry for a TM plane wave incident upon a perfectly conducting semicircular strip in the presence of a perfectly conducting circular cylinder.

The incident field is the plane wave

$$E^{i0} = \hat{z}e^{jkx} \qquad (30)$$

incident from the $+x$ axis. For this problem, all electric fields and currents will be $\hat{z}$ polarized. Thus for simplicity, in this section we will drop the vector notation, and the $\hat{z}$ component is understood. The solution to this problem is presented using:

1) a straight MM solution,
2) an MM/Green's function solution with a matrix Green's function,
3) an MM/Green's function solution with an exact Green's function,
4) an MM/Green's function solution with a GTD (geometrical optics) Green's function.

All computer CPU times are for the VAX 8550, which is about five times faster than a VAX 11/780. Also, by CPU time it is meant total CPU time, i.e., matrix fill and solution time. Although the matrices for this simple example have the Toeplitz property, we did not use this property in our solution so that the CPU times would be more typical of most problems which do not have Toeplitz matrices.

A. MM and MM/Matrix Green's Function Solution

The MM solution for TM scattering by a perfectly conducting cylinder of arbitrary cross section is well known [1], and the particular solution employed here is based upon that of Wang [80]. As illustrated in Fig. 4, to implement the MM solution, we make a piecewise straight approximation to the circular cylinder and strip. To obtain reasonable

Fig. 4. For the MM solution, a piecewise linear approximation is made to the strip and cylinder contour in Fig. 3.

results, the width of the straight segments should not exceed $\lambda/4$, with $\lambda/10$ being typical. If we denote the strip as Scatterer 1 and the cylinder as Scatterer 2, the strip is modeled as N_1 straight segments of equal length and the circular cylinder is modeled by an N_2-sided regular polygon. Referring to (6), the expansion functions are the piecewise constant or pulse functions
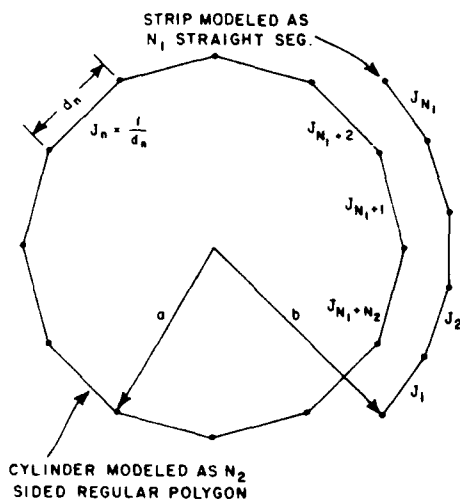
$$J_n = 1/d_n, \quad n = 1, 2, \cdots, N = N_1 + N_2 \quad (31)$$

which are numbered so that the first N_1 are on the strip (Scatterer 1) and the last N_2 are on the cylinder (Scatterer 2). The width of basis function n is denoted d_n. The weighting functions are chosen identical to the expression functions, i.e., $w_m = J_m$. This is referred to as a Galerkin solution, and results in a symmetric impedance matrix. The MM matrix equation, given by (8)-(10) and illustrated in Fig. 2, can then be evaluated using computer subroutines supplied by Wang [80].

Consider the specific example of a circular cylinder of radius $a = \lambda$, and a strip with radius $b = 1.01\lambda$ and angular sector $2\phi_s = 10°$. The radius b is chosen slightly larger than a to emphasize the coupling between the strip and the cylinder. For this geometry, Fig. 5 shows the magnitude and phase of the current density at the center of the strip versus N_2 = the number of basis functions used to model the cyl-
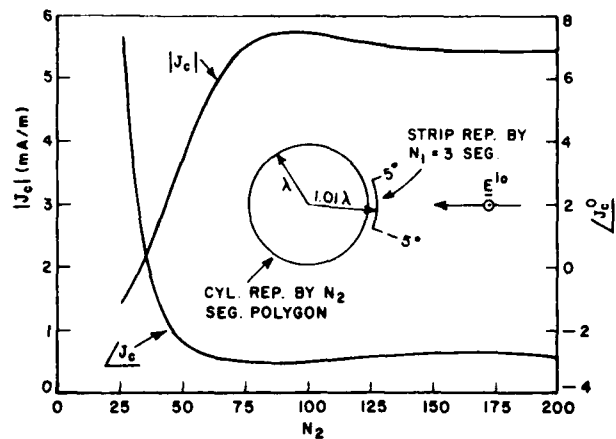
Fig. 5. The MM or MM/matrix Green's function solution for the center current of a circular strip in the presence of a circular cylinder versus N_2 = the number of basis functions on the cylinder.

inder. Numerical experimentation showed that $N_1 = 3$ basis functions on the strip results in a reasonably well converged result, and this will be used in all computations to follow. As is typical of MM solutions, as N_2 increases, the strip center current density converges, in this case to about 5.45 at an angle of $-2.8°$ mA/m. About $N_2 = 100$ basis functions are needed on the cylinder to obtain a reasonably converged result, which corresponds to a segment size of about 0.063λ. The computer CPU times for the MM solutions in Fig. 5 are shown by the solid line in Fig. 6. The CPU time
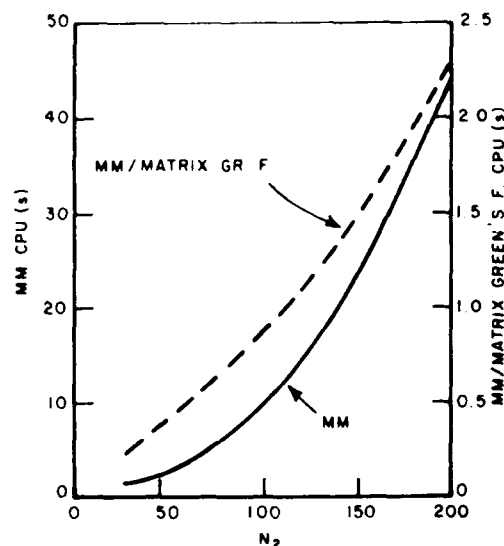
Fig. 6. The CPU time on a VAX 8550 for the MM and MM/matrix Green's function solution to the geometry of Fig. 5.

is roughly proportional to $(N_2)^2$, and about 10 s were required for the $N_2 = 100$ basis function solution.

The MM/matrix Green's function solution, defined by (26), is algebraically equivalent to the straight MM solution. Thus the data in Fig. 5 also applies to the MM/matrix Green's function solution. The corresponding CPU times for the MM/matrix Green's function solution are shown by the dashed line in Fig. 6, and are considerably less than that for the straight MM solution. It is important to point out that

these times do not include the time to compute and invert $[Z^0_{22}]$. If a series of problems is being run using the MM/ matrix Green's function formulation, with the cylinder fixed but with the strip geometry being varied, these CPU times would be for the second and subsequent runs. Also, if a large number of runs is being made, then these times represent the average CPU time for each run (including the first run where $[Z^0_{22}]$ is computed and inverted).

B. MM/Exact Green's Function Solution

This section describes the MM/Green's function solution to the problem of Fig. 3 using the exact eigenfunction cylinder Green's function. We begin by presenting the exact eigenfunction representation of the cylinder Green's function. Consider a unit amplitude line current located at the source point with cylindrical coordinates (ρ', ϕ') and radiating in the presence of a perfectly conducting circular cylinder of radius a which is located concentric with the z axis. The total field of this line source at the field point (ρ, ϕ), i.e., the cylinder Green's function, is given by [7]

$$G^2(\rho, \phi; \rho', \phi') = C \sum_{p=0}^{\infty} \epsilon_p F_p(\rho, \rho') \cos p(\phi - \phi') \quad (32)$$

in which $C = -k^2/4\omega\epsilon_0$, $\epsilon_p = 1$ if $p = 0$ and $\epsilon_p = 2$ if $p \neq 0$, and

$$F_p(\rho, \rho') = H^{(2)}_p(k\rho_>)[B_p(k\rho_<) + c_p H^{(2)}_p(k\rho_<)]$$

$$= F_{-p}(\rho, \rho') \quad (33)$$

$$c_p = -\frac{B_p(ka)}{H^{(2)}_p(ka)} = c_{-p} \quad (34)$$

$$\rho_< = \text{the minimum of } (\rho, \rho')$$

$$\rho_> = \text{the maximum of } (\rho, \rho'). \quad (35)$$

Here B_p denotes the Bessel function of the first kind and $H^{(2)}_p$ denotes the Hankel function of the second kind, both of order p.

If the same cylinder is illuminated by a unit amplitude plane wave incident from the $+x$ axis (30), then the total field at (ρ, ϕ) is

$$E^{i2} = \sum_{p=-\infty}^{\infty} D_p(\rho) e^{-jp\phi} \quad (36)$$

in which

$$D_p(\rho) = (-j)^{-p}[B_p(k\rho) + c_p H^{(2)}_p(k\rho)]. \quad (37)$$

While in the MM solution it was convenient to make a piecewise linear approximation to the curved cylinder and strip, when using the above eigenfunction expansion of the fields, it is advantageous to retain the true circular nature of the strip. Thus in Fig. 7 the semicircular strip is shown segmented into N_1 smaller semicircular strips. Each of the N_1 smaller strips corresponds to a piecewise constant basis function. The current density on expansion function n is given by

$$J_n = \frac{1}{b(\phi_{n2} - \phi_{n'})} \quad \phi_{n1} \leq \phi \leq \phi_{n2}. \quad (38)$$

Again we choose the weighting functions identical to the expansion functions, i.e., $w_m = J_m$.

We now show in some detail the evaluation of the ele-
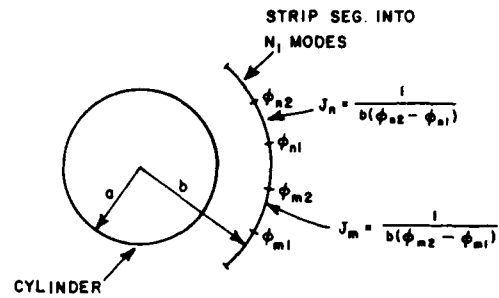
Fig. 7. For the MM/exact Green's function solution the semicircular strip is segmented into N_1 smaller semicircular strips corresponding to the MM basis functions.

ments in the MM/Green's function impedance matrix. Referring to (19), a typical element in our case is given by

$$Z^2_{mn} = -\int_{\phi_{m1}}^{\phi_{m2}} E^2(J_n) J_m b \, d\phi = Z^2_{nm}$$

$$m, n = 1, 2, \cdots, N_1. \quad (39)$$

Here $E^2(J_n)$ is the electric field of expansion function n, located on the semicircular strip, and radiating in the presence of the circular cylinder. $E^2(J_n)$ is computed by integrating over expansion function n the product of J_n and the cylinder Green's function

$$E^2(J_n) = \int_{\phi_{n1}}^{\phi_{n2}} J_n(\phi') G^2(b, \phi; b, \phi') b \, d\phi' \quad (40)$$

in which we have set $\rho = \rho' = b$ since in our case the source and field point are on the strip. Recognizing that $J_n(\phi')$ is constant for $\phi_{n1} \leq \phi \leq \phi_{n2}$, and inserting G^2 from (32) into (40) yields

$$E^2(J_n) = CJ_n b \sum_{p=0}^{\infty} \epsilon_p F_p(b, b) \int_{\phi_{n1}}^{\phi_{n2}} \cos p(\phi - \phi') \, d\phi'. \quad (41)$$

Equation (41) can now be easily integrated to yield

$$E^2(J_n) = CJ_n b \sum_{p=0}^{\infty} \epsilon_p F_p(b, b)$$

$$\cdot \begin{cases} \dfrac{1}{p} [\sin p(\phi - \phi_{n1}) - \sin p(\phi - \phi_{n2})], & p \neq 0 \\ (\phi_{n2} - \phi_{n1}), & p = 0. \end{cases}$$

$$(42)$$

Z_{mn} is now obtained by inserting $E^2(J_n)$ from (42) into (39). Again the integrations are easily done yielding

$$Z^2_{mn} = -CJ_m J_n b^2 \sum_{p=0}^{\infty} \epsilon_p F_p(b, b)$$

$$\cdot \begin{cases} \dfrac{1}{p^2} [\cos p(\phi_{m1} - \phi_{n1}) - \cos p(\phi_{m2} - \phi_{n1}) \\ \quad - \cos p(\phi_{m1} - \phi_{n2}) + \cos p(\phi_{m2} - \phi_{n2})], \\ \qquad\qquad\qquad\qquad p \neq 0 \\ (\phi_{n1} - \phi_{n2})(\phi_{m1} - \phi_{m2}), \quad p = 0. \end{cases}$$

$$(43)$$

Similarly, from (20), the elements in the voltage vector are

$$V_m^2 = \int_{\phi_{m1}}^{\phi_{m2}} E'^2 J_m b \, d\phi, \qquad m = 1, 2, \cdots, N_1. \qquad (44)$$

Inserting E'^2 from (36) into (44) and integrating yields

$$V_m^2 = J_m b \sum_{p=-\infty}^{\infty} D_p(b)$$

$$\cdot \begin{cases} \dfrac{j}{p} (e^{\,jp\phi_{m2}} - e^{\,jp\phi_{m1}}), & p \neq 0 \\[2mm] (\phi_{m2} - \phi_{m1}), & p = 0. \end{cases} \qquad (45)$$

The ability to carry out the integrations in closed form for the elements in the impedance matrix and the right-hand-side vector is typical for problems where the surface of Scatterer 1 is a constant coordinate surface for the functions being used to expand the Scatterer 2 Green's function [21], [23], [54], [81].

Although (43) for the Z_{mn}^2 is in a relatively simple form, a numerical problem arises in that the self-impedance terms (i.e., $m = n$) are slowly convergent. Referring to (22), it is the $[Z_{11}^0]$ or free-space part of $[Z^2]$ which is slowly convergent when basis functions m and n are electrically close. For this reason, it is numerically efficient to evaluate $[Z_{11}^0]$ separately as in a conventional MM solution for the strip in free-space [1], [80]. The problem then remains to evaluate $[Z^{52}]$ using the eigenfunction expansion of (43). F_p in (33) and D_p in (37) both contain a factor of the form $[B_p + c_p H_p^{(2)}]$. The term proportional to B_p corresponds to the free-space field, while the term proportional to $c_p H_p^{(2)}$ corresponds to the scattered field. Thus referring to (22), the B_p term contributes solely to $[Z_{11}^0]$ and $[V_1^0]$, while the $c_p H_p^{(2)}$ term contributes solely to $[Z^{52}]$ and $[V^{52}]$. It can then be seen that (43) and (45) can be used to compute $[Z^{52}]$ and $[V^{52}]$, respectively, by omitting the B_p term.

For the problem illustrated in Fig. 5, the $N_1 = 3$ basis function MM/exact Green's function solution yielded a current density at the center of the strip of 5.9 at an angle of $-2.7°$ mA/m, which is very close to the MM solution for $N_2 \geq 100$. This MM/Green's function solution required only three unknowns and 0.11 s of CPU time. As compared to the $N_1 = 3$ and $N_2 = 100$ basis function MM solution, this is about a factor of 100 reduction in CPU time and 1000 reduction in matrix storage requirements. As the cylinder size increases, the relative advantage of the MM/Green's function solution will also increase. Although the reduction in storage is a general characteristic of MM and MM/Green's function solutions, the reduction of CPU time is not. The fact that we could carry out the integrations in (39) and (44) in closed form greatly reduced the CPU time for the MM/Green's function solution. For most MM/Green's function solutions these integrations must be done numerically and can be very time-consuming. In some cases, the CPU time for the MM/Green's function solution can actually exceed that of the straight MM solution.

C. MM/GTD Green's Function Solution

Using the GTD to obtain the Green's function greatly expands the range of problems which can be treated via MM/Green's function techniques. This section describes the solution to the problem of Fig. 3 using the MM/Green's function technique with a GTD Green's function.

The GTD Green's function is described with the aid of Fig. 8, which shows a unit amplitude line source located at (ρ', ϕ') and radiating in the presence of a perfectly conducting cylinder of radius a. In describing the field of the line source
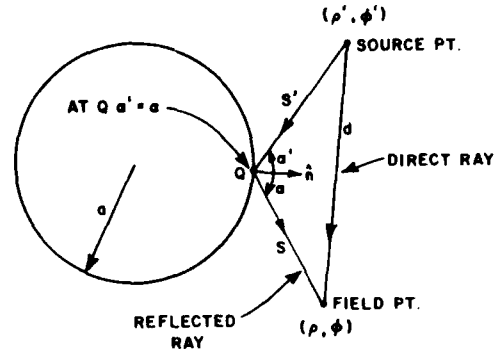
Fig. 8. The direct and reflected rays used in the GTD Green's function for a line source in the presence of a circular cylinder.

it is assumed that the field point (ρ, ϕ) is in the lit region, i.e., a line or ray from the source point to the field point does not pass through the cylinder. It is also assumed that $ka \gg 1$ and that the source and field point are not too near the surface of the cylinder. In the lit region the total field is dominated by two rays, shown in Fig. 8 as the direct ray and the reflected ray. The field of the direct ray is simply the free-space field of the line source. The reflected ray propagates along a straight-line path of length s' from the source point to the point Q on the cylinder, and then along a straight-line path of length s from Q to the field point. The point Q is defined by the requirement that the angle of incidence α' is equal to the angle of reflection, α. Then, using the notation of (21), the total field of the line source is [82]

$$G^2 = G^0 + G^{52} = C H_0^{(2)}(kd)$$

$$- C H_0^{(2)}(ks') \sqrt{\frac{\rho'}{\rho' + s}} \, e^{\,jks} \qquad (46)$$

where d is the distance from the source point to the field point, $C = -k^2/4\omega\epsilon_0$, and

$$\frac{1}{\rho'} = \frac{1}{s'} + \frac{2}{\alpha \cos \alpha}. \qquad (47)$$

Similarly, the field of the plane wave of (30) in the presence of the cylinder can be written as

$$E'^2 = E'^0 + E'^{52} = e^{\,jkx}$$

$$- e^{\,jkx_Q} \sqrt{\frac{\rho'}{\rho' + s}} \, e^{\,-jks} \qquad (48)$$

where ρ' and x_Q, the x coordinate of point Q, are evaluated for a source point at $(\rho' = \infty, \phi' = 0)$.

Referring to (22), the first term in (46) and (48) contribute to $[Z_{11}^0]$ and $[V_1^0]$, respectively, i.e., they result in the MM matrix elements for the strip in free-space. As described above, they are evaluated using computer subroutines developed by Wang [80]. The second term in (46) and (48)

contribute to $[Z^{S2}]$ and $[V^{S2}]$, respectively. These elements are evaluated by inserting G^{S2} from (46) into (39) and (40), inserting E^{IS2} from (48) into (44), and performing the integrations numerically. For this simple example, requiring only one ray, these integrations are very fast. However, for a more complicated Scatterer 2 geometry, more rays would be required, and the CPU time needed for the numerical integrations would increase.

The insert in Fig. 9 shows a semicircular strip located $\lambda/2$ above a circular cylinder. With $N_1 = 3$ basis functions
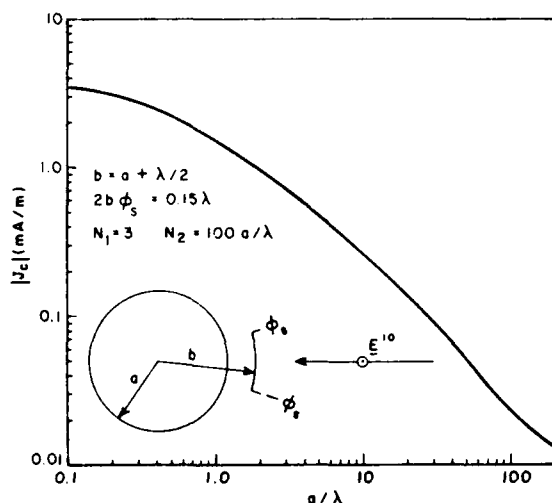

Fig. 9. The magnitude of the center current for a semicircular strip located $\lambda/2$ above a circular cylinder, computed by the MM, the MM/exact Green's function, or the MM/GTD Green's function methods.

on the strip, Fig. 9 shows the magnitude of the current density at the center of the strip versus a/λ. The angular sector of the strip is adjusted so that its width remains constant at $2b\phi_s = 0.15\lambda$. This data was generated with the MM, the MM/exact Green's function and the MM/GTD Green's function techniques, and essentially the same results for the strip current were obtained by each method. For the MM solution, $N_2 = 100a/\lambda$ basis functions were used on the cylinder. The strip current in Fig. 9 goes to zero as $a/\lambda \to \infty$ since the direct ray cancels the reflected ray on the strip, causing $[V_1^0] \to -[V^{S2}]$ and thus $[V^2] \to 0$. The CPU times for these three methods are shown in Fig. 10. Note that the left scale applies for the MM solution, and is 100 times as large as the right scale which is for the MM/Green's function solutions. For $a/\lambda > 1$, the CPU time for the MM solution is two orders of magnitude or more greater than that for the MM/Green's function solutions. The CPU time for the MM/exact Green's function solution increases as a/λ increases, since more terms must be retained in the eigenfunction summations. By comparison, for $a/\lambda > 1$, the CPU time for the MM/GTD Green's function solution is essentially constant at 0.25 s.

As compared with the MM/exact Green's function solution, the advantage of the MM/GTD solution is that it is applicable to a far wider class of Scatterer 2 (in this example, cylinder) geometries. As compared to the MM, the advantage of the MM/GTD solution is that it is much faster and requires far less computer storage as the electrical size of Scatterer 2 increases.
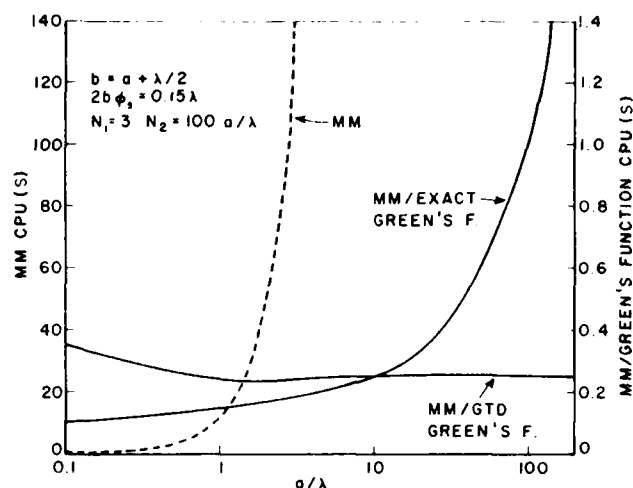

Fig. 10. The CPU times on a VAX 8550 for the data in Fig. 9 computed by the MM (dashed curve) and by the MM/Green's function methods (solid curves).

IV. Summary

This paper describes a technique for combining the MM and Green's function solutions in electromagnetics. The fundamental difference between the standard MM and MM/Green's function solutions is in the application of the equivalence theorems used in obtaining their respective integral equations. In a standard MM solution all matter is replaced by free-space and by equivalent currents. These currents are then found as the solution of an exact integral equation whose kernel contains the free-space Green's function. By comparison, in an MM/Green's function solution some, but not all, matter is replaced by free-space and by equivalent currents. Again the currents are found as the solution of an exact integral equation, but now the kernel contains the Green's function for that portion of the matter which was not replaced by free-space and equivalent currents. Both integral equations are solved by transforming them into a system of simultaneous linear equations, i.e., a matrix equation. The advantage of the MM/Green's function technique is that the number of unknowns, and thus the order of this matrix equation is reduced. This results in a reduction in computer storage and, in most cases, CPU time.

The number of problems which can be solved by MM/Green's function techniques can be tremendously increased by not requiring the Green's functions to be exact. In particular, using the GTD one can obtain the Green's function for a geometry as complicated as an aircraft. This is referred to as an MM/GTD solution [55].

It is shown that, by manipulating the MM matrix equation, a standard MM solution can be put into the format of an MM/Green's function solution. This is referred to as an MM/matrix Green's function solution. Such a solution is algebraically equivalent to the standard MM solution, and can be obtained for any geometry for which a standard MM solution is possible. The advantage of the MM/matrix Green's function solution is that it is faster than a standard MM solution if a series of problems is being analyzed in which only a small portion of the problem geometry changes from one run to the next.

In order to illustrate the MM/Green's function method, and to compare it to a standard MM solution, the problem

of plane wave scattering by a perfectly conducting semi-circular strip in the presence of a perfectly conducting circular cylinder is solved using the MM and the MM/Green's function technique with a matrix, an exact eigenfunction, and a GTD Green's function. Basically, all methods yield the same numerical results. However, the MM/Green's function solutions are substantially faster, and require far less storage (except for the matrix Green's function), especially as the cylinder size is increased.

REFERENCES

[1] R. F. Harrington, *Field Computation by Moment Methods.* New York, NY: Macmillan, 1968.

[2] ——, "Matrix methods for field problems," *Proc. IEEE*, vol. 55, pp. 136–149, Feb. 1967.

[3] J. H. Richmond, "Digital computer solutions of the rigorous equations for scattering problems," *Proc. IEEE*, vol. 53, pp. 796–804, Aug. 1965.

[4] C.-T. Tai, *Dyadic Green's Functions in Electromagnetic Theory.* Scranton, PA: Intext Educational Publishers, 1971.

[5] J. J. Bowman, T. B. A. Senior, and P. L. E. Uslenghi, *Electromagnetic and Acoustic Scattering by Simple Shapes.* Amsterdam: North-Holland, 1969.

[6] G. T. Ruck, *Radar Cross Section Handbook.* New York, NY: Plenem Press, 1970.

[7] R. F. Harrington, *Time-Harmonic Electromagnetic Fields.* New York, NY: McGraw-Hill, 1961.

[8] J. H. Richmond, "Scattering by a dielectric cylinder of arbitrary cross section shape," *IEEE Trans. Antennas Propagat.*, vol. AP-13, pp. 334–341, May 1965.

[9] ——, "TE wave scattering by a dielectric cylinder of arbitrary cross-section shape," *IEEE Trans. Antennas Propagat.*, vol. AP-14, pp. 460–464, July 1966.

[10] E. K. Miller, A. J. Poggio, G. J. Burke, and E. S. Seldon, "Analysis of wire antennas in the presence of a conducting half-space, part I. The vertical antenna in free space," *Can. J. Phys.*, vol. 50, pp. 879–888, 1972.

[11] ——, "Analysis of wire antennas in the presence of a conducting half-space, part II. The horizontal antenna in free space," *Can. J. Phys.*, vol. 50, pp. 2614–2627, 1972.

[12] G. J. Burke et al., "Computer-modeling of antennas near the ground," *Electromagnetics*, vol. 1, pp. 29–49, 1981.

[13] G. J. Burke, W. A. Johnson, and E. K. Miller, "Modelling of simple antennas near to and penetrating an interface," *Proc. IEEE*, vol. 71, no. 1, Jan. 1983.

[14] G. J. Burke and A. J. Poggio, "Numerical electromagnetic code (NEC)—method of moments," Naval Oceans Systems Center, Tech Doc. 116, AFWL-TR-320, July 1977.

[15] D. C. Chang and J. R. Wait, "Theory of a vertical tubular antenna located above a conducting half-space," *IEEE Trans. Antennas Propagat.*, vol. AP-18, pp. 182–188, Mar. 1970.

[16] R. Tiberio and G. Manara, "A hybrid technique for analyzing wire antennas in the presence of a plane interface," *IEEE Trans. Antennas Propagat.*, vol. AP-33, pp. 881–885, Aug. 1985.

[17] P. Parhami and R. Mittra, "Wire antennas over a lossy half-space," *IEEE Trans. Antennas Propagat.*, vol. AP-28, pp. 397–403, May 1980.

[18] L. Chommeloux, C. Pichot, and J. Bolomey, "Electromagnetic modeling for microwave imaging of cylindrical buried inhomogeneities," *IEEE Trans. Microwave Theory Tech.*, vol. MTT-34, pp. 1064–1074, Oct. 1986.

[19] C. M. Butler, X. Xu, and A. W. Glisson, "Current on a conducting cylinder located near the planar interface between two semi-infinite half-spaces," *IEEE Trans. Antennas Propagat.*, vol. AP-33, June 1985.

[20] X. Xu and C. M. Butler, "Scattering of TM excitation by coupled and partially buried cylinders at the interface between two media," *IEEE Trans. Antennas Propagat.*, vol. AP-35, pp. 529–538, May 1987.

[21] D. M. Pozar, "Input impedance and mutual coupling of rectangular microstrip antennas," *IEEE Trans. Antennas Propagat.*, vol. AP-30, pp. 1191–1196, Nov. 1982.

[22] ——, "A reciprocity method of analysis for printed slot and slot-coupled microstrip antennas," *IEEE Trans. Antennas Propagat.*, vol. AP-34, pp. 1439–1446, 1986.

[23] E. H. Newman and D. Forrai, "Scattering from a microstrip patch," *IEEE Trans. Antennas Propagat.*, vol. AP-35, pp. 245–251, Mar. 1987.

[24] M. C. Bailey and M. D. Deschamps, "Integral equation formulation of microstrip antennas," *IEEE Trans. Antennas Propagat.*, vol. AP-30, pp. 651–656, July 1982.

[25] I. E. Rana and N. G. Alexopoulos, "Current distribution and input impedance of printed dipoles," *IEEE Trans. Antennas Propagat.*, vol. AP-29, pp. 99–105, Jan. 1981.

[26] D. R. Jackson and N. G. Alexopoulos, "Analysis of planar strip geometries in a substrate-superstrate configuration," *IEEE Trans. Antennas Propagat.*, vol. AP-34, pp. 1430–1438, Dec. 1986.

[27] B. A. Munk and R. J. Luebbers, "Reflection properties of two-layer dipole arrays," *IEEE Trans. Antennas and Propagat.*, vol. AP-22, pp. 766–773, Nov. 1974.

[28] B. A. Munk, R. J. Luebbers, and R. D. Fulton, "Transmission through a two-layer array of loaded slots," *IEEE Trans. Antennas Propagat.*, vol. AP-22, pp. 804–809, Nov. 1974.

[29] B. R. Rao, "A two-element Yagi-type array in a parallel-plate waveguide—theoretical and experimental studies," *IEEE Trans. Antennas Propagat.*, vol. AP-13, pp. 675–682, Sept. 1965.

[30] ——, "Current distribution and impedance of an antenna in a parallel-plate region," *Proc. Inst. Elec. Eng.* (London), vol. 112, p. 259, Feb. 1965.

[31] C. D. Taylor, "Thin wire receiving antenna in a parallel plate waveguide," *IEEE Trans. Antennas Propagat.*, vol AP-15, pp. 572–574, July 1967.

[32] F. M. Tesche, "On the behavior of thin-wire antennas and scatterers arbitrarily located within a parallel plate region," *IEEE Trans. Antennas Propagat.*, vol. AP-20, pp. 482–486, July 1972.

[33] D. B. Seidel, "Aperture excitation of a wire in a rectangular cavity," *IEEE Trans. Microwave Theory Tech.*, vol. MTT-26, pp. 908–914, Nov. 1978.

[34] Y. Leviatan, P. G. Li, A. T. Adams, and J. Perini, "Single-post inductive obstacle in rectangular waveguide," *IEEE Trans. Microwave Theory Tech.*, vol. MTT-31, pp. 806–811, Oct. 1983.

[35] H. Auda and R. F. Harrington, "Inductive posts and diaphragms of arbitrary shape and number in a rectangular waveguide," *IEEE Trans. Microwave Theory Tech.*, vol. MTT-32, pp. 606–613, June 1984.

[36] J. M. Jarem, "A multifilament method-of-moments solution for the input impedance of a probe-excited semi-infinite waveguide," *IEEE Trans. Microwave Theory Tech.*, vol. MTT-35, pp. 14–19, Jan. 1987.

[37] J. J. H. Wang, "Analysis of a three-dimensional arbitrarily shaped dielectric or biological body inside a rectangular waveguide," *IEEE Trans. Microwave Theory Tech.*, vol. MTT-26, pp. 457–462, July 1978.

[38] A. S. Omar and K. Schunemann, "Scattering by material and conducting bodies inside waveguides, part 1: theoretical formulations," *IEEE Trans. Microwave Theory Tech.*, vol. MTT-34, pp. 266–272, Feb. 1986.

[39] C. G. Hsu and H. A. Auda, "Multiple dielectric posts in a rectangular waveguide," *IEEE Trans. Microwave Theory Tech.*, vol. MTT-34, pp. 883–891, Aug. 1986.

[40] T. V. Khac and C. T Carson, "Impedance properties of a longitudinal slot antenna in the broad face of a rectangular waveguide," *IEEE Trans. Antennas Propagat.*, vol. AP-21, pp. 708–710, Sept. 1973.

[41] V. K. Thong, "Solutions for some waveguide discontinuities by the method of moments," *IEEE Trans. Microwave Theory Tech.*, vol. MTT-20, pp. 416–418, June 1972.

[42] F. M. Tesche and A. R. Neureuther, "Radiation patterns for two monopoles on a perfectly conducting sphere," *IEEE Trans. Antennas Propagat.*, vol. AP-18, pp. 692–694, Sept. 1970.

[43] ——, "The analysis of monopole antennas located on a spherical vehicle: Part I—Theory," *IEEE Trans. Electromag. Compat.*, vol. EMC-18, pp. 2–8, Feb. 1976.

[44] F. M. Tesche, A. R. Neureuther, and R. E. Stovall, "The analysis of monopole antennas located on a spherical vehicle: Part II—Numerical and experimental results," *IEEE Trans. Electromag. Compat.*, vol. EMC-18, pp. 8–15, Feb. 1976.

[45] C. M. Butler and T. L. Keshavamurthy, "Analysis of a wire

antenna in the presence of a sphere," *IEEE Trans. Electromag. Compat.*, vol. EMC-22, pp. 113-118, May 1980.

[46] D. Misra and K. Chen, "Responses of electric-field probes near a cylindrical model of the human body," *IEEE Trans. Microwave Theory Tech.*, vol. MTT-33, pp. 447-452, June 1985.

[47] H. Steyskal, "Analysis of circular waveguides arrays on cylinders," *IEEE Trans. Antennas Propagat.*, vol. AP-25, pp. 610-616, Sept. 1977.

[48] M. D. G. Karunaratne, K. A. Michalski, and C. M. Butler, "TM scattering from a conducting strip loaded by a dielectric cylinder." *Proc. Inst. Elec. Eng.* (London), Apr. 1985.

[49] D. Lamensdorf and C. Ting, "An experimental and theoretical study of the monopole embedded in a cylinder of anisotropic dielectric," *IEEE Trans. Antennas Propagat.*, vol. AP-16, pp. 342-349, May 1968.

[50] D. M. Pozar and E. H. Newman, "Analysis of a monopole mounted near or at the edge of a half-plane," *IEEE Trans. Antennas Propagat.*, vol. AP-29, pp. 488-495, May 1981.

[51] ——, "Analysis of a monopole mounted near an edge or a vertex," *IEEE Trans. Antennas Propagat.*, vol. AP-30, pp. 401-408, May 1982.

[52] E. H. Newman. "TM scattering by a dielectric cylinder in the presence of half-plane," *IEEE Trans. Antennas Propagat.*, vol. AP-33, pp. 773-782, July 1985.

[53] ——, "TM and TE scattering by a dielectric/ferrite cylinder in the presence of a half-plane," *IEEE Trans. Antennas Propagat.*, vol. AP-34, pp. 806-813, June 1986.

[54] E. H. Newman and J. L. Blanchard, "TM scattering by an impedance sheet extension of a parabolic cylinder." *IEEE Trans. Antennas Propagat.*, accepted for publication.

[55] G. A. Thiele and T. H. Newhouse, "A hybride technique for combining moment methods with the geometrical theory of diffraction," *IEEE Trans. Antennas Propaga*· , vol. AP-23, pp. 62-69, Jan. 1975.

[56] R. G. Kouyoumjian, "Asymptotic high-frequency methods," *Proc. IEEE*, vol. 53, pp. 864-876, Aug. 1965.

[57] H. E. Green, "Impedance of a monopole on the base of a large cone," *IEEE Trans. Antennas Propagat.*, vol. AP-17, pp. 703-706, Nov. 1969.

[58] K. H. Awadalla and T. S. M. Maclean, "Input impedance of a monopole antenna at the center of a finite ground plane," *IEEE Trans. Antennas Propagat.*, vol. AP-26, pp. 244-248, Mar. 1978.

[59] ——, "Monopole antenna at center of a circular ground plane: Input impedance and radiation pattern," *IEEE Trans. Antennas Propagat.*, vol. AP-27, pp. 151-153, Mar. 1979.

[60] M. Marin and M. F. Catedra, "A study of a monopole arbitrarily located on a disk using hybrid MM/GTD techniques," *IEEE Trans. Antennas Propagat.*, vol. AP-35, pp. 287-292, Mar. 1987.

[61] E. P. Ekelman and G. A. Thiele, "A hybrid technique for combining the moment method treatment of wire antennas with the GTD for curved surfaces," *IEEE Trans. Antennas Propagat.*, vol. AP-28, pp. 831-839, Nov. 1980.

[62] L. W. Henderson and G. A. Thiele, "A hybrid MM-geometrical optics technique for the treatment of wire antennas mounted on a curved surface," *IEEE Trans. Antennas Propagat.*, vol. AP-30, pp. 1257-1261, Nov. 1982.

[63] ——, "A hybrid MM-GTD technique for the treatment wire antennas near a curved surface," *Radio Sci.*, vol. 16, pp. 1125-1130, Nov./Dec. 1981.

[64] G. A. Thiele and G. K. Chan, "Application of the hybrid technique to time domain problems," *IEEE Trans. Antennas Propagat.*, vol. AP-26, pp. 151-155, Jan. 1978.

[65] W. L. Ko and R. Mittra, "A new approach based upon a combination of integral equation and asymptoptic techniques for solving electromagnetic scattering problems," *IEEE Trans. Antennas Propagat.*, vol. AP-25, pp. 187-197, Mar. 1977.

[66] R. F. Harrington and J. R. Mautz, "Green's functions for surfaces of revolution," *Radio Sci.*, vol. 7, pp. 603-611, May 1972.

[67] A. W. Glisson and C. M. Butler, "Analysis of wire antenna in the presence of a body of revolution," *IEEE Trans. Antennas Propagat.*, vol. AP-28, pp. 604-609, Sept. 1980.

[68] K. J. Harker, "Partitioning method in method of moments scattering theory," presented at the National Radio Science Meeting, Boston, MA, June 25-29, 1984.

[69] W. D. Burnside, C. L. Yu, and R. J. Marhefka, "A technique to combine the geometrical theory of diffraction and the moment method," *IEEF Trans. Antennas Propagat.*, vol. AP-23, pp. 551-558, July 1975.

[70] C. W. Chuang and W. D. Burnside, "A diffraction coefficient for a truncated planar surface," *IEEE Trans. Antennas Propagat.*, vol. AP-28, pp. 177-182, Mar. 1980.

[71] S. Srikanth, P. H. Pathak, and C. W. Chuang, "Hy·, rid UTD-MM analysis of the scattering by a perfectly conducting semicircular cylinder," *IEEE Trans. Antennas Propagat.*, vol. AP 34, pp. 1250-1257, Oct. 1986.

[72] T. J. Kim and G. A. Thiele, "A hybrid diffraction technique—general theory and applications," *IEEE Trans. Antennas Propagat.*, vol. AP-30, pp. 888-897, Sept. 1982.

[73] P. K. Murthy, K. C. Hill, and G. A. Thiele, "A hybrid-iterative method for scattering problems," *IEEE Trans. Antennas Propagat.*, vol. AP-34, pp. 1173-1180, Oct. 1986.

[74] L. N. Medgyesi-Mitschang and D. S. Wang, "Hybrid solution for scattering from perfectly conducting bodies of revolution," *IEEE Trans. Antennas Propagat.*, vol. AP-31, pp. 570-583, July 1983.

[75] B. Azarbar and L. Shafai, "Application of moment method to large cylindrical reflector antennas," *IEEE Trans. Antennas Propagat.*, vol. AP-26, pp. 500-502, May 1978.

[76] J. H. Richmond, "Scattering by thin dielectric strips," *IEEE Trans. Antennas Propagat.*, vol. AP-33, pp. 64-68, Jan. 1985.

[77] E. H. Newman and P. Tulyathan, "Analysis of microstrip antennas using moment methods." *IEEE Trans. Antennas Propagat.*, vol. AP-29, pp. 47-53, Jan. 1981.

[78] E. H. Newman and R. L. Dilsavor, "A user's manual for the electromagnetic surface patch code: ESP version III," Ohio St. Univ. Research Foundation Rep. 716148, prepared under Grant NSG 1613 with the National Aeronautics and Space Administration, May 1987.

[79] E. H. Newman and D. M. Pozar, "Electromagnetic modeling of composite wire and surface geometries," *IEEE Trans. Antennas Propagat.*, vol. AP-26, pp. 784-789, Nov. 1978.

[80] N. N. Wang, "Reaction formulation for radiation and scattering from plates, corner reflectors, and dielectric-coated cylinders," Ph.D. dissertation. The Ohio St. Univ., Dept. of Elec. Engr., Columbus, OH, Apr. 1974.

[81] J. H. Richmond and E. H. Newman "Mutual impedance between vertical dipoles over a flat earth," *Radio Sci.*, vol. 14, pp. 957-959, Nov.-Dec. 1979.

[82] P. H. Pathak, W. D. Burnside, and R. J. Marhefka, "A uniform GTD analysis of the diffraction of electromagnetic waves by a smooth convex surface," *IEEE Trans. Antennas Propagat.*, vol. AP-28, pp. 631-642, Sept. 1980.

Edward H. Newman (Senior Member, IEEE) was born in Cleveland, OH, on July 9, 194· He received the B.S.E.E., M.S., and Ph.D. degrees in electrical engineering from The Ohio State University in 1969, 1970, and 1974, respectively.

Since 1974 he has been a member of the Ohio State University, Department of Electrical Engineering, ElectroScience Laboratory. His primary research interest is in the development of method of moments, techniques for the analysis of general antenna or scattering problems, and he is the primary author of the "Electromagnetic Surface Patch Code" (ESP). Other research interests include electrically small antennas, arrays, printed circuit antennas, antennas in inhomogeneous media, and scattering from material coated edges. He has published over 35 journal articles in these areas.

Dr. Newman is a member of Commission B of URSI, and is a past Chairman of the Columbus sections of the IEEE Antennas and Propagation and Microwave Theory and Techniques Societies.

TM Scattering by an Impedance Sheet Extension of a

Parabolic Cylinder

Edward H. Newman

John L. Blanchard

TM Scattering by an Impedance Sheet Extension of a Parabolic Cylinder

EDWARD H. NEWMAN, SENIOR MEMBER, IEEE, AND JOHN L. BLANCHARD

Abstract—An integral equation and method of moments (MM) solution is presented for the two-dimensional (2D) problem of the transverse magnetic (TM) scattering by an impedance sheet extension of a perfectly conducting parabolic cylinder. First an integral equation is formulated for a dielectric cylinder of general cross section in the presence of a perfectly conducting parabolic cylinder. It is shown that the solution for a general dielectric cylinder considerably simplifies for the special case of TM scattering by a thin multilayered dielectric strip which can be represented as an impedance sheet. The solution is termed an MM/ Green's function solution where the unknowns in the integral equation are the electric surface currents flowing on the impedance sheet, and the presence of the parabolic cylinder is accounted for by including its Green's function in the kernel of the integral equation. The MM solution is briefly reviewed, and expressions for the elements in the matrix equation and the scattered fields are given. Finally, sample numerical results are presented.

I. INTRODUCTION

THIS PAPER will present an integral equation and method of moments (MM) [1] solution to the two-dimensional (2D) problem of transverse magnetic (TM) scattering by an impedance sheet in the presence of a perfectly conducting parabolic cylinder. Previously, the authors have presented an MM solution for a material cylinder in the presence of a half-plane [2], [3]. The previous solution could be used to study scattering by a material coated knife edge. The present solution represents an extension or generalization of that solution in that the parabolic cylinder can be used to model a thick edge.

The method is based upon an MM solution of the integral equation for the electric surface currents representing the impedance sheet. The solution is termed an MM/Green's function solution [4] since the presence of the perfectly conducting parabolic cylinder is accounted for by including the parabolic cylinder Green's function in the kernel of the integral equation. This can be compared to a conventional MM solution where one would solve for the electric surface currents representing the impedance sheet and the parabolic cylinder. The advantage of the MM/Green's function technique is that the unknowns in the MM solution are limited to the surface occupied by the impedance sheet and do not explicitly include the current distribution on the parabolic cylinder. The disadvantage is that the evaluation of the

elements in the MM/Green's function impedance matrix and right-hand-side vector involve the parabolic cylinder Green's function, as opposed to the much simpler free-space Green's function in a conventional MM solution. The MM/Green's function solution is especially advantageous here, since the parabolic cylinder is one of the few shapes for which the exact Green's function is known. However, an entirely new analysis would be required to treat the impedance sheet in the presence of a cylinder of other than parabolic cross section.

Section II begins with a derivation of the MM/Green's function volume integral equation for a dielectric cylinder of general cross section in the presence of a perfectly conducting parabolic cylinder. By a small extension of the methods of Harrington and Mautz [5], Senior [6], or Andreason [7], it is shown that for the TM polarization a thin multilayered dielectric slab can be represented as a sheet impedance, and the volume integral equation reduces to a surface integral equation. Next the MM solution for the impedance sheet in the presence of the parabolic cylinder is presented. Finally, numerical results are shown which illustrate the accuracy of the method and also show sample results for the echo width and the electric field on the impedance strip.

II. THE INTEGRAL EQUATION

A. The General Dielectric Cylinder

This section will develop an integral equation for the 2D scattering by a dielectric cylinder in the presence of a perfectly conducting parabolic cylinder. We will be brief, since the derivation exactly parallels that for a dielectric cylinder in the presence of a half-plane [2], [3]. Fig. 1(a) shows a perfectly conducting parabolic cylinder, with its focus on the z axis. If we denote the focal length by F, then the surface of the parabola is given by

$$y^2 = 4F(x + F). \tag{1}$$

The parabolic cylinder coordinates (ξ, η, z) are related to the rectangular (x, y, z) coordinates by

$$x = \frac{1}{2}(\xi^2 - \eta^2) \qquad y = \xi\eta, \qquad z = z, \tag{2}$$

and to the (ρ, ϕ, z) circular cylindrical coordinates by

$$\xi = \sqrt{2\rho} \cos\frac{\phi}{2} \qquad \eta = \sqrt{2\rho} \sin\frac{\phi}{2}, \qquad z = z. \tag{3}$$

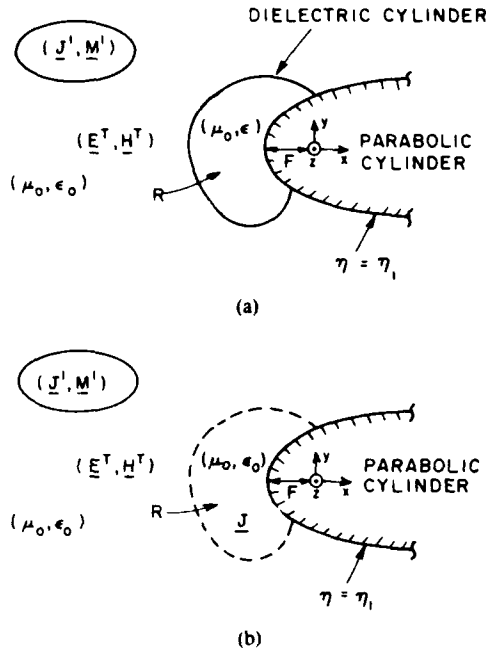In terms of the parabolic cylinder coordinates, the surface of

Fig. 1. (a) Geometry for dielectric cylinder in presence of perfectly conducting parabolic cylinder. (b) Dielectric cylinder is replaced by free-space and equivalent electric volume polarization currents.

the parabola is the surface of constant η

$$\eta = \eta_1 = \sqrt{2F}. \qquad (4)$$

Confined to the region R is a dielectric cylinder with permeability and permittivity (μ_0, ϵ). The dielectric cylinder may be lossy and inhomogeneous. The ambient medium is free space with parameters (μ_0, ϵ_0). The impressed electric and magnetic currents are denoted $(\mathbf{J}^i, \mathbf{M}^i)$. All fields and currents are two-dimensional (z independent) and time harmonic with the $e^{-j\omega t}$ time dependence supressed. We will denote $(\mathbf{E}^T, \mathbf{H}^T)$ as the total fields of the impressed currents in the presence of the dielectric and parabolic cylinder. In the absence of the dielectric cylinder, but with the parabolic cylinder, the fields of the impressed currents are $(\mathbf{E}^i, \mathbf{H}^i)$.

In Fig. 1(b), the volume equivalence theorem [1], [9] is used to replace the dielectric cylinder by free space and the volume polarization currents

$$\mathbf{J} = -j\omega(\epsilon - \epsilon_0)\mathbf{E}^T \qquad (5)$$

confined to the region R. We will let $(\mathbf{E}^J, \mathbf{H}^J)$ denote the fields of $\mathbf{J}$ radiating in the presence of the parabolic cylinder. In the equivalent problem of Fig. 1(b), the total fields are the sum of the fields of the impressed currents and $\mathbf{J}$ radiating in the presence of the parabolic cylinder. Then using (5) we obtain

$$-\mathbf{E}^J + \frac{\mathbf{J}}{-j\omega(\epsilon - \epsilon_0)} = \mathbf{E}^i \text{ in } R, \qquad (6)$$

which is the basic equation for $\mathbf{J}$. It is an integral equation, since $\mathbf{E}^J$ is an integral through R of the vector dot product of $\mathbf{J}$ and the parabolic cylinder dyadic Green's function.

We now restrict the excitation to be a TM plane wave. In free space the incident electric field at (x, y) is

$$\mathbf{E}^{i0} = \hat{z} \exp \left[-jk(x \cos \phi_0 + y \sin \phi_0) \right] \qquad (7)$$

where ϕ_0 is the angle of incidence measured counterclockwise from the positive x axis and $k = 2\pi/\lambda$ is the free-space wavenumber. In this case all electric fields and electric currents are $\hat{z}$ polarized only, and the vector equations (5), (6) reduce to scalar equations, applying to the $\hat{z}$ component. For this reason we will henceforth drop the vector notation, and it should be understood that we are referring to the $\hat{z}$ component of all electric fields and electric currents.

B. The Impedance Sheet Approximation

In this section we will show that for the case of a thin inhomogeneous dielectric slab, (6) for the volume current J can be reduced to a simpler equation for an equivalent surface current J_s. Fig. 2 shows a thin dielectric slab of thickness T, which, for convenience, is oriented parallel to the x axis. The slab is shown having two layers of thickness T_1 and T_2 and permittivity ϵ_1 and ϵ_2, respectively. This represents a geometry of practical interest. For example, layer 1 might be an extremely thin lossy material (commonly referred to as a resistive strip [6]), while layer 2 would be the dielectric substrate on which the resistive strip is deposited. Below we will generalize to any $\epsilon(x, y)$ or $T(x)$.

To apply the sheet impedance approximation it is necessary that the dielectric slab be sufficiently thin that the electric field is essentially uniform in the y direction. This will be the case if

$$|k_1| T_1 + |k_2| T_2 \ll 1$$

where $k_i = \omega\sqrt{\mu_0\epsilon_i}$ is the wavenumber in region i.

Following the above procedure, the layered slab is replaced by free-space and the equivalent volume polarization current J. Since the total electric field is assumed to be uniform through the thickness of the slab, it follows from (5) that

$$\frac{J_1}{\Delta\epsilon_1} = \frac{J_2}{\Delta\epsilon_2}, \qquad (8)$$

where J_i is the value of J in layer i and $\Delta\epsilon_i = (\epsilon_i - \epsilon_0)$.

If the dielectric slab is sufficiently thin, then the fields radiated by the volume current J will be approximately the same as the fields radiated by the surface current

$$J_s = \int_0^T J \, dy = \int_0^{T_1} J_1 \, dy + \int_{T_1}^T J_2 \, dy \qquad (9)$$

and located at $y = T/2$. Using (8), this becomes

$$J_s = \frac{J_1}{\Delta\epsilon_1} (T_1\Delta\epsilon_1 + T_2\Delta\epsilon_2) \text{ or } J_1 = \frac{J_s\Delta\epsilon_1}{T_1\Delta\epsilon_1 + T_2\Delta\epsilon_2}. \qquad (10)$$

Using (10) and applying the approximation that the fields of J are essentially the same as the fields of J_s (i.e., $E^J = E^{J_s}$) to (6) in layer 1 results in

$$-E^{J_s} + Z_s J_s = E^i \qquad (11)$$
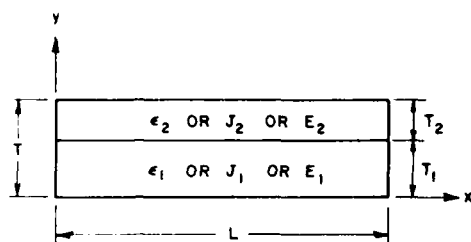
Fig. 2.   Geometry for electrically thin two-layered dielectric strip.

Fig. 3.   Impedance strip of length L is split into N smaller strips.

where the sheet admittance or impedance are given by

$$Y_s = 1/Z_s = -j\omega(T_1\Delta\epsilon_1 + T_2\Delta\epsilon_2). \tag{12}$$

Equation (12) shows that the two layers appear in parallel. For a slab with I layers, the generalization of (12) is

$$Y_s = 1/Z_s = -j\omega \sum_{i=1}^{I} T_i\Delta\epsilon_i. \tag{13}$$

For a slab where ϵ is some function of x and y, and T is also a function of x:

$$Y_s(x) = 1/Z_s(x) = -j\omega \int_0^{T(x)} (\epsilon(x, y) - \epsilon_0) \, dy. \tag{14}$$

If $Z_s = 0$, (11) is identical to that of a perfectly conducting strip. For the special case of a homogeneous slab, (11)–(14) reduce to the sheet impedance approximations of Harrington and Mautz [5], the resistive strip approximation of Senior [6], or the very thin material plate of Newman and Schrote [8].

III. MOMENT METHOD SOLUTION

A. The MM Matrix Equation

This section will present a pulse basis MM solution [1], [2] of (11), using the impedance sheet approximation to a thin dielectric slab in the presence of a perfectly conducting parabolic cylinder. The impedance sheet will be located on the negative x axis. As illustrated in Fig. 3, the impedance sheet is segmented into N smaller strips of width W_n. R_n will denote the region of strip n. The strips must be small enough so that the total electric field and Z_s can be assumed to be reasonably constant in each strip. The equivalent current can then be approximated by
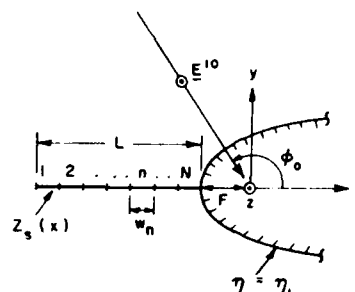
$$J_s = \sum_{n=1}^{N} I_n J_{sn} \tag{15}$$

where the I_n are a sequence of N unknown coefficients, and the J_{sn} are the N ($\hat{z}$ polarized) pulse basis expansion modes defined by

$$J_{sn} = \begin{cases} 1/W_n, & \text{within } R_n \\ 0, & \text{otherwise.} \end{cases} \tag{16}$$

We employ a Galerkin [1] MM solution, with weighting functions chosen identical to the expansion modes. In this case, (11) reduces to the matrix equation

$$[Z + \Delta Z]I = V \tag{17}$$

where $[Z + \Delta Z]$ is the symmetric $N \times N$ impedance matrix, V is the N element right-hand-side vector, and I is the N element solution vector whose components are the unknown I_n in (15). Typical elements in the impedance matrix are given by

$$Z_{mn} = -\int_m E_n^T J_{sm} \, dx \tag{18}$$

where E_n^T is the total ($\hat{z}$ component of the) electric field of J_{sn} radiating in the presence of the parabolic cylinder, and the integral is over R_m. A typical element of the $[\Delta Z]$ matrix is given by

$$\Delta Z_{mn} = \int_{m \bullet n} Z_s J_{sm} J_{sn} \, dx \tag{19}$$

where the integration is over regions R_m and R_n. Since we are using the subsectional basis functions of (16), $[\Delta Z]$ is a diagonal matrix whose typical element is given by

$$\Delta Z_{nn} = \frac{1}{W_n^2} \int_n Z_s(x) \, dx. \tag{20}$$

Note that ΔZ_{nn} can be evaluated in closed form for any simple choice of $Z_s(x)$. Typical elements of the right-hand-side vector are

$$V_m = \int_m E^i J_{sm} \, dx \tag{21}$$

where E^i is the total electric field of the TM incident wave in the presence of the parabolic cylinder.

The numerical evaluation of the self-impedance terms in the MM impedance matrix always presents a challenge. According to (18), to find Z_{nn} we must find the electric field of J_{sn} on the surface of J_{sn}. The integrand of the resulting integral will have a singularity which must be properly treated. To treat this problem it is convenient to write the total field radiated by J_{sn} in the presence of the parabolic cylinder as

$$E_n^T = E_n^0 + E_n^S \tag{22}$$

where E_n^0 is the free-space field of J_{sn} and E_n^S is the so-called scattered field. Using the notation of (22), we can write

$$[Z] = [Z^0] + [Z^S] \tag{23}$$

where $[Z^0]$ is the impedance matrix for the perfectly conducting strip in free-space and $[Z^S]$ is a correction matrix which accounts for the field which is scattered from the parabolic

cylinder. Using this notation, (18) becomes

$$Z_{mn} = Z_{mn}^0 + Z_{mn}^S$$

$$= -\int_m E_n^0 J_m \, dx - \int_m E_n^S J_m \, dx. \qquad (24)$$

The advantage of (24) is that the only singularities are in the integrands of the terms of Z_{mn}^0 for which $|m - n| \leq 1$. However, since they involve the relatively simple free-space Green's function, they can be easily treated [10], [11]. By contrast, the Z_{mn}^S involve the far more complicated parabolic cylinder Green's function, but contain no singularities. In a similar manner it is advantageous to write (21) as

$$V_m = V_m^0 + V_m^S$$

$$= \int_m E^{i0} J_m \, dx + \int_m E^{iS} J_m \, dx. \qquad (25)$$

The elements of Z_{mn}^0 and V_m^0 are identical to the elements in the impedance matrix and right-hand-vector for the perfectly conducting strip in free space. Expressions and computer codes for the evaluation of these elements are available [10]. In the next section we discuss the efficient evaluation of Z_{mn}^S and V_m^S. These both require the evaluation of fields in the presence of a perfectly conducting parabolic cylinder. An excellent summary of such field expressions is given by Christiansen [12].

B. Evaluation of the Z_{mn}^S

Fig. 4 shows a perfectly conducting parabolic cylinder with surface $\eta = \eta_1$. On the negative x axis ($\xi = 0$) are the strip current modes J_{sn} and J_{sm}. Z_{mn}^S from (24) can be written as

$$Z_{mn}^S = -\frac{1}{W_m} \int_m \left[\frac{1}{W_n} \int_n G^S(x_s, x_f) \, dx_s \right] dx_f \qquad (26)$$

where $G^S(x_s, x_f)$ is the scattered electric field at $(x_f, y_f = 0)$ radiated by a unit amplitude electric line current at $(x_s, y_s = 0)$. Note that by scattered field we mean the difference between the total field radiated by the line source in the presence of the parabolic cylinder and the free-space fields of the line source. The following expression for G^S can be obtained by converting the contour integral representation of Robin [13] to a summation using the same method as Ivanov [16][1]

$$G^S(x_s, x_f) = C \sum_{p=0}^{\infty} D_p^2(0) D_{-p-1}(\eta_> \alpha) D_{-p-1}(\eta_< \alpha)$$

$$\cdot \left[(-1)^p + \frac{D_{-p-1}(-\eta_1 \alpha)}{D_{-p-1}(\eta_1 \alpha)} \right] \qquad (27)$$

where D_p is the (integer) order p parabolic cylinder function [14], [15], and

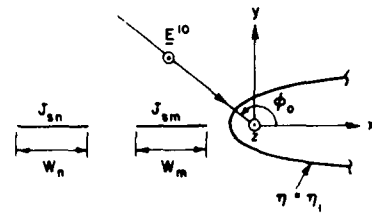$$C = -\frac{jk^2}{2\pi\omega\epsilon_0} \qquad (28)$$

Fig. 4. Modes J_{sm} and J_{sn} in presence of perfectly conducting parabolic cylinder $\eta = \eta_1$.

$$\alpha = \sqrt{2k}\, \epsilon^{-j\pi/4} \qquad (29)$$

$\eta_> = $ the larger of $(\sqrt{-2x_s}, \sqrt{-2x_f})$

$\eta_< = $ the smaller of $(\sqrt{-2x_s}, \sqrt{-2x_f})$. $\qquad (30)$

Recognizing that G^S is a separable function of x_s and x_f, the double integral in (26) separates also, yielding (even for $m = n$)

$$Z_{mn}^S = -C \sum_{p=0}^{\infty} D_p^2(0) \left[(-1)^p + \frac{D_{-p-1}(-\eta_1 \alpha)}{D_{-p-1}(\eta_1 \alpha)} \right]$$

$$\cdot A_m(p) A_n(p) \qquad (31)$$

in which

$$A_n(p) = \frac{1}{W_n} \int_n D_{-p-1}(\sqrt{2|x|}\, \alpha) \, dx. \qquad (32)$$

The evaluation of the symmetric $[Z^S]$ matrix in principal requires $(N^2 + N)/2$ evaluations of (31). However, it is more efficient to recognize that the Z_{mn}^S are a separable function of m and n and evaluate the entire $[Z^S]$ matrix in the course of performing the summation. For each term p in the summation one must numerically evaluate the N integrals $A_n(p)$, $n = 1$, $2, \cdots, N$. The result is that the computer CPU time to evaluate $[Z^S]$ is proportional to N rather than N^2.

C. The Evaluation of the V_m^S

The elements of V_m^S are defined by (25). As illustrated in Fig. 4, a plane wave is incident upon the parabolic cylinder, making an angle ϕ_0 with respect to the $+x$ axis. The free-space electric field is given by (7). When this plane wave hits the perfectly conducting parabolic cylinder, the scattered field at a field point with parabolic coordinates (ξ, η) is [16]

$$E^{iS}(\phi_0) = \frac{-1}{\sin\dfrac{\phi_0}{2}} \sum_{p=0}^{\infty} \frac{\left(j\cot\dfrac{\phi_0}{2}\right)^p}{p!}$$

$$\cdot D_p(-\xi\alpha) \frac{D_p(\eta_1\alpha^*)}{D_{-p-1}(\eta_1\alpha)} D_{-p-1}(\eta\alpha), \qquad (33)$$

provided $\pi/2 < \phi_0 \leq \pi$ and where the asterisk denotes complex conjugate. Inserting (33) into (25), and noting that the field points will be on the negative x axis ($\xi = 0$, $\eta = \sqrt{-2x}$,

the scattered part of V_m becomes

$$V_m^S(\phi_0) = \frac{-1}{\sin\frac{\phi_0}{2}} \sum_{p=0}^{\infty} \frac{\left(j\cot\frac{\phi_0}{2}\right)^p}{p!}$$

$$\cdot\; D_p(0)\,\frac{D_p(\eta_1\alpha^*)}{D_{-p-1}(\eta_1\alpha)}\,A_m(p). \quad (34)$$

The major computational effort in evaluating the Z_{mn}^S of (31) and the V_m^S of (34) is the evaluation of the $A_m(p)$ which occur in both. Prior to evaluating the matrix elements it is most efficient to form a table of the $A_m(p)$ for $m = 1, 2, \cdots$, N and $p = 1, 2, \cdots, P$, where P is the largest value of p required to obtain convergence of the summations. P is typically chosen as 15. This table then contains all the $A_m(p)$ integrals needed in the solution, and its use insures that each $A_m(p)$ integral is evaluated only once. Note that for fixed m, using the recursive relation for the parabolic cylinder functions [15] allows efficient computation of the P values $A_m(p)\, p = 1, 2, \cdots, P$. However, it is essential to recurse in the stable direction as described in [14]. We also note that since $D_p(0) = 0$ for p odd, the summations in (31) and (34) need only include the even values of p.

D. Evaluation of the Electric Field

Once the elements in the MM matrix equation have been evaluated, (17) can be solved for I, and the total field at any point in space can be found from

$$E^T = E^i + \sum_{n=1}^{N} I_n E_n^T \quad (35)$$

where as indicated in (22), E_n^T is the total electric field of mode n radiating in the presence of the parabolic cylinder, and E^i is the total electric field of the incident plane wave in the presence of the parabolic cylinder. Using the volume equivalence theorem of (5), it is particularly simple to evaluate the total field within the dielectric cylinder. The average electric field on mode n is simply given by

$$E^T = Z_s I_n / W_n. \quad (36)$$

Now consider the evaluation of the far-zone scattered fields, that is, as $\rho \to \infty$. The scattered field is given by (35), except that we replace E^i by E^{iS}. Then, assuming that the I_n are known, we need expressions for E_n^T and E^{iS} in the far zone.

Referring to (22), E_n^T can be written as the sum of the free-space field of mode n plus the scattered field of mode n. Here we will only present an expression for the scattered field. The far-zone scattered field of mode n at the far-zone field point (ρ, ϕ) can be most easily obtained from (34) and reciprocity. The result is

$$E_n^S(\rho, \phi) = \left(\frac{-k^{3/2}}{4\omega\epsilon_0}\sqrt{\frac{2}{\pi}}\, e^{j\pi/4}\right)\frac{e^{jk\rho}}{\sqrt{\rho}}\, V_n^S(\phi). \quad (37)$$

To obtain an expression for E^{iS} in the far zone, we replace

the integer order parabolic cylinder functions in (33) by their large argument approximation [15]

$$D_p(z) \sim z^p e^{-z^2/4}, \qquad |z| \gg 1 \text{ and } |z| \gg |p|, \quad (38)$$

which is valid for all integers $p \geq 0$ and all negative integers p provided $|\underline{/z}| < 3\pi/4$. Since the parabolic cylinder functions in (33) meet these conditions, in the far zone

$$E^{iS} = \frac{-e^{j(k\rho + \pi/4)}}{2\sqrt{k\rho}\,\sin\frac{\phi_0}{2}\sin\frac{\phi}{2}} \sum_{p=0}^{\infty}$$

$$\frac{\left(-j\cot\frac{\phi_0}{2}\cot\frac{\phi}{2}\right)^p}{p!}\,\frac{D_p(\eta_0\alpha^*)}{D_{-p-1}(\eta_0\alpha)},$$

$$\left|\cot\frac{\phi_0}{2}\cot\frac{\phi}{2}\right| < 1. \quad (39)$$

IV. Numerical Results

This section will present numerical results based upon the above MM/Green's function solution for TM scattering by an impedance sheet in the presence of a parabolic cylinder. The first example is designed to illustrate the accuracy of the MM/Green's function solution by comparison with a limiting case where an exact solution is available. The frequency is 300 MHz, and the problem geometry is illustrated in the insert in Fig. 5. Here we have a perfectly conducting half-plane (i.e., a parabolic cylinder with $F = \eta_1 = 0$) with a sheet impedance extension of length $L = \lambda/2$ and impedance $Z_s = 0$ (i.e., a perfectly conducting strip). The net result is that we simply have a half-plane. We analyzed the strip extension of the $\eta_1 = 0$ parabolic cylinder using an $N = 10$ equal segment MM/Green's function solution, as already described. Fig. 5 shows a comparison of the magnitude and phase of the MM/Green's function and the exact (see [12, ch. 8]) current induced on a half-plane by a unit amplitude TM plane wave with edge on incidence, i.e., $\phi_0 = 180°$. The MM/Green's function points are plotted in the center of the segments and represent the average current over the segment, since we employed piecewise constant expansion modes. Fig. 5 shows that the current obtained from the MM/Green's function solution are very close to the exact half-plane currents. The only exception is the current adjacent to the edge at $x = 0$. Here the MM/Green's function value is about 5.8 A/m, while the exact value at $x = 0.025\lambda$ is 4.0 A/m. Thus one might conclude that for the edge segment the MM/Green's function value is high by a factor of about 1.45. However, it must be remembered that the MM/Green's function points represent the average current over the segment and not the current at the center of the segment. It is well known that the exact current has a $1/\sqrt{x}$ edge singularity as $x \to 0$. For a function with a $1/\sqrt{x}$ singularity, the ratio of its average value from 0 to W, divided by its value at $W/2$, is $\sqrt{2} \approx 1.41$. Thus the MM/Green's function value, which is a factor of 1.45 above the exact current at the center of the segment, is very close to the average of the exact current and is as well as the pulse basis function solution can do. It is also
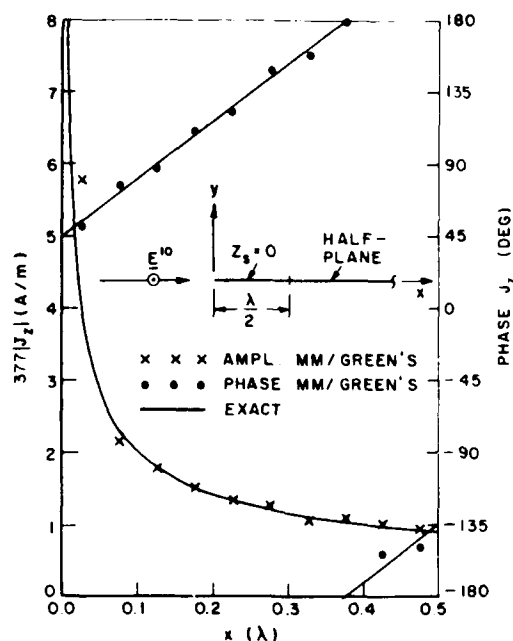
Fig. 5.   Comparison of exact and MM/Green's function solution for current on perfectly conducting strip extension of half-plane.

TABLE I
CPU TIMES IN 0.01 s FOR VARIOUS NUMBER OF MODES N

N	Compute $[Z^S]$	Compute $[Z^0]$	Crout sol.
5	15	1	3
10	17	5	3
20	26	20	3
40	45	82	19
80	105	336	143

interesting to note that, in the absence of the half-plane, the MM solution for the strip current would have an edge singularity at $x = 0.5\lambda$. However, by adding $[Z^S]$ and V^S to the free-space impedance matrix and right-hand-vector, respectively, the MM/Green's function solution was able to "see" that there was no real edge at $x = 0.5\lambda$.

Table I shows the CPU times for the above problem with N = 5, 10, 20, 40, and 80 modes. All CPU times are for a VAX 8550. The times shown are an average of five runs on a time-sharing system. The CPU clock unit was 0.01 s, and thus the smaller times are not reliable. CPU times are shown for the computational of $[Z^S]$, the computation of $[Z^0]$, and the solution of the order N simultaneous linear equations via Crout's method. The CPU time to compute the right-hand-vector $[\Delta Z]$ or the far-zone field is negible. Note in Table I that the CPU time to compute $[Z^S]$ is roughly linear with N, while that to compute $[Z^0]$ is quadratic. In fact, for N greater than about 20, it takes longer to compute $[Z^0]$ than to compute $[Z^S]$.

The next set of data will be for the geometry illustrated in Fig. 6 at 1 GHz. Here we have a perfectly conducting parabolic cylinder with a multilayer dielectric strip extension of length $L = \lambda = 30$ cm. The multilayer strip consists of a resistance strip of R Ω sitting on top of a lossless dielectric strip of thickness $T = 0.0106\lambda = 1/8$ in = 0.3175 cm and

$\epsilon_r = 10$ $f = 1$ GHz

$L = 30$ cm $T = 0.3175$ cm

$R = \infty \longrightarrow Z_s = j628.9 \Omega$

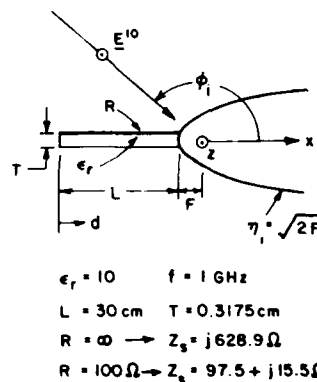$R = 100 \Omega \rightarrow Z_s = 97.5 + j15.5 \Omega$

Fig. 6.   TM plane wave incident upon parabolic cylinder with multilayer dielectric strip extension. Multilayer strip is of length 30 cm and consists of R ohm resistance card on top of $\epsilon_r = 10$ dielectric strip of thickness 0.3175 cm.

relative dielectric constant $\epsilon_r = 10$. Setting $R = \infty$ corresponds to removing the resistive strip, and from (12) the lossless dielectric strip is equivalent to the sheet admittance $Y_s = -j0.00159$ ℧ or the sheet impedance $Z_s = j628.9$ Ω. If we let $R = 100$ Ω, then the 100-Ω resistive strip on top of the lossless dielectric strip is equivalent to $Y_s = 0.01 - j0.00159$ ℧ or $Z_s = 97.5 + j15.5$ Ω. For parabolic cylinders of focal length $F = 0$, 1, 10, and 30 cm, Figs. 7(a)–(d) show the backscatter echo width for these two cases and, for comparison, the bare parabolic cylinder. The parabola $F = 0$ corresponds to a half-plane. In this case the data in Fig. 7(a) were found to be in excellent agreement with the authors' previous MM/Green's function solution for TM scattering by a general dielectric cylinder in the presence of a half-plane, and where the dielectric cylinder is represented by equivalent electric volume polarization currents [2]. For edge on incidence ($\phi_i = 180°$) and for the $F = 1$ cm parabola, Fig. 8 shows the magnitude and phase of the total electric field in the dielectric strip.
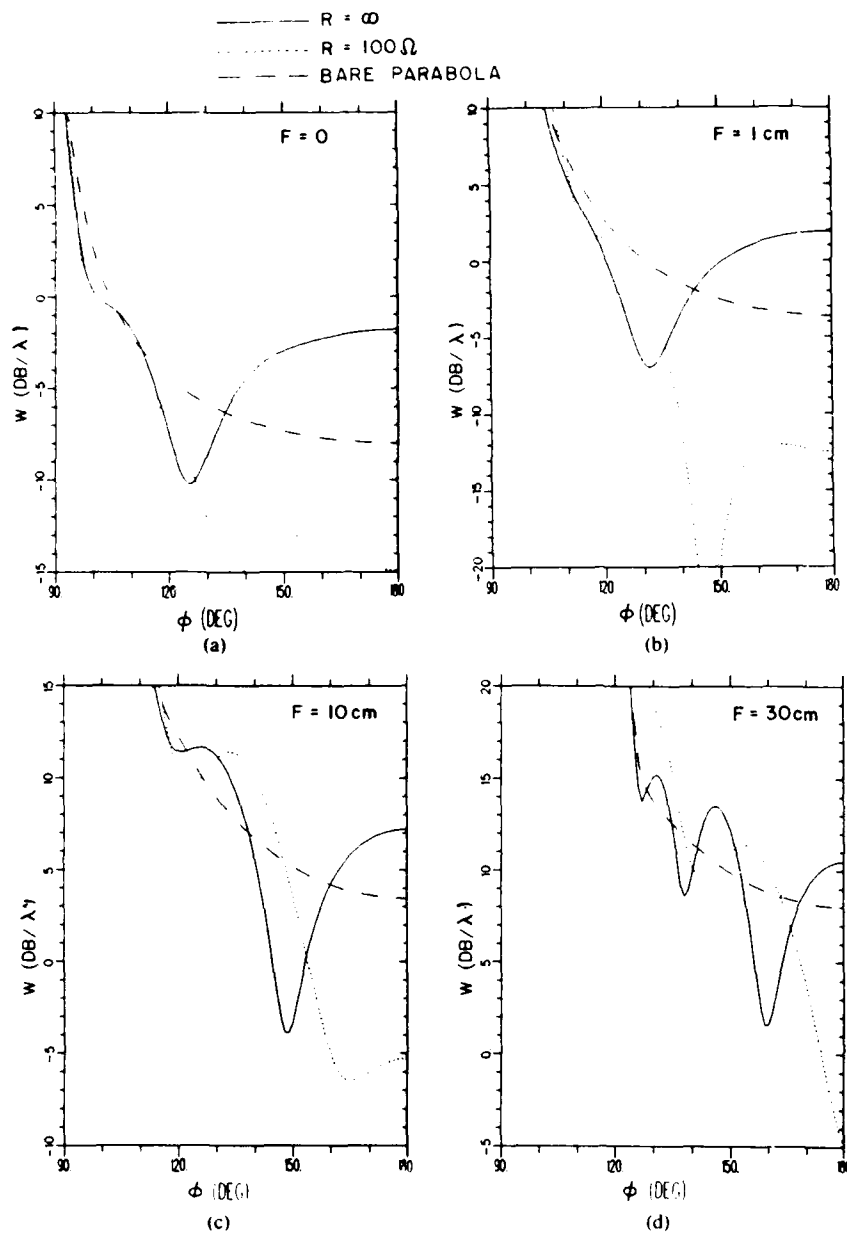
R = ∞
R = 100 Ω
BARE PARABOLA

Fig. 7. Backscatter echo width at 1 GHz for geometry in Fig. 6 for parabolic cylinders of various focal lengths. (a) $F = 0$, i.e., half-plane. (b) $F = 1$ cm. (c) $F = 10$ cm. (d) $F = 30$ cm.
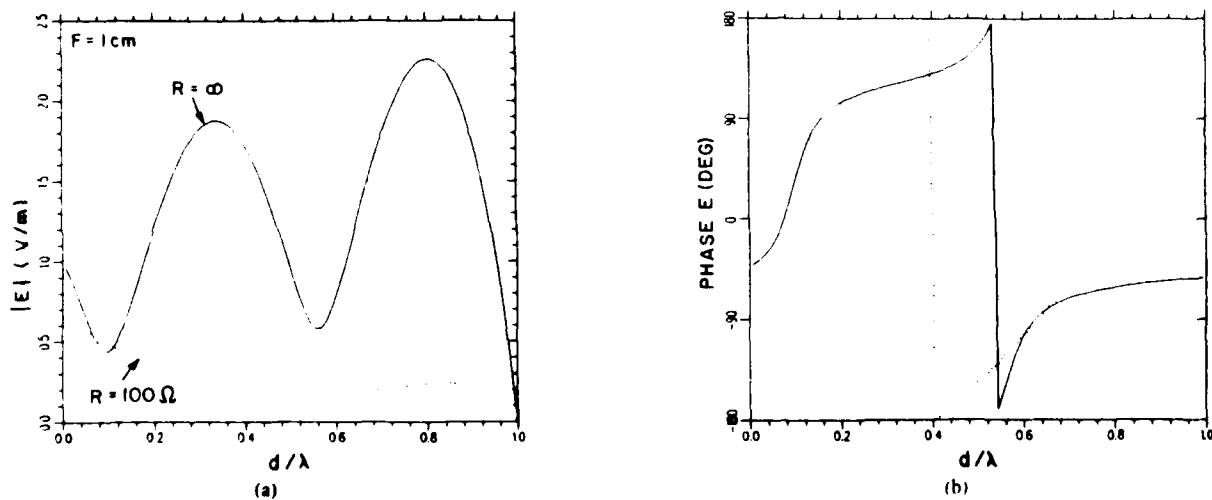
Fig. 8. For geometry of Fig. 6 and for parabolic cylinder of focal length $F = 1$ cm, total electric field in strip.

V. Summary

This paper has presented the MM/Green's function solution to the problem of TM scattering by an impedance sheet in the presence of a perfectly conducting parabolic cylinder. The impedance sheet is an approximate model for a thin multilayered dielectric slab. Explicit expressions for the elements in the MM matrix equation are obtained. The impedance matrix is written as the sum of the free-space impedance matrix plus a scattered field matrix which accounts for the presence of the parabolic cylinder. It is shown that the elements in the scattered field matrix are a separable function of modes J_{sm} and J_{sn}. The result is that the CPU time to evaluate the $(N^2 + N)/2$ elements in this symmetric impedance matrix is proportional to N, rather than to N^2 as in a conventional MM solution. Numerical results are shown to illustrate the accuracy of the method and to show sample results.

References

[1] R. F. Harrington, *Field Computations by Moment Methods*. New York: Macmillan, 1968.

[2] E. H. Newman, "TM scattering by a dielectric cylinder in the presence of a half-plane," *IEEE Trans. Antennas Propagat.*, vol. AP-33, pp. 773-782, July 1985.

[3] ——, "TM and TE scattering by a dielectric/ferrite cylinder in the presence of a half-plane," *IEEE Trans. Antennas Propagat.*, vol. AP-34, pp. 804-813, June 1986.

[4] ——, "An overview of the hybrid MM/Green's function method in electromagnetics," *Proc. IEEE*, vol. 76, pp. 270-282, Mar. 1988.

[5] R. F. Harrington and J. R. Mautz, "An impedance sheet approximation for thin dielectric shells," *IEEE Trans. Antennas Propagat.*, vol. AP-23, pp. 531-534, July 1975.

[6] T. B. A. Senior, "Backscattering from resistive strips," *IEEE Trans. Antennas Propagat.*, vol. AP-27, pp. 808-813, Nov. 1979.

[7] M. G. Andreasen, "Back-scattering cross section of a thin, dielectric, spherical shell," *IEEE Trans. Antennas Propagat.*, vol. AP-5, pp. 267-270, July 1957.

[8] E. H. Newman and M. R. Schrote, "An open surface integral formulation for electromagnetic scattering by material plates," *IEEE Trans. Antennas Propagat.*, vol. AP-32, pp. 672-678, July 1984.

[9] R. F. Harrington, *Time Harmonic Electromagnetic Fields*. New York: McGraw-Hill, 1961, sec. 3-8.

[10] N. N. Wang, "Reaction formulation for radiation and scattering from plates, corner reflectors and dielectric-coated cylinders," Ph.D. dissertation, Dep. Elec. Eng., Ohio State Univ., Columbus, 1974.

[11] E. H. Newman, "The equivalent separation(s) for the self-impedance of thin strips," *IEEE Trans. Antennas Propagat.*, vol. AP-35, pp. 110-113, Jan. 1987.

[12] P. L. Christiansen, in *Electromagnetic and Acoustic Scattering by Simple Shapes*, J. J. Bowman, T. B. A. Senior, and P. L. E. Uslenghi, Eds. Amsterdam, The Netherlands: North Holland, 1969, ch. 7.

[13] R. Robin, "Diffraction d'une onde cylindrique (ou plane) par un cylindre parabolique de génératrices parallèles à l'onde," *Ann. Télécommun.*, vol. 19, pp. 257-269, 1964.

[14] M. Abramowitz and I. A. Stegun, *Handbook of Mathematical Functions*, Applied Mathematics Series 55. National Bureau of Standards, 1964, ch. 19.

[15] I. S. Gradshteyn and I. M. Ryzhik, *Tables of Integrals, Series, and Products*. New York: Academic, 1980, ch. 9.

[16] V. I. Ivanov, "Diffraction of short plane waves on a parabolic cylinder," *USSR Comp. Math. Math. Phys.*, 2, pp. 255-271, 1963 (English translation of *Zh. vych. mat.*, 2, pp. 241-254, 1962).

Edward H. Newman (S'67-M'74-SM'86) was born in Cleveland, OH, on July 9, 1946. He received the B.S.E.E., M.S., and Ph.D. degrees in electrical engineering from The Ohio State University, Columbus, in 1969, 1970, and 1974, respectively.

Since 1974 he has been a member of the ElectroScience Laboratory in The Ohio State University Department of Electrical Engineering. His primary research interest is in the development of method of moments techniques for the analysis of general antenna or scattering problems, and he is the primary author of the "Electromagnetic Surface Patch Code" (ESP). Other research interests include electrically small antennas, superdirective arrays, printed circuit antennas, and antennas in inhomogeneous media.

Dr. Newman is a member of Commission B of URSI, and is a Past Chairman of the Columbus sections of the IEEE Antennas and Propagation and Microwave Theory and Techniques Societies.

John L. Blanchard was born in Waltham, MA, in 1959. He received the B.A. degree from The University of Maine, Orono, in 1982, and the M.S. degree from The Ohio State University, Columbus, in 1987, both in mathematics.

Currently he is a Ph.D. candidate in the Department of Mathematics at The Ohio State University, and also a Graduate Research Associate at the ElectroScience Laboratory. His primary research interest is in the numerical solution of integral and partial differential equations.

Electromagnetic Diffraction of an Obliquely Incident Plane Wave Field by a Wedge with Impedance Faces

ROBERTO G. ROJAS, MEMBER, IEEE

Abstract—A uniform asymptotic solution is presented for the electromagnetic diffraction by a wedge with impedance faces and with included angles equal to 0 (half-plane), $\pi/2$ (right-angled wedge), π (two-part plane) and $3\pi/2$ (right-angled wedge). The incident field is a plane wave of arbitrary polarization, obliquely incident to the axis of the wedge. The formal solution, which is expressed in terms of an integral, was obtained by the generalized reflection method. A careful study of the singularities of the integrand is done before the asymptotic evaluation of the integral can be carried out. The asymptotic evaluation of the integral is performed taking into account the presence of the surface wave poles in addition to the geometrical optics (GO) poles near the saddle points. This results in a uniform solution which is continuous across the shadow boundaries of the GO fields as well as the surface wave fields.

I. INTRODUCTION

THE SCATTERING of electromagnetic and acoustic waves by objects that are not perfectly conducting has many practical applications. For example, radar absorbing materials are used to cover objects to reduce their scattering. To study the scattering properties of objects that are not perfectly conducting. Leontovich [1] developed a boundary condition known as the impedance or Leontovich boundary condition. Although the impedance boundary condition is an approximation to the exact boundary conditions satisfied by the fields at the surface of the scatter. it is a very useful approximation since it allows the solution of many practical problems which otherwise could not be solved.

Among the various shapes studied in the past, the scattering by wedge-shaped objects has received a lot of attention [2]–[26]. There are basically two methods to solve for the fields scattered by wedge-shaped objects, namely, the Wiener–Hopf and Maliuzhinets methods. Maliuzhinets [2] introduced a method to solve the problem of the scattering of a normally incident plane wave by a wedge with impedance faces. Note that for the case of normal incidence, the problem can be scalarized by separating the fields into TM$_z$ and TE$_z$ polarized components. The Maliuzhinets method basically consists of expressing the total field as a spectrum of plane waves which can be written as an integral with an unknown spectral function. The unknown spectral function is then determined

with the application of the boundary, radiation and edge conditions. The key step in the Maliuzhinets method is the transformation of an integral equation into a first-order functional difference equation whose solution yields the unknown spectral function. Once the difference equation is solved, the integral representation of the fields can be asymptotically evaluated. The problem becomes much more complicated for the case of oblique incidence. Several authors have studied the scattering of an obliquely incident plane wave by a wedge [3], [9], [13], [24], [25]; however, each of the solutions in [3], [9], [13], [24], [25] is valid for only a single wedge angle. Moreover, all of the above asymptotic solutions, except for [9], do not take into account the presence of the surface waves excited at the edge of the impedance wedge. In other words, the surface wave poles near the saddle point were ignored. In [9], the integral representation of the fields scattered by a half-plane with different impedances on each face is given. but the asymptotic evaluation of the integral for the case of oblique incidence is not performed. The present author obtained an exact solution using the Wiener–Hopf method for the the field scattered from a planar surface with an impedance discontinuity and from an impedance half-plane [19]. The asymptotic evaluation of the exact solution in [19], which is expressed in terms of an integral, was carried out taking into account the presence of the surface wave poles near the saddle point. It is noted that the scattering from a right-angled wedge can also be solved with the traditional separation of variables technique by making a change of variables first suggested by Lewy [27] and Stoker [28]. This method was followed by Hwang [22] and Karal et al. [23].

This paper is based on the generalized reflection method (GRM) which is more general than the Wiener–Hopf method [19]. The GRM, which is a generalization of the Maliuzhinets method, was developed by Vaccaro [12]. [13] to study the scattering from an impedance wedge excited by an obliquely incident plane wave as depicted in Fig. 1 where the z-axis coincides with the wedge-axis. Since the TM$_z$ and TE$_z$ polarized fields are coupled for the case of oblique incidence, a two-element column vector $\vec{J}_z$, whose elements are the z components of the electric and magnetic fields, is defined. It is then sufficient to obtain a solution for $\vec{J}_z$ since all the other field components can be determined from $\vec{J}_z$. Next, as in the Maliuzhinets method, the vector $\vec{J}_z$ is expressed as an integral along the Sommerfield contour with an integrand that can be written as the product of an unknown spectral function $\vec{F}_z$ and a known exponential function. Since the integral satisfies the

scalar Helmholtz equation, the next step is to impose the boundary conditions which yield an integral equation for the column vector $\bar{F}_z$. The integral equation is then converted into a functional difference equation which is referred to as the generalized reflection equation (GRE) [12]. Unlike the case considered by Maliuzhinets, the GRE is a second-order difference equation which is much more difficult to solve than a first-order one. It turns out that the GRE can be solved in terms of the Maliuzhinets functions for four wedge angles, namely, the half-plane and the two-part impedance plane with arbitrary impedance values on each face and the $\pi/2$- and $3\pi/2$-wedges with one face a perfect electric conductor (PEC) or a perfect magnetic conductor (PMC). Recently, Senior [26] described a procedure similar to that followed by Vaccaro [12]; however, one face of the wedge is always a PEC in [26]. Furthermore, the spectral function for the $3\pi/2$-wedge in [26] does not reduce to the known spectral function when $\beta = \pi/2$ because the constant c_2 in [26] is incorrectly evaluated.

The purpose of this paper is to obtain a uniform asymptotic solution for the four special cases mentioned above. The asymptotic evaluation is performed taking into account the presence of the geometrical optics (GO) poles as well as the surface wave poles (complex poles). This results in a uniform expression across the shadow boundaries of the GO and surface wave fields.

The expressions for $\bar{f}_z$ and $\bar{F}_z$ are given in a very compact matrix notation. This is especially useful when the unknown constants appearing in the spectral function $\bar{F}_z$ have to be determined. Besides being compact, the matrix notation also helps in the physical interpretation of the results, and it is suitable for numerical computations. Several numerical examples are presented and the effect of the impedance values on the diffracted and surface wave fields is discussed. Note that all the fields in the following discussion have the $e^{-i\omega t}$ time dependence which is suppressed. Throughout this paper, a bar and a double bar on top of a function name denotes a two-element column vector and a two-by-two matrix, respectively.

II. STATEMENT OF THE PROBLEM

The problem to be considered here is the electromagnetic (EM) diffraction by a wedge with impedance faces as shown in Fig. 1. The faces of the wedge are labeled 0 and n and the exterior wedge angle is $n\pi$. Let ρ, ϕ, and z denote the cylindrical coordinates with the z-axis coinciding with the wedge axis. As depicted in Fig. 1, the angles ϕ and ϕ' are measured from the 0 face. The impedance of face 0 is Z_1, while the impedance of face n is Z_2, where both Z_1 and Z_2 are scalar constants. In other words, the impedance faces are isotropic and homogeneous. The faces of the wedge satisfy the Leontovich boundary condition, namely

$$\bar{E} - \hat{\phi}(\hat{\phi} \cdot \bar{E}) = \pm \hat{\phi} \times \bar{H} Z_{\frac{1}{2}}$$

$$\bar{H} - \hat{\phi}(\hat{\phi} \cdot \bar{H}) = \mp \hat{\phi} \times \bar{E} Y_{\frac{1}{2}} \qquad \phi = \begin{cases} 0 \\ n\pi \end{cases} \quad (1)$$

where $\hat{\phi}$ is the unit vector normal to the plane ϕ = constant, $Y_{1,2} = 1/Z_{1,2}$ and $\bar{E}$ and $\bar{H}$ are the electric and magnetic vector fields, respectively.

The incident field is assumed to be a plane wave of arbitrary

polarization, obliquely incident on the axis of the wedge as depicted in Fig. 1. As shown in [17], [29], if all the fields have the same exponential z-dependence exp ($ikz \cos \beta$), which is the case here, then it is sufficient to find the solution for the z components of the electric and magnetic fields. Thus let $\bar{f}_z$ be defined as follows:

$$\bar{f}_z(\rho, \phi, z) = \begin{bmatrix} E_z \\ \eta_0 H_z \end{bmatrix} \qquad (2)$$

where E_z and H_z are the z components of the electric and magnetic fields, respectively, and η_0 is the free-space intrinsic impedance. The column vector $\bar{f}_z$ plays the role of a vector potential since all the other field components can be obtained in terms of $\bar{f}_z$. It follows from (2) that the incident field can be defined in terms of $\bar{f}_z^i$, i.e.,

$$\bar{f}_z^i = \begin{bmatrix} E_z^i \\ \eta_0 H_z^i \end{bmatrix}$$

$$= \bar{F}_{0z} \exp (-iK\rho \cos (\phi - \phi')) \exp (ikz \cos \beta)$$

$$\bar{F}_{0z} = \begin{bmatrix} E_{0z} \\ \eta_0 H_{0z} \end{bmatrix}, \qquad 0 < \phi' < n\pi, \ 0 < \beta < \pi$$

$$(3)$$

where $0 \leqslant \phi \leqslant n\pi$, $K = k \sin \beta$ and $\rho = \sqrt{x^2 + y^2}$. Note that E_{0z} and H_{0z} are arbitrary constants and k is the free-space wavenumber. To obtain a unique solution, the fields have to satisfy two more conditions; namely, the radiation and edge conditions.

III. GENERALIZED REFLECTION METHOD

Following Maliuzhinets approach, the total field $\bar{f}_z$ is expressed in terms of a spectrum of plane waves. This spectrum can be written as an integral along the so-called twofold Sommerfeld contour γ depicted in Fig. 2, i.e.,

$$\bar{f}_z(\rho, \phi, z) = \frac{e^{ikz \cos \beta}}{2\pi i} \int_\gamma \bar{F}_z \left(\alpha + \frac{n\pi}{2} - \phi \right)$$

$$\cdot \exp (-iK\rho \cos \alpha) \, d\alpha \quad (4)$$

where the function $\bar{F}_z$ is unknown at this stage of the analysis. However, due to the radiation and edge conditions, one can deduce that $\bar{F}_z$ is an analytic function for $|\text{Im } \alpha| > d$, where d is a positive real constant. Note that the integral in (4) converges uniformly, and satisfies the scalar Helmholtz equation and the radiation condition provided that the contour γ, shown in Fig. 2, lies on the half-planes defined by $|\text{Im } \alpha| > d$. It also follows from the edge conditions that the asymptotic behavior of $\bar{F}_z$ is

$$\lim_{|\text{Im } (\alpha)| \to \infty} \bar{F}_z(\alpha) = \text{constant vector.} \qquad (5)$$

Moreover, the presence of the incident field, given in (3), implies that $\bar{F}_z(\alpha)$ must have one first-order pole singularity at $\alpha = n\pi/2 - \phi'$.

After applying the boundary conditions, (4) becomes an integral equation which can be transformed into a functional
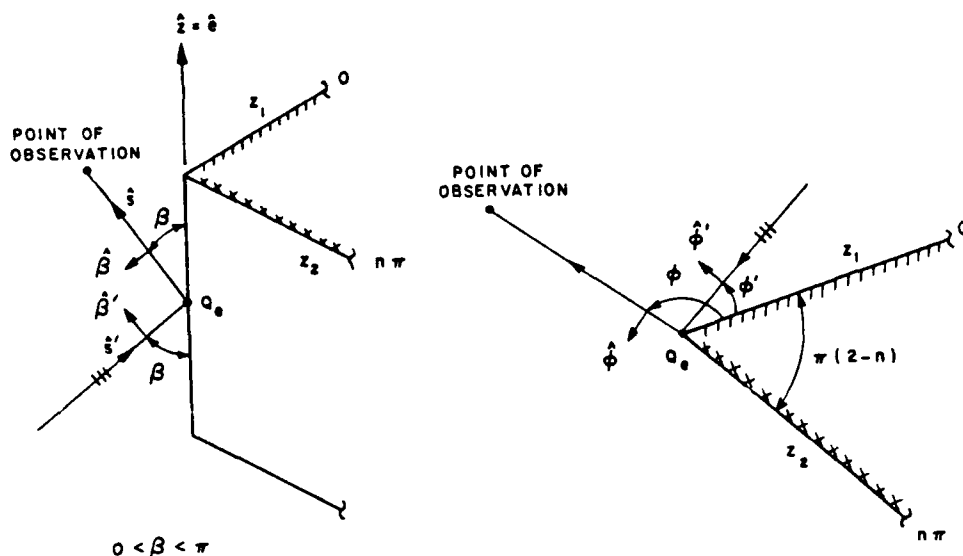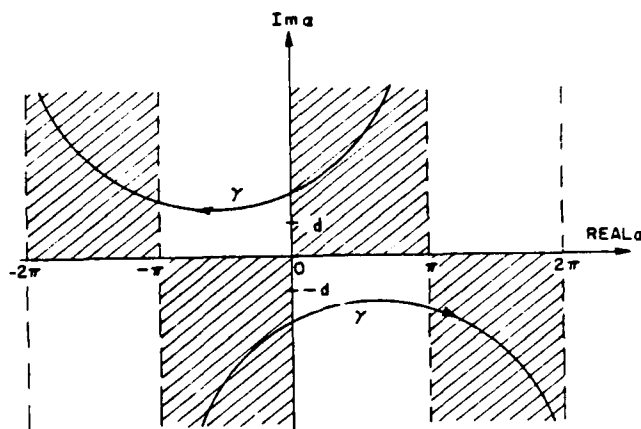
$$0 < \beta < \pi$$

Fig. 1.   Impedance wedge with obliquely incident plane wave.

Fig. 2.   Sommerfeld contour γ. Shaded area: real $(-iK\rho \cos \alpha) < 0$.

difference equation [2], namely,

$$\left(\overline{I} \sin \alpha \pm \sin \overline{\nu}_1 \right) \overline{C}(\alpha) \vec{F}_z \left(\alpha \pm \frac{n\pi}{2} \right)$$

$$= \left(-\overline{I} \sin \alpha \pm \sin \overline{\nu}_1 \right) \overline{C}(-\alpha) \vec{F}_z \left(-\alpha \pm \frac{n\pi}{2} \right) \quad (6)$$

where

$$\overline{C}(\alpha) = \overline{I} \cos \alpha + \overline{J} \sin \alpha \cos \beta$$

$$\overline{I} = \begin{bmatrix} 1 & 0 \\ 0 & 1 \end{bmatrix} \qquad \overline{J} = \begin{bmatrix} 0 & -1 \\ 1 & 0 \end{bmatrix}. \quad (7)$$

The diagonal matrix $\sin \overline{\nu}_{1,2}$, sometimes referred to as the modified Brewster matrix, is given by

$$\sin \overline{\nu}_{1,2} = \begin{bmatrix} \sin \nu^e_{1,2} & 0 \\ 0 & \sin \nu^h_{1,2} \end{bmatrix}$$

$$= \begin{bmatrix} \dfrac{Y_{1,2}}{Y_0 \sin \beta} & 0 \\ 0 & \dfrac{Z_{1,2}}{\eta_0 \sin \beta} \end{bmatrix} \qquad 0 \leqslant \mathrm{Re}\,(\nu) \leqslant \pi/2$$

$$\quad (8)$$

where $Y_0 = 1/\eta_0$ is the free-space admittance and $\nu = \nu_r +$

$i\nu_I$. The real part of ν is restricted to the interval $[0, \pi/2]$ because it is assumed that Re $(Z_{1,2}) \geqslant 0$. Equation (6) is called the generalized reflection equation which is very difficult to solve because of the nondiagonal matrix $\overline{C}(\alpha)$. In fact, (6) can be reduced to two scalar second-order functional difference equations for the fields E_z and H_z, respectively. Note that for the case of normal incidence, i.e., $\beta = \pi/2$, $\overline{C}(\alpha)$ becomes diagonal and (6) reduces to two first-order functional difference equations which are easier to solve. This special case was treated by Maliuzhinets [2] and a uniform expression has been obtained in [16]; however, the presence of the surface wave poles near the saddle points was not taken into account in [16].

In general, if one finds a solution $\vec{F}_z$ for (6), another solution is given by $\vec{F}_z(\alpha)\vec{\sigma}(\alpha)$, where $\vec{\sigma}(\alpha)$ satisfies the difference equation

$$\vec{\sigma}\left(\alpha \pm \frac{n\pi}{2} \right) = \vec{\sigma}\left(-\alpha \pm \frac{n\pi}{2} \right). \quad (9)$$

Thus the most general solution of (6) can be written as follows

$$\vec{F}_z(\alpha) = \vec{F}_z(\alpha)\vec{\sigma}(\alpha) = [\vec{F}_1 \ \vec{F}_2]\vec{\sigma}(\alpha) \quad (10)$$

where $\vec{F}_1$ and $\vec{F}_2$ are solutions of (6). It can be shown that a solution for (6), i.e., $\vec{F}_z(\alpha)$, can be found in terms of the Maliuzhinets functions, introduced in [2], for the following
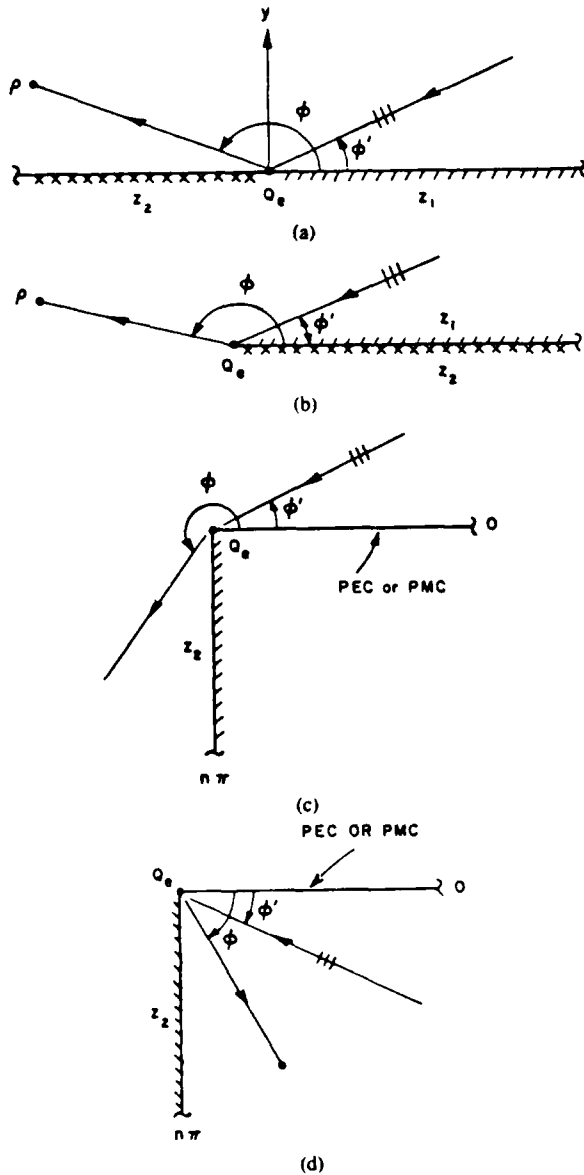
Fig. 3. Geometries for which generalized reflection equation has been solved (a) $n = 1$. (b) $n = 2$. (c) $n = 3/2$. (d) $n = 1/2$.

four cases (see Fig. 3) when $\beta \neq \pi/2$:

a) two-part impedance plane, $n = 1$
b) half-plane, $n = 2$
c) $\pi/2$-wedge where $Z_1 = 0$ or $Z_1 = \infty$, $n = 3/2$
d) $3\pi/2$-wedge, where $Z_1 = 0$ or $Z_1 = \infty$, $n = 1/2$.

Thus, the solution of (6) for the cases described above can be written as follows:

$$\bar{F}_z(\alpha) = \bar{S}^{-1}(\alpha)\bar{\Psi}(\alpha)$$

$$\bar{S}(\alpha) = \begin{cases} \bar{C}\left(\alpha - \dfrac{\pi}{2}\right), & \text{for } n = 1 \\[2ex] \bar{C}(\alpha), & \text{for } n = 2 \\[2ex] \bar{C}\left(\alpha + \dfrac{n\pi}{2}\right), & \text{for } n = 3/2, 1/2 \\[2ex] \text{and } Z_1 = 0 \text{ or } Z_1 = \infty \end{cases} \qquad (11)$$

where

$$\bar{\Psi}(\alpha) = \begin{bmatrix} \Psi_e(\alpha) & 0 \\ 0 & \Psi_h(\alpha) \end{bmatrix}. \qquad (12)$$

It also can be shown that $\Psi_{e,h}(\alpha)$ can be expressed in terms of another function, namely,

$$\Psi_{e,h}(\alpha) = \psi_n\left(\alpha + \frac{n\pi}{2} + \nu_1^{e,h} - \frac{\pi}{2}\right) \psi_n\left(\alpha + \frac{n\pi}{2} + \frac{\pi}{2} - \nu_1^{e,h}\right)$$

$$\cdot \psi_n\left(\alpha - \frac{n\pi}{2} + \nu_2^{e,h} - \frac{\pi}{2}\right) \psi_n\left(\alpha - \frac{n\pi}{2} + \frac{\pi}{2} - \nu_2^{e,h}\right)$$

$$(13)$$

where $\psi_n(\alpha)$ is the well-known Maliuzhinets function. The function $\psi_n(\alpha)$ and its properties are discussed in [2]. For our purposes, it is enough to mention that

$$\lim_{|\text{Im }(\alpha)| \to \infty} \psi_n(\alpha) = 0 \left[\exp\left(\frac{|\text{Im }\alpha|}{4n}\right) \right]$$

$$\psi_n(\alpha - \pi) = \psi_n(\alpha + \pi) \frac{\cos\left(\dfrac{\alpha - \pi/2}{2n}\right)}{\cos\left(\dfrac{\alpha + \pi/2}{2n}\right)}. \qquad (14)$$

The next step in the analysis is to find a solution for (9). It is easy to verify that one solution of (9) is the function $\bar{a} \sin (\alpha/n)$ where $\bar{a}$ is an arbitrary constant. Furthermore, one can also show that $\bar{a} \sin^l (\alpha/n)$, where l is an integer, is still a solution of (9). Thus keeping in mind that $\bar{\sigma}(\alpha)$ must have a first-order pole at $\alpha = n\pi/2 - \phi'$, the most general solution of (9) can be expressed as a Laurent series around the point $\sin (n\pi/(2n) - \phi'/n) = \cos (\phi'/n)$. By enforcing (5), which was derived from the edge conditions, it turns out that for the cases being considered here ($n = 1/2, 1, 2, 3/2$), the series for $\bar{\sigma}(\alpha)$ must stop at the second term, i.e.,

$$\bar{\sigma}(\alpha) = \frac{\bar{a}_{-1}}{\sin\left(\dfrac{\alpha}{n}\right) - \cos\left(\dfrac{\phi'}{n}\right)} + \bar{a}_0 + \bar{a}_1 \sin\left(\frac{\alpha}{n}\right). \qquad (15)$$

Since $\bar{a}_{-1}$, $\bar{a}_0$, and $\bar{a}_1$ are unknown constants in (15), the solution for $\bar{F}_z$ is not unique. To obtain a unique solution, the unknown coefficients in (15) must be determined. The first coefficient $\bar{a}_{-1}$ can be easily evaluated by noting that the residue of $\bar{F}_z$ at the pole $\alpha = n\pi/2 - \phi'$ must be equal to the incident field. Thus $\bar{a}_{-1}$ is given by

$$\bar{a}_{-1} = \frac{\sin (\phi'/n)}{n} \bar{\Psi}^{-1}\left(\frac{n\pi}{2} - \phi'\right) \bar{S}\left(\frac{n\pi}{2} - \phi'\right) \bar{F}_{0z},$$

$$0 < \phi' < n\pi. \qquad (16)$$

The other two coefficients are determined by first observing that the matrix $\bar{S}^{-1}(\alpha)$ introduces complex poles whose residues are fields which have no physical interpretation. Thus the unknown coefficients $\bar{a}_0$ and $\bar{a}_1$ are adjusted in such a way that the complex poles of $\bar{S}^{-1}(\alpha)$ are removed. This is done by solving for $\bar{a}_0$ and $\bar{a}_1$ in a system of linear simultaneous equations (see (38a) in the Appendix). When $Z_{1,2} = 0$ or $Z_{1,2} = \infty$, some of these equations become linearly dependent and thus are not sufficient to solve for $\bar{a}_0$ and $\bar{a}_1$. However, the

edge conditions will dictate that some of the constant must be equal to zero. Thus once the constants have been evaluated, the solution for the function $\bar{F}_z$ can be written as follows:

$$\bar{F}_z(\alpha + n\pi/2 - \phi) = \bar{A}_z(\alpha + n\pi/2 - \phi)\bar{F}_{0z}, \qquad 0 \leqslant \phi \leqslant n\pi$$

(17a)

where

$$\bar{A}_z(\alpha + n\pi/2 - \phi) = \bar{S}^{-1}(\alpha + n\pi/2 - \phi)$$

$$\cdot \bar{\Psi}(\alpha + n\pi/2 - \phi) \sin\left(\frac{\phi'}{n}\right)\bigg/n$$

$$\cdot \left\{ \frac{\bar{I}}{\cos\left(\dfrac{\alpha - \phi}{n}\right) - \cos\left(\dfrac{\phi'}{n}\right)} \right.$$

$$\left. + \bar{B}_n + \bar{D}_n \cos\left(\frac{\alpha - \phi}{n}\right) \right\}$$

$$\cdot \bar{\Psi}^{-1}(n\pi/2 - \phi')\bar{S}(n\pi/2 - \phi')$$

(17b)

and the constant (two-by-two) matrices $\bar{B}_n$ and $\bar{D}_n$ are given in the Appendix. Thus a formal solution for $\bar{F}_z$ has been found for four wedge angles in terms of an integral along the Sommerfeld contour. For the cases being considered here, $\psi_n(\alpha)$ is given by

$$\psi_1(\alpha) = \exp\left\{\frac{1}{4\pi}\int_0^\alpha \frac{2u - \pi \sin u}{\cos u}\,du\right\}$$

(18a)

$$\psi_2(\alpha) = \exp\left\{\frac{-1}{8\pi}\int_0^\alpha \frac{\pi \sin u - 2\sqrt{2}\pi \sin (u/2) + 2u}{\cos u}\,du\right\}$$

(18b)

$$\psi_{3/2}(\alpha) = \frac{\cos\left(\dfrac{\alpha - \pi}{6}\right)\cos\left(\dfrac{\alpha + \pi}{6}\right)}{\cos^2\left(\dfrac{\pi}{6}\right)\cos\left(\dfrac{\alpha}{6}\right)}$$

$$\psi_{1/2}(\alpha) = \cos (\alpha/2). \quad (18c)$$

When $\beta = \pi/2$ (normal incidence), (17b) becomes

$$\bar{A}_z(\alpha + n\pi/2 - \phi) = \bar{\Psi}(\alpha + n\pi/2 - \phi)\bar{\Psi}^{-1}(n\pi/2 - \phi')$$

$$\cdot \frac{\sin (\phi'/n)/n}{\cos\left(\dfrac{\alpha - \phi}{n}\right) - \cos\left(\dfrac{\phi'}{n}\right)}. \quad (19)$$

Unlike (17), the expression in (19) is valid for any wedge angle.

An important identity that will be very useful when the diffracted field is developed is the following:

$$\bar{\Psi}(\alpha - \pi) = \bar{\Psi}(\alpha + \pi)\bar{M}(\alpha). \quad (20a)$$

Equation (20a) is obtained by a repeated use of the identity given in (14). The diagonal matrix $\bar{M}(\alpha)$ is given by

$$\bar{M}(\alpha) = \begin{bmatrix} M^e(\alpha) & 0 \\ 0 & M^h(\alpha) \end{bmatrix}$$

$$M^{e,h}(\alpha) = m(\alpha, \nu_1^{e,h})/m(-\alpha, \nu_2^{e,h}) \quad (20b)$$

where

$$m(\alpha, \nu) = \frac{\cos\left(\dfrac{\alpha + n\pi/2 - \nu}{2n}\right)\cos\left(\dfrac{\alpha - \pi + n\pi/2 + \nu}{2n}\right)}{\cos\left(\dfrac{\alpha + \pi + n\pi/2 - \nu}{2n}\right)\cos\left(\dfrac{\alpha + n\pi/2 + \nu}{2n}\right)}.$$

(20c)

For the $\pi/2$- and $3\pi/2$-wedges ($n = 3/2, 1/2$), where Z_1 is equal to 0 or ∞, the functions $\Psi_{e,h}(\alpha)$ and $M^{e,h}(\alpha)$ have to be carefully examined. Table I summarizes these special cases.

Note that spectral function $\bar{F}_z(\alpha + n\pi/2 - \phi)$ is equal to zero when $\phi' = 0$, $n\pi$ (grazing incidence) as long as $\bar{\Psi}(n\pi/2 - \phi')$ does not have any zeros at $\phi' = 0$, $n\pi$. However, for the right-angled wedge problem where $Z_1 = 0$ or $Z_1 = \infty$, the function $\bar{\Psi}(n\pi/2 - \phi')$ does have a zero at $\phi' = 0$. Thus for $n = 1/2, 3/2$, and with the help of Table I, $\bar{\Psi}^{-1}(n\pi/2 - \phi')$ $\sin (\phi'/n)/n$ can be evaluated at $\phi' = 0$ by taking the limit as ϕ' goes to zero, namely,

$$\lim_{\phi' \to 0} \bar{\Psi}^{-1}\left(\frac{n\pi}{2} - \phi'\right) \sin\left(\frac{\phi'}{n}\right)\bigg/n = \frac{2}{n}\begin{bmatrix} g_e & 0 \\ 0 & g_h \end{bmatrix} \quad (21a)$$

where

$$g_e = 1\bigg/\left(\psi_n\left(\nu_2^e - \frac{\pi}{2}\right)\psi_n\left(-\nu_2^e + \frac{\pi}{2}\right)\right)$$

$$g_h = 0 \text{ for } Z_1 = 0, \ n = \frac{3}{2}, \frac{1}{2} \quad (21b)$$

and

$$g_e = 0 \qquad g_h = 1\bigg/\left(\psi_n\left(\nu_2^h - \frac{\pi}{2}\right)\psi_n\left(-\nu_2^h + \frac{\pi}{2}\right)\right)$$

$$\text{for } Z_1 = \infty, \ n = \frac{3}{2}, \frac{1}{2}. \quad (21c)$$

Note that when $\phi' = 0$ the pole $\alpha = \phi$ (see (17b)), which appears to be a double pole, is still a simple pole. Furthermore, it also follows from (17b)–(21) that for $\phi' = 0$ and $Z_1 = 0$, only a TE$_z$-polarized incident plane wave ($E_{0z} = 0$, $H_{0z} \neq 0$) will excite a nonzero scattered field. This agrees with the boundary conditions satisfied by the fields on face 0 of the wedge. On the other hand, if $Z_1 = \infty$, the incident plane wave has to be TM$_z$-polarized, i.e., $E_{0z} \neq 0$, $H_{0z} = 0$ (which also agrees with the boundary conditions), to have a nonzero spectral function $\bar{F}_z$ when $\phi' = 0$. It is important to keep in mind that since (21) was derived by taking the limit of ϕ' going to zero, the constant $\bar{F}_{0z}$ in (17a) must be divided by 2 for the case of grazing incidence.

TABLE I
$n = 3/2, 1/2$

$Z_1 = 0, Z_2 \neq 0$, finite	$\Psi_e(\alpha) = \cos\left(\dfrac{\alpha}{2n} + \dfrac{\pi}{4}\right) \psi_n\left(\alpha - \dfrac{n\pi}{2} + \nu_2^e - \dfrac{\pi}{2}\right) \psi_n\left(\alpha - \dfrac{n\pi}{2} - \nu_2^e + \dfrac{\pi}{2}\right)$
	$\Psi_h(\alpha) = \psi_n\left(\alpha - \dfrac{n\pi}{2} + \nu_2^h - \dfrac{\pi}{2}\right) \psi_n\left(\alpha - \dfrac{n\pi}{2} + \dfrac{\pi}{2} - \nu_2^h\right)$
	$M^h(u) = 1/m(-u, \nu_2^h)$
	$M^e(u) = \cos\left(\dfrac{u - \pi + n\pi/2}{2n}\right) / m(-u, \nu_2^e) / \cos\left(\dfrac{u + \pi + n\pi/2}{2n}\right)$
$Z_1 = \infty, Z_2 \neq 0$, finite	$\Psi_e(\alpha) = \psi_n\left(\alpha - \dfrac{n\pi}{2} + \nu_2^e - \dfrac{\pi}{2}\right) \psi_n\left(\alpha - \dfrac{n\pi}{2} + \dfrac{\pi}{2} - \nu_2^e\right)$
	$\Psi_h(\alpha) = \cos\left(\dfrac{\alpha}{2n} + \dfrac{\pi}{4}\right) \psi_n\left(\alpha - \dfrac{n\pi}{2} + \nu_2^h - \dfrac{\pi}{2}\right) \psi_n\left(\alpha - \dfrac{n\pi}{2} - \nu_2^h + \dfrac{\pi}{2}\right)$
	$M^h(u) = \cos\left(\dfrac{u - \pi + n\pi/2}{2n}\right) / m(-u, \nu_2^h) / \cos\left(\dfrac{u + \pi + n\pi/2}{2n}\right)$
	$M^e(u) = 1/m(-u, \nu_2^e)$

As mentioned before, Senior [26] obtained an expression for the spectral function $\bar{F}_z(\alpha)$ for $n = 1/2$, i.e., $s_1(\alpha)$ and $s_2(\alpha)$ in (57) and (58), respectively, of [26]. However, $s_1(\alpha)$ does not reduce to the known result when $\beta = \pi/2$. The reason for the error is that the constant c_2, given in [26], is incorrectly calculated since it should be equal to zero as dictated by the edge conditions. In other words, with c_2 as computed in [26], the spectral functions $s_1(\alpha)$ and $s_2(\alpha)$ do not satisfy (5) (in this paper), which all valid functions must satisfy. Although the constant c_2 is incorrect, the field E_z obtained in (59) of [26] for the $3\pi/2$-wedge is correct because it turns out that c_1 and c_2 do not contribute to the fields E_z and H_z when $n = 1/2$. This important point will be explained in more detail in Section IV.

IV. ASYMPTOTIC ANALYSIS

In general, the integral in (4) cannot be evaluated in closed form due to the complicated nature of the integrand. However, as is the case in most diffraction problems, one can apply asymptotic integration techniques to obtain useful solutions. Here the method of steepest descents will be used to obtain the leading term of $\bar{f}_z$ for large $K\rho$.

The exponential function in (4) has two isolated simple saddle points at $\alpha = \pi$ and $\alpha = -\pi$. Furthermore, $\bar{F}_z(\alpha + n\pi/2 - \phi)$ is an analytic function, except for some real and complex simple poles. The real poles are located at

$$\alpha_N^{\pm} = \phi \pm \phi' + 2n\pi N, \qquad N = 0, \pm 1, \pm 2, \cdots. \quad (22)$$

For $n = 1/2$, all the pole singularities of $\bar{F}_z(\alpha + n\pi/2 - \phi)$ are given in (22), i.e., $\bar{F}_z(\alpha + \pi/4 - \phi)$ does not have complex poles. Moreover, as shown later, the integral in (4) can be evaluated in closed form when $n = 1/2$. Thus the asymptotic evaluation of (4) for $n = 1, 3/2$, and 2 will be

discussed first. At the end of this section, a closed-form expression of (4) will be obtained for $n = 1/2$.

In addition to the real poles in (22), $\bar{F}_z(\alpha + n\pi/2 - \phi)$ also has complex poles when $n = 1, 3/2, 2$. Actually, these complex poles are the poles of the function $\bar{\Psi}(\alpha + n\pi/2 - \phi)$ and the ones closest to the saddle points $\alpha = \pm\pi$ are

$$\alpha_{1sw}^{e,h} = \phi + \pi + \nu_1^{e,h} \qquad \alpha_{2sw}^{e,h} = -\nu_2^{e,h} - \pi + \phi - n\pi. \quad (23)$$

The pole α_{1sw} is closest to the saddle point $\alpha = \pi$ and, if captured, its residue contribution can be interpreted as a surface wave traveling away from the edge on face 0. Likewise, α_{2sw} is the pole closest to the saddle point $\alpha = -\pi$ and, if captured, its residue contribution is a surface wave traveling away from the edge on face n of the wedge. The poles listed in (22) and (23) are depicted in Fig. 4. It is noted that since $\sin \nu_{1,2}^e \cdot \sin \nu_{1,2}^h = 1/\sin^2 \beta$, only two surface wave poles can be captured for given values of Z_1 and Z_2.

The first step in the asymptotic evaluation of (4) is to introduce two steepest descent paths $\text{SDP}(\pm\pi)$ passing through the saddle points $\alpha = \pm\pi$ as shown in Fig. 4. After deforming the original integration contour into $\text{SDP}(\pi)$ and $\text{SDP}(-\pi)$, $\bar{f}_z$ becomes

$$\bar{f}_z(\rho, \phi, z) = \bar{f}_z^i(\rho, \phi, z) + \bar{f}_{z1}^r(\rho, \phi, z)$$
$$+ \bar{f}_{z2}^r(\rho, \phi, z) + \bar{f}_{z1}^{sw}(\rho, \phi, z) + \bar{f}_{z2}^{sw}(\rho, \phi, z)$$
$$+ \bar{f}_z^d(\rho, \phi, z), \qquad n = 1, 3/2, 2. \quad (24)$$

The functions $\bar{f}_z^i, \bar{f}_{z1}^r, \bar{f}_{z2}^r, \bar{f}_{z1}^{sw}$, and $\bar{f}_{z2}^{sw}$ are the residues of $\bar{F}_z$ evaluated at the poles that are captured when the integration contour is deformed. Thus $\bar{f}_z^i$ is the incident field, $\bar{f}_{z1}^r$ and $\bar{f}_{z2}^r$ are the fields reflected from the 0 and n faces of the wedge,
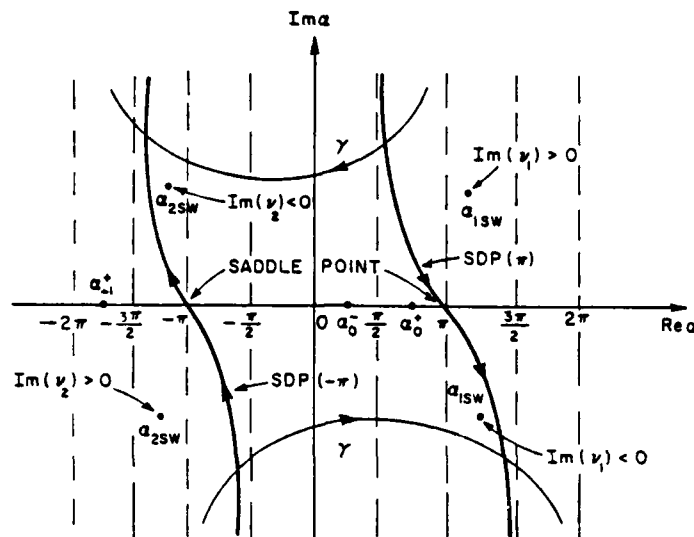
Fig. 4. Steepest descent paths and pole singularities of function $\bar{F}_z(\alpha + n\pi/2 - \phi)$.

respectively. Likewise, $\bar{J}_{z1}^{sw}$ and $\bar{J}_{z2}^{sw}$ are the surface wave fields traveling away form the edge on the 0 and n faces of the wedge, respectively. These fields are given by ($n = 1, 3/2, 2$)

$$\bar{J}_z^i = \bar{r}_1 \bar{F}_{0z} \exp(-iK\rho \cos \beta_0^-)$$

$$\cdot \exp(ikz \cos \beta)[U(\beta_0^- + \pi) - U(\beta_0^- - \pi)] \quad (25a)$$

$$\bar{J}_{z1}^r = \bar{r}_2 \bar{F}_{0z} \exp(-iK\rho \cos \beta_0^+)$$

$$\cdot \exp(ikz \cos \beta) U(\pi - \beta_0^+) \quad (25b)$$

$$\bar{J}_{z2}^r = \bar{r}_3 \bar{F}_{0z} \exp(-iK\rho \cos(\beta_0^+ - 2n\pi))$$

$$\cdot \exp(ikz \cos \beta) U(\beta_0^+ - 2n\pi + \pi) \quad (25c)$$

$$\bar{J}_{z1}^{sw} = \begin{cases} \bar{r}_4 \bar{F}_{0z} \exp(-iK\rho \cos \alpha_4) \exp(ikz \cos \beta) \\ \quad \cdot U(\phi_{s1}^e - \phi), \quad \text{if Im}(Z_1) > 0 \\ \bar{r}_5 \bar{F}_{0z} \exp(-iK\rho \cos \alpha_5) \exp(ikz \cos \beta) \\ \quad \cdot U(\phi_{s1}^h - \phi), \quad \text{if Im}(Z_1) < 0 \end{cases} \quad (25d)$$

$$\bar{J}_{z2}^{sw} = \begin{cases} \bar{r}_6 \bar{F}_{0z} \exp(-iK\rho \cos \alpha_6) \exp(ikz \cos \beta) \\ \quad \cdot U(\phi - \phi_{s2}^e), \quad \text{if Im}(Z_2) > 0 \\ \bar{r}_7 \bar{F}_{0z} \exp(-iK\rho \cos \alpha_7) \exp(ikz \cos \beta) \\ \quad \cdot U(\phi - \phi_{s2}^h), \quad \text{if Im}(Z_2) < 0 \end{cases} \quad (25e)$$

where U is the unit step function, $\beta_0^{\pm} = \phi \pm \phi'$, and it is not to be confused with β. The residues $\{\bar{r}_l\}$ are computed as follows:

$$\bar{r}_l = \lim_{\alpha \to \alpha_l} (\alpha - \alpha_l) \bar{A}_z \left(\alpha + \frac{n\pi}{2} - \phi\right), \quad l = 1, 2, \cdots, 7 \quad (26)$$

where the poles $\{\alpha_l\}_{l=1}^7$, and the angles $\phi_{s1}^{e,h}$ and $\phi_{s2}^{e,h}$ are

given, respectively, by

$$\alpha_1 = \phi - \phi' \qquad \alpha_2 = \phi + \phi'$$

$$\alpha_3 = \phi + \phi' - 2n\pi \qquad \alpha_{4,5} = \phi + \pi + \nu_1^{e,h}$$

$$\alpha_{6,7} = \phi - n\pi - \pi - \nu_2^{e,h} \quad (27a)$$

and

$$\phi_{s1}^{e,h} = -\nu_{r1}^{e,h} + \arccos(1/\cosh \nu_{l1}^{e,h})$$

$$\phi_{s2}^{e,h} = n\pi + \nu_{r2}^{e,h} - \arccos(1/\cosh \nu_{l2}^{e,h}). \quad (27b)$$

Evaluating (26) yields

$$\bar{r}_1 = \bar{I} \quad (28a)$$

$$\bar{r}_2 = \begin{cases} \bar{C}^{-1}(\pi + \phi')\bar{\Lambda}(\phi', \nu_1)\bar{C}(\pi - \phi'), \\ \quad n = 1, 2 \\ -\bar{C}^{-1}\left(\frac{3\pi}{2} + \phi'\right) \bar{\Lambda}_1 \bar{C}\left(\frac{3\pi}{2} - \phi'\right) = \bar{\Lambda}_1, \\ \quad n = 3/2, \end{cases} \quad (28b)$$

$$\bar{r}_3 = \begin{cases} \bar{C}^{-1}(\pi + \phi')\bar{\Lambda}(n\pi - \phi', \nu_2)\bar{C}(\pi - \phi'), \\ \quad n = 1, 2 \\ \bar{C}^{-1}\left(\phi' - \frac{3\pi}{2}\right) \bar{\Lambda}(n\pi - \phi', \nu_2)\bar{C}\left(\frac{3\pi}{2} - \phi'\right), \\ \quad n = 3/2, \end{cases} \quad (28c)$$

where

$$\bar{\Lambda}(\alpha, \nu) = \begin{bmatrix} R(\alpha, \nu^e) & 0 \\ 0 & R(\alpha, \nu^h) \end{bmatrix} \quad R(\alpha, \nu) = \frac{\sin \alpha - \sin \nu}{\sin \alpha + \sin \nu}$$

(28d)

and

$$\bar{\Lambda}_1 = \begin{cases} -\bar{L}, & \text{for } Z_1 = 0 \\ \bar{L}, & \text{for } Z_1 = \infty \end{cases} \quad \bar{L} = \begin{bmatrix} 1 & 0 \\ 0 & -1 \end{bmatrix}.$$

(28e)

Note that $\bar{r}_1$, $\bar{r}_2$, and $\bar{r}_3$ are the residues of $\bar{A}_z(\alpha + n\pi/2 - \phi)$ evaluated at the GO poles. The residues corresponding to the complex surface wave poles are given by ($n = 1, 2$)

$$\bar{r}_{4,5} = \bar{S}^{-1} \left(\pi + \nu_1^{e,h} + \frac{n\pi}{2} \right) 2 \sin \left(\frac{\pi}{2n} \right)$$

$$\cdot \sin \left(\frac{\phi'}{n} \right) \bar{P}_{1e,1h} \psi_n \left(n\pi - \frac{\pi}{2} \right)$$

$$\cdot \left\{ \frac{\bar{I}}{\cos \left(\frac{\pi + \nu_1^{e,h}}{n} \right) - \cos \left(\frac{\phi'}{n} \right)} \right.$$

$$\left. + \bar{B}_n + \bar{D}_n \cos \left(\frac{\pi + \nu_1^{e,h}}{n} \right) \right\}$$

$$\cdot \bar{\Psi}^{-1} \left(\frac{n\pi}{2} - \phi' \right) \bar{S} \left(\frac{n\pi}{2} - \phi' \right),$$

(29a)

and ($n = 1, 2, 3/2$)

$$\bar{r}_{6,7} = -\bar{S}^{-1} \left(-\frac{n\pi}{2} - \pi - \nu_2^{e,h} \right) 2 \sin \left(\frac{\pi}{2n} \right)$$

$$\cdot \sin \left(\frac{\phi'}{n} \right) \bar{P}_{2e,2h} \psi_n \left(n\pi - \frac{\pi}{2} \right)$$

$$\cdot \left\{ \frac{\bar{I}}{-\cos \left(\frac{\pi + \nu_2^{e,h}}{n} \right) - \cos \left(\frac{\phi'}{n} \right)} \right.$$

$$\left. + \bar{B}_n - \bar{D}_n \cos \left(\frac{\pi + \nu_2^{e,h}}{n} \right) \right\}$$

$$\cdot \bar{\Psi}^{-1} \left(\frac{n\pi}{2} - \phi' \right) \bar{S} \left(\frac{n\pi}{2} - \phi' \right)$$

(29b)

where the matrices $\bar{P}_1$ and $\bar{P}_2$, introduced in (29) can be

written as follows:

$$\bar{P}_{1e} = \begin{bmatrix} a_e & 0 \\ 0 & 0 \end{bmatrix} \quad \bar{P}_{1h} = \begin{bmatrix} 0 & 0 \\ 0 & a_h \end{bmatrix}$$

$$\bar{P}_{2e} = \begin{bmatrix} b_e & 0 \\ 0 & 0 \end{bmatrix} \quad \bar{P}_{2h} = \begin{bmatrix} 0 & 0 \\ 0 & b_h \end{bmatrix}. \quad (30a)$$

The constants $a_{e,h}$ and $b_{e,h}$ can be expressed in terms of the Maliuzhinets function ψ_n, namely,

$$a_{e,h} = \psi_n \left(n\pi + 2\nu_1^{e,h} + \frac{\pi}{2} \right) \psi_n \left(\nu_1^{e,h} + \nu_2^{e,h} + \frac{\pi}{2} \right)$$

$$\cdot \psi_n \left(\frac{3\pi}{2} + \nu_1^{e,h} - \nu_2^{e,h} \right), \quad n = 1, 2 \quad (30b)$$

$$b_{e,h} = \psi_n \left(\nu_1^{e,h} - \nu_2^{e,h} - \frac{3\pi}{2} \right) \psi_n \left(-\nu_2^{e,h} - \nu_1^{e,h} - \frac{\pi}{2} \right)$$

$$\cdot \psi_n \left(-n\pi - \frac{\pi}{2} - 2\nu_2^{e,h} \right), \quad n = 1, 2 \quad (30c)$$

$$b_e = \psi_n \left(-n\pi - \frac{\pi}{2} - 2\nu_2^e \right) \cos \left(\frac{\pi + \nu_2^e}{3} \right)$$

$$b_h = \psi_n \left(-n\pi - \frac{\pi}{2} - 2\nu_2^h \right), \quad \text{for } n = \frac{3}{2}, \ Z_1 = 0 \quad (30d)$$

$$b_e = \psi_n \left(-n\pi - \frac{\pi}{2} - 2\nu_2^e \right) \quad b_h = \psi_n \left(-n\pi - \frac{\pi}{2} - 2\nu_2^h \right)$$

$$\cdot \cos \left(\frac{\pi + \nu_2^h}{3} \right) \text{ for } n = \frac{3}{2}, \ Z_1 = \infty. \quad (30e)$$

It is obvious that for the $\pi/2$-wedge ($n = 3/2$), $\bar{r}_{4,5} = \bar{0}$. In other words, no surface wave can exist on the 0 face of the wedge when $Z_1 = 0$ or $Z_1 = \infty$.

The last term that needs to be defined in (24) is $\bar{f}_z^d$, which is referred to as the diffracted field, and it can be expressed as follows:

$$\bar{f}_z^d(\rho, \phi, z) = \frac{\exp (ikz \cos \beta)}{2\pi i} \int_{SDP(\pi)} \bar{A}_z \left(\alpha + \frac{n\pi}{2} - \phi \right)$$

$$\cdot \bar{F}_{0z} \exp (-iK\rho \cos \alpha) \, d\alpha$$

$$+ \frac{\exp (ikz \cos \beta)}{2\pi i}$$

$$\cdot \int_{SDP(-\pi)} \bar{A}_z \left(\alpha + \frac{n\pi}{2} - \phi \right)$$

$$\cdot \bar{F}_{0z} \exp (-iK\rho \cos \alpha) \, d\alpha \quad (31)$$

where SDP($\pm \pi$) are the steepest descent paths depicted in Fig. 4. The asymptotic evaluation of (31) is based on the work of Gennarelli and Palumbo [30]. Actually, the simplified expressions given in [31] are used here.

Without going over the details, the asymptotic evaluation of (31), taking into account the presence of all the poles of $\bar{F}_z$ near the saddle points $\alpha = \pm \pi$, and keeping only the leading

terms of order $(K\rho)^{-1/2}$, yields

$$\bar{f}_z^d(\rho, \phi, z) \sim \bar{D}_z(\phi, \phi', L, \nu_1, \nu_2)$$

$$\cdot \bar{f}_z^i(x=0, y=0, z) \frac{e^{iK\rho}}{\sqrt{\rho \sin \beta}} \sin \beta \quad (32a)$$

where

$$\bar{D}_z(\phi, \phi', L, \nu_1, \nu_2) = \frac{e^{i\pi/4} \sin (\phi'/n)}{n\sqrt{2\pi k} \sin \beta} \bar{S}^{-1}(n\pi/2 - \phi)\bar{\Psi}(\pi + n\pi/2 - \phi)$$

$$\cdot \left\{ \left[\frac{\bar{I}}{\cos\left(\frac{\pi-\phi}{n}\right) - \cos\left(\frac{\phi'}{n}\right)} + \bar{B}_n + \bar{D}_n \cos\left(\frac{\pi-\phi}{n}\right) \right] \right.$$

$$\left. - \bar{M}\left(\frac{n\pi}{2} - \phi\right)\left[\frac{\bar{I}}{\cos\left(\frac{\pi+\phi}{n}\right) - \cos\left(\frac{\phi'}{n}\right)} + \bar{B}_n + \bar{D}_n \cos\left(\frac{\pi+\phi}{n}\right)\right] \right\}$$

$$\cdot \bar{\Psi}^{-1}(n\pi/2 - \phi')\bar{S}(n\pi/2 - \phi') - \frac{i}{\sqrt{4\pi k} \sin \beta} \sum_{l=1}^{7} \frac{\bar{F}_l(1 - \mathcal{F}(ikLs_l^2))}{s_l} \quad (32b)$$

and $L = \rho \sin \beta$. The matrix $\bar{M}(\alpha)$ was defined in (20b), and the constants $\bar{B}_n$ and $\bar{D}_n$ are given in the Appendix. The function s_l is given by

$$s_l = -\exp (i\pi/4)\sqrt{2} \cos\left(\frac{\tilde{\alpha}_l}{2}\right), \qquad l = 1, 2, \cdots, 7. \quad (33a)$$

where

$$\tilde{\alpha}_l = \begin{cases} \alpha_l, & \text{if } |\text{Re } (\alpha_l)| \leqslant 2\pi \\ 2\pi + i\text{Im } (\alpha_l), & \text{if Re } (\alpha_l) > 2\pi \\ -2\pi + i\text{Im } (\alpha_l), & \text{if Re } (\alpha_l) < -2\pi \end{cases} \quad (33b)$$

and the poles $\{\alpha_l\}$ were defined in (27a).

For practical applications, it is convenient to express the diffracted field in the ray-fixed coordinate system [32]. Thus the unit vectors $\hat{\phi}'$, $\hat{\phi}$, $\hat{\beta}'$, $\hat{\beta}$, and $\hat{e}$ depicted in Fig. 1 and the column vectors $\bar{f}_e^d$ and $\bar{f}_e^i$ are defined as follows:

$$\hat{e} = \hat{z}; \quad \hat{\phi}' = \frac{\hat{s}' \times \hat{e}}{|\hat{e} \times \hat{s}'|} \qquad \hat{\phi} = -\frac{\hat{s} \times \hat{e}}{|\hat{e} \times \hat{s}|}$$

$$\hat{\beta}' = \hat{\phi}' \times \hat{s}' \qquad \hat{\beta} = \hat{\phi} \times \hat{s} \qquad \bar{f}_e^d = \begin{bmatrix} E_\beta^d \\ E_\phi^d \end{bmatrix}$$

$$\bar{f}_e^i = \begin{bmatrix} E_{\beta'}^i \\ E_{\phi'}^i \end{bmatrix}. \quad (34)$$

The diffracted field $\bar{f}_e^d$ can then be easily obtained from (32), namely,

$$\bar{f}_e^d(s, \phi, \beta) \sim \bar{D}_e(\phi, \phi', \beta, L, \nu_1, \nu_2)\bar{f}_e^i(QE) \frac{e^{iks}}{\sqrt{s}} \quad (35a)$$

where QE is the point of diffraction, s is the distance from QE

to the observation point, and $L = s \sin^2 \beta$. The diffraction coefficient $\bar{D}_e$ is given by

$$\bar{D}_e(\phi, \phi', \beta, L, \nu_1, \nu_2) = -\bar{L}\bar{D}_z(\phi, \phi', \beta, L, \nu_1, \nu_2)\bar{L} \quad (35b)$$

where $\bar{L}$ was defined in (28e).

The diffracted field given in (32) and (35) is valid as long as all the poles $\{\alpha_l\}$ are simple. However, when there is the possibility of double or higher order poles; i.e., when $\phi' = 0$, $n\pi$, $\phi = 0$, $n\pi$ and/or $Z_{1,2} = 0$, ∞, the integral in (4) can be evaluated in a manner suggested in [30]. Note that for the case of grazing incidence, the spectral function $\bar{F}_z$ in (17) is equal to zero, except when Z_1 or Z_2 is zero or infinity. It can be shown for $n = 1$ and 2, as was done in (21) for $n = 1/2$ and 3/2, that $\bar{F}_z$ still has simple poles when $Z_1 = 0$, ∞ and $\phi' = 0$ or when $Z_2 = 0$, ∞ and $\phi' = n\pi$.

The function $\mathcal{F}(x)$ introduced in (32b) is the well-known [19], [32] transition function

$$\mathcal{F}(x) = 2i\sqrt{x}e^{ix} \int_{\sqrt{x}}^{\infty} e^{-it^2} dt \qquad -\frac{3\pi}{2} < \arg (x) < \frac{\pi}{2} \quad (36)$$

where x is allowed to be complex due to the presence of complex surface wave poles. However, because of the square-root function $x^{1/2}$, it is necessary to introduce a branch cut on the x plane so that $\mathcal{F}(x)$ will be a single-valued function. Furthermore, to assure the convergence of $\mathcal{F}(x)$ as $|x| \to \infty$, the branch cut that is chosen runs from the branch point $x = 0$ to infinity along the positive imaginary axis on the complex x plane. Thus the argument of x is restricted to the interval $-3\pi/2 < \arg (x) < \pi/2$.

The evaluation of (4) for $n = 1/2$ proceeds in the same fashion followed for $n = 1$, 3/2, and 2. That is, the original integral in (4) can be expressed as the sum of the residues corresponding to the poles enclosed by the integration paths depicted in Fig. 4 plus the two integrals given in (31). In addition to the poles $\alpha = \phi - \phi'$, $\alpha = \phi + \phi'$, $\alpha = \phi + \phi' - \pi$, one of the poles $\alpha = \phi - \phi' \pm \pi$ will also be captured, depending on the angles of incidence and observation. Furthermore, it is easy to show that the periodic spectral

function $\bar{F}_z(\alpha)$ has a period of 2π for $n = 1/2$, which means that the two integrals in (31) cancel each other. Thus the field $\bar{f}_z$ can be expressed as the sum of four residues, namely,

$$\bar{f}_z = \left\{ \begin{array}{l} \bar{T} \exp\left(-iK\rho \cos \beta_0^-\right) + \bar{\Lambda}_1 \exp\left(-iK\rho \cos \beta_0^+\right) \\ + \bar{T} \left(\exp\left(iK\rho \cos \beta_0^+\right) \pm \bar{L} \exp\left(iK\rho \cos \beta_0^-\right)\right) \end{array} \right\}$$

$$\cdot \bar{F}_{oz} \exp\left(ikz \cos \beta\right) \quad (37a)$$

where

$$\bar{T} = \bar{C}^{-1}(\phi' - \pi/2)\bar{\Lambda}(\pi/2 - \phi', \nu_2)\bar{C}(\pi/2 - \phi') \quad (37b)$$

and $\bar{L}$, $\bar{\Lambda}_1$, and $\bar{\Lambda}$ were already defined. The minus and plus signs in (37a) correspond to the case when $Z_1 = 0$ and $Z_1 = \infty$, respectively. Since the field $\bar{f}_z$ in (37a) is made up of residues corresponding to the GO poles, the constant matrix $\bar{B}_n$ in (17b) does not contribute to $\bar{f}_z$ ($\bar{D}_n$ is zero for $n = 1/2$). This is why the field E_z in [26] is correct even though the constant c_2 (in [26]) is incorrectly evaluated.

V. NUMERICAL RESULTS

To obtain numerical results, an efficient algorithm was developed to compute the Maliuzhinets functions. A 16-point Gaussian integration algorithm was used to compute the Maliuzhinets functions for the half-plane and the two-part, impedance plane.

In Fig. 5, the field scattered by the two-part planar surface is depicted. The scattered field was computed for various values of Z_2 while Z_1 was kept constant. As expected, when $Z_1 = Z_2$, the diffracted field is zero and the scattered field is equal to the reflected field. When Z_2 is twice the value of Z_1, the diffracted field starts to contribute to the scattered field. Thus, due to the interaction of the reflected and diffracted fields, the magnitude of the scattered field starts to fluctuate. The fluctuations become larger when Z_2 is equal to the complex conjugate of Z_1, which means that the diffracted field is larger. Besides the diffracted field, surface waves are also excited along the z axis where the impedance discontinuity occurs. One surface wave travels on the Z_1-impedance half-plane, while the other travels on the Z_2-impedance half plane. The effect of the surface waves is stronger near the surface of the two-part impedance plane. Thus in Fig. 5 the surface wave effects can be observed from 0 to about $10°$ and from 170 to $180°$. It is important to mention that in addition to the copolarized scattered field, i.e., reflected, diffracted and surface wave fields, there is also a cross-polarized component when the incident field is obliquely incident.

The second geometry considered here is the half-plane with different impedances on both sides. An important result for practical applications is the study of the fields excited by the edge of the half-plane, i.e., the diffracted and surface wave fields. In Fig. 6, the edge excited fields (diffracted and surface wave) are plotted for two different values of Z_1, while Z_2 is kept constant. For reference, the diffracted field for a perfectly conducting half-plane ($Z_1 = Z_2 = 0$) is also depicted. Note that for the perfectly conducting half-plane, the diffracted field (of order $(K\rho)^{-1/2}$) has the same polarization as the incident field. However, for the impedance half-plane, the diffracted (of order $(K\rho)^{-1/2}$) and surface wave fields have a cross-
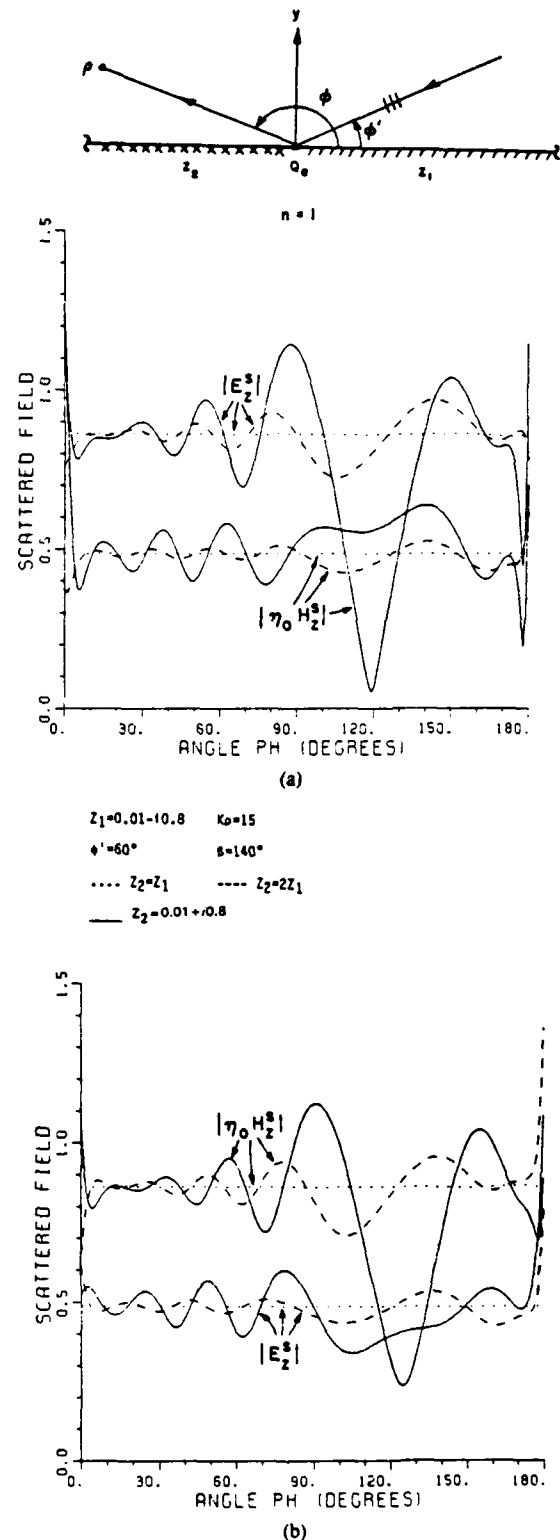
Fig. 5. Field scattered by two-part impedance plane for obliquely incident plane wave. (a) TM$_z$ polarization: $E_{0z} = 1$, $H_{0z} = 0$. (b) TE$_z$ polarization: $E_{0z} = 0$, $\eta_0 H_{0z} = 1$.

polarized component in addition to the copolarized fields when $\beta \neq \pi/2$. Note that when the direction of propagation of the incident field is normal to the wedge axis, the cross-polarized fields vanish. Another important difference between the PEC and impedance half-planes is the presence of the surface wave

(a)

$Z_2 = 0.01 + i0.5$ $K\rho = 10$

$\phi' = 60°$ $\theta = 135°$

——— $Z_1 = 0.01 - i0.8$

- - - - $Z_1 = 0.01 - i0.15$

· · · · $Z_2 = Z_1 = 0$

(b)

Fig. 6. Edge excited fields (diffracted plus surface wave fields) for impedance half-plane. (a) TM$_z$ polarization: $E_{0z} = 1$, $H_{0z} = 0$. (b) TE$_z$ polarization: $E_{0z} = 0$, $\eta_0 H_{0z} = 1$.

(a)

$Z_1 = 0.01 + i0.8$ $K\rho = 10$

$\phi' = 120°$ $\theta = 135°$

——— $Z_2 = 0.05 + i2.5$

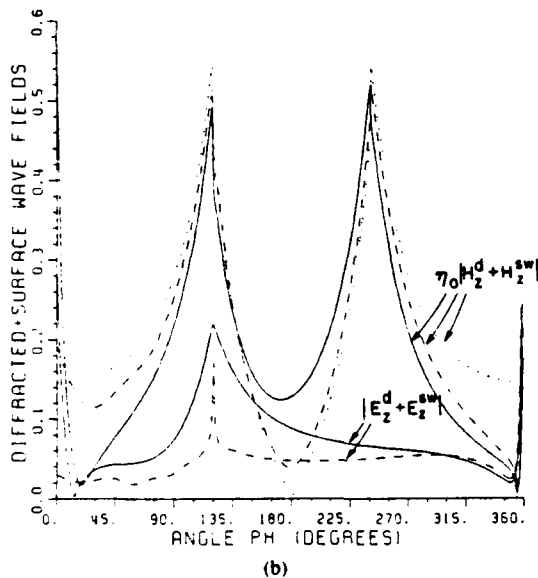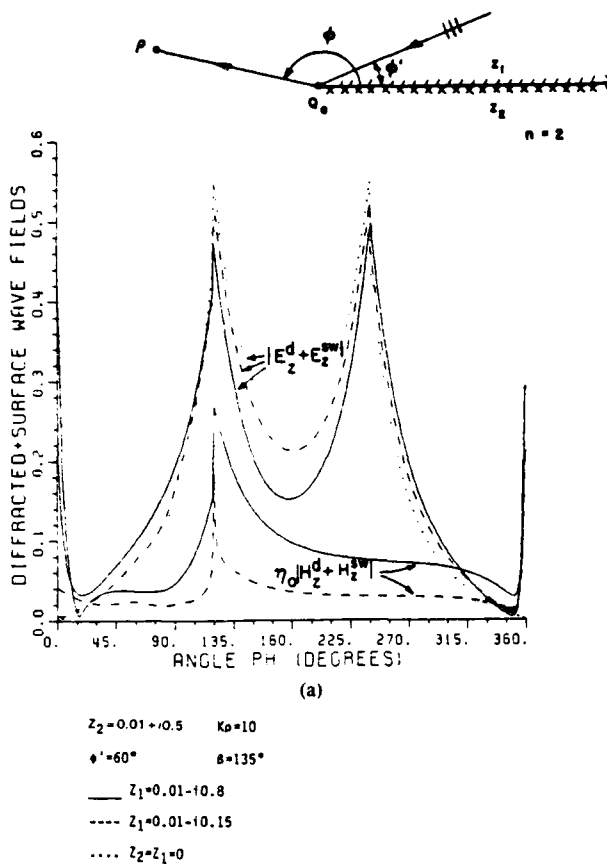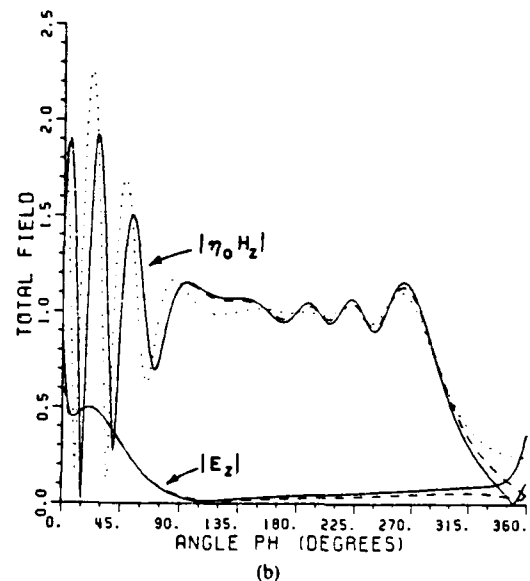- - - - $Z_2 = 0.05 + i0.5$

· · · · $Z_2 = Z_1 = 0$

(b)

Fig. 7. Total field excited by plane wave obliquely incident on impedance half-plane. (a) TM$_z$ polarization: $E_{0z} = 1$, $H_{0z} = 0$. (b) TE$_z$ polarization: $E_{0z} = 0$, $\eta_0 H_{0z} = 1$.

fields. Since the diffracted field (of order $(K\rho)^{-1/2}$) tends to zero as the observation angle approaches the surface of the half-plane, the surface wave becomes important in this region. In Fig. 6, the effect of the surface waves can clearly be seen from 0° to 20° and from 340° to 360°.

In Fig. 7, the effect of increasing the reactance of Z_2 on the surface wave traveling on the Z_2-surface is studied. When Z_2 = 0.05 + i0.5, the surface wave traveling on the Z_2-surface

is small. However, when the imaginary part of Z_2 is increased to 2.5, the surface wave becomes much stronger, especially the copolarized component. Although not shown here, note that the agreement between the solutions presented here for n = 1 and n = 2 ($Z_1 = Z_2$) and the solutions presented in [19], which are based on the Wiener–Hopf technique is very good.

The last geometry considered is the $\pi/2$-wedge. In Fig. 8, the incident field illuminates the PEC-face of the wedge and
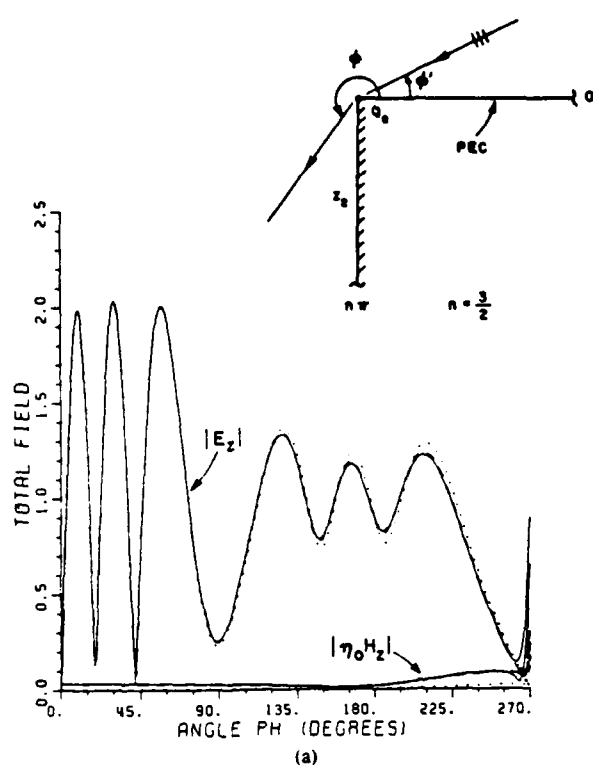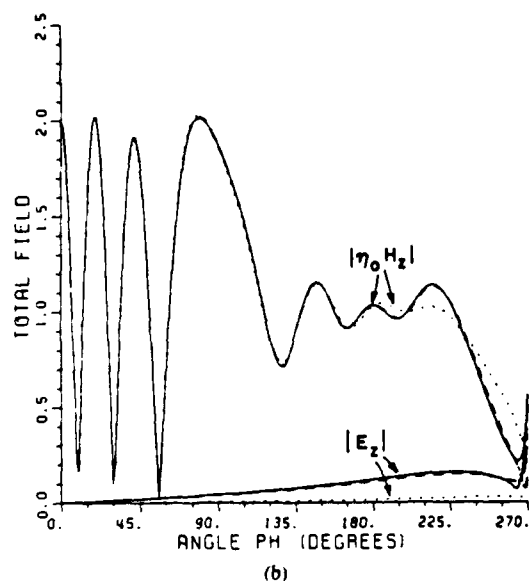
Fig. 8.   Total field excited by plane wave obliquely incident on $90°$ wedge. (a) TM$_z$ polarization: $E_{0z} = 1$, $H_{0z} = 0$. (b) TE$_z$ polarization: $E_{0z} = 0$, $\eta_0 H_{0z} = 1$.

Fig. 9.   Total field excited by plane wave obliquely incident on $90°$ wedge with one PMC wall. (a) TM$_z$ polarization: $E_{0z} = 1$, $H_{0z} = 0$. (b) TE$_z$ polarization: $E_{0z} = 0$, $\eta_0 H_{0z} = 1$.

plots for three values of Z_2 are shown. The effect of Z_2 on the scattered field is not very significant when the incident field illuminates the PEC face, except on the region from 260 to $270°$ where the surface wave effects are important. In other words, Z_2 does not play an important role on the diffracted field (for the case considered in Fig. 8); however, as expected, it still plays an important role on the surface wave field. The last example is shown in Fig. 9, where the incident field illuminates the Z_2-surface and the other face of the wedge is a PMC. The total field for two values of Z_2 is depicted, and

it can be seen that the effect of Z_2 is very significant. When the reactance of Z_2 is increased (in magnitude) from -0.05 to -0.8, the cross-polarized component becomes much more important. This makes sense, because if Z_2 were set equal to zero (PEC), the cross-polarized components of the reflected and diffracted (order $(K\rho)^{-1/2}$) fields would be zero.

VI. Conclusion

A uniform asymptotic solution for the fields scattered by four special cases of an impedance wedge was presented. The incident field was assumed to be a plane wave of arbitrary polarization, obliquely incident to the axis of the wedge. The uniform solution, which is valid for large $K\rho$, was obtained by means of the method of steepest descents. The asymptotic evaluation of the integral was carried out by taking into account the presence of the geometrical optic poles (real poles) as well as the surface wave poles (complex poles). This resulted in an expression which is continuous across the shadow boundaries of the GO and surface wave fields.

The diffracted field developed here is of order $(K\rho)^{-1/2}$ with respect to the incident field. Thus, for nonzero finite values of $Z_{1,2}$, and when $K\rho$ is large, the diffracted field is zero on the surfaces of the wedge. To obtain a more accurate diffracted field on the surface the wedge, it is necessary to include the next term of order $(K\rho)^{-3/2}$ as suggested in [15], [16]. The diffracted field presented here is valid for any combination of incidence and observation angles, except that special care must be taken for the cases of grazing incidence and/or when $Z_{1,2}$ is zero or infinity.

The expressions for the reflected, diffracted, and surface wave fields were written in a very compact matrix notation. Besides being compact, the matrix notation is suitable for numerical computations, and it helps in the physical interpretation of the results. For example, each field component of $\vec{f}_z$ (see (24)), not including the incident field, was written as the product of three matrices and the incident field $\vec{f}'_z(z = 0, y = 0, z) = \vec{F}_{0z} \exp (ikz \cos \beta)$, namely,

$$\vec{S}^{-1} \begin{bmatrix} \text{reflection,} \\ \text{diffraction, etc.} \\ \text{coefficients} \end{bmatrix} \vec{S}\vec{f}'_z(z = 0, y = 0, z).$$

Thus one starts with $\vec{f}'_z(x = 0, y = 0, z)$ and after multiplying $\vec{f}'_z(x = 0, y = 0, z)$ times the transformation matrix $\vec{S}$. one obtains an expression which is proportional to the field components normal to the wedge walls. Next, multiplying $\vec{S}\vec{f}'_z(x = 0, y = 0, z)$ times the reflection, diffraction, or surface wave launching coefficient, one gets the "normal" components of the reflected, diffracted or surface wave fields, respectively. The last step is to multiply these "normal" components times the inverse of the transformation matrix $\vec{S}$ to obtain the tangential field components, i.e., z-components.

It is important to keep in mind that for the case of oblique incidence with respect to the axis of the wedge, the fields scattered by the impedance wedge will have TM_z and TE_z polarized components regardless of the polarization (TM_z or TE_z) of the incident plane wave field. Finally, note that the elements of the column vector $\vec{f}^d_z$ are proportional to the ray-fixed coordinate system used in the geometrical theory of

diffraction [32]. Thus the representation of the fields in terms of $\vec{f}_z$ is the most appropriate in diffraction problems.

Appendix

The constants $\vec{B}_n$ and $\vec{D}_n$ are obtained by solving the following equation:

$$\underline{v}^{\pm} \cdot \vec{\Psi}(\alpha_k^{\pm}) \left\{ \frac{\vec{I}}{\sigma_n(\alpha) - \sigma_n\left(\frac{n\pi}{2} - \phi'\right)} + \vec{B}_n + \vec{D}_n \sin\left(\frac{\alpha_k^{\pm}}{n}\right) \right\}$$

$$\cdot \vec{\Psi}^{-1}\left(\frac{n\pi}{2} - \phi'\right) \vec{S}\left(\frac{n\pi}{2} - \phi'\right) \vec{F}_{oz} = 0 \quad (38a)$$

where $\alpha_k^{\pm}$ are the poles of $\vec{S}^{-1}(\alpha)$ and

$$\underline{v}^{\pm} = [\pm i, 1] \qquad \sigma_n(\alpha) = \sin\left(\frac{\alpha}{n}\right). \quad (38b)$$

Note that $\underline{v}^{\pm}$ is a one-by-two row vector. The details of the solution of (38a) are given in [12], [13], and they will not be repeated here. Only the final results for the cases considered in the previous sections, i.e., $n = 1, 2, 3/2$, and $1/2$, are given here.

It is convenient first to introduce the following functions:

$$\vec{Z}_n(\alpha) = \sigma_n(\alpha)\vec{L} - \sigma_n(n\pi/2 - \phi')\vec{I} \qquad \vec{N}_n(\alpha) = \begin{bmatrix} \underline{v}^+\vec{\Psi}(\alpha) \\ \underline{v}^-\vec{\Psi}(-\alpha) \end{bmatrix}$$

(39)

where $\vec{L}$ and $\sigma_n(\alpha)$ were defined in (28e) and (38b), respectively, and $\vec{I}$ is the identity matrix.

Case 1, $n = 1$:

$$\vec{B}_1 = -\vec{N}_1^{-1}(\alpha_0^+)\vec{Z}_1^{-1}(\alpha_0^+)\vec{N}_1(\alpha_0^+) \qquad \vec{D}_1 = \begin{bmatrix} 0 & 0 \\ 0 & 0 \end{bmatrix}$$

(40)

where $\alpha_0^{\pm} = \pm i\xi$ and $\xi = \ln((1 - \cos\beta)/\sin\beta)$.

Case 2, $n = 2$:

$$\vec{B}_2 = \frac{2 \sin \beta\vec{I} + \vec{\Gamma}(\alpha_0^+)\vec{\Gamma}^{-1}(-\alpha_0^{+*}) + \vec{\Gamma}(-\alpha_0^{+*})\vec{\Gamma}^{-1}(\alpha_0^+)}{(2 \sin \beta + K(\alpha_0))\sigma_2\left(\frac{n\pi}{2} - \phi'\right)}$$

(41a)

$$\vec{D}_2 = 2 \sin \beta\frac{[\vec{G}(\alpha_0^+)\vec{G}^{-1}(-\alpha_0^{+*}) + \vec{G}(-\alpha_0^{+*})\vec{G}^{-1}(\alpha_0^+) - 2\vec{I}]}{2 \sin \beta + K(\alpha_0)}$$

(41b)

where $\alpha_0^{\pm} = \pi/2 \pm i\xi$, and $\alpha_0^{+*} = \alpha_0^-$.

The matrices $\vec{G}(\alpha)$ and $\vec{\Gamma}(\alpha)$ are given by the following expressions

$$\vec{G}(\alpha) = \vec{N}_2^{-1}(\alpha)\vec{Z}_2(\alpha)\vec{N}_2(\alpha)$$

$$\vec{\Gamma}(\alpha) = \vec{N}_2^{-1}(\alpha)\vec{L}\vec{Z}_2(\alpha)\vec{N}_2(\alpha). \quad (42)$$

Finally, $K(\alpha_0)$ can be written in terms of the functions $\vec{M}(\alpha)$

and $\tilde{D}(\alpha, -\alpha^*)$, namely,

$$K(\alpha_0) = 2 + \frac{4\tilde{D}(\alpha_0^+, -\alpha_0^{+*})\tilde{D}(-\alpha_0^+, \alpha_0^{+*})}{\tilde{M}(\alpha_0^+)\tilde{M}(-\alpha_0^{+*})} \quad \text{(43a)}$$

where

$$\tilde{D}(\alpha, -\alpha^*) = \Psi_h(\alpha)\Psi_e(-\alpha^*) - \Psi_e(\alpha)\Psi_h(-\alpha^*) \quad \text{(43b)}$$

$$\tilde{M}(\alpha) = \Psi_e(\alpha)\Psi_h(-\alpha) + \Psi_h(\alpha)\Psi_e(-\alpha). \quad \text{(43c)}$$

Note that α^* is the complex conjugate of α.

Case 3, n = 3/2:

$$\bar{B}_{3/2} = -\bar{Q}^{-1}\bar{T} \qquad \bar{D}_{3/2} = \bar{u}\underline{c} \quad \text{(44a)}$$

where

$$\bar{T} = \begin{bmatrix} \underline{t}^+ \\ \underline{t}^- \end{bmatrix} \qquad \bar{Q} = \begin{bmatrix} \underline{q}^+ \\ \underline{q}^- \end{bmatrix} \qquad \bar{u} = \begin{cases} \bar{u}_e, & \text{for } Z_1 = \infty \\ \bar{u}_h, & \text{for } Z_1 = 0 \end{cases}.$$

$$\text{(44b)}$$

The column vectors $\bar{u}_e$ and $\bar{u}_h$ are given by

$$\bar{u}_e = \begin{bmatrix} 1 \\ 0 \end{bmatrix} \qquad \bar{u}_h = \begin{bmatrix} 0 \\ 1 \end{bmatrix}, \quad \text{(44c)}$$

and the row vectors $\underline{q}^{\pm}$ and $\underline{t}^{\pm}$ can be written as follows:

$$\underline{q}^{\pm} = \underline{v}^{\pm} \left\{ \Psi(\alpha_0^{\pm}) - \frac{\Psi(\alpha_1^{\pm})\sigma_n(\alpha_0^{\pm})\Psi_x(\alpha_0^{\pm})}{\sigma_n(\alpha_1^{\pm})\Psi_x(\alpha_1^{\pm})} \right\}$$

$$x = \begin{cases} h, & \text{if } Z_1 = 0 \\ e, & \text{if } Z_1 = \infty \end{cases} \quad \text{(45a)}$$

$$\underline{t}^{\pm} = \underline{v}^{\pm} \left\{ \frac{\Psi(\alpha_0^{\pm})}{\sigma_n(\alpha_0^{\pm}) - \sigma_n(n\pi/2 - \phi')} \right.$$

$$\left. - \frac{\Psi(\alpha_1^{\pm})\sigma_n(\alpha_0^{\pm})\Psi_x(\alpha_0^{\pm})}{[\sigma_n(\alpha_1^{\pm}) - \sigma_n(n\pi/2 - \phi')]\sigma_n(\alpha_1^{\pm})\Psi_x(\alpha_1^{\pm})} \right\} \quad \text{(45b)}$$

where $\alpha_0^{\pm} = -\pi/4 \pm i\xi$ and $\alpha_1^{\pm} = 3\pi/4 \pm i\xi$. Finally, the row vector $\underline{c}$ is given by

$$\underline{c} = \frac{\underline{v}^- \Psi(\alpha_1^-)y_1}{\sigma_n(\alpha_1^-)\Psi_x(\alpha_1^-)} \bar{Q}^{-1}\bar{W} = \frac{\underline{v}^+ \Psi(\alpha_1^+)y_2}{\sigma_n(\alpha_1^+)\Psi_x(\alpha_1^+)} \bar{Q}^{-1}\bar{W} \quad \text{(46a)}$$

where

$$\bar{W} = \begin{bmatrix} \underline{w}^+ \\ \underline{w}^- \end{bmatrix}$$

$$\underline{w}^{\pm} = \underline{v}^{\pm} \Psi(\alpha_0^{\pm}) \frac{1}{\sigma_n(\alpha_0^{\pm}) - \sigma_n\left(\dfrac{n\pi}{2} - \phi'\right)}$$

$$- \frac{1}{\sigma_n(\alpha_1^{\pm}) - \sigma_n\left(\dfrac{n\pi}{2} - \phi'\right)} \quad \text{(46b)}$$

and

$$y_1 = y_2 = 1 \text{ if } Z_1 = 0 \text{ or } y_1 = -y_2 = i \text{ if } Z_1 = \infty.$$

Case 4, n = 1/2:

$$\bar{B}_{1/2} = -\bar{u}\underline{d} \qquad \bar{D}_{1/2} = \begin{bmatrix} 0 & 0 \\ 0 & 0 \end{bmatrix} \quad \text{(47a)}$$

where

$$\underline{d} = \frac{\underline{v}^+ \Psi(\alpha_1^+)y_2}{\Psi_x(\alpha_1^+)\{\sigma_n(\alpha_1^+) - \sigma_n(n\pi/2 - \phi')\}} \qquad \alpha_1^+ = \frac{\pi}{4} + i\xi$$

$$\text{(47b)}$$

and the subscript x is defined in (45a). The column vector $\bar{u}$ and the row vector $\underline{v}^+$ are given in (44b) and (38b), respectively:

REFERENCES

[1] M. B. Leontovich, *Investigations of Propagation of Radio Waves*, Part II. Moscow, 1948.
[2] G. D. Maliuzhinets, "Excitation, reflection and emission of surface waves from a wedge with given face impedances," *Soviet Phys. Dokl.*, vol. 3, pp. 752–755, 1959.
[3] T. B. A. Senior, "Diffraction tensors for imperfectly conducting edges," *Radio Sci.*, vol. 10, pp. 911–919, Oct. 1975.
[4] ——, "Impedance boundary condition for imperfectly conducting surfaces," *Appl. Sci. Res.*, Section B, vol. 8, pp. 418–436, 1960.
[5] ——, "Some problems involving imperfect half-planes," in *Electromagnetic Scattering*, P. L. E. Uslenghi, Ed. New York: Academic, 1978, pp. 185–219.
[6] A. F. Kay, "Scattering of a surface wave by a discontinuity in reactance," *IRE Trans. Antennas Propagat.*, vol. AP-7, pp. 22–31, Jan. 1959.
[7] G. Tyras, *Radiation and Propagation of Electromagnetic Waves*. New York: Academic, 1969.
[8] J. Bazer and S. N. Karp, "Propagation of plane electromagnetic waves past a shoreline," *J. Res. Nat. Bureau Standards, D. Radio Propagation*, vol. 66D, no. 3, pp. 319–334, May–June 1962.
[9] O. M. Bucci and G. Franceschetti, "Electromagnetic scattering by a half-plane with two face impedances," *Radio Sci.*, vol. 11, pp. 49–59, Jan. 1976.
[10] ——, "Rim loaded reflector antennas," *IEEE Trans. Antennas Propagat.*, vol. 28, pp. 297–305, May 1980.
[11] J. J. Bowman, "High frequency backscattering from an absorbing infinite strip with arbitrary face impedances," *Canadian J. Phys.*, vol. 45, pp. 2409–2430, 1967.
[12] V. G. Vaccaro, "The generalized reflection method in electromagnetism," *AEU*, vol. 34, pp. 493–500, 1980.
[13] ——, "Electromagnetic diffraction from a right-angled wedge with soft conditions on one face," *Opt. Acta*, vol. 28, pp. 293–311, Mar. 1981.
[14] R. Tiberio, F. Bessi, G. Manara, and G. Pelosi, "Scattering by a strip with two face impedances at edge-on incidence," *Radio Sci.*, vol. 17, pp. 1199–1210, Sept.–Oct. 1982.
[15] R. Tiberio and G. Pelosi, "High-frequency scattering from the edges of impedance discontinuities on a flat plane," *IEEE Trans. Antennas Propagat.*, vol. AP-31, pp. 590–596, July 1983.
[16] R. Tiberio, G. Pelosi, and G. Manara, "A uniform GTD formulation for the diffraction by a wedge with impedance faces," *IEEE Trans. Antennas Propagat.*, vol. AP-33, pp. 867–873, Aug. 1985.
[17] R. G. Rojas, "A uniform GTD analysis of the EM diffraction by a thin dielectric/ferrite half-plane and related configurations," Ph.D. dissertation, Dept. Elec. Eng., Ohio State Univ., Columbus, Winter 1985.
[18] ——, "A uniform formulation for the EM diffraction by a wedge with impedance faces and with included angles equal to 0, $\pi/2$ and π (oblique incidence)," presented at the IEEE/APS Symp. and Nat. Radio Science Meeting, Philadelphia, PA, June 1986.
[19] ——, "Wiener–Hopf analysis of the EM diffraction by an impedance discontinuity in a planar surface and by an impedance half-plane," *IEEE Trans. Antennas Propagat.*, vol. 36, pp. 71–83, Jan. 1988.
[20] P. H. Pathak and R. G. Rojas, "A UTD analysis of the EM diffraction by an impedance discontinuity in a planar surface," *J. Wave-Material Interaction*, vol. 1, pp. 16–33, Jan. 1986.
[21] O. M. Bucci, C. Gennarelli, and L. Palumbo, "Parabolic antennas with a loaded flange," *IEEE Trans. Antennas Propagat.*, vol. AP-33, pp. 755–762, 1985.

[22] Y. M. Hwang, "The diffraction at the edge of a uniform impedance surface," Ph.D. dissertation, Dept. Elec. Eng., Ohio State Univ., Columbus, 1973.

[23] F. C. Karal, Jr., S. N. Karp, J. S. Chu, and R. G. Kouyoumjian, "Scattering of a surface wave by a discontinuity in the surface reactance on a right angled wedge," *Comm. Pure Appl. Math.*, vol. XIV, pp. 35–48, 1961.

[24] J. L. Volakis, "A uniform geometrical theory of diffraction for an imperfectly conducting half-plane," *IEEE Trans. Antennas Propagat.*, vol. AP-34, pp. 172–180, Feb. 1986.

[25] T. B. A. Senior and J. L. Volakis, "Scattering by an imperfect right-angled wedge," *IEEE Trans. Antennas Propagat.*, vol. AP-34, pp. 681–689, May 1986.

[26] T. B. A. Senior, "Solution of a class of imperfect wedge problems for skew incidence," *Radio Sci.*, vol. 21, pp. 185–191, Mar.–Apr. 1986.

[27] H. Lewy, "Waves on sloping beaches," *Bull. Amer. Math Soc.*, vol. 52, pp. 737–775, 1946.

[28] J. J. Stoker, "Surface waves in water of variable depth," *Quart. Appl. Math.*, vol. 5, pp. 1–54, 1947.

[29] J. J. Bowman, T. B. A. Senior, and P. L. E. Uslenghi, *Electromagnetic and Acoustic Scattering by Simple Shapes (Part I)*, North Holland Publishing Company, 1969.

[30] C. Gennarelli and L. Palumbo, "A uniform asymptotic expansion of a typical diffraction integral with many coalescing simple pole singularities and a first-order saddle point," *IEEE Trans. Antennas Propagat.*, vol. AP-32, pp. 1122–1124, Oct. 1984.

[31] R. G. Rojas, "Comparison between two asymptotic methods," *IEEE Trans. Antennas Propagat.*, vol. AP-35, pp. 1489–1492, Dec. 1987.

[32] R. G. Kouyoumjian and P. H. Pathak, "A uniform geometrical theory of diffraction for an edge in a perfectly conducting surface," *Proc. IEEE*, vol. 62, pp. 1448–1461, Nov. 1974.

Roberto G. Rojas (S'80–M'81–S'82–M'85), for a photograph and biography please see page 83 of the January 1988 issue of this TRANSACTIONS.

GENERALISED IMPEDANCE BOUNDARY CONDITIONS FOR EM SCATTERING PROBLEMS

Indexing terms: EM field theory, EM waves, Scattering, Mathematical techniques

Generalised impedance boundary conditions (GIBC) are derived for a planar, homogeneous, magnetic dielectric slab grounded by a perfect electric conducting plane. These boundary conditions, which are expressed in terms of linear differential operators of infinite order, reduce to the Weinstein boundary conditions in the limiting case of small thickness of the dielectric slab.

Introduction: The motivation of this work arose when an attempt was made to solve the problem of diffraction of a plane wave by a magnetic dielectric half-plane of thickness t backed by a perfect electric conducting plane (PEC) as shown in Fig. 1. Without loss of generality, the medium outside the
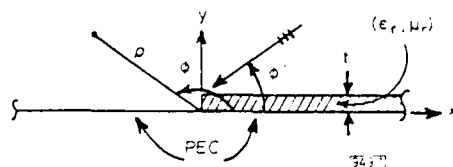

Fig. 1 *Grounded magnetic dielectric half-plane*

material is assumed to be free space. The exact solution to this problem requires finding expressions for the fields inside and outside the material and then matching these two solutions at the boundary of the slab by means of the boundary conditions satisfied by the electric and magnetic fields. Since in scattering problems one is interested in solving for the fields outside the material, it is convenient to replace the grounded slab by a set of equivalent boundary conditions. That is, the original configuration in Fig. 1 can be replaced by the two-part configuration depicted in Fig. 2, where the boundary conditions for
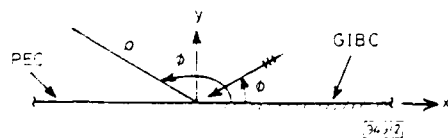

Fig. 2 *Two-part planar configuration*

$x > 0$, $y = 0$ can be expressed in terms of linear differential operators. Weinstein[1] appears to be the first to obtain a set of boundary conditions for the configuration illustrated in Fig. 1 ($x > 0$, $y = 0$). Basically, Weinstein's procedure involves the transfer of the boundary conditions from the plane $y = 0$, where $E_x = E_z = 0$, to the plane $y = t^+$, just outside the material, by means of a Taylor series expansion in powers of t. Next, the new boundary conditions are transferred back to the $y = 0$ plane by means of another Taylor series expansion assuming that the medium in $0 < y < t$, $x > 0$ is free space.

Weinstein[1] only kept terms of $O(t)$ in his expansion, and thus, his boundary conditions are valid for a very thin slab. Bernard[2] generalised the Weinstein procedure for the special case when the fields have no z-dependence ($\partial/\partial z = 0$) and obtained a boundary condition for the field H_z at the plane $y = t$. The purpose of this paper is to obtain GIBC at the plane $y = 0$ for the general case where the fields also depend on z. Note that it is convenient for analysis purposes to obtain GIBC at the $y = 0$ plane rather than the $y = t$ plane. The GIBC developed here are accurate to $O(t^M)$ where M is arbitrarily large. Actually, the results obtained here are valid for $M \rightarrow \infty$ because the GIBC are expressed in terms of infinite order linear differential operators.

Generalised impedance boundary conditions (GIBC): The first step in finding the GIBC for the geometry shown in Fig. 1 ($x > 0$, $y = 0$) is to expand the fields E_x and E_z in a Taylor series centred at $y = t^-$, namely

$$E_z^x(y) = \sum_{n=0}^{\infty} \left\{ \frac{\partial^n}{\partial y^n} E_z^x(\bar{y}) \Big|_{\bar{y}=t^-} \right\} \frac{(y-t^-)^n}{n!} \qquad 0 \leq y < t \quad (1)$$

Evaluating eqn. 1 at $y = 0$, where $E_x = E_z = 0$, and with the help of Helmholtz and Maxwell equations one obtains two very complicated expressions in terms of the tangential components E_x, E_z, H_x and H_z. Following the Weinstein method, these two equations are transferred to the $y = t^-$ plane (by applying the boundary conditions satisfied by the fields at $y = t$) and eventually to the $y = 0$ plane by means of another Taylor series expansion. It turns out that by appropriately combining the two expressions, two decoupled boundary conditions can be obtained in terms of E_y and H_y, namely

$$\left\{ \frac{\partial}{\partial y} Z^e(i\nabla_{xz}) + ik_0 \eta_0 L^e(i\nabla_{xz}) \right\} H_y = 0 \qquad y = 0 \quad x > 0 \quad (2a)$$

and

$$\left\{ \frac{\partial}{\partial y} L^h(i\nabla_{xz}) + i \frac{k_0}{\eta_0} Z^h(i\nabla_{xz}) \right\} E_y = 0 \qquad y = 0 \quad x > 0 \quad (2b)$$

where

$$Z^e(.) = \frac{\sin (\beta_0(.)t) \cos (\beta_1(.)t)}{\mu_r \beta_0(.)}$$

$$- \frac{\sin (\beta_1(.)t) \cos (\beta_0(.)t)}{\beta_1(.)} \qquad (3a)$$

$$L^e(.) = \frac{1}{ik_0 \eta_0} \left\{ \frac{\cos (\beta_1(.)t) \cos (\beta_0(.)t)}{\mu_r} \right.$$

$$\left. + \frac{\beta_0(.) \sin (\beta_1(.)t) \sin (\beta_0(.)t)}{\beta_1(.)} \right\} \qquad (3b)$$

$$L^h(.) = \cos (\beta_1(.)t) \cos (\beta_0(.)t)$$

$$+ \frac{\beta_1(.) \sin (\beta_1(.)t) \sin (\beta_0(.)t)}{\varepsilon_r \beta_0(.)} \qquad (3c)$$

$$Z^h(.) = \frac{\eta_0}{ik_0} \left\{ \frac{\beta_1(.) \cos (\beta_0(.)t) \sin (\beta_1(.)t)}{\varepsilon_r} \right.$$

$$\left. - \beta_0(.) \sin (\beta_0(.)t) \cos (\beta_1(.)t) \right\} \qquad (3d)$$

$$\beta_{0,1}(.) = (k_{0,1}^2 - (.)^2)^{1/2}$$

$$(i\nabla_{xz})^2 = -\frac{\partial^2}{\partial x^2} - \frac{\partial^2}{\partial z^2}$$

$$k_1 = Nk_0 \quad (3e)$$

Note that k_0 and η_0 are the free-space wavenumber and intrinsic impedance, respectively, and $N = \sqrt{(\varepsilon_r \mu_r)}$ is the index of refraction. Also, ε_r and μ_r, which are assumed to be complex constants, are the relative permittivity and permeability of the

slab, respectively. Furthermore, the notation cos (.) and sin (.) should be interpreted as follows

$$\cos(.) = \sum_{n=0}^{\infty} (-1)^n \frac{(.)^{2n}}{(2n)!}$$

$$\sin(.) = \sum_{n=0}^{\infty} (-1)^n \frac{(.)^{2n+1}}{(2n+1)!} \qquad (4)$$

Note that for the special case when the fields have no z-dependence ($\partial/\partial z = 0$), the GIBC in eqns. 2a and b can be expressed in terms of E_z and H_z, respectively.

From eqn. 2, it is possible to obtain boundary conditions of $O(t^M)$, where $M \geq 1$. This is done by keeping only terms of $O(t^M)$ in the series representation of $L^{e,h}$ and $Z^{e,h}$. That is, eqn. 2a can be approximated by

$$\left\{ \sum_{n=0}^{M} a_n(M) \frac{\partial^n}{\partial y^n} \right\} H_y$$

$$= \prod_{n=1}^{M} \left(\frac{\partial}{\partial y} + ik_0 \eta_0 \lambda_n^e(M) \right) H_y = 0 \qquad (5a)$$

and eqn. 2b by

$$\left\{ \sum_{n=0}^{M+1} b_n(M) \frac{\partial^n}{\partial y^n} \right\} E_y$$

$$= \prod_{n=1}^{M+1} \left(\frac{\partial}{\partial y} + i\frac{k_0}{\eta_0} \lambda_n^h(M) \right) E_y = 0 \qquad (5b)$$

where the coefficients a_n and b_n are obtained from eqns. 2–3. When $M = 1$, eqns. 5a and b reduce to the boundary conditions obtained by Weinstein, i.e.,

$$\left(\frac{\partial}{\partial y} + ik_0 \eta_0 \lambda_1^e(1) \right) H_y = 0$$

$$\lambda_1^e(1) = \frac{-1}{ik_0 t\eta_0(\mu_r - 1)} \qquad (6a)$$

$$\prod_{n=1}^{2} \left(\frac{\partial}{\partial y} + i\frac{k_0}{\eta_0} \lambda_n^h(1) \right) E_y = 0$$

$$\lambda_1^h(1) = \frac{\eta_0 K^h}{2} \left\{ 1 \mp \left(1 + \frac{4(N^2 - 1)}{(K^h)^2(\varepsilon_r - 1)} \right)^{1/2} \right\} \qquad (6b)$$

where $K^h = (ik_0 t(1 - 1/\varepsilon_r))^{-1}$. Finally, when $\varepsilon_r \to 1$ eqn. 6b also reduces to the Leontovich boundary condition where $\lambda_1^h(1) = 1/\lambda_1^e(1)$.

Conclusion: GIBC are obtained for a planar magnetic dielectric slab backed by a PEC plane. These boundary conditions are written in terms of linear differential operators of infinite order. It turns out that the GIBC can be decoupled into two equations in terms of E_y and H_y only. This result is not surprising since it is shown in Reference 3 that the exact Fresnel reflection coefficient for the PEC-backed slab depicted in Fig. 1 can be expressed in terms of E_y and H_y only. Note that boundary conditions of $O(t^M)$ can be obtained from the GIBC by keeping terms of $O(t^M)$ in the series expansion of the linear differential operators $L^{e,h}$ and $Z^{e,h}$. These boundary conditions are very useful because they simplify the analysis of canonical diffraction problems as the one illustrated in Fig. 1. Finally, it should be emphasised that the GIBC developed here recovers the exact Fresnel reflection coefficient for the grounded slab depicted in Fig. 1.

R. G. ROJAS   30th June 1988

ElectroScience Laboratory
Ohio State University
1320 Kinnear Road
Columbus, OH 43212, USA

References

1 WEINSTEIN, L. A.: 'The theory of diffraction and the factorisation method' (The Golem Press, Boulder, Colorado, 1969), pp. 295–302
2 BERNARD, J. M. L.: 'Diffraction by a metallic wedge covered with a dielectric material', J. Wave Motion, 1987, 9, pp. 543–561
3 ROJAS, R. G.: 'A uniform GTD analysis of the EM diffraction by a thin dielectric/ferrite half-plane and related configurations'. PhD Dissertation, Ohio State University, Department of Electrical Engineering, Columbus, Ohio, 1985

GaInP/AlGaInP DOUBLE-HETEROSTRUCTURE LASER GROWN ON A (111)B-ORIENTED GaAs SUBSTRATE BY METALORGANIC CHEMICAL VAPOUR DEPOSITION

Indexing terms: Semiconductor lasers, Semiconductor growth, Vapour deposition

Room temperature continuous-wave operation of a $Ga_{0.5}In_{0.5}P/(Al_{0.5}Ga_{0.5})_{0.5}In_{0.5}P$ double-heterostructure laser grown on a (111)B-oriented GaAs substrate by metalorganic chemical vapour deposition was obtained for the first time. The threshold current was 99 mA. The emission wavelength was around 650 nm, which was about 30 nm shorter than that of a similar laser grown on a (100)-oriented GaAs substrate.

Although the stable operation of a 680 nm-band GaInP AlGaInP double-heterostructure (DH) laser grown by metalorganic chemical vapour deposition (MOCVD) for more than 2000 hours at 50°C has been reported,[1] the 684 nm emission wavelength of the laser was about 30 nm longer than the 650 nm wavelength emitted by lasers grown by other methods. It has been shown that the difference between the two wavelengths can be attributed to ordering of the elements on the column III sublattice.[2] Several groups have investigated the order of the elements and verified that 1/2 (111) ordering occurs in GaInP layers grown on (100) GaAs by MOCVD.[3–5] Because the formation of an ordered structure is accompanied by a decrease in bandgap energy of up to 70 meV, the emission wavelength of a laser with an ordered crystal is longer than that of a laser with a disordered crystal. If the ordering in the crystal can be suppressed, the emission wavelength can be shortened to about 650 nm. This shortening of wavelength ($\Delta\lambda \sim 30$ nm) corresponds to the extent the wavelength can be shortened by substituting an $(Al_{0.16}Ga_{0.84})_{0.5}In_{0.5}P$ active layer for a $Ga_{0.5}In_{0.5}P$ active layer. However, because the threshold current tends to increase with increasing AlP content in the active layer,[6] shortening the emission wavelength by suppressing the ordering, not by adding AlP in the active layer, is a promising method for growing lasers with low threshold current.

Recently, we have established by transmission electron microscopy and photoluminescence measurements that GaInP and AlGaInP grown on (111)B GaAs by MOCVD show no trace of ordering. Therefore, a disordered crystal can be obtained simply by growing it on a (111)B GaAs substrate by MOCVD.

In this letter, we report on the first GaInP/AlGaInP DH laser which was grown on a (111)B GaAs substrate by MOCVD.

The epitaxial layers were grown on a Si-doped (111)B GaAs substrate tilted 2° towards the ⟨110⟩ direction by atmospheric pressure MOCVD using ethyl-organometallics, phosphine, and arsine as source materials. The growth temperature of 680°C and the V/III ratio of 340 were the same as those for the DH lasers grown on (100) GaAs substrates. The p-type dopant was dimethylzinc and the n-type dopant H_2Se, but the amount of H_2Se was reduced by a factor of seven compared with that used in growth on (100) substrates, because the doping efficiency of Se-doped AlGaInP on the 2° off (111)B

Simple Examples of the Method of Moments in Electromagnetics

EDWARD H. NEWMAN, SENIOR MEMBER, IEEE

Abstract—The purpose of this paper is to present three simple examples of the method of moments in electromagnetics. The examples shown are the input impedance of a short dipole, plane wave scattering from a short dipole, and two coupled short dipoles. The relative simplicity of the examples is a direct result of obtaining simple expressions for the elements in the method of moments impedance matrix.

I. Introduction

THE METHOD of moments (MM) is a numerical procedure for solving a linear operator equation by transforming it to a system of simultaneous linear algebraic equations, commonly referred to as a matrix equation. Since Harrington's classic paper [1] and book [2] there has been a virtual explosion of research and engineering involving the application of the MM to electromagnetic radiation and scattering problems. It is safe to say that most universities with a strong graduate program in electromagnetics include the MM in their curriculum.

In introducing a new subject to a student, there is nothing as valuable as a simple and yet meaningful example which can be solved in a short period of time. The purpose of this paper is to present such an example for the MM in time harmonic electromagnetics. The example chosen is the radiation and scattering from an electrically short, perfectly conducting dipole antenna. This example is chosen because the short dipole is probably the simplest of all antennas, and thus the student is most likely to have a feel for its characteristics. The MM solution employs the piecewise sinusoidal expansion and weighting functions. This choice was made for two reasons. First, the piecewise sinusoids constitute a rapidly converging basis set for the currents on a thin wire. Thus, reasonable results can be obtained with only three modes on the wire. Due to the symmetry of the dipole current, one unknown can be eliminated and we will need to deal with matrices of size 2 × 2. Second, for the short dipole the elements in the MM matrix equation can be approximated in terms of simple functions typically found on a scientific calculator.

Section II outlines the MM solution for the current on a dipole antenna. The presentation is brief, and the reader

is referred to several books [2]-[6] as well as hundreds of articles in such journals as the IEEE TRANSACTIONS ON ANTENNAS AND PROPAGATION for the details and limitations of the method. Of the many papers, the author recommends Harrington's description of the MM [1], Richmond's description of the solution of scattering problems using a system of linear equations [7], and Tsai and Smith's particularly simple explanation of the MM [8]. Section II also presents simple expressions for the elements in the MM matrix equation. Based upon these equations, Section III presents three simple examples which can be worked in about one hour. These include the input impedance of a short dipole, plane wave scattering from a short dipole, and two coupled short dipoles.

II. Theory

A. The Integral Equation

Fig. 1(a) shows the basic problem to be solved. Here we have a perfectly conducting dipole of length L and radius a in free space with constitutive parameters (μ, ϵ). The dipole is illuminated by the fields of the known impressed electric and magnetic currents (J^i, M^i). In this paper, all fields and currents are considered to be time harmonic with the $e^{j\omega t}$ time dependence suppressed. λ will denote the free space wavelength. In the absence of the dipole, the impressed currents radiate the assumed known incident electric and magnetic fields (E^i, H^i). In the presence of the dipole, the impressed currents radiate the unknown total fields (E^t, H^t).

As illustrated in Fig. 1(b), the first step in obtaining an integral equation for the currents on the dipole is to use the surface equivalence principle [9] to replace the dipole by free space and by the electric surface current density

$$J = \hat{n} \times H^t. \tag{1}$$

J exists on the entire surface S which encloses the dipole and has outward normal $\hat{n}$. The use of the equivalence principle is central to the development of the integral equation for J since it allows us to deal strictly with the fields of sources in *free space*. In the equivalent problem of Fig. 1(b), the total fields are produced by (J^i, M^i) and J radiating in free space. In free space, J radiates the so-called scattered fields defined by

$$E^s = E^t - E^i \tag{2}$$
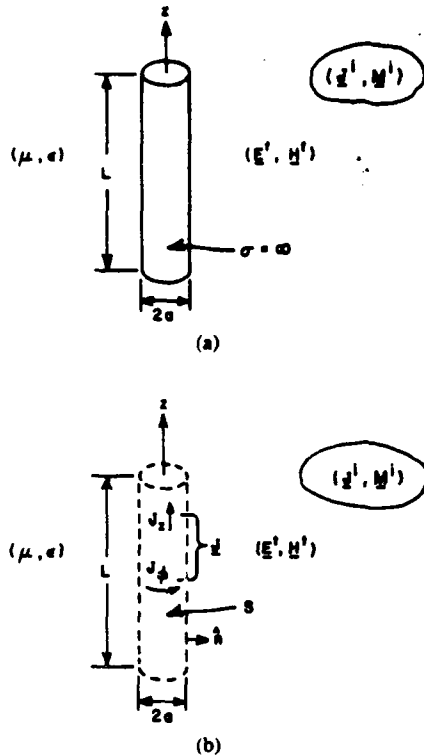
$$H^s = H^t - H^i. \tag{3}$$

(a)

(b)

Fig. 1. (a) The geometry for a perfectly conducting dipole illuminated by the impressed currents. (b) The equivalent problem in which the dipole is replaced by free space and by equivalent electric currents flowing on its surface.

An equation for J is obtained by enforcing the boundary condition that the total electric field tangential to the surface S must vanish, i.e.,

$$\hat{n} \times (E^s + E^i) = 0 \quad \text{on } S. \qquad (4)$$

Equation (4) is an integral equation for J written in symbolic form since the scattered electric field E^s can be written as an integral over S of the dot product of J and the dyadic free space Green's function [10].

For a thin-wire dipole, whose radius $a \ll \lambda$, the following simplifications are made:

1) The current on the endcaps of the wire is ignored.

2) The longitudinal component of current J_z is much greater than the circumferential component J_ϕ. Thus, we ignore J_ϕ. As a consequence, (4) is applied only to the $\hat{z}$ components of the electric fields.

3) Instead of enforcing (4) on the surface S, we will enforce it on the center line of the dipole. This is reasonable since the center line is electrically so close to the surface; however, we note that this approximation can result in the numerical problem of relative convergence [11].

With these approximations, we are solely interested in the $\hat{z}$ component of all electric fields and currents. Thus, the vector notation will now be dropped and the $\hat{z}$ component is understood. For example, the vector (4) now reduces to the scalar equation

$$-E^s = E^i \quad \text{on the dipole center-line.} \qquad (5)$$

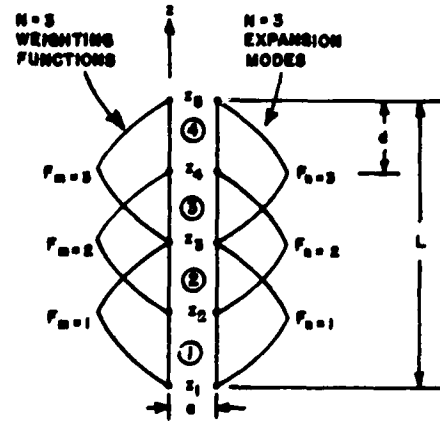In the next section, (5) will be solved using the MM.

Fig. 2. An example showing three piecewise sinusoidal dipole modes on a dipole which has been split into four equal segments.

B. MM Solution of the Integral Equation

Instead of solving (5) for the surface current density J, it is more convenient to solve for the total current

$$I(z) = 2\pi a J(z). \qquad (6)$$

The first step in the MM solution is to expand the unknown current in terms of some basis set. Thus, we write

$$I(z) \approx \sum_{n=1}^{N} I_n F_n \qquad (7)$$

where the I_n are a sequence of N unknown complex coefficients, and the F_n are a sequence of N known modes or basis functions. In our case, we choose the F_n as the piecewise sinusoidal dipole modes used by Richmond [12]. For example, Fig. 2 shows a dipole of length L split into four equal segments of length $d = L/4$. In Fig. 2, the segment numbers are shown circled. Segment n goes from z_n to z_{n+1}. The piecewise sinusoidal modes are placed on the dipole in an overlapping fashion with mode n existing on segment n and $n + 1$. Mode n has endpoints z_n and z_{n+2}, and center or terminals at z_{n+1}. F_n is a filament of electric current, located at radius a from the wire center line (i.e., on the surface of the wire) and with current

$$F_n(z) = \frac{\sin k(d - |z - z_{n+1}|)}{\sin kd} \text{ amps} \qquad (8)$$

in which $k = 2\pi/\lambda$ is the free-space wavenumber. $F_n(z)$ is zero at its endpoints and rises sinusoidally to a maximum at its center with terminal current of $F_{n0} = F_n(z_{n+1}) = 1$ A. Note that the piecewise sinusoidal modes produce a current which is continuous on the wire and also zero at the dipole endpoints [3]. Since the expansion modes have unit terminal current, the dipole current at z_{n+1} is I_n amps (except at the dipole endpoints where the current is always zero). Equation (8) produces a sinusoidal interpolation of the current values at the $N + 2$ points on the dipole.

Substituting (7) into (5) yields

$$-\sum_{n=1}^{N} I_n E_n^s \approx E^i \quad \text{on the dipole center-line} \qquad (9)$$

where E_n^z is the free-space z component of the electric field of F_n and is available in terms of simple functions [13], [14].

The weighting functions in the MM solution will be chosen identical to the expansion functions, except that they are located along the center line of the dipole. This is because we chose to enforce (5) on the center line. The next step in the MM solution requires an inner product. We will define the inner product between the functions $f(z)$ and $g(z)$ as

$$\langle f(z), g(z) \rangle = \int_0^L f(z)\, g(z)\, dz$$

where the integration is over the length of the dipole. Now taking the inner product of both sides of (9) with the sequence of N weighting functions F_m ($m = 1, 2, \cdots, N$), (9) becomes an $N \times N$ system of simultaneous linear algebraic equations which can written compactly in matrix form as

$$[Z]I = V. \tag{10}$$

Here I is the current column vector whose N components hold the I_n of (7). $[Z]$ is the $N \times N$ impedance matrix whose typical term is

$$Z_{mn} = -\int_m E_n^z F_m\, dz. \tag{11}$$

For the dipole, the $[Z]$ matrix is symmetric and also toeplitz since Z_{mn} is only dependent upon $|m - n|$. In general, $[Z]$ is dependent upon the geometry and material composition of the scatterer, but not on the incident fields. A typical element of the right-hand side or voltage vector V is given by

$$V_m = \int_m E^i F_m\, dz. \tag{12}$$

The integrations in (11), (12) are on the dipole center line, and over the extent of F_m, i.e., from $z = z_m$ to z_{m+2}. The dimensions of the elements of $[Z]$ and V are volt-amps (VA), while the elements of I are dimensionless. If the Z_{mn} were divided by $F_{m0}F_{n0}$, then the Z_{mn} would have dimensions of ohms. Since in our case the modal terminal currents are $F_{n0} = 1$ A, our Z_{mn} can be considered to have the dimensions of ohms. In any case, the $[Z]$ matrix is usually referred to as an impedance matrix and V as a voltage vector since the matrix (10) resembles an N port generalization of Ohm's law.

As $N = $ the number of terms retained in the expansion for the current increases, the MM solution should approach the exact result. In order to obtain results suitable for engineering accuracy, typically $N = 4$–10 piecewise sinusoidal modes per wavelength of wire are required. As the electrical length of the wire increases, N must increase and thus so does the computer CPU time and storage needed to set up and solve the matrix equation (10). For this reason, MM solutions are often referred to as low-frequency solutions, which are applicable when the antenna or scatterer is not too large in terms of a wavelength.

C. Simple Expressions for Z_{mn} and V_m

Simple Expressions for Z_{mn}: The major problem in an MM solution is usually the evaluation of the elements in the impedance matrix. Usually this involves numerical integrations and/or the evaluation of special functions. As a result, most MM solutions are done on a digital computer and require a great deal of programming time and effort. For this reason, most MM solutions are not suitable as a simple example problem which can be accomplished in about an hour using only a scientific calculator. Below we will present relatively simple expression for the elements in the dipole MM impedance matrix, thus eliminating the need for a digital computer to carry out the MM solution to the examples given in the next section.

For the dipole antenna, the elements in the impedance matrix, as given by (11), are the mutual impedance between parallel piecewise sinusoidal dipole modes. Fig. 3 shows two parallel piecewise sinusoidal dipole modes of length $2d$. The bottom of weighting mode m is located a distance h above the center of expansion mode n, and the modes are staggered by the distance r. For convenience, the expansion mode has its center at $z = 0$. Exact expressions for the mutual impedance between these modes has been given by King [14]. Unfortunately, King's expressions are very lengthy and also require the evaluation of sine and cosine integrals. In order to simplify King's expressions, we will assume that the modes are electrically small and electrically close. This will always be the case for modes on an electrically short dipole. Specifically, if we assume that kd, kh, and kr are all $\ll 1$, then in the Appendix we show that King's expressions for the mutual impedance between modes m and n reduce to

$$Z_{mn} = R_{mn} + jX_{mn} \tag{13}$$

where the real and imaginary parts of Z_{mn} are given by

$$R_{mn} = 20(kd)^2 \tag{14}$$

$$X_{mn} = -\frac{30}{kd^2} \left[-4A + 6B - 4C + D \right.$$

$$+ E + 4h \ln(2A + 2h)$$

$$- 6(d + h) \ln(2B + 2h + 2d)$$

$$+ 4(2d + h) \ln(2C + 2h + 4d)$$

$$+ (d - h) \ln(2D + 2h - 2d)$$

$$\left. - (3d + h) \ln(2E + 2h + 6d) \right] \tag{15}$$

where

$$A = \sqrt{r^2 + h^2}$$

$$B = \sqrt{r^2 + (d + h)^2}$$
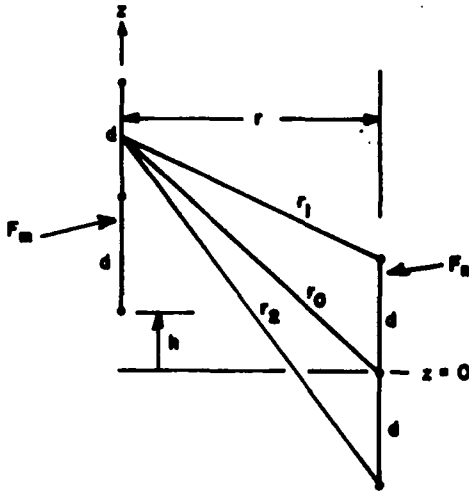
$$C = \sqrt{r^2 + (2d + h)^2}$$

Fig. 3. Geometry for the mutual impedance between two parallel piecewise sinusoidal dipoles.

$$D = \sqrt{r^2 + (d - h)^2}$$

$$E = \sqrt{r^2 + (3d + h)^2}.$$

Equations (14) and (15) can be said to be suitable for a scientific calculator since they involve no operations more complicated than the natural log and square root. Note that R_{mn} is the well known formula for the radiation resistance of a short dipole and is independent of mode separation. Equation (15) will further simplify if we assume $r = a \ll d$ (the wire radius is much less than the segment length) and also consider certain special values of h. For self-impedance terms $m = n$ and

$$X_{mm}(h = -d) = -\frac{30}{kd}\left[-4 + 4\ln(d/a)\right]. \quad (16)$$

For adjacent modes with one overlapping segment $|m - n| = 1$ and

$$X_{mn}(h = 0) = -\frac{30}{kd}\left[1 + 2\ln(1.54a/d)\right]. \quad (17)$$

If $|m - n| = 2$, then the modes share a single point and

$$X_{mn}(h = d) = -\frac{30}{kd}\left[-0.68\right]. \quad (18)$$

If $|m - n| \geq 3$, then the modes are not touching and

$$X_{mn}(h \geq 2d) = -\frac{30}{kd}\left[\frac{h}{d}\ln\frac{h^4(2d + h)^4}{(d + h)^6(h - d)(3d + h)}\right.$$
$$\left. + \ln\frac{(2d + h)^8(h - d)}{(d + h)^6(3d + h)^3}\right]. \quad (19)$$

Voltage Generators: Now consider the evaluation of the right-hand side vector V. As seen in (12), V is dependent upon the ℓ component of the incident electric field.

First, consider the case where the dipole is excited by a voltage generator. The simplest and probably the most commonly used model for a voltage generator is the so-

called delta-gap model [3]. A delta-gap generator is one which creates an extremely large, but highly localized electric field polarized parallel to the wire center-line. A v volt delta-gap generator located at $z = z'$ has the incident field

$$E^i = v\delta(z - z') \quad (20)$$

where $\delta(z)$ is the unit area Dirac delta function. Normally, the generators are placed at the center or terminals of the piecewise sinusoidal modes. Thus, referring to Fig. 2 for a dipole with $N = 3$ modes, the generator could be placed at points 2, 3, or 4 which would be at the terminals of modes 1, 2, or 3, respectively. Inserting the incident field from (20) into (12) shows that if a delta-gap generator of v_m volts is placed at the terminals of mode m, then

$$V_m = v_m. \quad (21)$$

Element m of V is nonzero only if a nonzero generator is placed at the terminals of mode m.

Lumped Loads: Now consider the effect of placing a lumped load in the wire. A lumped load of Z_{lm} ohms, placed at the terminals of mode m, will produce a voltage of $-I_m Z_{lm}$ volts at these terminals. If we treat this voltage as a dependent delta-gap generator, then according to (21) we should add $-I_m Z_{lm}$ to V_m. However, this is an unknown voltage since initially I_m is unknown. Since it is conventional to write all unknowns on the left-hand side of the matrix equation, we add $I_m Z_{lm}$ to both sides of row m of the matrix equation. Thus, it can be seen that a lumped load of Z_{lm} ohms placed at the terminals of mode m simply results in Z_{mm} being replaced by $Z_{mm} + Z_{lm}$.

There is no physical break or gap in the wire where a generator or load is placed. Thus, the current is continuous through generators and loads. There is a slope discontinuity, or jump in the derivative of the current, at the generator or load. Note that the piecewise sinusoidal modes account for this behavior by enforcing continuity of current on the wire and by allowing a slope discontinuity at their terminals.

Plane Wave Excitation: Next consider the situation where the wire is excited by a normally incident plane wave. If a ℓ polarized plane wave is incident from the $+x$ axis with magnitude E_0, then

$$E^i = E_0 e^{jkx}. \quad (22)$$

Inserting (22) into (12) and integrating yields

$$V_m = \frac{2E_0}{k}\tan(kd/2). \quad (23)$$

III. Numerical Examples

A. Example 1—Dipole Input Impedance

In Example 1, we compute the current distribution and input impedance of a center fed dipole antenna. Referring to Fig. 1(a), we will consider a dipole of length $L = 0.1$ m, radius $a = 0.0001$ m, and at a frequency of 300 MHz or $\lambda = 1$ m. As illustrated in Fig. 2, we will use $N = 3$ piecewise sinusoidal modes on the dipole, and segment

the dipole into $N + 1 = 4$ equal segments of length $d = L/4 = 0.025$ m. In this case the 3×3 MM matrix (10) can be explicitly written as

$$\begin{bmatrix} Z_{11} & Z_{12} & Z_{13} \\ Z_{21} & Z_{22} & Z_{23} \\ Z_{31} & Z_{32} & Z_{33} \end{bmatrix} \begin{bmatrix} I_1 \\ I_2 \\ I_3 \end{bmatrix} = \begin{bmatrix} V_1 \\ V_2 \\ V_3 \end{bmatrix}. \qquad (24)$$

Since the current on the center fed dipole will be symmetric, $I_1 = I_3$. In this case, we can add column 3 of the matrix equation to column 1 and reduce the order 3 matrix equation to the order 2 matrix equation

$$\begin{bmatrix} (Z_{11} + Z_{13}) & Z_{12} \\ (Z_{21} + Z_{23}) & Z_{22} \end{bmatrix} \begin{bmatrix} I_1 \\ I_2 \end{bmatrix} = \begin{bmatrix} V_1 \\ V_2 \end{bmatrix}. \qquad (25)$$

Reducing the order of the matrix equation from 3 to 2 greatly reduces the effort in the hand calculations required to solve the matrix equation.

Although $[Z]$ in (24) and (25) contain nine elements, only three are distinct since from the symmetry of the dipole

$$Z_{11} = Z_{22} = Z_{33}$$

$$Z_{12} = Z_{21} = Z_{23} = Z_{32}$$

$$Z_{13} = Z_{31}.$$

The real part of each Z_{mn} is given by (14) as

$$R_{mn} = 0.4935 \text{ VA}.$$

The imaginary part of the Z_{mn} can be computed from (15); however, here we choose to use the simpler (16)–(18). Table I shows the elements in the first row of the $[Z]$ matrix of (24) computed by (13), (16)–(18) and by King's exact expressions [14], [15]. Note that the approximate values of $[Z]$ are within 11 percent of the exact values.

If the approximate values of $[Z]$ from Table I are substituted into (25) we obtain

$$\begin{bmatrix} 0.9869 - j3324 & 0.4935 + j1753 \\ 0.9869 + j3506 & 0.4935 - j3454 \end{bmatrix} \begin{bmatrix} I_1 \\ I_2 \end{bmatrix} = \begin{bmatrix} 0 \\ 1 \end{bmatrix} \qquad (26)$$

where we have set $V_2 = 1$ VA since there is a 1 V generator at the terminals of mode 2. Equation (26) can be easily solved using Cramer's rule. The results for the elements in the dimensionless current vector are

$$I_1 = I_3 = 0.0003286 \angle 89.892^0$$

$$I_2 = 0.0006230 \angle 89.926^0.$$

The dipole current can now be obtained by inserting these coefficients into (7) with $N = 3$. The dipole current will have dimensions of amps, since the expansion modes F_n have dimensions of amps. Also, since the current expansion modes have a terminal current of 1 A, I_m is nu-

TABLE I
EXAMPLE 1 ELEMENTS OF THE $[Z]$ MATRIX (VA)

Element	Approximation	Exact
Z_{11}	$0.4935 - j3454$	$0.4944 - j3426$
Z_{12}	$0.4935 + j1753$	$0.4945 + j1576$
Z_{13}	$0.4935 + j129.9$	$0.4885 + j132.2$

merically equal to the current in amps at the center of mode m. Thus, the dipole input or terminal current is I_2 A. The input impedance is given by the ratio of the input voltage to the input current, i.e.,

$$Z_{in} = 1/I_2 = 2.083 - j1605 \; \Omega.$$

By contrast, if we were to use the exact values of $[Z]$ from Table I, then the results for the current distribution and input impedance would be

$$I_1 = I_3 = 0.0002498 \angle 90.0^0$$

$$I_2 = 0.0005219 \angle 89.9^0$$

$$Z_{in} = 1.892 - j1916 \; \Omega.$$

B. Example 2—Scattering from a Dipole

In Example 2, we will compute the broadside plane wave scattering from the same dipole considered in the above example, except that it is terminated in a conjugate matched load. To terminate the dipole in its conjugate matched load, we place a lumped load of Z_{in}^* at the center of the dipole, i.e., at the terminals of mode 2. Using the value of Z_{in} computed above,

$$Z_{l2} = Z_{in}^* = 2.083 + j1605 \; \Omega.$$

As discussed in Section II, the impedance matrix for the loaded dipole is identical to that of the unloaded dipole except that we add Z_{l2} to the self-impedance of mode 2 to obtain

$$Z_{22} = (0.4935 - j3454) + (2.083 + j1605)$$

$$= 2.576 - j1849 \text{ VA}.$$

If the incident electric field is a unit amplitude, $\hat{z}$ polarized plane wave incident from the $+x$ axis, then the elements of the right-hand side vector are identical and given by (23) with $E_0 = 1$,

$$V_m = 0.02505 \text{ VA} \qquad m = 1, 2, 3.$$

Since the excitation and loading of the antenna are symmetric with respect to the center of the dipole, the current on the dipole remains symmetric. Thus, the current vector can still be computed from the order 2 matrix (25),

$$\begin{bmatrix} 0.9869 - j3324 & 0.4935 + j1753 \\ 0.9869 + j3506 & 2.576 - j1849 \end{bmatrix} \begin{bmatrix} I_1 \\ I_2 \end{bmatrix}$$

$$= \begin{bmatrix} 0.02505 \\ 0.02505 \end{bmatrix}. \qquad (27)$$

Equation (27) can be solved using Cramer's rule. The results for the elements in the dimensionless current vector are

$$I_1 = I_3 = 0.006515 \angle 0.581^0$$

$$I_2 = 0.01235 \angle 0.548^0.$$

The scattered field is given by

$$E^s = \sum_{n=1}^{N} I_n E_n^s \tag{28}$$

where as in (9), E_n^s is the free-space electric field of expansion mode F_n. For a field point on the $+x$ axis (i.e., in the backscatter direction) and in the far-zone of the dipole, E_n^s will be $\hat{z}$ polarized and given by

$$E_n^s = j60 \tan (kd/2) \frac{e^{-jkx}}{x} \text{ V/m}. \tag{29}$$

Using (29) and the above values for the I_n, the far-zone backscattered electric field is

$$E^s = 0.1199 \angle 90.6^0 \frac{e^{-jkx}}{x} \text{ V/m}.$$

The radar-cross-section of the dipole is

$$\sigma = 4\pi x^2 \frac{|E^s|^2}{|E_0|^2} = 0.1806 \text{ m}^2. \tag{30}$$

By contrast, if we were to repeat this example with the exact values of $[Z]$ from Table I, the results would be

$$I_1 = I_3 = 0.006199 \angle 0.0^0$$

$$I_2 = 0.01295 \angle 0.0^0$$

$$\sigma = 0.1801 \text{ m}^2.$$

C. Example 3—Coupled Dipoles

In Example 3, we analyze the mutual coupling between two short dipoles. As illustrated in Fig. 4, the dipoles are identical to that considered in the Example 1 above ($L = 0.1$ m, $a = 0.0001$ m, and $f = 300$ MHz), and are separated by a distance $s = 0.01$ m. Here we wish to compute the input impedance of dipole 1 in the presence of dipole 2. To minimize the computations, we will place only one piecewise sinusoidal mode on each dipole. Thus, the order $N = 2$ matrix equation for this problem is

$$\begin{bmatrix} Z_{11} & Z_{12} \\ Z_{21} & Z_{22} \end{bmatrix} \begin{bmatrix} I_1 \\ I_2 \end{bmatrix} = \begin{bmatrix} V_1 \\ V_2 \end{bmatrix}. \tag{31}$$

Only Z_{11} and Z_{12} need be computed since from the symmetry of the dipoles $Z_{11} = Z_{22}$ and $Z_{12} = Z_{21}$. Z_{11} is evaluated from (14) and (16) with $d = -h = L/2 = 0.05$ m and $r = a = 0.0001$ m. Z_{12} is evaluated from (14) and (16) with a replaced by $s = 0.01$ m since $h = -d$. The results for Z_{11} and Z_{12} are shown in Table II where they are compared with the exact values [14], [15].

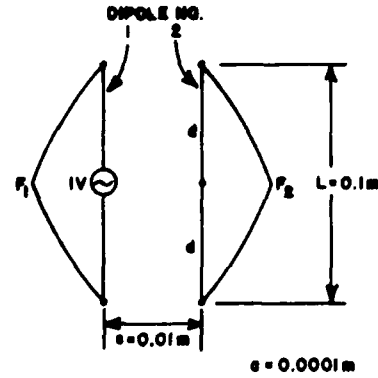Inserting the approximate values from Table II into (31)

Fig. 4. Geometry for the two coupled dipoles in Example 3.

TABLE II
EXAMPLE III ELEMENTS OF THE [Z] MATRIX (VA)

Element	Approximation	Exact
Z_{11}	$1.9739 - j1992$	$2.0000 - j1921$
Z_{12}	$1.9739 - j232.8$	$1.9971 - j325.1$

we obtain

$$\begin{bmatrix} 1.9739 - j1992 & 1.9739 - j232.8 \\ 1.9739 - j232.8 & 1.9739 - j1992 \end{bmatrix} \begin{bmatrix} I_1 \\ I_2 \end{bmatrix} = \begin{bmatrix} 1 \\ 0 \end{bmatrix}. \tag{32}$$

In (32) we have set $V_1 = 1$ since to compute the input impedance of dipole 1 we place a 1 V generator at the terminals of mode 1. Equation (32) has the solution

$$I_1 = 0.0005090 \angle 89.955^0 \text{ and}$$

$$I_2 = 0.00005949 \angle -89.616^0.$$

The input impedance is

$$Z_{in} = 1/I_1 = 1.539 - j1964 \ \Omega.$$

In the absence of dipole 2, the $N = 1$ mode solution for the input impedance of dipole 1 is numerically equal to Z_{11}. Thus, in the absence of dipole 2, the input impedance of dipole 1 would be $1.9739 - j1992 \ \Omega$.

If the exact values of $[Z]$ in Table II were used, then the input impedance of dipole 1 in the presence of dipole 2 would be $1.382 - j1866 \ \Omega$.

IV. SUMMARY

The purpose of this paper has been to present simple examples of the method of moments (MM) in time harmonic electromagnetics. By simple it is meant an example which can be worked in about an hour with a scientific calculator. Such examples are not common because typically MM solutions require dealing with relatively large systems of simultaneous equations. Also, the evaluation of the elements in the MM matrix equation usually require either numerical integrations or the evaluation of special functions. By contrast, the examples shown here required

dealing with matrix equations of size 2 × 2, required no numerical integrations, and involved no special functions not commonly found on a scientific calculator. It is hoped that these examples will be of value in a graduate or senior level course in applied electromagnetics.

The examples chosen involved the radiation and scattering by an electrically short thin-wire dipole or pair of dipoles. These examples were chosen because of the geometric simplicity of the dipole, and also because there is a reasonable chance of the student being familar with the basic characteristics of the short dipole. The MM solution used the piecewise sinusoidal modes. This choice was made for two reasons. First, approximate expressions were obtained which allowed the elements of the MM impedance matrix to be evaluated from simple expressions involving only the log and square root functions. Second, on a dipole, this choice results in a very rapidly converging MM solution. This permitted reasonably accurate results to be obtained with only three unknowns, and using the symmetry of the dipole current 2 × 2 matrices.

Appendix

Derivation of Z_{mn} in (14) and (15)

The main factor which allowed the examples in Section III to be easily evaluated was that the elements of the impedance matrix were expressed in (14) and (15) in relatively simple form. In this Appendix we will outline the derivation of (14) and (15). Z_{mn} is defined by (11).

Fig. 3 shows modes m and n staggered by the distance r and with the bottom of mode m at a height h above the center of mode n. For convenience, the center of mode n is at $z = 0$. The two modes have identical segment length d and piecewise sinusoidal current given by (8). The exact $\hat{z}$ component of the electric field of F_n at a point on F_m is given by [13], [14]

$$E_n^s = \frac{30}{\sin kd} \left[-j \frac{e^{-jkr_1}}{r_1} - j \frac{e^{-jkr_2}}{r_2} \right.$$

$$\left. + j2 \cos kd \frac{e^{-jkr_0}}{r_0} \right] \qquad (33)$$

where as seen in Fig. 3

$$r_0 = \sqrt{r^2 + z^2} \qquad (34)$$

$$r_1 = \sqrt{r^2 + (d - z)^2} \qquad (35)$$

$$r_2 = \sqrt{r^2 + (d + z)^2}. \qquad (36)$$

Note that the electric field of a sinusoidal dipole appears to be three spherical waves emanating from its endpoints and terminals. Equation (11) for Z_{mn} now becomes

$$Z_{mn} = -\frac{1}{\sin kd} \left[\int_h^{h+d} E_n^s \sin k(z - h) \, dz \right.$$

$$\left. + \int_{h+d}^{h+2d} E_n^s \sin k(2d + h - z) \, dz \right] \qquad (37)$$

with E_n^s given by (33). King [14] showed that (37) can be integrated exactly. Unfortunately, the result is a very lengthy expression which requires the evaluation of many sine and cosine integrals. Thus, although King's expression are well suited to programming on a digital computer [15], they are not as suitable for calculations with a hand calculator.

In order to obtain a relatively simple result from (37) we assume kd, kr, and kh are all $\ll 1$. In this case, the following small argument approximations are valid:

$$\sin k(z - h) \approx k(z - h)$$

$$\sin k(2d + h - z) \approx k(2d + h - z)$$

$$\sin kd \approx kd$$

$$e^{-jkr_i} \approx 1 - jkr_i + j(kr_i)^3/6$$

$$i = 0, 1, 2.$$

Using these approximations, (37) can be integrated [16] to yield (14) and (15). Although (15) is still rather lengthy, it can be further simplified to (16)–(18) for the examples in Section III.

References

[1] R. F. Harrington, "Matrix methods for fields," *Proc. IEEE*, vol. 55, pp. 136–149, Feb. 1967.

[2] ——, *Field Computation by Moment Method*. New York: Macmillan, 1968.

[3] W. L. Stutzman and G. A. Thiele, *Antenna Theory and Design*. New York: Wiley, 1981, ch. 7.

[4] G. A. Thiele, *Computer Techniques for Electromagnetics*. New York: Pergamon, 1973, ch. 2.

[5] E. K. Miller and F. J. Deadrick, *Numerical and Asymptotic Techniques in Electromagnetics*. New York: Springer, 1975, ch. 4.

[6] W. A. Inbriale, *Numerical and Asymptotic Techniques in Electromagnetics*. New York: Springer, 1975, ch. 2.

[7] J. H. Richmond, "Digital computer solution of the rigorous equations for scattering problems," *Proc. IEEE*, vol. 53, pp. 796–804, Aug. 1965.

[8] L. L. Tsai and C. E. Smith, "Moment methods in electromagnetics for undergraduates," *IEEE Trans. Educ.*, vol. E-21, pp. 14–22, Feb. 1978.

[9] R. F. Harrington, *Time-Harmonic Electromagnetic Fields*. New York: McGraw-Hill, 1971.

[10] Chen-To Tai, *Dyadic Green's Functions in Electromagnetic Theory*. Scranton, PA: Intext Education, 1971.

[11] R. E. Collin, "Equivalent line current for cylindrical dipole antennas and its asymptotic behavior," *IEEE Trans. Antennas Propagat.*, vol. AP-32, pp. 200–204, July 1984.

[12] J. H. Richmond, "Coupled linear antennas with skew orientations," *IEEE Trans. Antennas Propagat.*, vol. AP-18, pp. 694–696, Sept. 1970.

[13] S. A. Schelkunoff and H. T. Friis, *Antennas Theory and Practice*. New York: Wiley, 1952, pp. 369, 370.

[14] H. E. King, "Mutual impedance of unequal length antennas in echelon," *IEEE Trans. Antennas Propagat.*, vol. AP-5, pp. 306–313, July 1957.

[15] J. H. Richmond, "Radiation and scattering by thin-wire structures in a homogeneous conducting medium," *IEEE Trans. Antennas Propagat.*, vol. AP-22, p. 365, Mar. 1974.

[16] I. S. Gradsheyn and I. M. Ryzhik, *Table of Integrals, Series, and Products*. New York: Academic, 1980.

Edward H. Newman ████████████████
████████████████████████. He re-
ceived the B.S.E.E., M.S., and Ph.D. degrees in
electrical engineering from Ohio State University,
Columbus, in 1969, 1970, and 1974, respec-
tively.

Since 1974 he has been a member of the
ElectroScience Laboratory, Department of Elec-
trical Engineering, Ohio State University. His pri-
mary research interest is in the development of
method of moments techniques for the analysis of
general antenna or scattering problems, and he is the primary author of the
"Electromagnetic surface patch code" (ESP). Other research interests in-
clude electrically small antennas, superdirective arrays, printed circuit an-
tennas, and antennas in inhomogeneous media.

Dr. Newman is a member of Commission B of URSI, and is a past
chairman of the Columbus sections of the IEEE Antennas and Propagation
and Microwave Theory and Techniques Societies.